Stellingen

1. The structure of solid films, exhibiting surface mobility, can be uniquely determined by Monte Carlo simulation of the fluorescence anisotropy.

   (This Thesis, Chapter 4, 5)

2. By comparing the X-ray structure and the ratio of the intra- and inter-stack energy transfer rate constants in a two-dimensional model of porphyrin films the relative contributions of the Coulombic and exchange interaction to the transfer mechanism can be determined.

   (This Thesis, Chapter 5)

3. The economic effects of the inflow of foreign investments in countries with a developing market economy can be best predicted by Monte Carlo simulation of this process.

4. The start of an epidemic can only be analyzed effectively by Monte Carlo computer simulation.

5. The distribution of effort over time in marathon running can be optimized using Monte Carlo simulation.

6. Winter soccer matches, as exercised in Belarus, should be included to the program of the Olympic Games.

7. The chemistry of cooking is underdeveloped.

Stellingen belonging to the Thesis

"Computer simulation of energy relaxation and -transport in organized porphyrin systems"

Mikalai M. Yatskou

Wageningen, April 25, 2001

COMPUTER SIMULATION OF ENERGY RELAXATION AND -TRANSPORT IN ORGANIZED PORPHYRIN SYSTEMS

Mikalai M. Yatskou

Promotoren: Prof. Dr. Tjeerd J. Schaafsma
              Hoogleraar in de Moleculaire Fysica
              Wageningen Universiteit

              Prof. Dr. Vladimir V. Apanasovich
              Department of Systems Analysis
              Belarusian State University

Samenstelling promotiecommissie:

              Prof.dr. R. van Grondelle   (Vrije Universiteit Amsterdam)

              Prof.dr. J. Knoester   (Rijksuniversiteit Groningen)

              Prof.dr. E.J.R. Sudhölter   (Wageningen Universiteit)

              Prof.dr. B.M. Dzhagarov   (Institute of Molecular and Atomic Physics,

                                             National Academy of Sciences of Belarus, Minsk)

COMPUTER SIMULATION OF ENERGY RELAXATION AND -TRANSPORT IN ORGANIZED PORPHYRIN SYSTEMS

Mikalai M. Yatskou

To my parents who provided the opportunities and to my wife Anna for her love and understanding.

Contents

List of abbreviations

ET	Energy transfer
TCSPC	Time-correlated single photon counting
MC	Monte Carlo
FWHM	Full width at half maximum
WU	Wageningen University
BSU	Belarusian State University

Preface

Scope of the Thesis

The light harvesting of solar energy by plants and its conversion to chemically useful forms is a fascinating phenomenon, which sets an example how to use natural energy resources in an effective way. It is therefore highly relevant to construct a synthetic device that derives energy from sunlight by using the basic principles of natural photosynthesis. Of course this idea is not new and schemes for using energy from the sun have been around for hundreds of years. In the last tens years there has been increasing interest in synthetic organic molecular devices, including photodetectors, molecular semiconductors, light -harvesting systems, emitting diodes, solar cells, etc [1,2,3,4,5,6,7,8]. Organic materials as compared to inorganic have several advantages for these applications, i.e. low processing cost, large variety in molecular structures, and the natural character of energy transformation [9,10,11]. From experience with other opto-electronic devices it can be concluded that it is of critical importance to construct the synthetic solar cells in the form of ultra thin solid organic films. Recently, in particular such films of porphyrins have gained much interest because the porphyrins are well-known as the initiators of many biological processes in nature [12] and attractive chemical species for the construction of self-organizing structures [13,14,15] that provide insight into the mechanisms of biological processes such as photosynthesis. The porphyrin compounds also occupy a relevant position in the rapidly developing field of supramolecular chemistry [16,17], since these compounds are frequently used as building blocks for the construction of artificial systems, designed to feature a number of functions [18], i.e. light-harvesting and charge separation, as also occur in photosynthesis. The photophysical properties of thin porphyrin films mainly related to the mechanisms of electronic and hole conduction, energy transfer, and radiationless deactivation, etc. are still far from completely understood. This is a one of the strongest motivations for the work reported in this Thesis.

Thin organic films used in photovoltaic cells may contain one or more photoactive molecular layers. In binary cells the layers act as an energy donor and –acceptor, respectively [19,20,21]. The efficiency of these films may be improved by making use of a light-collecting antenna transferring the excitation energy to the photoactive region of the cell, where charge separation takes place. The main subjects of the study of the thin porphyrin films are:

1. The structure and photophysical properties of a tetrameric porphyrin model system self-organizing into a tetramer, exhibiting internal energy transfer.

2. The structure and photophysics of a self-organizing porphyrin layer on an inert substrate.

3. The energy transfer processes in these films and the transfer efficiency analyzed by simulation techniques, with the application as a light-harvesting antenna in solar cells devices in mind. The understanding of energy transfer and excited state relaxation following excitation in thin porphyrin films is still in an early stage.

Goals of this work

This Thesis can be considered as a combination of advanced computer simulation algorithms and the molecular photophysics of porphyrins. This combined approach has resulted in unique methods to analyze the complex time-dependence of the fluorescence decay and fluorescence polarization anisotropy of the porphyrin oligomers in solution as well as in thin solid films in the presence of energy transfer and relaxation. There are several goals to be pursued during the development of a computer simulation approach for the analysis of energy relaxation and energy transport processes in the organized porphyrin systems:

- Elucidating the steady state and time-resolved spectroscopy of self-organized tetramers of substituted porphyrin compounds in solution.

- Obtain quantitative data on energy relaxation and transport processes in thin organic solid films of substituted porphyrin using the developed computer simulation method.

Monte Carlo simulation methods [22,23,24,25] are often an effective approach to analyze the processes involving excitation energy transport in a variety of systems [26,27]. This Thesis employs a more general approach resulting in the combination of Monte Carlo simulations and the appropriate optimization algorithms. Usually, the optimization algorithms [28,29,30,31] are used with well-known analytical expressions, which are often far too simple to describe the real physical processes. For the interpretation of the experimental data making use of computer simulations these methods have to be carefully analyzed. The new computer-simulation method has been proven to be a powerful tool for the exploration of the systems for which energy relaxation and -transport processes are difficult to analyze by analytical approximations.

2

The research reported in this Thesis relates to several organized porphyrin systems starting from model systems in organic solvents and finishing with solid porphyrin films, containing two different porphyrins, one acting as an energy donor and the other as an energy acceptor.

A logical way to investigate the above mentioned processes in defined porphyrin systems would lead to the following systems:

i) self-organized tetramers of substituted porphyrin compounds in various organic solutions;

ii) solid films of self-organized tetramers as a model system for more complex porphyrin films;

iii)ordered assemblies of substituted porphyrin compounds on an inert substrate;

iv)solid porphyrin films containing two different porphyrins (donor – acceptor pair).

Subjects i), iii) and iv) have been successfully completed, subject ii) needs further investigation.

A number of tetra-phenyl-porphyrin derivatives including zinc tetraphenylporphyrin (ZnTPP), zinc mono-(4-pyridyl)-triphenylporphyrin (ZnM(4-Py)TrPP), zinc tetra-(octylphenyl)-porphyrin (ZnTOPP), copper tetra-(octylphenyl)-porphyrin (CuTOPP), free base tetra-(octylphenyl)-porphyrin (H_2TOPP) etc. were investigated, representing the abovementioned systems. The photophysical and self-organizing properties in majority of these porphyrins are described in detail in literature [32,33,34,35,36,37].

History

Survey of porphyrin aggregates and assemblies. Various types of porphyrin aggregates and assemblies have been designed and synthesized with the goal of applying these molecular oligomers to molecular photonic devices and artificial light-harvesting systems. Frequently the construction porphyrin aggregates is based on the use of several types of linking groups usually *via* meso position attachment. These include porphyrin structures joined by ethene-, ethyne-, butadiyne-, furan-, enyne-, hexatriene-, p-phenylene-, phenylethene-, biphenyl-, pyridine-linkage, etc [38,39,40,41,42,43,44]. Although there are a large variety of these pigments and linkage structures, the particular choice of the most suitable attachment is mainly determined by their function in a particular application, since the number of porphyrin units in the aggregate, their size, and their spectral- and electronic properties strongly affect the overall photophysical properties of the organized porphyrin system.

The various types of connecting motifs can be divided into two basic groups:

i) side-by-side connection involving the formation of covalent links between the porphyrin rings (usually at the meso position);

ii) side-to-face connection which usually involves axial coordination of one porphyrin by a substituent at the meso position of another porphyrin.

Using these and other connection motifs a large variety of multi-porphyrin systems have been made in the past and recent years with different shape, 3D architecture, and functions [45,46,47,48,49]. Notable examples of different multi-porphyrin systems, e.g. linear and star-shaped pentamers, dimeric, trimeric and large linear or cyclic porphyrin arrays and polymers, etc. have been reported in literature [50,51,52,53,54,55,56]. Recently, much attention has been paid to porphyrin oligomers of metalloporphyrins such as Zn-(tetraphenyl)porphyrin derivatives. These compounds are interesting as they show rather easily detectable S_2 fluorescence, are simple building blocks for the construction of molecular aggregates and are still effective for energy transport without too large losses due to radiationless transitions. Various Zn porphyrin structures and aggregates have been synthesized and analyzed in different organic solutions [8,37,57,58,59,60,61]. These investigations have provided a useful database for the photophysical properties and self-organization of Zn-porphyrins in solutions. These properties could be effectively used in understanding those properties in thin organic films, but on the other hand, and in contrast with dilute solutions, intermolecular interactions between neighboring molecules in solid, undiluted dye films cannot be neglected. In thin layers of solid films the photophysics of self-organized porphyrin assemblies are often affected by the effects of a changed environment resulting from their close packing and ordering in large assemblies of aggregates in (micro)crystalline structures. A systematic approach of the photophysical properties of these solid films may therefore start with a study of the photophysics and excited state kinetics of well-defined aggregates.

History of porphyrins films. The first thin films of organic molecules were synthesized in the second half of last century and the interest to investigation of them has been rapidly growing since the end of seventieth tears of last century [62,63,64,65,66,67,68]. Much less attention have been paid for the thin porphyrin films especially to that of Zn-porphyrins. From the limited list of these researches the works of Gregg [69], Takahashi [70], Fleischer [34], Krupitsky [37], Schaafsma [71], Savenije [72], Leray [73], Kanayama [74], Donker [75] could be selected in view of this Thesis.

History of energy transfer processes in porphyrin assemblies. The recent progress in synthesizing capabilities of various porphyrin aggregates in solutions and solid films raises a

fundamental question regarding the relation between the photophysical properties, in particular energy relaxation and transport and the molecular architecture. Natural systems have the unique property of extremely efficient energy transfer even over long distances. Although much progress has been made in understanding the photophysics of such complex systems, the excited state dynamics of organized porphyrin assemblies and the reasons for such high efficiency of energy transfer in natural systems are far from complete. The same is true for energy transport processes in liquid crystalline materials and thin films where relatively little work has been done [76,77,78,79,80,81].

The problems of energy transport in solid films can be outlined as follows: to act as an antenna layer the film should have strongly anisotropic transport properties, with the highest excitation mobility in the direction perpendicular to the substrate, with the charge separation (acceptor) layer. The excitation transport properties of the film are strongly influenced by the ordering, sizes of the porphyrin aggregates, the distances and the mutual orientation of the molecules in the film. Examples of ordered porphyrin structures for which the mechanism of intermolecular energy transfer is known in some detail are very limited, however [82,83,84,85,86,87].

The first theory of energy transfer was developed by Förster [88] based on the assumption of a weak interaction between the transition moments of the molecules participating in the energy transfer process. Then, this interaction could be approximated by a dipole-dipole interaction and the rate constant for energy transfer is proportional to the overlap integral of the absorption- and emission spectra. Although this theory often yields results that agree with the experimental data, the conditions under which it may be applied are still debated. Afterwards Dexter generalized this theory including multipole- and exchange interactions [89]. Although a large number of analytical expressions based Förster and Dexter theory approximations have been developed describing energy transfer phenomena observed *via* time-resolved fluorescence and fluorescence anisotropy, very often these expressions are unsuitable for complex, non-isotropic molecular systems, e.g. linear molecular aggregates in solution, liquid crystals, and solid films containing ordered domains [90,91,92,93,94]. There are several reasons why the application of these theories to energy transfer in thin porphyrin films is questionable:

i) sometimes it is hardly possible to sort the energy transfer process in the system with the mathematical expression for the analytical solving;

ii) often the analytical description is so complicated that its physical meaning is hidden;

iii) if the Förster radius is comparable with the molecular size the dipole-dipole approximation may not be valid, and one needs an extended dipole model or more terms of the multipole expansion;

iv) if important properties of the medium of the solid film are unknown, e.g. the refractive index, it may not be possible to calculate the rate constant for energy transfer.

History of Monte Carlo method for the problem of energy transfer in porphyrin aggregates. One of the most efficient non-analytical methods which in principle can describe the energy transfer processes in complex systems including non-isotropic ones is the Monte Carlo simulation method [24,25,95]. Although this method has been used extensively to test the validity of the approximations made in analytical theories [96,97,98,99], its possibilities stretch much further. One of the advantages of simulating energy transfer processes in molecular assemblies using Monte Carlo simulations is that it allows to understand straightforwardly how various parameters of the model affect the properties of the system, e.g. the time dependence of the absorption spectrum. Recently, Monte Carlo algorithms have been applied to several types of energy transfer mechanisms in isotropic as well as in non-isotropic molecular systems [90,92,93,94,95,97,98]. These algorithms need to assume *a priori* a particular type of energy transfer, i.e. by a Förster-, multipole- or exchange mechanism. Often, in systems with donor-acceptor distances comparable to the molecular dimensions such an *a priori* assumption cannot be made, however, since it is then unclear to what extent each mechanism contributes to the energy transfer process.

Questions

Summarizing the history excursion, there are a number of key questions to be asked:

- What are photophysical properties of self-organizing porphyrin aggregates in organic solvents and in solid films?

- How are the porphyrin structures formed in solid films?

- How quantitatively and qualitatively explain energy transfer occurring in self-organized porphyrin structures?

- What is the efficiency of the energy transfers and how can it be improved?

This Thesis addresses in particular the following questions:

6

- How can the Monte Carlo simulation method be used for the analysis of energy transfer processes in porphyrin aggregates in solid films?

- What are the photophysical properties of self-organizing porphyrin tetramers in organic solvents and solid films?

- How can the rate constants for energy transfer in self-organized tetramers in solution be explained qualitatively as well as quantitatively?

- What is the energy transfer efficiency in the system of ZnTOPP-CuTOPP/H_2TOPP spincoated films?

A general remark should be made about the computer simulations applied in this work. These simulations could also be used to determine the energy transfer parameters for a large variety of artificial molecular systems as well as synthetic non-molecular systems. The application facilities of the method are mainly limited by the power of the computer.

Contents

Chapter 1 introduces a theoretical description of the principles of artificial photosynthesis and time-resolved spectroscopy. The methods of time-resolved fluorescence measurements and their data analysis methods are reviewed. Computer modeling and principles of computer simulation approach are described.

Chapter 2 describes the porphyrin systems, which have been analyzed. Chemicals, experimental methods, equipment, and results of the photophysics of porphyrin systems are presented.

Chapter 3 treats the optimization methods for parametric fitting *via* Monte Carlo simulation of time-resolved fluorescence decays are analyzed. Also testing of the optimization methods and statistical criteria is performed on the examples of several analytical and simulation models. Error analysis and statistical characteristics of the estimated parameters are discussed.

Chapter 4 discusses the simulation model for energy transport and relaxation yielding time-resolved fluorescence and fluorescence anisotropy decay. The simulation-based fitting of energy relaxation processes are tested and the results of the tests discussed.

Chapter 5 describes the photophysics of organized porphyrin systems. Steady state spectra are described by simple Kasha theory and non-calorimetric thermodynamic method. Computer

simulations of energy transfer processes in self-organized porphyrin tetramer and porphyrin aggregates on the quartz films are presented. The results of computer simulations are discussed and compared with Förster theory.

References

[1] M. Quillec (1996) *Materials for Optoelectronics* Kluwer Academic Publishers, Boston.

[2] S. Donati (2000) *Photodetectors, Devices, Circuits and Applications* Plenum Press, New York.

[3] S.R. Das (1983) *Thin Film Solar Cells* Plenum Press, New York.

[4] J.J. Andre, K. Holczer, P. Petit, M.-T. Riou, C. Clarisse, R. Even, M. Fourmigue, J. Simon, *Chem. Phys. Lett.*, 115 (1985) 463.

[5] B.M. Hoffman, J.A. Ibers, *Acc. Chem. Res.*, 16 (1983) 15.

[6] B.A. Gregg, M.A. Fox, A.J. Bard, *J. Phys. Chem.*, 94 (1990) 1586.

[7] H.L. Anderson, S.J. Martin, D.D.C. Bradley, *Angew. Chem., Int. Ed. Engl.*, 33 (1994) 655.

[8] H.L. Anderson, *Inorg. Chem.*, 33 (1994) 972.

[9] J. Simon, J.J. André (1985) *Molecular Semiconductors* Springer-Verlag, Berlin.

[10] D. Wöhrle, D. Meissner, *Adv. Mater.*, 3 (1991) 129.

[11] K. Gurunathan, A. Vadivael Murugan, R. Marimuthu, U.P.Mulic, D.P. Amalnerkar, *Mat. Chem. Phys.*, 61 (1999) 173.

[12] D. Dolphyn (1978) *The Porphyrins* Vols. 1-5 Academic Press, New York.

[13] C.M. Drain, D. Mauzerall, *Biophys. J.*, 63 (1992) 1556.

[14] C.M. Drain, D. Mauzerall, *Biophys. J.*, 63 (1992) 1544.

[15] C. Liu, H.-I. Pan, M.A. Fox, A.J. Bard, *Science*, 261 (1993) 897.

[16] J.L. Atwood, J.E. Davies, D.D. MacNicol, F. Vögtle (1996) *Comprehensive Supramolecular Chemistry* Pergamon, Oxford.

[17] J.-M. Lehn (1995) *Comprehensive Supramolecular Chemistry: Concepts and Perspectives* WCH, Weinheim.

[18] V. Balzani, F. Scandola (1991) *Supramolecular Photochemistry* Horwood, Chichester, UK.

[19] T.J. Savenije, R.B.M. Koehorst, T.J. Schaafsma, *Chem. Phys. Lett.*, 244 (1995) 363.

[20] S. Günster, S. Siebentritt, D. Meissner, *Mol. Cryst. Liq. Cryst. A*, 230 (1993) 351.

[21] D. Wöhrle, B. Tennigkeit, J. Elbe, L. Kreienhop, G. Schnurpfeil, *Mol. Cryst. Liq. Cryst. A*, 230 (1993) 221.

[22] N. Metrpolis, A.W. Rosenbluth, A.H. Teller, E. Teller, *J. Chem. Phys.*, 6 (1953) 1087.

[23] H. Gould, J. Tobocknik (1988) *Computer Simulation Methods* Addison-Wesley, Reading, MA.

[24] R. Rubinstein, A. Shapiro (1998) *Modern Simulation and Modelling* John Willey & Sons Inc., New York.

[25] K. Binder, D.V. Heerman (1992) *Monte Carlo Simulation in Statistical Physics* Springer-Verlag, Berlin.

[26] S. Ohmori, S. Ito, M. Yamamoto, *Macromolecules*, 42 (1991) 2377.

[27] B. Kalman, L.B.-Å. Johansson, M. Lindberg, S. Engström, *J. Phys. Chem.*, 93 (1989) 8371.

[28] R. Flecher (1987) *Practical Methods of Optimization* John Willey & Sons Inc., New York.

[29] D.M. Himmelblau (1970) *Process Analysis by Statistical Methods* John Willey & Sons Inc., New York.

[30] P.E. Gill, W. Murray, M.A. Saunders, M.H. Wright (1989) *Practical Optimization* Academic Press, New York.

[31] P.R. Bevington (1969) *Data Reduction and Error Analysis for the Physical Sciences* McGraw-Hill, New York.

[32] J.V. Nardo and J.H. Dawson, *Inorg. Chem. Acta.*, 123 (1986) 9.

[33] E. Alessio, S. Gremia, S. Mestroni, E. Iengo, I. Srnova, M. Slof, *Inorg. Chem.*, 38 (1999) 869.

[34] E.B. Fleiscer and A.M. Shachter, *Inorg. Chem.*, 30 (1991) 3763.

[35] A.M. Shachter, E.B. Fleiscer, R.C. Haltiwanger, *J. Chem. Soc. Chem. Commun.*, (1998) 60.

[36] I.V. Rubtsov, Y. Kobuke, H. Miyaji, K.Yoshihara, *Chem. Phys. Let.*, 308 (1999) 323.

[37] H. Krupitsky, Z. Stein, I. Goldberg, *J. Inclusion Phenom. and Molec. Recognit. Chem.*, 18 (1994) 177.

[38] H. Higuchi, M. Takeuchi, J. Ojima, *Chem. Lett.*, (1996) 593.

[39] V.S.-Y. Lin, S.G. DiMagno, M.J. Therien, *Science*, 264 (1994) 1105.

[40] D. Arnold, L. Nitschinsk, *Tetrahedron Lett.*, 48 (1992) 8781.

[41] D. Arnold, L. Nitschinsk, *Tetrahedron Lett.*, 48 (1992) 972.

[42] M.G.H. Vicente, K. Smith, *J. Org. Chem.*, 56 (1991) 4407.

[43] A. Osuka, B.-L. Lui, K. Maruyama, *Chem. Lett.*, (1993) 949.

[44] A. Burrell, D. Officer, D. Reid, *Angew. Chem, Int. Ed. Engl.*, 34 (1995) 900.

[45] V. Marvaud, J.-P. Launay, *J. Am. Chem. Soc.*, 109 (1993) 1376.

[46] M. Ikonen, D. Guez, V. Marvaud, D. Markovitsi, *Chem. Phys. Lett.*, 231 (1994) 93.

[47] C.J. Walters, H.L. Anderson, J.K.M. Sanders, *J. Chem. Soc. Chem. Commun.*, (1993) 458.

[48] P.N. Taylor, A.P. Wylie, J. Huuskonen, H.L. Anderson, *Angew. Chem.*, *Int. Ed. Engl*, 110 (1998) 1033.

[49] C.M. Drain, J.-M. Lehn, *J. Chem. Soc. Chem. Commun.*, (1994) 2313.

[50] J. Davila, A. Harriman, L.R. Milgrom, *Chem. Phys. Lett.*, 136 (1987) 427.

[51] A. Prodi, M.T. Indelli, C.J. Kleverlaan, F. Scandola, E. Alessio, T. Gianferrara, L.G. Marzilli, *Chem. Eur. J.*, 5 (1999) 2668.

[52] K. Ichihara, Y. Naruta, *Chem. Lett.*, (1995) 631.

[53] A. Osuka, N. Tanabe, S. Nakajima, K. Maryama, *J. Chem. Soc., Perkin. Trans.2*, (1996) 199.

[54] H. Aota, Y. Itai, A. Matsumoto, M. Kamachi, *Chem. Lett.*, (1994) 2043.

[55] D.L. Officer, A.K. Burrell, D.C.W. Reid, *Chem. Commun.*, (1996) 1657.

[56] T. Nagata, A. Osuka, K. Maruyama, *J. Am. Chem. Soc.*, 112 (1990) 3054.

[57] F. Li, S. Gentemann, W.A. Kalsbeck, J. Seth, J.S. Lindsey, D. Holten, D.F. Bocian, *J. Mater. Chem.*, 7 (1997) 1245.

[58] H.S. Cho at al., *J. Phys. Chem. A*, 104 (2000) 3287.

[59] D. Lawrence, I. Jiang, M. Levett, *Chem. Rev.*, 95 (1995) 2229.

[60] P.J. van Patten, A.P. Shreve, J.S. Lindsey, R.J. Donohoe, *J. Phys. Chem. B*, 102 (1998) 4209.

[61] K. Takahashi, T. Komura, H. Imanaga, *Bull. Chem. Soc. Jpn.*, 62 (1989) 386.

[62] F.J. Kampas, K. Yamashita, J. Fajer, *Nature*, 40 (1980) 284.

[63] K. Yamashita, *Chem. Lett.*, (1982) 1085.

[64] K. Yamashita, Y. Harima, Y. Matsumura, *Bull. Chem. Soc. Jpn.*, 58 (1985) 1761.

[65] G.E. Fanucci, C.R. Bowers, and D.R. Talham, *J. Am. Chem. Soc.*, 121 (1999) 1088.

[66] T.-A. Pham et al., *Chem.Phys.Lett.*, 318 (2000) 459.

[67] M.A. Petruska, D.R. Talham, *Chem. Mater,* 10 (1998) 3672.

[68] G.E. Fanucci, C.T. Seip, M.A. Petruska, C.M. Nixon, S. Revaine, D.R. Talham, *Thin Solid Films,* 327-329 (1998) 331.

[69] B.A. Gregg, M.A. Fox, A.J. Bard, *J. Phys. Chem.*, 93 (1989) 4227.

[70] K. Takahashi, T. Komura, H. Imanaga, *Bull. Chem. Soc. Jpn.*, 62 (1989) 386.

[71] T.J. Schaafsma, *Sol. Energy Mat. Sol. Cells*, 38 (1995) 349.

[72] T.J. Savenije (1997) *Ph.D. Thesis "Artificial Photosynthesis Towards the Development of Molecular Photodiodes"*, Wageningen, The Netherlands.

[73] I. Leray, M.C. Verniéres, R. Pansu, C. Bied-Charreton, J. Faure, *Thin Solid Films*, 303 (1997) 295.

[74] N. Kanayama, T.Kanbara, H. Kitano, *J. Phys. Chem. B*, 104 (2000) 271.

[75] H. Donker, R.B.M. Koehorst, A. van Hoek, W. van Schaik, M.M. Yatskou, T.J. Schaafsma, submitted to *J. Phys. Chem B.*

[76] B. Blanzat, C. Barthou, N. Tercier, J.J. André, J. Simon, *J. Am. Chem. Soc.*, 109 (1987) 6193.

[77] J. Blasse at al., *Chem. Phys. Lett.*, 154 (1989) 420.

[78] D. Markovitsi at al., *Chem. Phys. Lett.*, 135 (1987) 236.

[79] D. Markovitsi at al., *J. Am. Chem. Soc.*, 110 (1988) 2001.

[80] U. Gómesz, M. Leonhardt, H. Port, H.C. Wolf, *Chem. Phys .Lett.*, 268 (1997) 1.

[81] B. Richter, S. Kirstein, *J. Chem. Phys.*, 111 (1999) 5191.

[82] J.S. Lindsey, P.A. Brown, D.A. Siesel, Tetrahedron, 45 (1989) 4845.

[83] D. Gust at al., *J. Am. Chem. Soc.*, 107 (1985) 3631.

[84] D. Gust at al., *J. Am. Chem. Soc.*, 114 (1992) 3590.

[85] R. Hermant at al., *J. Am. Chem. Soc.*, 115 (1993) 2080.

[86] F. Effenberger at al., *Angew Chem.*, *Int. Edn. Engl.*, 27 (1988) 281.

[87] A. Osuka at al., *J. Am. Chem. Soc.*, 115 (1993) 9439.

[88] T. Förster, *Ann. Physik.*, 2 (1948) 55.

[89] D.L. Dexter, *J. Chem. Phys.*, 21 (1953) 836.

[90] D. Markovitsi at al., *J. Phys. Chem.*, 99 (1995) 1005.

[91] C. Bacchiocchi, C. Zannoni, *Chem. Phys. Lett.*, 268 (1997) 541.

[92] M.N. Berberan-Santos, P. Choppinet, A. Fedorov, L. Jullien, B. Valeur, *J. Am. Chem. Soc.*, 121 (1999) 2526.

[93] N. Sato, S. Ito, K. Sugiura, M. Yamamoto, *J. Phys. Chem. A*, 103 (1999) 3402.

[94] L.M.S. Loura, M.Prieto, *J. Chem. Phys. B*, 104 (2000) 6911.

[95] L. Andrews, A. Demidov (1999) *Resonance Energy Transfer* John Willey & Sons LtdInc., New York.

[96] S.C. Harvey, H.C. Cheung., *Proc. Nat. Acad. Sci. USA*, 69(12) (1972) 3670.

[97] M.N. Berberan-Santos, B. Valeur, *J. Chem. Phys.*, 95(11) (1991) 8049.

[98] L.B.Å. Johansson, S. Engström,M. Lindberg, *J. Phys. Chem.*, 96(5) (1992) 3845.

[99] D.M. Hussey, S. Matzinger, M.D. Fayer, *J. Chem. Phys.*, 109 (1998) 8708.

Chapter 1

General Introduction

This Chapter describes the elementary photophysical processes, which play a crucial role in artificial photosynthesis, as an introduction to the porphyrin systems investigated in this Thesis. The basics of time-resolved fluorescence spectroscopy and -measurements to characterize these processes are reviewed, including the methods of data analysis for the time domain spectroscopy. Modeling concepts and computer methods to analyze the experimental data by simulating the photophysical processes are discussed.

1.1. Photophysical processes in artificial photosynthesis

Natural photosynthesis [1,2] comprises a host of biochemical processes which convert sunlight into energy-rich products, which are necessary for the growth and the reproduction of organisms [3,4]. The primary steps of this process concern the collection of light and its conversion to chemical potential energy by electronic charge separation. The photosynthetic process starts with absorption of light by the antenna system of the organism, usually consisting of chlorophyll and a number of other pigments. This antenna system collects light energy in various regions of the solar spectrum and transfers the absorbed photon energy with transfer rates of ~ 1 ps^{-1} to a reaction center where photochemistry occurs. In the reaction center charge separation occurs so that the produced electrons can reduce carbon dioxide in a long chain of biochemical events, eventually resulting in storage of the captured photon energy in the form of chemical energy.

Artificial photosynthesis [5] is broadly defined and includes many fields of science, for example solid-state physics, chemistry, biochemistry, organic and inorganic chemistry [6,7,8,9]. The primary objects in artificial photosynthesis research are

- how to induce energy- and/or charge transfer from a donor in one of its excited states to a final acceptor at a time-scale faster then other optical processes involving these excited states;

- how to improve the efficiency of the charge separation process and stabilize the charged products in a photochemical reaction center.

The Thesis deals with the first subject.

Charge transfer in photosynthesis is a widely studied mechanism [10,11,12,13,14,15,16]. Many groups have investigated charge- and in particular electron transfer processes in porphyrin dimers, -trimers, -dyads, and analogous compounds [17,18,19,20,21]. These studies have shown, that the distance and relative orientation of the electron donor and –acceptor components in these compounds are of crucial importance for fast charge separation, requiring a high degree of organization. In view of these findings, self-assembling porphyrin oligomers and self-organizing films are very interesting candidates for artificial photosynthetic devices, in particular organic solar cells [15,18,20]. There are relatively few studies of ET in such systems, however. In this work mainly ET processes in the organized porphyrin systems have been investigated. Therefore, this Chapter focuses on radiationless ET and the subsequent photophysical processes involving the porphyrin excited states.

Generally, the chromophores in a molecular system, playing a role of a synthetic antenna, can be divided in energy donor and -acceptor molecules. The donors absorb incident excitation light and thereby are excited to one of the singlet states S_n or triplet states T_n. The excitation energy is subsequently transferred directly or trough several donor units to one or more acceptors, usually the system components where charge separation takes place. The photophysical processes occurring in the excited states of a donor and acceptor chromophore are illustrated by the Jabłoński diagram [22] (Fig. 1).
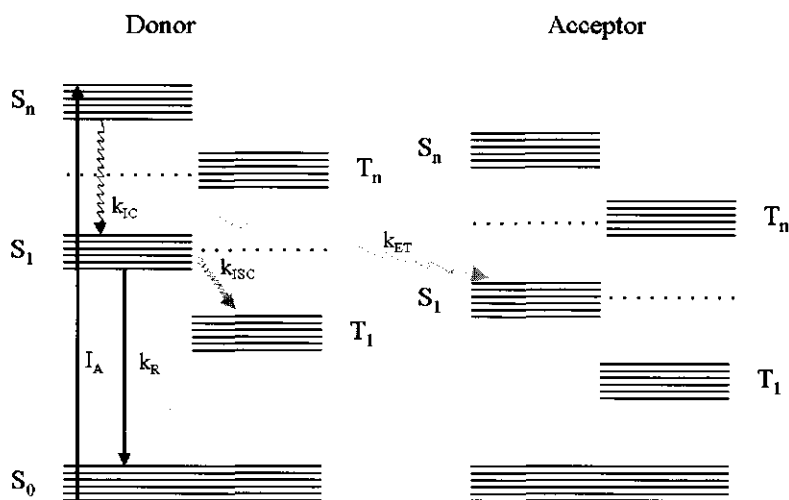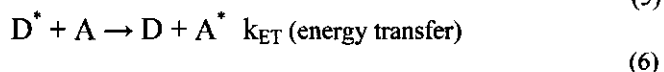

Fig.1. Jabłoński diagram for photophysical processes in donor-acceptor molecular systems.

This simple kinetic scheme for the various processes following donor (D) singlet excitation represents the following equations:

$$D + h\nu \rightarrow {}^1D^* \qquad I_A \text{ (absorption)}$$

(1)

$$^1D^* \rightarrow D + h\nu \qquad k_R \text{ (fluorescence)}$$

(2)

$$^1D^* \rightarrow {}^3D^* \qquad k_{ISC} \text{ (intersystem crossing)}$$

(3)

$$^1D^* \rightarrow D \qquad k_{IC} \text{ (internal conversion)}$$

(4)

$$^1D^* \rightarrow \text{products} \qquad k_D \text{ (formation of products)}$$

(5)

$$D^* + A \rightarrow D + A^* \qquad k_{ET} \text{ (energy transfer)}$$

(6)

The energy relaxation processes in the donor excited states competing with non-radiative energy transfer to an acceptor (A) are:

- vibrational relaxation to the lowest excited singlet state followed by radiative or non-radiative fluorescence decay,

- intersystem crossing to the triplet manifold with subsequent phosphorescence,

- internal conversion to the ground state,

- photochemical reaction [23].

These energy relaxation pathways have been widely investigated for a variety of molecular systems in solution as well in solids [24].

An important topic of interest in organized porphyrin systems concerns the radiationless excitation energy transfer processes and its efficiency, both for basic reasons and with applications in mind. A large number of studies have been devoted to radiationless ET processes in various molecular systems [25,26,27,28,29,30] following the classic discoveries of Förster [31], Dexter [32], and Galanin [33]. According to these theories all ET mechanisms can be distinguished in three basic groups on the basis of the mutual donor-acceptor interaction and their environment:

Coulombic ET. This type of ET usually occurs at distances that are much less than the emission wavelength. For allowed transitions the main contribution to energy transfer is due to dipole-dipole interactions given by

$$E_{dd} = \frac{\mu_D \cdot \mu_A}{R^3} - 3\frac{(\mu_D \cdot R)(\mu_A \cdot R)}{R^5}$$

(7)

where μ_D and μ_A are the transition dipole moments of donor and acceptor, respectively, and R is the center-to-center distance between μ_D and μ_A. Following from eqn. (7) the dipole-dipole interaction energy can be related to the angles θ_1, θ_2, φ defining the mutual orientation between the transition dipole moments

$$\kappa(\theta_1, \theta_2, \varphi) = \sin\theta_1 \sin\theta_2 \cos\varphi - 2\cos\theta_1 \cos\theta_2$$

(8)

where $\kappa(\theta_1, \theta_2, \varphi)$ is the orientation factor (see below), θ_1 and θ_2 are the angles between μ_D and R, and μ_A and R, respectively; φ is the azimuth angle between μ_D and μ_A. Typically, for porphyrins $E_{dd} < 10$ cm^{-1} ~ 10^{-3} eV.

The Coulombic energy transfer rate constant k_{dd} is then given by

$$k_{dd} = k_R^D \kappa^2 \left(\frac{R_0^{dd}}{R} \right)^6$$

(9)

where k_R^D is the rate constant for radiative decay of the energy donor and R_0^{dd} is the critical or Förster distance at which the energy transfer is 50% efficient; k_{dd} can be calculated from

$$R_0^{dd} = \frac{9000\,(\ln 10)\,q_D}{128\pi^5 n^4 N_A} \int_0^\infty Em_D(\lambda)\varepsilon_A(\lambda)\lambda^4 d\lambda$$

(10)

where q_D is the absolute fluorescence quantum yield of the unquenched energy donor, n is the solvent refractive index, N_A is Avogadro's number, Em_D is the normalized donor emission spectrum, and ε_A is the acceptor extinction coefficient.

Eqn. (7) shows that the probability of Coulombic energy transfer is proportional to $1/R^6$ and the spectral overlap of the donor emission and the acceptor absorption spectra. The spectral overlap, and thus the energy transfer rate constant k_{dd} decreases with decreasing temperature. For the interacting porphyrins the Coulombic energy transfer rate constants are in the range of 0.1 - 500 ps^{-1}. Typical distances of the Coulombic ET for the interacting porphyrin molecules are 5 - 60 Å.

In principle Coulombic energy transfer may also occur through singlet - triplet or triplet - singlet excited states of energy donor and -acceptor molecules, respectively. Although these transitions are forbidden, they often compete successfully with radiative emissions.

Multipole ET. Sometimes the dipole transitions are not allowed and ET can be due to multipole interactions, for example dipole-quadruple, quadruple - quadruple, or exchange interactions (see below).

For dipole-quadruple interaction, the energy transfer constant is given by

$$k_{dq} = k_R^D k_R^A \frac{135\,\pi\,\eta c^8}{4R^8} \int_0^\infty Em_D(\lambda)\varepsilon_A(\lambda)\lambda^8 d\lambda$$

(11)

where k_R^A is the rate constant for radiative decay of the energy acceptor and c is light speed in vacuum. According to eqn. (11) the probability of dipole-quadruple energy transfer is proportional to $1/R^8$; for quadruple - quadruple energy transfer is $\sim 1/R^{10}$ whereas dipole-dipole energy transfer is $\sim 1/R^6$.

Exchange ET. In this case energy transfer can occur including triplet excited states or more generally using excited states of different multiplicity. The physical reason for the exchange ET is an overlap of the electron wavefunctions of donor and acceptor molecules.

For the exchange interaction the transfer rate is given by

$$k_{Exc} = \frac{2\pi}{\eta} e^{-2R/L} \int_0^\infty Em_D(\lambda)\varepsilon_A(\lambda) d\lambda$$

(12)

where L is the average effective Bohr radius. Typical distances for exchange-controlled ET between the interacting porphyrin molecules are 1 - 4 Å.

It should be noted that exchange ET can also be operative for singlet-singlet transitions if the molecules form a tight-bonded complex.

Diffusion collisional ET. The theory of the diffusion collisional ET applies if there is diffusional molecular motion. Then, the excited donor molecule moves towards an unexcited acceptor and an encounter of both within a certain energy transfer distance causes excitation of the acceptor.

The rate constant for the diffusion collisional ET is time-dependent and in the simplest case obeys the Smoluchowski diffusion theory [34] which can be expressed as

$$k_{Dif} = 4\pi R \tilde{N}_A D\rho (1 + R\rho \sqrt{\pi D t})$$

(13)

where D is the diffusion coefficient, ρ is the ET probability per collision, and $\tilde{N}_A$ is the number density of the acceptors.

The diffusion collisional ET theory can be also applied to a migration of excitation energy in molecular crystals by excitons (see below).

Exciton ET. For strong molecular interaction with $E > 100$ cm^{-1} ($> 10^{-2}$ eV), then energy transfer can be faster than vibration relaxation and – expressing this situation in popular terms -the excitation has no time to become localized at a particular molecule. In this case the wavefunction describing the excitation has a finite amplitude at a set of molecules up to several hundreds. This coherent, mobile excitation is called an exciton. This type of energy transfer is typical for molecular crystals.

In conclusion, with respect to the main energy transfer mechanisms it should be noted that:

- several ET mechanisms can act simultaneously especially when the intermolecular distances between donor- and acceptor molecules are comparable with their sizes;

- pure radiative ET processes are also possible;

- in solutions where additional molecular diffusion occurs collisional ET is often the dominant process.

Basic models for energy relaxation and – transport in molecular systems. For an ideal energy transfer system of static donor- and acceptor molecules in vacuum, separated by a constant distance R, the density probability function for the donor to be still excited after a period t is given by

$$f_D(t) = e^{-(k_R^D + k_{ET})t}$$

(14)

where k_{ET} is the rate constant for energy transfer from the excited donor to the ground state acceptor. In real physical systems in e.g. solution, condensed matter, and crystalline solids, the functional form of eqn. (14) gets more complicated since other factors, such as the spatial

distribution of molecules, the kind of intermolecular interaction must be included in eqn. (14). Some basic analytical models for energy relaxation in molecular systems of randomly distributed donors and acceptors in solutions are considered below.

The model of energy transfer in a donor acceptor system which is immobile at the time scale of energy transfer by Coulombic interactions was developed by M. Hauser *et al.* [35] and eqn. (14) takes the form

$$f_D(t) = e^{-k_R^D t} e^{-\int \left(1.5\kappa^2 (\tilde{c}_s / 6) a_s \Gamma(1-s/6)(R_0^{dd} \sqrt[6]{k_R^D})^s t^{(s/6)-1} \right) dx}$$

(15)

where s is the dimension of the system, $\Gamma(x)$ is the gamma function, $\tilde{c}_s$ is the volume or linear concentration of the acceptor molecules in one, two or there dimensions, respectively, and the spatial factor a_s is given by: $a_1 = 2$, $a_2 = 2\pi$, and $a_3 = 4\pi$.

According to the model for the Dexter mechanism of ET eqn. (14) can be written as [36]

$$f_D(t) = e^{-k_R^D t} e^{-(\pi/6)L^3 N_A g(k_R^D e^{2R_T/L} t)}$$

(16)

with

$$g(z) = -\int_0^1 e^{-zy} (\ln^3 y) dy$$

(17)

where R_T is the critical distance at which the exchange ET is 50% efficient, k_R^D is the rate constant for radiative decay of the energy donor and L is the average effective Bohr radius.

The model of diffusional ET in the presence of Coulombic ET has been developed by Yokota and Tanimoto [37], and then eqn. (14) is modified to

$$f_D(t) = e^{-k_R^D t} e^{-\Gamma(1/2)\tilde{c}(3\pi/4)(R_0^{dd})^3 \left(\frac{1+10.87x+15.5x^2}{1+8.743x} \right)^{3/4} \sqrt{k_R^D t}}$$

(18)

with

$$x = D\left((R_0^{dd})^6 k_R^D\right)^{-1/3} t^{2/3}$$

(19)

A variety of other models to describe the ET processes has been designed and successfully applied in studies of complex molecular systems using fluorescence and fluorescence anisotropy measurements [24,23,33,36,38].

1.2. Principles of the time-resolved fluorescence spectroscopy

Fluorescence lifetimes and quantum yields. Time-resolved fluorescence spectroscopy provides a powerful methodology for investigating the photophysical processes in excited states [23]. This potential is primarily a result of the lifetime of the excited states and quantum yield since these are the main characteristics of a fluorophore. The lifetime of the excited state is the average time the molecule spends in the excited state prior to its return to the ground state and is defined as

$$\tau = (k_R + k_{ISC} + k_{IC} + k_D + k_{ET})^{-1}$$

$$(20)$$

The lifetime determines the time available for the fluorophore to interact by energy transfer processes or diffusion with its environment, and hence the information available from its fluorescence emission.

The quantum yield is the number of emitted photons relative to the number of absorbed photons and is given as

$$q = k_R^{-1}/(k_R + k_{ISC} + k_{IC} + k_D + k_{ET})^{-1}$$

$$(21)$$

(see Fig. 1) Substances with strong emission have quantum yields approaching unity. Generally molecular fluorescence lifetimes are in the range of tens of nanoseconds. For example, the lifetimes of free base and zinc monomer porphyrins in organic solvents are typically 9 - 12 ns and 1.8 - 2.6 ns, and quantum yields are 0.1 - 0.14 and 0.02 - 0.04, respectively.

Fluorescence anisotropy. The second set of important characteristics like the shape, size, and orientation of a fluorophore, which are important for energy transfer processes, can be obtained through time-resolved fluorescence anisotropy spectroscopy [23]. The fluorescence anisotropy phenomenon is based on the principle of photoselective excitation of fluorophores by polarized light. Fluorophores preferentially absorb photons whose electric vectors are aligned parallel to the transition moment of the fluorophore. The transition moment has a defined orientation in the fluorophore. In an isotropic solution, the fluorophores are randomly oriented. Upon excitation with polarized light, one selectively excites those fluorophore molecules whose absorption transition dipole is parallel to the electric vector of the excitation. This selective excitation of a partially oriented population of fluorophores (photoselection) results in partially polarized

fluorescence emission. The transition moments for absorption and emission have fixed orientations within each fluorophore, and the relative angle between these moments determines the maximum measured anisotropy r_0. The fluorescence anisotropy r is defined by

$$r = \frac{I_\parallel - I_\perp}{I_\parallel + 2I_\perp}$$

(22)

where $I_\parallel$ and $I_\perp$ are the fluorescence intensities of the vertically ($\parallel$) and horizontally ($\perp$) polarized emission, when the sample is excited with vertically polarized light. Several phenomena can decrease the measured anisotropy to values lower than the maximum values of r_0, the most common being rotational diffusion and energy transfer.

Generally fluorescence spectroscopy can be broadly classified into two types, steady-state and time-resolved. Steady-state spectroscopy uses continuous excitation and emission. The recorded steady state fluorescence emission spectra (I_{SS}) or fluorescence anisotropy spectra (r_{SS}) are averaged in time and defined by eqns. (23) and (24).

$$I_{SS} = \int_0^\infty I(t)dt$$

(23)

$$r_{SS} = \frac{\int_0^\infty r(t)I(t)dt}{\int_0^\infty I(t)dt}$$

(24)

In time-resolved spectroscopy the sample is excited by a pulse of light with a pulse width which is typically shorter than the decay time of the sample. The emission is recorded with a high-speed detection system that permits the fluorescence intensity $I(t)$ or anisotropy $r(t)$ to be measured at the nanosecond or shorter timescale.

A fluorophore with a single lifetime τ and a single rotational correlation time ϕ such as for free base or zinc porphyrin in toluene (see Section 5.2.2), then the time-dependent fluorescence and anisotropy are given by eqns. (25) and (26) and their steady state values by eqns. (27) and (28), respectively.

$$I(t) = I_0 e^{-\frac{t}{\tau}}$$

(25)

19

where

$$r(t) = r_0 e^{-\frac{t}{\phi}}$$

(26)

where I_0 and r_0 are the intensities and anisotropy at $t = 0$, immediately following the excitation pulse. Note that

$$I_{SS} = I_0 \tau$$

(27)

and

$$r_{SS} = \frac{r_0}{1 + \frac{\tau}{\phi}}$$

(28)

In general, I_0 is a parameter that depends on the fluorophore concentration and a number of instrumental parameters; r_0 characterizes the shape of the fluorophore; the correlation time ϕ of the rotational diffusion processes is given by the Stokes-Einstein relation

$$\phi = \frac{\eta V}{kT}$$

(29)

where η is the viscosity of the solution, k is the Boltzmann constant, T is the absolute temperature, and V is the effective volume of the rotating molecule.

Whereas steady-state fluorescence measurements have the great advantage of being simple, time-resolved measurements frequently contain more information e.g. about lifetimes, the molecular shape and its flexibility, static and dynamic quenching, and energy transfer processes.

1.2.1. Time-resolved fluorescence measurements (review)

The methods of measuring the time-resolved fluorescence can be divided into two main groups: i) frequency-domain and ii) time-domain methods.

Frequency-domain methods [23]. Using frequency-domain methods the sample is excited by intensity-modulated light, typically using a sine wave modulation at a frequency which is high as compared to the reciprocal of the fluorescence lifetime τ. The emission is measured at the same modulation frequency. As a result of the finite lifetime of the sample, the emission is delayed in time relative to the moment of excitation. This delay is measured as a phase shift,

which can be used to calculate the lifetime. Since this Thesis deals with time-domain methods, no detailed description of the frequency-domain methods is presented here.

Time-domain methods [23]. In time-domain methods, the sample is excited with a pulse of light. The width of the pulse is made as short as possible and is preferably much shorter than the lifetime τ of the fluorophore. The time-dependent intensity is measured following the excitation pulse, and the lifetime τ is calculated from the slope of a plot of logarithm of the fluorescence intensity. There are a number of time-domain methods for time-resolved measurements:

Time correlated single photon counting method. The principles of TCSPC can be understood by inspection of a schematic diagram of the instrument (Fig. 2).
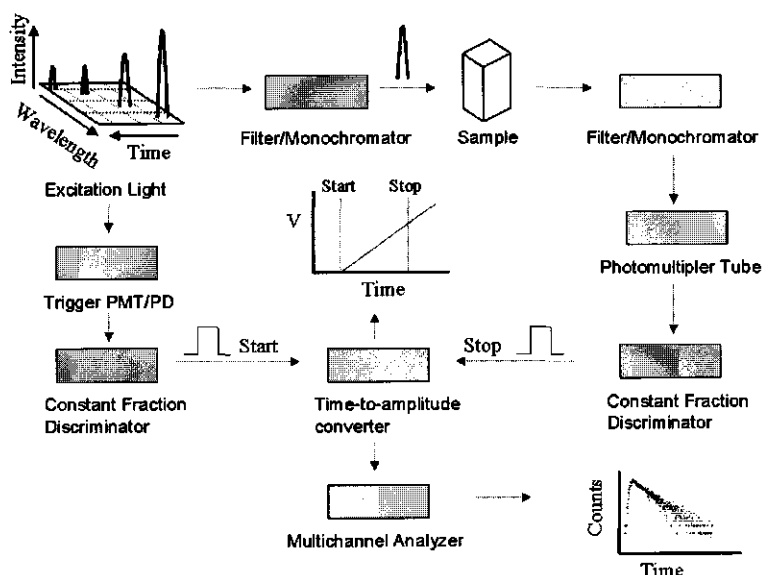
Fig.2 Schematic diagram of time-correlated single photon counting.

The experiment starts with the excitation pulse, which excites the sample and starts the time measurement clock. TCSPC is a digital technique, counting photons that are time-correlated in relation to the excitation pulse. The heart of the method is a time-to-amplitude converter, which can be considered to be analogous to a fast stopwatch. The sample is repetitively excited using a pulsed light source, often from a laser or flash lamp. A high-speed photodiode or photomultiplier optically monitors each pulse, to produce a start signal, which is used to trigger the voltage ramp of the time-to-amplitude converter. The voltage ramp is stopped when the first fluorescence photon from the sample is detected. The time-to-amplitude converter provides an output pulse

whose voltage is proportional to the time between the start and stop signals. A multichannel analyzer converts this voltage to a time channel using an analog-to-digital converter. Summing over many pulses, the multichannel analyzer builds up a probability histogram of counts versus time channels. The experiment is continued until one has collected more than 10^3 counts in the peak channel. Under these conditions, the histogram of photon arrival times represents the intensity decay of the sample. This measured intensity decay $F^E(t)$ is a convolution of the actual response function $i(t)$ of the sample with the δ-function of the lamp, usually represented by the finite instrument response function $e(t)$. Mathematically, the convolution decay can be written as

$$F^E(t) = e(t) \otimes i(t) = \int_0^t e(t-x)i(x)dx$$

(30)

Streak camera detection. Streak cameras have a time resolution of several picoseconds and an instrument response function of a few hundreds of femtoseconds, that is considerably faster than with TCSPC. Streak cameras operate by dispersing the photoelectrons across an imaging screen. This can be accomplished at high speed using deflection plates within the detector (Fig. 3).
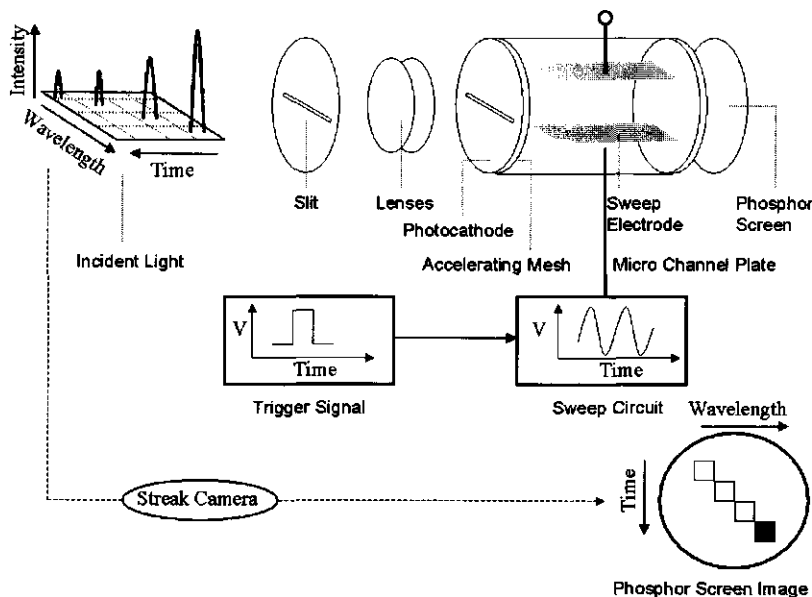

Fig. 3. Schematic diagram of streak camera.

The streak cameras allows simultaneous measurement of the wavelength and the time-resolved decays. Such data are valuable in the study of time-dependent spectral relaxation of samples that contain fluorophores emitting at different wavelengths. In spite of the high time resolution, the

22

streak cameras also have several disadvantages. The main disadvantage is the low dynamic range of the measured intensities. Also, the signal-to-noise ratio is poor compared to that for TCSPC. These factors limit the ability of streak cameras to resolve complex decays.

Upconversion methods. The extremely high time resolution is achieved by methods which bypass the limited time resolution of the detectors and rely on the picosecond and femtosecond pulse widths available with modern lasers. The basic idea is to pass the fluorescence signal through an upconversion crystal and to gate the crystal with another picosecond or femtosecond light pulse. One observes the shorter-wavelength harmonic generated by the combined effects of the laser pulse and the emission. The intensity decay is sampled by sweeping the gating pulse with a time delay. The time resolution is determined by the width of the laser pulse. The signals are typically weak, so that an optical chopper and lock-in detector are needed to measure the upconverted signal in the presence of considerable background. The time-resolved decay is obtained by measuring the intensity of the upconverted signal as the delay time is varied. Also, decay times of more than 1 - 2 ns are difficult to measure owing to the use of a delay line (~1 ns/ft). Alignment of the delay line can be difficult to maintain as the time delay is altered.

Gated detection. The basic idea of gated detection is to sample the intensity decay repetitively following pulsed excitation. The detection gate is displaced across the intensity decay until the entire decay is measured. Gated detection can be accomplished in two ways: i) the first method is to turn on or gate the gain of the detector for a short period during the intensity decay. This can be accomplished at a timescale adequate for measurement of nanosecond lifetimes; ii) the detector can be on during the entire decay, and the electrical pulse measured with a sampling oscilloscope. In such a set up such devices can sample electrical signals with a resolution of tens of picoseconds. An advantage of this method is that one can detect many photons per lamp pulse, which should provide improved statistics. A disadvantage of this method is the lack of knowledge of the noise level for each data point, so that one needs to estimate the experimental uncertainties during data analysis.

1.2.2. Methods for the analysis of the TCSPC data (review)

The methods for analyzing the TCSPC data are used to solve eqn. (30), i.e. the deconvolution of $I(t)$ to calculate the fluorescence and anisotropy decay parameters. The most commonly used methods are briefly reviewed here.

Nonlinear least squares [39]. Curve fitting using nonlinear least squares techniques is the most widely used method of deconvolution to solve eqn. (30). The method usually involves linearization of the fitting function and a least squares solution. Because the method is a statistical fitting method, large data sets must be used to insure the validity of the results. As in any fitting procedure, the parameters derived from it should be judged against a physically meaningful model. Several nonlinear least squares methods are analyzed in Chapter 3 of this Thesis.

Method of moments [40]. The second most popular deconvolution method is the so-called method of moments. This method is only used for a multiexponential decay functions. The idea of the method is as follows:

i) definition of a statistical moment for all the j parameters for both the decay function $f(t)$ and the excitation function $e(t)$;

ii) transformation of eqn. (30), using a statistical moment, to a set of $2n$ linear equations;

iii) solving the $2n$ equations by determinant methods to produce the n values of τ that are further used to yield the pre-exponential factors.

Phase plane method [40]. This method is suitable for single exponential decays for which the lifetime is relatively long compared to the excitation pulse. It is a linearization method which, similar to others, directly delivers τ as a slope of a line. Advantages of this method are the extreme ease of the method and the sensitivity of the plots to non-exponentiality. However, because of the widespread availability of computers capable of performing least-squares and other more sophisticated methods of analysis at higher precision than the phase plane method, the use of this method is declining.

Transform methods [40,45]. The basic convolution eqn. (30) can be transformed using either Laplace or Fourier formalisms and the transformed equations solved. However, since the transformed equations run over infinite time while the data runs only to finite times, immediate problems arise concerning how to judge the convergence. That is, cut off corrections are required. Iterative techniques are employed to judge the cut off, and in general suitable convergence can be obtained after five iterations. For multiple exponential decays where the lifetimes are similar ($\tau_1/\tau_2 < 2$), errors accumulate rapidly.

24

Global analysis [41]. The simultaneous analysis of several related experimental sets of data is referred to as global analysis. Brand and coworkers [41] have developed and popularized this method of deconvolution and applied it to several complex analysis problems. In a global analysis, related experiments are simultaneously analyzed by considering the total collected fluorescence decay surface at once. This approach leads to a better parameter recovery with less uncertainty on the estimates, and to a better model discrimination power. A decay data surface is obtained by collecting decay samples across the wavelength range of an emission spectrum, for example, or along any other experimental axis. The total decay surface is then analyzed for all the different parameters, to reveal those parameters, which are linked.

Target analysis [42]. In this method, one analyzes the decay directly in terms of discrete physical models, rather than relying on the empirical nature of the pre-exponential factors and relaxation times derived from conventional deconvolution. A global target analysis combines the two approaches into a very powerful method of analysis. It is the recommended methodology for solving complex problems involving linked emission decay experiments, e.g., those sets of experiments involving series of quencher concentration variations, or temperatures, or some other variable that leads to data sets that together constitute a functional block that needs to be solved cohesively. This method is amenable to solution using transform formalisms also.

Deconvolution against a reference [43]. Improved ease and accuracy of fitting can often be obtained by using the experimental decay profile of a reference emitter in place of the instrument response function obtained with a scattering solution. The reference emitter can either emit at the same wavelength as the sample under study, or it may be a component of the emission to be fitted. The virtue of this method is that instrument response functions as well as complex kinetic components can be accommodated within a single set of reference data.

Maximum entropy methods (MEM) [44]. This method promises to have great utility for complex systems since it is capable of recovering lifetime distributions over broad lifetime range. In the MEM method, one does not analyze a discrete set of multi-exponential functions to fit the decay, but rather probes for a distributed set of N decay functions logarithmically spaced across the time spectrum. Decay function amplitudes are reconstructed from an entropy-like function with the imposed constraint that the goal function of the χ^2 criterion must be near unity. The calculated spectrum of decay functions is known to be unique.

1.3. Mathematical modeling and Monte Carlo methods (review)

Mathematical Modeling. The methods of mathematical modeling are widely used in a variety of science fields and have undergone significant changes today [45,46,47,48,49,50]. Modeling like other interdisciplinary fields of science uses specific terms and concepts. Such terms as "model", "modeling", "parameters", "simulation", etc. have been used in quite different connotations. For example "modeling" denotes an actual series of operations as contrasted with the model, which represents a mathematical description of the real process. Other frequently encountered terms and their use in the text are: "model" is such a mathematical or simulation description designed to help to analyze and understand a complex physical process; "parameter" is a property of the process or its environment, that can be assigned arbitrary numerical values; "simulation" is the study of a system or its parts by manipulation of its mathematical representation or its physical model [51].

Modeling can facilitate the understanding of almost all physical processes and systems and often has the following advantages:

- economical experimentation;

- extrapolation of operating conditions, some of which might be impractical or impossible to use in real systems;

- reproduction of experiments;

- testing the sensitivity of basic system parameters;

- possibility to study of system stability.

MC methods. Mathematical modeling includes a large group of methods that is applied in this Thesis and is called Monte Carlo simulation methods[*] [52,53,54,55]. MC methods are stochastic techniques, meaning that they are based on the use of random numbers and probability statistics to investigate problems.

The MC methods provide approximate solutions to a variety of mathematical problems by performing statistical sampling experiments on a computer. The methods applies to problems with no probabilistic content as well as to those with inherent probabilistic structure. Among all

---

[*]The methods are called after the city in the Monaco principality, because of a roulette, a simple random number generator. The name and the systematic development of Monte Carlo methods dates from about 1944.

numerical methods that rely on N - point evaluations in M - dimensional space to produce an approximate solution, the MC methods have an absolute error of estimate that decreases as $N^{-\frac{1}{2}}$ whereas in the absence of special data structure all other methods have errors that decrease as $N^{-\frac{1}{M}}$ at best.

MC methods for molecular simulations. Although MC methods are used in a number of ways, in the context of molecular spectroscopy application there are five types which are most commonly encountered:

- **"classical"** MC: samples are drawn from a probability distribution, often the classical Boltzmann distribution, to obtain thermodynamic properties, minimum-energy structures and/or rate coefficients, or perhaps just to sample conformers as part of a global conformer search algorithm

- **"quantum"** MC: random walks are used to compute quantum mechanical energies and wavefunctions, often to solve electronic structure problems, using Schroedinger's equation as a formal starting point

- **"path-integral" quantum** MC: quantum statistical mechanical integrals are computed to obtain thermodynamic properties, or even rate coefficients, using Feynman's path integral as a formal starting point

- **"volumetric"** MC: random and quasirandom number generators are used to generate molecular volumes and sample molecular phase-space surfaces

- **"simulation"** MC: stochastic algorithms are used to generate initial conditions for quasiclassical trajectory simulations, or to actually simulate processes using scaling arguments to establish time scales or by introducing stochastic effects into molecular dynamics. "Kinetic MC" is an example of an SMC method. So is "thermalization" of a molecular dynamics trajectory.

There are many variations on these basic themes in the literature. For example, molecular dynamics is often coupled to stochastic engines to provide rapid thermalization, including for example Nose walks and Brownian dynamics. The results of "Molecular MC" calculations can be used to predict for example thermally averaged structures, molecular charge distributions,

reaction rate constants, free energies, dielectric constants, compressibility, heat capacities, phase transition temperatures.

MC methods for simulation energy transport. MC simulation methods are also often used to solve the problem of energy transfer processes in fluorescence spectroscopy, where they can directly simulate energy transport processes and generate the data that are close to those in real physical experiments [56].

Generally, the MC methods have been used in two ways:

- to test the validity of the approximations made in analytical theories, and confirm the developed theory by a numerical experiment [57,58,59,60];

- to compare simulated and experimental results and from that comparison gain further insight into the origin of the results [61,62,63].

This Thesis rather deals with the second utilization of the MC methods.

References

[1] H.A. Spoehr (1926) *Photosynthesis* Chemical Catalog Company, New York.

[2] D. Guest, T.A. Moore, *Science*, 244 (1989) 35.

[3] J.S. Katz, J.C. Hindman (1982) in *Photochemical Conversion and Storage of Solar Energy* Academic Press, New York, p.27-28.

[4] G. Renger, *Angew. Chem.*, 99 (1987) 660.

[5] R.C. Jennings, R. Bassi, G. Zucchelli, *Topics in Current Chemistry*, 177 (1996) 147.

[6] A.R. Grofts, C.A. Wright, *Biochimica et Biophysica Acta*, 726 (1983) 149.

[7] G. Feher, J.P. Allen, M.Y. Okamura, D.C. Rees, *Nature*, 6220 (1989) 111.

[8] R. Lahtinen, D.J. Fermin, K. Kontturi, H.H. Girault, *J. Electroanalytical Chem.*, 483 (2000) 81.

[9] D. Gust, T. A. Moore, A. L. Moore, D. Kuciauskas, P. A. Liddell, and B. D. Halbert, *J. Photochem. Photobiol. B: Biology*, 43 (1998) 209.

[10] R.A. Marcus, N. Sutin, *Biochim. Biophysica Acta*, 811 (1985) 265.

[11] S.G. Boxer, D.J. Lockhart, T.R. Middendorf, *Chem. Phys. Lett.*, 123 (1986) 476.

[12] M.W. Windsor, *Faraday Trans.*, 82 (1986) 2237.

[13] J.S. Conolly (1982) in *Photochemical Conversion and Storage of Solar Energy* Academic Press, New York, p. 175-204.

[14] M. Sykora, K.A. Maxwell, J.M. DeSimone, T.J. Meyer, *Proc. Nat. Acad. Sci. USA*, 97 (14) (2000) 7687.

[15] T.J. Savenije, R.B.M. Koehorst, T.J. Schaafsma, *Chem. Phys. Lett.*, 244 (1995) 363.

[16] W.-H. Han, E. N. Durantini, T. A. Moore, A. L. Moore, D. Gust, P. Rez, G. Letherman, G. R. Seely, N. Tao and S. M. Lindsay, *J. Phys. Chem. B*, 101 (1997) 10719.

[17] N. I. Maniga, J. P. Sumida, S. Stone, A. L. Moore, T. A. Moore, D. Gust, *J. Porphyrins Phthalocyanines*, 3 (1999) 32.

[18] U. Hofstra, R.B.M. Koehorst, T.J. Schaafsma, *Magn. Reson. Chem.*, 25 (1987) 1069.

[19] J. P. Sumida, P. A. Liddell, A. N. Macpherson, G. R. Seely, A. L. Moore, T. A. Moore and D. Gust, *J. Phys. Chem. A*, 102 (1998) 5512.

[20] R.B.M. Koehorst, G.K Boschloo, T.J. Savenije, A. Goossens, T.J. Schaafsma, *J. Phys. Chem. B*, 104(10) (2000) 2371.

[21] D. Gust, and T. A. Moore, In *The Porphyrin Handbook*, K. M. Kadish, K. M. Smith and R. Guilard, Eds., Academic Press: New York, in press.

[22] A. Jabłoński, *Z. Phys.*, 94 (1935) 38.

[23] J.R. Lakowicz (1999) *Principles of Fluorescence Spectroscopy* Kluwer Academic/Plenum Publishers, New York.

[24] N.J. Turro (1991) *Modern molecular photochemistry* University Science Books, Mill Valley.

[25] B. Blanzat, C. Barthou, N. Tercier, J.J. André, J. Simon, *J. Am. Chem. Soc.*, 109 (1987) 6193.

[26] J. Blasse at al., *Chem. Phys. Lett.*, 154 (1989) 420.

[27] J.S. Lindsey, P.A. Brown, D.A. Siesel, *Tetrahedron*, 45 (1989) 4845.

[28] C. Bacchiocchi, C. Zannoni, *Chem. Phys. Lett.*, 268 (1997) 541.

[29] N. Gleffer, G. Calzaferri, *J. Phys. Chem. B*, 101 (1997) 1396.

[30] N. Gleffer, S. Megelski, G. Calzaferri, *J. Phys. Chem. B*, 103 (1999) 1250.

[31] T. Förster, *Ann. Physik.*, 2 (1948) 55.

[32] D.L. Dexter, *J. Chem. Phys.*, 21 (1953) 836.

[33] V.M. Agranovich and M. D. Galanin (1982) *Electronic Excitation Energy Transfer in Condensed* Matter, North-Holland, New York.

[34] M. von Smoluchovsky, *Z. Phys. Chem.*, 92 (1917) 192.

[35] M.Hauser, U.K.A. Klein, U. Gösele, *Z. Phys. Chem. Neue. Folge, Bd.*, 101 (1976) 255.

[36] M. Kaschke, K. Vogler, *Laser Chem.*, 8 (1988) 19.

[37] M. Yokota, O. Tanimoto, *J. Phys. Soc. Jap.*, 22 (1967) 779.

[38] K.P. Ghiggino, T.R. Smith, *Prog. Reaction Kinetics*, 18 (1993) 375.

[39] D.V. O'Connor, D. Phillips (1984) *Time-correlated Single Photon Counting*, Academic Press, London.

[40] J.N. Demas (1984) *Excited State Lifetime Measurement* Academic Press, New York.

[41] J.M. Beechem, M. Ameloot, L. Brand, *Chem. Phys. Letts.*, 120 (1985) 466.

[42] J.M. Beechem, M. Ameloot, L. Brand, *Analytical Instruments*, 14 (1985) 379.

[43] K. Vos, A. van Hoek, A.J.W.G. Visser, *Biochemistry*, 165 (1987) 55.

[44] A.K. Levesey, J.C. Brochon, *Biophys. J.*, 52 (1987) 693.

[45] M. Niss, W. Blum, I. Huntley (1991) *Teaching of mathematical modelling and applications* Horwood, New York.

[46] R. Dautray, J.L. Lions (1988-1993) *Mathematical analysis and numerical methods for science and technology Vol.1-6* Springer-Verlag, Berlin.

[47] E.L. Allgower, K. Georg (1990) *Numerical Continuation: An Introduction* Springe-Verlag, Berlin.

[48] M.Iri, K. Tanabe (1989) *Mathematical Programming-Recent Developments and Applications* Kluwer-Nijhoff, Boston.

[49] R. Rubinstein, A. Shapiro (1998) *Modern Simulation and Modelling* John Willey & Sons Inc., New York.

[50] J. Banks (1998) *Handbook of Simulation: Principles, Methodology, Advances, Applications, and Practice* John Willey & Sons Inc., New York.

[51] D.M. Himmelblau, K.B. Bischoff (1970) *Process Analysis and Simulation: Deterministic Systems* John Willey & Sons Inc., New York.

[52] R. Rubinstein (1981) *Simulation and the Monte Carlo Method* John Willey & Sons Inc., New York.

[53] J. M. Hammersley and D.C. Handscomb (1964) *Monte Carlo Methods* Methuen, London.

[54] H. Gould, J. Tobocknik (1988) *Computer Simulation Methods* Addison-Wesley, Reading, MA.

[55] K. Binder, D.V. Heerman (1992) *Monte Carlo Simulation in Statistical Physics* Springer-Verlag, Berlin.

[56] L. Andrews, A. Demidov (1999) *Resonance Energy Transfer* John Willey & Sons LtdInc., New York.

[57] S.C. Harvey, H.C. Cheung., *Proc. Nat. Acad. Sci. USA*, 69 (1972) 3670.

[58] M.N. Berberan-Santos, B. Valeur, *J. Chem. Phys.*, 95 (1991) 8049.

[59] L.B.Å. Johansson, S. Engström,M. Lindberg, *J. Phys. Chem.*, 96 (1992) 3845.

[60] D.M. Hussey, S. Matzinger, M.D. Fayer, *J.Chem.Phys.*, 109 (1998) 8708.

[61] M.N. Berberan-Santos, P. Choppinet, A. Fedorov, L. Jullien, B. Valeur, *J. Am. Chem. Soc.*, 121 (11) 2526.

[62] N. Sato, S. Ito, K. Sugiura, M. Yamamoto, *J. Phys. Chem. A*, 103 (1999) 3402.

[63] L.M.S. Loura, M.Prieto, *J. Chem. Phys. B*, 104 (2000) 6911.

Chapter 2

Experimental Methods

This Chapter describes in some detail the investigated porphyrin systems, their preparation and characterization, experimental methods, equipment, and a few typical examples of the results of the steady state and the time-resolved measurements. For the application of the methods, described in this Chapter, see Chapter 4 and 5.

2.1. Investigated systems

Tetramers of substituted porphyrin compounds in solution have much interest since these tetramers may be considered as simple models for plant pigments at close and fixed distance, such as various forms of chlorophyll in complexes with the surrounding proteins. As in photosynthesis, these model systems show

(i) energy transfer from a particular excited porphyrin to one or more of its neighbors;

(ii) loss of excitation energy by relaxation to the ground state.

ZnM(4-Py)TrPP has been selected as a good candidate for self-assembling aggregates [1,2,3] of which the photophysics has been studied in two organic solvents i.e. toluene and a mixture of polystyrene in toluene. In order to get a better understanding of the photophysical properties of solid, organized porphyrin films, attempts were made to spincoat porphyrin tetramers onto an inert substrate, and compare the properties of such a film with those of the solution. In such an organized film the monomers in the tetrameric units were expected to have a mutually fixed position and relative orientation. By this property such films are expected to show similar properties as natural energy transferring pigments, which are also kept in fixed positions by their protein surroundings. These attempts were unsuccessful, however, because tetramers on an inert substrate turn out to have a much lower fluorescence yield than in solution, ruling out accurate time-resolved experiments. This problem does not apply to ZnTOPP films spincoated on an inert substrate under the same experimental conditions, since the fluorescence yield of ZnTOPP films is relatively high and quite suitable for the analysis of the energy relaxation and transport processes in ZnTOPP aggregates, known to self-assemble into stacks on inert solid surfaces [4]. Solid ZnTOPP films have been investigated containing two different porphyrins, of which one is

acting as an energy donor and the other as an energy acceptor. Such organized, mixed films could be easily produced by doping the film with a varying fraction of acceptor compound, in this work CuTOPP or H₂TOPP.

2.1.1. Porphyrin tetramers in dry non-ligating organic solvents

H₂TPP and a derivative H₂M(4-Py)TrPP, were synthesized from pyrrole and benzaldehyde, and from pyrrole and a mixture of benzaldehyde and 4-pyridinecarbaldehyde, respectively, by standard procedures [5]. Zinc was inserted into the free base by refluxing a solution in dimethylformamide (DMF) in the presence of excess zinc(II)chloride [6] yielding ZnTPP and ZnM(4-Py)TrPP, respectively. The zinc porphyrins were purified by chromatography over silica gel (Merck) with chloroform (Merck p.a.) as the eluent. The porphyrins were estimated to be >99% pure by thin-layer chromatography, absorption- and fluorescence spectroscopy. All reagents (Merck) were synthetic grade.

A solution of ZnTPP in dry toluene and in toluene/pyridine 1:10 v/v is used as a reference for the non-ligated and ligated ZnM(4-Py)TrPP species, respectively. Schematically, ZnTPP, ZnTPP ligated by pyridine, and ZnM(4-Py)TrPP monomers are shown in Fig. 1.
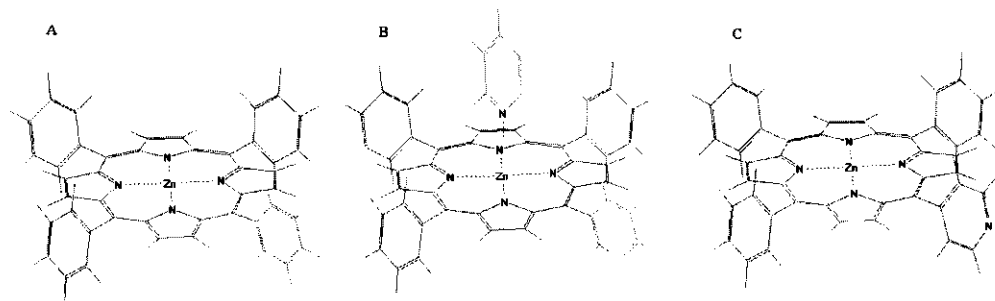

Fig. 1. Structures of ZnTPP (A), ZnTPP·Py (B), and Zn(4-Py)TrPP (C)

For spectroscopic measurements solutions were prepared in toluene (Merck, p.a.) dried on sodium wire, and in viscous solutions of polystyrene (PS)/ toluene mixtures (further denoted as PS/Tol), and stored over molecular sieve. Anhydrous pyridine (Aldrich) was used without additional drying or purification. All solvents used were p.a. grade, unless stated otherwise.

2.1.2. Solid porphyrin films

ZnTOPP and H₂TOPP (Fig. 2) were synthesized by the same procedure as in section 2.1.1., and using CuCl₂.2H₂O (Merck, p.a.) to prepare CuTOPP.
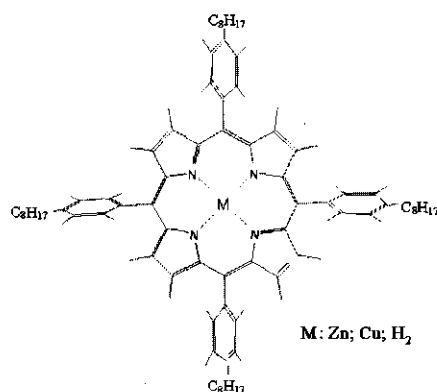
Fig. 2. Structure of Zn-, Cu-, and H$_2$TPP

H$_2$TPP, H$_2$TOPP and H$_2$M(4-Py)TrPP were synthesized by condensation of benzaldehyde , 4-(n-octyl)benzaldehyde and a mixture of benzaldehyde and 4-pyridinecarbaldehyde, respectively, with pyrrole (Janssen Chimica, 99%) in refluxing propionic acid (Merck, z.s.) [7,8]. The porphyrins were purified by chromatography on silica (Merck, silica gel 60) with toluene (ZnTOPP, CuTOPP) or chloroform (ZnTPP, ZnM(4-Py)TrPP) as eluent.

Thin porphyrin films on quartz plates (suprasil, Ø 15 mm, 1 mm thickness) were prepared by spincoating from solutions with different concentrations of the compound. Thin ZnTOPP films doped with various concentrations of CuTOPP/H$_2$TOPP were prepared in the same way since the solutions already contained the appropriate amounts of ZnTOPP and CuTOPP/ H$_2$TOPP. It can be assumed that in the films the CuTOPP/ H$_2$TOPP molecules are distributed statistically among the ZnTOPP molecules. Before spincoating the quartz plates were subsequently rinsed with aqua regia, water, methanol and toluene and blown dry with nitrogen.

2.2. Steady state optical spectroscopy

A Cary 5E spectrophotometer and a Perkin Elmer LS5 fluorimeter or a Fluorolog 3-22 Jobin Yvon spectrophotometer, equipped with a cuvette chamber for liquid samples and an integrating diffuse reflectance sphere for the spincoated films, were used to record the absorption- and fluorescence spectra. The Fluorolog spectrophotometer was also equipped with two electronically actuated Glann-Thompson UV polarizers (Model 1008 Dual Auto Polarizer) for measurement of polarized steady state fluorescence spectra.

The unpolarized and polarized absorption- and fluorescence spectra of the porphyrin solutions were measured at 10°, 15°, 25°, 35°, 45°, 55° C and those of the ZnTOPP spincoated films at room temperature. The degree of polarization, denoted as anisotropy, is expressed as

$$r(t) = \frac{I_{\parallel}(t) - GI_{\perp}(t)}{I_{\parallel}(t) + 2GI_{\perp}(t)}$$

(1)

where G is geometry factor. Typical spectra are shown in Figs. 3 and 4.
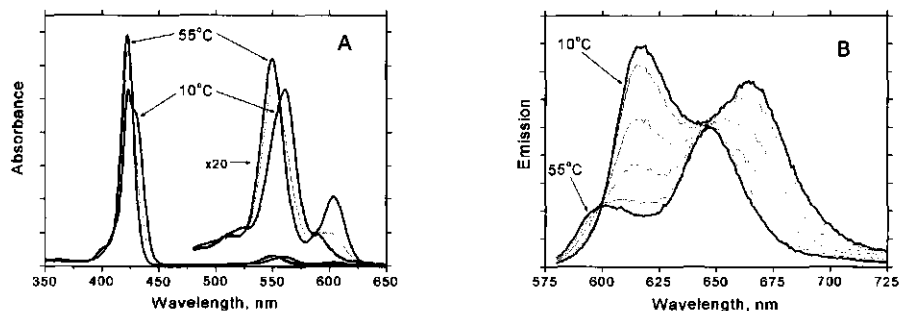
Fig. 3. Unpolarized absorption- and fluorescence spectra (λ_{exc} = 565 nm) of $2.2 \cdot 10^{-5}$ M Zn(4-Py)trPP in toluene at: (A) 10°, 35°, 55° C; (B) 10°, 15°, 25°, 35°, 45°, 55° C.

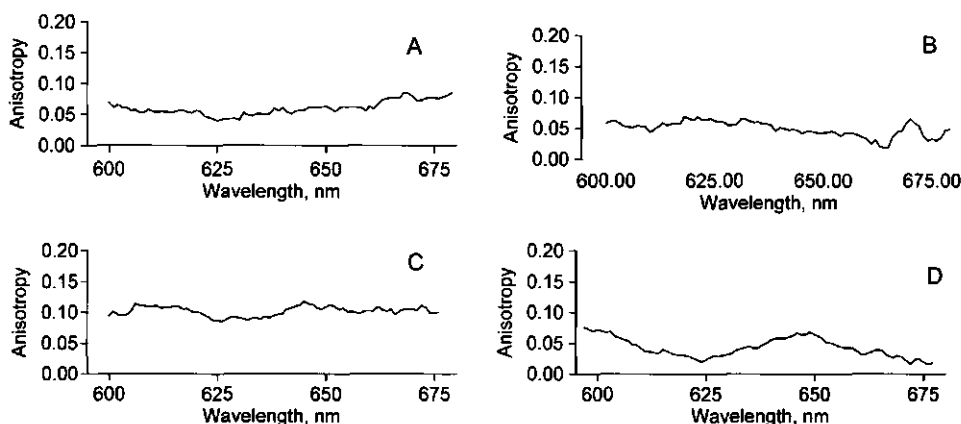Fig. 4. Steady state anisotropy spectra of: $1.6 \cdot 10^{-5}$ M ZnTPP in Ps/Tol at (A) T = 55°C and (C) T = 10°C; λ_{exc} = 550 nm; $1.6 \cdot 10^{-5}$ Zn(4-P)TrPP in Ps/Tol at (B) T = 55°C, and (D) T = 10°C; λ_{exc} = 565 nm.

2.3. Time-resolved laser spectroscopy

The components $I_{\parallel}(t)$ and $I_{\perp}(t)$ of the time-resolved fluorescence polarized parallel and perpendicular to the polarization direction of the excitation light were collected using two different experimental methods [9]: i) time-correlated single photon counting and ii) streak camera detection.

2.3.1. Picosecond laser TSCPS instrumentation and streak camera

TCSPC instrumentation. Time-resolved fluorescence measurements were carried out using excitation with mode-locked lasers and detection using TCSPC electronics. A mode-locked continuous wave Nd:YLF laser (Coherent model Antares 76-YLF [10]), was equipped with a LBO frequency doubler with temperature controller (Coherent model 7900 SHGTC) and BBO frequency tripler (Coherent model 7950 THG), to obtain up to 1 W of continuous wave mode-locked output power at $\lambda = 351$ nm, synchronously pumping a continuous wave dye laser. Stilbene 420 (Exciton Inc.) was used as the dye for excitation at 435 nm and Coumarin 460 for excitation at 465 nm. The dye laser was a Coherent Radiation model CR 590, standard three mirror cavity design, but the output mirror was placed at the correct distance for a perfect matching of the cavity lengths of the pump and the dye laser. The high reflector pump and fold mirror radii were R = 75 mm, whereas the high reflector end mirror radius was R = 50 mm. The output mirror was flat and had a transmission of about ≈ 7% over the tuning range 415- 465 nm. Provisions were made to reduce the effective temperature dependence of the dye laser cavity length to a negligible value. To reduce the pulse rate of the excitation pulses to 594 kHz, a set-up was used with an electro-optic modulator in a dual pass configuration [11]. The final pulse width of the excitation pulses was ≈ 4 ps FWHM, the wavelength 435 nm and the maximum pulse energy about 100 pJ.

Porphyrin solutions of 0.5 cm^3 volume were contained in 1 cm light path fused silica cuvettes (Hellma model 114F-QS), placed in a thermostated sample holder. The laser beam used the full 1 cm pathlength to travel (≈ 45 ps) through the solution for excitation. The spincoated samples were fixed on a thermostated, spring-loaded holder at an angle of 15° with respect to the direction of excitation. The reflections and the scatter of the excitation beam incident on the substrate were caught by highly absorbing black paper to prevent multiple excitation of the sample. The sample holder was placed in a housing, which also contained the main detection optics. Extreme care was taken to avoid artifacts from depolarization effects. At the front of the sample housing a Glan-laser polarizer was mounted, optimizing the vertical polarization of the

input light beam. The fluorescence was collected at an angle of 90° with respect to the direction of the exciting light beam. Between the sample and the photomultiplier detector were placed: a single fast lens (uncoated fused silica, F/3.0), two cut-off filters (Schott KV500), a rotatable sheet type polarizer in between and a second single fast lens (uncoated fused silica, F/3.0), focusing the fluorescence on the photomultiplier cathode. The polarizer sheet was in a dc motor driven ball-bearing holder with mechanical stops, allowing computer controlled rotation to parallel and perpendicular polarized detection of the fluorescence. For experiments with detection of the fluorescence polarized at the magic angle a separate mechanical stop was used. The sheet polarizer was Polaroid type HNP'B. The detection monochromator was a CVI model Digikröm 112 double monochromator (F/3.9) with the two gratings placed in a subtractive dispersion configuration. The G-factors of the monochromator at different wavelengths, i.e. the relative detection sensitivities for horizontally and perpendicularly polarized light, were determined using two different methods: (i) using unpolarized and depolarized light from a incandescent lamp, (ii) detecting the decay of a fast rotating fluorescence probe and applying a so-called tail matching procedure. The orientations of the polarizers were carefully aligned and the performance of the instrument was finally checked by measuring reference samples.

The detection electronics were standard TCSPC modules. The start signal for the time-to-amplitude converter (TAC, Tennelec model TC 864) was generated by exciting a fast PIN-photodiode (Hewlett Packard model 5082-4204 at 45 V reverse bias) using a small fraction of the intensity of the exciting light pulses. That signal was fed into a wide band amplifier (Becker & Hickl model ACA 35 dB, 1.8 GHz) and then into one channel of a quad constant fraction discriminator (CFD, Tennelec modified model TC 454). Single fluorescence photon responses from a microchannel plate photomultiplier (Hamamatsu model R3809U-50 at 3100 V) were amplified by a wide-band amplifier (Becker & Hickl model ACA-2; 21 dB, 1.8 GHz), analyzed in another channel of the CFD and then used as the stop signal for the TAC. The output pulses of the TAC were analyzed by an ADC (Analog to Digital Converter, Nuclear Data model 8715, 800 ns fixed dead-time), used in the Coincidence and Sampled Voltage Analysis mode, triggered by the Valid Conversion Output pulses of the TAC. The output of the ADC was collected in 1024, 2048, 4096 or 8192 channels of a multichannel analyzer (MCA board, Nuclear Data model AccuspecB, incorporated in a personal computer).

By reducing the intensity of the excitation pulses, a maximum photon frequency of 30 kHz ($\approx 5\%$ of 594 kHz) was chosen [12] to prevent pile-up distortion. Also other instrumental sources for distortion of data were minimized [13] to below the noise level of normal photon statistics.

36

Extreme care was taken to prevent artifacts from background luminescence. One cycle of measurements consisted of collecting parallel polarized fluorescence for ten seconds, followed by collecting perpendicularly polarized fluorescence during the same time interval. These cycles were repeated until an integrated content of the MCA of 10^5 to 10^6 registrated start-stop events was reached. To obtain a dynamic instrumental response for deconvolution purposes, the fast single exponential fluorescence decay of Erythrosin B in water and the scatter of a rough-hewn, uncoated quartz substrate of 1 mm thickness, were used as a reference for liquid and solid samples, respectively. One complete measurement consisted of measuring the (polarized) fluorescence from reference, sample, and reference compound again. In that way a possible temporal shift can easily be verified and corrected for, if necessary.

Streak camera. The experimental set-up for streak camera detection has been previously described [14]. The 100 fs pulses for the excitation at 550 and 565 nm were generated with a 125 kHz repetition rate using a Titanium: sapphire based oscillator (Coherent, MIRA), a regenerative amplifier (Coherent, REGA) and a double pass optical parametric amplifier (Coherent, OPA-9400). The pulse energy was typically 25 nJ. The polarization of the exciting light was alternated between horizontal and vertical. The vertically and horizontally polarized fluorescence components were detected using a Hamamatsu C5680 synchroscan streak camera equipped with a Chromex 250IS spectrograph. The overall time response of the system was 3.5 ps (FWHM) at 8 nm spectral resolution. One streak image measured 315 nm in the spectral domain (1018 pixels) and 200 ps/2200 ps (1000 pixels) in the time-domain.

2.3.2. Measurement of fluorescence decays

Using the TCSPC streak camera methods the total fluorescence $F^E(t)$ (Chapter 1, eqn.(30)) can be calculated from the observed polarized components $I_{\parallel}(t)$ and $I_{\perp}(t)$ of the time resolved fluorescence as

$$I(t) = I_{\parallel}(t) + 2GI_{\perp}(t)$$

(2)

with and $I_{\parallel}(t)$ and $I_{\perp}(t)$ are given by

$$I_{\parallel}(t) = \int_0^t e(t-x) f_{\parallel}(x) dx$$

(3)

$$I_{\perp}(t) = \int_0^t e(t-x) f_{\perp}(x) dx$$

(4)

where $e(t)$ is the instrumental response function.

TCSPC fluorescence measurements. The TCSPC method has been applied to solutions of ZnTPP in toluene, toluene/pyridine, and PS/Tol, and to ZnM(4-Py)TrPP in toluene and PS/Tol. The sample temperature was adjusted to 10, 15, 25 and 55°C, using a cold nitrogen gas flow from an Oxford ITC4 temperature controller. The excitation wavelength was 435 nm and the fluorescence wavelengths were selected by a cut-off filter (Schott KV 500) and line filters of 595 and 625 nm with a 16 nm band width for the liquid samples. The number of the channels of the multichannel analyzer was 4096 (2.081 ps/channel). For the spincoated films, the excitation wavelength was 465 nm and the fluorescence wavelengths were selected by a cut-off filter (Schott KV 500) and line filters of 580 and 725 nm with a 16 nm band. The number of the channels of the multichannel analyzer was 8192 (3.125 ps/channel). Some typical results of the time-resolved fluorescence decays for a ZnTOPP film at different fluorescence wavelengths are shown in Fig. 5.
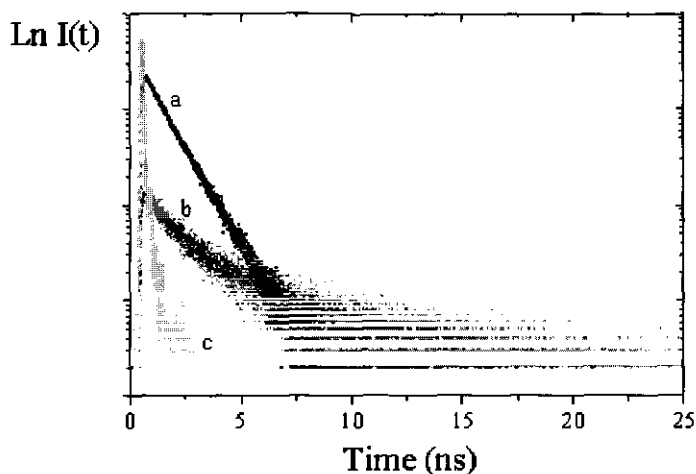
Fig. 5. Fluorescence decay curves for a ZnTOPP film; (a) λ_{det} = 580 nm, (b) λ_{det} = 725 nm (c) instrumental response at 465 nm (λ_{exc} = 465 nm, 3.125 ps/channel).

Streak camera measurements. The streak camera detection was applied to a $2.2 \cdot 10^{-5}$ M ZnM(4-Py)TrPP solution in toluene. The porphyrin solution was excited at 550 nm at 55°C and 565 nm at 10°C. Typical time-resolved fluorescence spectra at 55°C are presented in Fig.6.
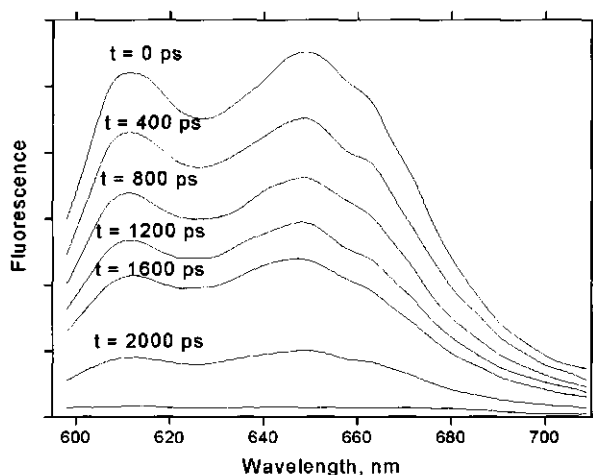
Fig. 6. Time-resolved fluorescence spectra of a $2.2 \cdot 10^{-5}$ M ZnM(4-Py)TrPP solution in toluene (λ_{exc} = 465 nm, 2.2 ps/pixel).

2.3.3. Measurements of the time-dependent fluorescence polarization anisotropy

The time dependence of the fluorescence anisotropy cannot be measured directly, but must instead be extracted from the observed polarized components $I_\parallel(t)$ and $I_\perp(t)$ of the time resolved fluorescence. Some typical time-resolved fluorescence anisotropy decays using TSCPS and streak camera are presented in Figs. 7 and 8.

Fig. 7. Time-resolved fluorescence anisotropy decays *vs.* temperature for 2.2 10^{-5}·M Zn(4-PyTrPP) in Ps/Tol (λ_{exc} = 435 nm, 2.081 ps/pixel)
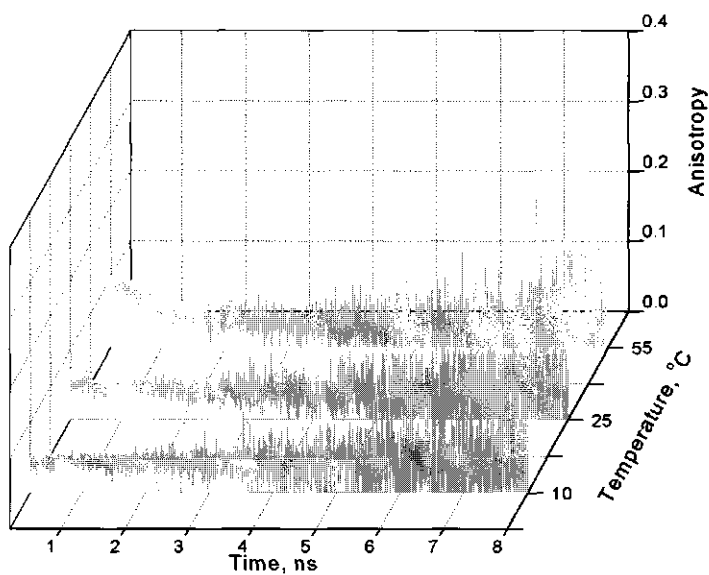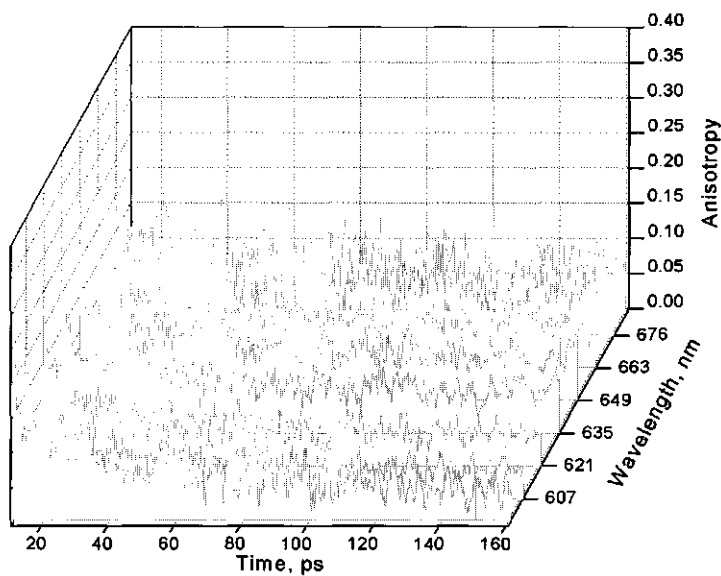

Fig. 8. Time-resolved fluorescence anisotropy spectra for 2.2 10^{-5}·M Zn(4-PyTrPP) in toluene at 10°C (λ_{exc} = 465 nm, 0.2 ps/pixel).

References

[1] E. Alessio, S. Gremia, S. Mestroni, E. Iengo, I. Srnova, M. Slof, *Inorg. Chem.*, 38 (1999) 869.

[2] E.B. Fleiscer and A.M. Shachter, *Inorg. Chem.*, 30 (1991) 3763.

[3] A.M. Shachter, E.B. Fleiscer, R.C. Haltiwanger, *J. Chem. Soc. Chem. Commun.*, (1998) 60.

[4] H. Donker, R.B.M. Koehorst, A. Van Hoek, W. van Schaik, M.M. Yatskou, T.J Schaafsma, *J. Phys. Chem.*, submitted.

[5] A.D. Adler, F.R. Longo, J.D. Finarelli, J. Goldmacher, J. Assour, L. Korsakoff, *J. Organic Chem.*, 32 (1967) 476.

[6] A.D. Adler, F.R. Longo, F. Kampas, J. Kim, *J. Inorg. Nucl. Chem.*, 32 (1970) 2443.

[7] A.D. Adler, F.R. Longo, W. J. Shergalis, *J. Am. Chem. Soc.*, 86 (1964) 3145.

[8] R.G. Little, J.A. Anton, P.A. Loach, J.A. Ibers, *J. Heterocycl. Chem.*, 12 (1975) 343.

[9] J.R. Lakowicz (1991) *Topics in Fluorescence Spectroscopy* Vol. 1 Plenum Press, New York.

[10] E. Reed, G. Frangineas, *Proc. SPIE*, 1223: *Solid State Lasers* (1990).

[11] A. van Hoek, A.J.W.G. Visser, *Rev. Sci. Instrs*, 52 (1981) 1199.

[12] K. Vos, A. van Hoek, A.J.W.G. Visser, *Eur. J. Biochem.*, 165 (1987) 55.

[13] A. van Hoek, A.J.W.G. Visser, *Analytical Instrumentation*, 14 (1985) 359.

[14] F.J. Kleima, E. Hofmann, B. Gobets, I.H.M. van Stokkum, R. van Grondelle, K. Diederichs, H. van Amerongen, *Biophys. J.*, 78 (2000) 344.

Chapter 3

Optimization methods for fluorescence decay fitting

Comparative analysis of the optimization methods for fluorescence decay fitting has been performed with the aim to discover the ones most appropriate for application in the investigation of energy transfer processes by Monte Carlo simulations. Testing of the optimization methods has been implemented on the base of models developed for the fluorescence intensity decay (single, double, three and "stretched" exponentials). Statistical criteria for judging the simulation-based fits, error analysis, and confidence interval evaluation have been tested and their numerical performance are discussed.

3.1. Introduction

The method of time-resolved fluorescence spectroscopy is a very reliable and sensitive tool in many chemical and physical applications [1]. However, the potential of this method has not yet been completely revealed. One of the approaches for further improvements is related to the development of consistent mathematical models, which could adequately describe experimental data. Traditionally, the kinetics of photo-physical processes are analyzed in terms of a sum of exponentials [2,3]. This option is supported by very well established and worked out procedures of multi-exponential fitting [2,3,4,5,6]. Although such procedures allow to obtain a very good quality of the fit, the real physical nature of the fitted parameters is hidden and those parameters may only serve as a kind of compressed representation of the experimental data. The same drawback is concerned in the methods of fluorescence decay analysis (see Chapter 1), that are set for rather simple analytical models. Much deeper understanding of the photo-physical phenomena might be reached by MC methods [7,8].

In this Chapter the methods of fluorescence decay fitting, criteria for judging the quality of fits and the confidence intervals evaluation have been tested by single, double, three and "stretched" exponential models for the fluorescence intensity decays as well as by MC simulations.

3.2. Optimization algorithms

Commonly used fitting or optimization algorithms for the fluorescence decay analysis might be divided into two big groups: *gradient* and *non-derivative* methods. *Gradient* methods use a partial parameter derivative in the fitting procedure, whereas *non-derivative* ones don't [9]. The core of optimization is finding a global minimum for a function Φ with a corresponding set a of parameters $a_1,...,a_N$:

$$\Phi(a,t) = \pounds(F^E(t), F^T(a,t)$$

(1)

where $\pounds$ is a mathematical operator for a function Φ, $F^E(t)$ is a histogram of experimental data, $F^T(a,t)$ is a histogram obtained from the analytical equation or simulation model. Regarding the particularities of a function Φ, there are several sorts of optimizations such as global, constrained, unconstrained, uni-modal, multi-modal, uni-directional, multi-directional, etc. [10,11,12].

3.2.1. Non-derivative optimization methods

Non-derivative optimization methods (often also called search methods) are useful for solving two problems: i) when $\partial\Phi(a,t)/\partial a_i$ i=1,...,N cannot be taken; ii) when $\Phi(a,t)$ contains noise. These two properties of non-derivative methods make them promising candidates for the application in MC simulation for the fluorescence decay analysis. By the optimization procedure, the search algorithms may be grouped into: i) direct search methods (grid, Hooke-Jeeves, Powell methods, etc. [13]); ii) simplex methods (simplex, Nelder and Mead, complex methods, etc. [14]); and iii) stochastic methods (random walk, simulated annealing, etc. [15]). Several methods from each group are considered in this Chapter.

Grid method (GM) [16]. If the variations of $\Phi(a,t)$ with respect to each parameter a_i are independent on the quality of the approximation on the other parameters, then the parameter values can be determined by the minimization of $\Phi(a,t)$ with respect to each parameter one by one. Reliability for non-unimodal functions, simplicity of implementation and satisfactory accuracy of the parameter search are the main advantages of the GM. However, if the variations of $\Phi(a,t)$ with respect to the parameters are dependent, convergence can be extremely slow.

Hooke-Jeeves method (HJM) [13,14]. The HJM implements a sequence of investigating coordinate searches around a basic point with a constant value of a search step h. The HJM is

accelerated by using an extrapolation for a search step value h, that promotes increasing its general efficiency.

Powell method (PM) [13,14]. The PM uses the building of a vector set in parameter space and processing a one-direction search along each vector direction. The PM is an iterative procedure and one cycle of the iteration has finished when a vector set is updated to a new direction of maximal success.

Rosenbrock method (RM) [13,14]. The RM searches a global minimum along a break of derivatives. The combination of the rotation of a direction vector with the regulation of the scale makes the RM quite effective with the decision of complex optimization tasks, in particular, for optimization of $\Phi(a,t)$ from many variables. At the same time the method successfully works in conditions of deep ravine surfaces of $\Phi(a,t)$. Disadvantage is that the method only optimizes uni-modal $\Phi(a,t)$.

Simplex method (SM) [17]. The SM moves a fixed size pattern of $N + 1$ trials in N variables towards the optimum response. The SM works stable for systems of large dimensions. However, it can hardly be applied for ravine-like surfaces of $\Phi(a,t)$.

Nealder and Mead method (NM) [18]. The NMM is a hill-climbing modification of the simplex method that moves a variable size pattern of $N + 1$ trials in N variables towards the optimum response. However, the NMM is inapplicable for non-unimodal $\Phi(a,t)$. The time of the convergence and the amount of calculations may depend on an initial simplex.

Simulated annealing method (SAM) [19]. A method that is resistant to becoming trapped by a local extreme is the SAM. The usefulness of SAM arises from its willingness to accept a "bad" move in parameter space (a move in a direction for the value of $\Phi(a,t)$ becomes worse) and so to extricate itself from a local minimum in further search of a possible global minimum.

Modification Nealder and Mead method (MNMM) [20]. The basic disadvantage of the search algorithms is a poor application to multi-modal optimization. The solution to this problem can be the combination of the considered methods, for example, the NMM with SAM. A combination of two methods can avoid local minima and at the same time the search is not slowed down due to the fast NMM.

Box method (BM) [14]. The BM or the complex method in essence is an update of the NMM, however, which includes restrictions in a parameter space. The main requirement is a convex shape of $\Phi(a,t)$. The method consists of iterative algorithm using the calculation of 2N points.

3.2.2. Gradient optimization methods

Application of the gradient optimization algorithms, which normally, compared to the non-derivative methods, ensure faster convergence to the optimum value of $\Phi(a,t)$, may cause extra difficulties due to the fact that they require calculation of $\partial\Phi(a,t)/\partial a_i$ i = 1,...,N. Generally, the derivative can be approximated by the following finite difference:

$$\frac{\partial\Phi(t,a)}{\partial a_i} \approx \frac{\Phi(t,\{a_1,...,a_i,...,a_N\}) - \Phi(t,\{a_1,...,a_i + \Delta a_i,...,a_N\})}{\Delta a_i}, i = 1,...,N,$$

(2)

where Δa_i is the increment for parameter a_i. However, when a MC simulation is used for fitting or a theoretical histogram $F^T(a,t)$ has noise, the calculation of eqn. (2) is essentially ill-posed and may result in significant numerical distortions. The approach for solving this problem is to control the process of the simulations by establishing identical initial values for a random variable generator, used in the MC model. Then the simulated statistical fluctuations in any two realizations of the simulated theoretical histograms $F^T(t,\{a_1,...,a_i,...a_N\})$ and $F^T(t,\{a_1,...,a_i+ \Delta a_i,...a_N\})$ are highly correlated and eqn. (2) can be calculated with higher accuracy. Among the variety of gradient optimization algorithms, the most widely used in time-resolved fluorescence spectroscopy are Levenberg-Marquardt, Gaus-Newton, Line Search, Large Scale [21,22,23,24]. A short excursion to the theory of gradient methods is presented below.

Steepest descent method (SDM) [21]. The SDM searches along the gradient of $\Phi(a,t)$ to obtain a better estimate of the parameters. This method is especially useful for large problems, as it requires the least computer memory. However, the SDM does require many more iterations than other known gradient optimization methods and converges linearly.

Gauss-Newton method (GNM) [22]. The GNM is a less general but computationally simpler optimization method because it can only minimize the least-squares norm, whereas parabolic extrapolation of $\Phi(a,t)$ might be used to minimize any norm of the data and fitting function. The method exhibits a "quadratic convergence" which, simply put, means that the uncertainty in the parameters after i+1 iterations is proportional to the square of the uncertainty after i iterations.

Once these uncertainties begin to get small they decrease quite rapidly. The major problem with the GNM is that it sometimes diverges instead of converges. The algorithm of the method is formulated as a system of Taylor series expansions of the fitting function.

Modified Gauss-Newton method (MGNM) [25]. The MGNM is a combination of the Gauss-Newton and quasi-Newton strategies. The MGNM uses a decision whether to take the Gauss-Newton step or the step that is computed by the quasi-Newton approximation. Applying a quasi-Newton algorithm is logical since quasi-Newton algorithms are superlinearly convergent.

Levenberg-Marquardt method (LMM) [23,24]. The LMM is the most commonly used procedure of improving the convergence properties of the GNM. It is essentially a linear combination of the SDM and GNM. The LMM retains the robust, but linear, convergence properties of the steepest descent method when the parameter values are far from their final values, and it still has the rapid quadratic convergence properties of the GNM when the parameter values are close to the final converged values. The advantages of the LMM are that the algorithm is relatively easy to implement, usually converges rapidly, and does not require large storage arrays.

3.3. Statistical Criteria and Error Analysis

χ^2 *criterion* [26]. χ^2 criterion for MC simulation analysis is defined in Section 4.1. and its practical application for the fitting problem is given in Sections 4.2. and 4.3.

Kolmogorov-Smirnov criterion [26]. The Kolmogorov-Smirnov test examines the maximum deviations between the expected and observed distribution functions and sometimes more for detecting local defects. The Kolmogorov-Smirnov statistics is

$$K_n = \sqrt{n} \max_{0 < t_i < n} \left| \widetilde{F}^E(t_i) - \widetilde{F}^T(t_i, a) \right| = \max(K_n^+, K_n^-)$$

(3)

$$\widetilde{F}^E(t_i) = \sum_{j=0}^{i} F^E(t_j)$$

(4)

$$\widetilde{F}^T(t_i, a) = \sum_{j=0}^{i} F^T(t_j, a)$$

(5)

where max denotes the maximum deviation between K_n^+ and K_n^-, K_n^+ is related to the maximum observed positive deviation from expected $F^E(t_i)$, and K_n^- is related to the maximum

negative deviation. After statistics of K_n^+ and K_n^- calculated they should be compared with predicted values of K_n^+ and K_n^- distribution in the tables.

Romanovsky criterion [27,28]. Romanovsky test checks statistics

$$\rho(t_i) = \frac{F^E(t_i) - F^T(t_i, \boldsymbol{a})}{\sqrt{w(t_i)}}$$

(6)

to be Gaussian distribution with $N(m, \sigma)$, where $m = 0$ and $\sigma = (\chi^2(\boldsymbol{a}))^{1/2}$. Hence, after calculating the $\chi^2(\boldsymbol{a})$ statistics the Romanovsky value is

$$\Re = \left| \frac{\chi^2(\boldsymbol{a}) - \nu}{\sqrt{2\nu}} \right|$$

(7)

If $\Re < 3$ then with high probability it is Gaussian distribution.

Graphical composition of observed and calculated curves. An additional test, which can help to distinguish a poor fit, is sometimes just direct graphical visualization of observed and fitted decay curves. However, it can be a poor tool when instrumental artifacts are present in the observed curve and therefore the quality of the fit may hardly be distinguished.

Plot of the weighted residuals. The weighted residuals calculated in i-th channel can be plotted against the time channels. Residuals from successful fits should be randomly distributed around zero.

Autocorrelation function of the weighted residuals [1,2,3]. The autocorrelation function is

$$Cr(t_j) = \frac{\frac{1}{m} \sum_{i=1}^{m} \rho(t_i)\rho(t_{i+j})}{\frac{1}{n} \sum_{i=1}^{n} \rho^2(t_i)}$$

(8)

where $m = n - j$. The autocorrelation function from a successful fit should be randomly distributed around zero.

Durbin-Watson parameter [2,3]. Durbin and Watson introduced a parameter that has some resemblance to the autocorrelation function of the residuals for an autocorrelation channel $j = 1$. The defining equation is

$$DW = \frac{\sum_{i=2}^{n} [\rho(t_i) - \rho(t_{i-1})]^2}{\sum_{i=1}^{n} \rho^2(t_i)}$$

(9)

Durbin and Watson tabulated upper and lower limits for the parameter for different numbers of data points and numbers of estimated parameters. Success of the fits can be checked with tables designed by Durbin and Watson.

Measure of skewness [2,3]. A measure of skewness of a fit can be estimated with equation

$$SK = \left[\frac{n-1}{\left(\sum_{i=1}^{n} [\rho(t_i) - \overline{\rho}]^2 \right)^3} \right]^{1/2} \times \sum_{i=1}^{n} [\rho(t_i) - \overline{\rho}]^3$$

(10)

with

$$\overline{\rho} = \sum_{i=1}^{n} \rho(t_i)/(n-1)$$

(11)

For a normal distribution SK is approximately normally distributed with a mean of zero and a standard deviation given by $[6/(n-1)]^{1/2}$. Absolute values of SK greater than $[6/(n-1)]^{1/2}$ are therefore indicative of a skewed fit.

Measure of Kurtosis [2,3]. A most sensitive measure of departure from the Gaussian distribution can be calculated as

$$K = \frac{(n-1) \sum_{i=1}^{n} [\rho(t_i) - \overline{\rho}]^4}{\left(\sum_{i=1}^{n} [\rho(t_i) - \overline{\rho}]^2 \right)^2}$$

(12)

For the Gaussian distribution this ratio has the value 3.

Other tests [16,26]. Other suggested fitting criteria include the standard normal variety, variation of fitting range and initial guesses, the root mean square deviation of the residuals, run and sequence tests, etc. These tests and criteria are not so important and sensitive to the analysis by the simulation fitting approach and therefore may be omitted from the tests.

3.4. Confidence interval estimation

The critical importance in the parameter fitting is the determination of the accuracy of the estimated parameters. There are numerous methods of evaluating the confidence intervals of determined parameters [29] and only several are briefly considered.

MC method [30]. Once a set of parameters has been determined a set of synthetic data based on these parameters can be generated. This set of data should be as close an approximation to the actual experimental data set as possible using the same independent variables. Realistic pseudorandom experimental uncertainties are then added to the synthetic data set, and the parameter estimation procedure is repeated to obtain a new set of parameters. This process is repeated many times to obtain a description of parameter values. Confidence intervals can then be generated from the parameter probability distribution obtained for each of the parameters. When the MC method is used for the confidence interval evaluation of the parameters from MC simulation then it is enough to collect a set of data just by generating different initial values for the random generator used in a MC model.

Grid search method [31]. The grid search involves creating a grid of parameter values and evaluating the χ^2 value at each of the grid vertexes. The confidence intervals are the regions surrounding the minimum over which the χ^2 values do not increase significantly with regards to the minimum value. This method is quite precise but requires substantial computer time.

Asymptotic standard errors [32]. The most common method of evaluating confidence intervals of estimated parameters is to use the diagonal elements of the variance covariance matrix:

$$VC = (A^T A)^{-1} \chi^2 / \nu$$

(13)

where A is a normalized matrix of the partial derivatives of $\Phi(a,t)$. The square roots of diagonal elements of the VC matrix are asymptotic standard errors of the estimated parameters. The calculation of the confidential interval of estimated parameters from the standard error follow below.

A β percent confidence interval on the parameter a_j, $j = 1,...,N$ is given by

$$a_j - t_{\alpha/2,\nu}\sqrt{\overline{\sigma}^2 C_{jj}} \leq a_j \leq a_j + t_{\alpha/2,\nu}\sqrt{\overline{\sigma}^2 C_{jj}}$$

(14)

where $\alpha = 1 - \beta$; $t_{\alpha/2,\nu}$ is the upper $\alpha/2$ percentage point of the t is distribution (Student distribution [33]) with ν degrees of freedom; a_j is the value of estimated parameter j; C_{jj} is the jj element of the VC matrix; β is the confidential probability ($0<\beta<1$); $\overline{\sigma}^2$ is the estimate of the error variance ($\overline{\sigma}^2 \equiv \chi^2 \approx 1$ for good fits). Errors must be normally and independently distributed with mean zero and variance σ^2.

Other methods of evaluating the confidence intervals [29,31] like linear joint, support plane, exhaustive search, etc. are not so promising for the simulation approach described in this Thesis and therefore are omitted from the consideration.

3.5. Simulation-based testing of the fitting algorithms

A collection of the models for the fluorescence intensity decay have previously been developed [1,2,3], among them exponential, multi-exponential and "stretched" exponential models are widely popular. These models have been chosen for the tests since they are excessively understood and can allow a wide-variation range for the parameter fitting.

3.5.1. Analytical and simulation models

Exponential model. The simplest model of the fluorescence intensity decay, as that of a low-concentration solution of non-interacting molecules, is a single exponential. Its analytical presentation is given by eqn. (25) of the Chapter 1. The MC simulation is performed by the generation of the time t_{det} of the photon arrivals at a detector with equation

$$t_{det} = -\tau \ln(\text{rand}(1))$$

(15)

where $\text{rand}(1)$ is a generator of random variables in the range of [0,1]. The set of N_{SC} excitations are played for one individual molecule and after generating t_{det} the channel number, that will serve as the current accumulator of the considered event of excitation decay, can be calculated as $K_{det} = (t_{det}/\Delta t)$ where Δt is the time channel width of a multichannel detector. The decay times of the photon arrivals t_{det} are stored in the $F^E(t)$ or $F^T(a,t)$ histograms.

Mult-exponential model. The multi-exponential model can describe the fluorescence decay of a mixture of dye molecule with corresponding lifetimes τ_i (i = 1,...,j). The analytical representation of the multi-exponentials is

$$I(t) = \sum_{i=1}^{j} \frac{p_i}{\tau_i} e^{-\frac{t}{\tau_i}}$$

(16)

with

$$\sum_{i=1}^{j} p_i = 1$$

(17)

To generate the time t_{det} of i -th dye to be used in the MC simulation, two random numbers $z_1 = \text{rand}(1)$ and $z_2 = \text{rand}(1)$ have to be played. After that, the interval [0,1] is divided into j channels, which i-th channel width assumed to be proportional to the contribution of i-th dye molecule. If z_1 falls in i -th channel than t_{det} is generated as

$$t_{det} = -\tau_i \ln(z_2)$$

(18)

Then filling a histogram is performed in the same manner as in the upper algorithm. Finally, after N_{SC} simulation runs the multi-exponential fluorescence decay has been collected in the $F^E(t)$ or $F^T(\boldsymbol{a},t)$ histograms.

"Stretched" exponential model. The "stretched" exponential model is a represent of the donor fluorescence intensity decay in the presence of Förster type ET in a donor-acceptor molecular system. Regarding Chapter 1, the eqn. (23) for the donor fluorescence in 3D space can be written as

$$I(t) = I_0 \exp\{-t/\tau_d - q_A(t/\tau_d)^{1/2}\}$$

(19)

where $I_0 = I(t = 0)$; $q_A = 0.5[C_A]/[C_{A0}]$, C_{A0} and C_A are critical and actual acceptor concentrations, respectively [34]. The MC simulation of the donor fluorescence affected by the Förster type ET has been previously described [35,36]. In this Chapter the MC simulation model of the donor fluorescence has been implemented through the simplified algorithm based on the Neumann method [37]. Regarding this algorithm, the donor decay time t_{det} can be generated with eqn. (15) whereas the ET time t_{ET} is differently: if $z_1 < \exp\{-q_A(t_{ET}/\tau_d)^{1/2}\}$ (where $z_1 = \text{rand}(1)$ and $t_{ET} = T_w \text{rand}(1)$, T_w is the detecting timewindow width) then t_{ET} is accepted.

Afterward if $t_{det} < t_{ET}$ then t_{det} is stored into the $F^E(t)$ or $F^T(a,t)$ histograms otherwise to stop without detection (assumed that acceptors are the energy traps). Running N_{SC} times the simulation procedure, the donor fluorescence of two parameters (q_A and τ_d) is collected in the $F^E(t)$ or $F^T(a,t)$ histograms.

3.5.2. Comparative analysis of the fitting procedures

The tests on the abovementioned algorithms have been spent on synthetic data, generated in accordance with the TCSPC method [38] on an IBM PII 233MHz PC. All numerical procedures have been coded using the programming language C++ for IBM computers. The actual parameters for the modeling of the numerical "experimental" decays $F^E(t)$ were set to demonstrate the properties of the fitting methods as well as to investigate the extremal borders of their applicability. Several characteristics for the quality of the optimization methods have been used:

i) the stability St of the fitting method that is defined by

$$St = N_{IG}^+ N_{IG}^{-1}$$

(20)

where N_{IG}^+ and N_{IG} are numbers of successful and total optimizations. When a global minimum (for instance, its 99% critical region) of $\Phi(a,t)$ is reached then the N_{IG}^+ is counted;

ii) the number N_F of the calculations of $\Phi(a,t)$;

iii) the time t^+ (milliseconds) needed for a successful fitting;

iv) the number N_{SC} of simulated counts which controls the statistical noise in each histogram $F^E(t)$ or $F^T(a,t)$. Typically, $N_{SC} = 10^3, ..., 10^6$;

v) the segment region S_{IG} defining the remoteness of the initial guesses from the actual parameter values. S_{IG} is built around the actual parameters and %- sized relative to the values from which the initial guess is generated. Typically, S_{IG} = [0;10%], [10%;30%], [30%;50%], [50%;100%], [100%;150%], [150%;200%], [200%;300%], [300%;400%], ...

The number of time channels in the $F^E(t)$ or $F^T(a,t)$ histograms is varied from 128 up to 8192 with the channel width from 0.001 up to 0.050 of a.u. (arbitrary units). In every numerical

experiment, an optimization procedure has been repeated N_{IG} times, each one with a different set of the initial guesses randomly generated in a segment region S_{IG}. Then, after N_{IG} optimizations, the St`, $N_F$`, and t^+` are mean values of the statistics $\{St_1 , ..., St_{N_{IG}}\}$, $\{N_{F1}, ..., N_{FN_{IG}}\}$, and $\{t^+_1, ..., t^+_{N_{IG}}\}$. The stopping criterion for the optimization methods is chosen as follows. Since the values of parameters as well as the value of the χ^2 criterion in the global minimum can be exactly determined beforehand, one can easily calculate the region of the χ^2 criterion values, around the global minimum at any confidence level, according to F-statistics [16]. As soon as the value of χ^2 during the fit becomes less than the border of that region, the iterative procedure stops. In our numerical experiments, the critical region is calculated at the 99% confidence level.

Testing of criteria and confidence interval evaluations. The tests of statistical criteria and methods of error analysis are directed to answer two important questions: which criterion is the best for judging the goodness of the fits and how does it influence the convergence? The typical results of the computer tests on the selected criteria are presented in Table 1. In a most of tests, the χ^2 criterion has been observed to be sensitive for the goodness of the fits and at the same time providing fast convergence as a "fitting" function. The Kolmogorov-Smirnov criterion judges well for relatively large number of the channels (> 1024) and even better then χ^2 criterion for 8192 channels.

Table 1. The mean values N_T` for different criteria and channels obtained by MC simulation fitting of the "stretched" exponential intensity decay (see section 3.5.1.). N_{IG} = 100, S_{IG}=[200%;300%], N_T = $6\cdot10^6$, (KS) Kolmogorov-Smirnov criterion, (R) Romanovsky criterion.

Criterion/ Channels	256	1024	4096	8192
χ^2	28	30	29	33
KS	212	135	51	29
R	436	401	389	375

Romanovsky criterion can in principle acceptably judge but is less effective then the χ^2 or Kolmogorov-Smirnov criteria. Any additional important advantages of the χ^2, Kolmogorov-Smirnov, and Romanovsky criteria to simulation fitting have not been found. Other criteria and methods of error analysis (see section 3.3.) are also might be used for the analysis of experimental data by MC simulation fits and their properties are not much different from the standard fitting.

Tests on the methods presented in section 3.4. support their application for the confidence interval evaluation of the parameters retrieved via a MC simulation fit. Sizes of the confidence

intervals are strongly influenced by the number N_{SC} of the simulated counts in both histograms as it can be concluded from the χ^2 contours plots in Fig. 1.
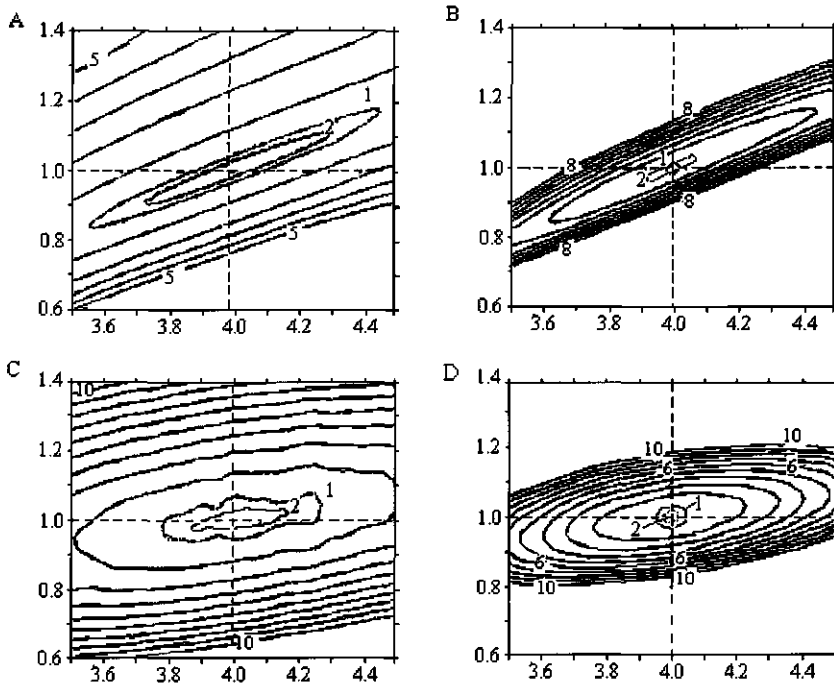

Fig. 1. The χ^2 contours built with the analytical (eqn. (19)): (A),(B) and MC simulation model: (C),(D) for the "stretched" exponential intensity decay. 1 and 2 denote the 75% and 99% confidence intervals, respectively. Simulated counts N_{SC}: (A) - 10^4; (B) - 10^5; (C) - $2 \cdot 10^5$; (D) - $6 \cdot 10^5$. The parameters $q_A = 1$ and $\tau_d = 4$ are corresponded to the minimum.

As the value N_{SC} increases, the estimated confidence interval climbs to the actual confidence interval of the parameter. The grid search methods and MC methods have been found accurate in the estimation of the confidence intervals but require too much computer time for acceptable evaluation. Since it is better to have a compromise between accuracy and the time, the method using VC matrix has the highest priority. The method of asymptotic standard errors is very fast but less accurate. For instance, for a "good" fit ($N_{SC} = 10^5 - 10^6$) errors in the confidence intervals are in 10 - 30%.

Testing of the fitting algorithms. The results of the comparative analysis of the optimization methods for the estimating the fluorescence decay parameters of two, three and "stretched" exponential intensity decays by both analytical and MC simulations are presented in Fig. 2.

Fig. 2. The 3D diagrams of the mean value $N_F`$ (z- axis) for different segment regions S_{IG} (x- axis) and optimization methods (y- axis). (A):- analytical two exponential fitting ($N_{SC} = 10^5$); (B): analytical three exponential fitting ($N_{SC} = 5 \cdot 10^5$); (C): analytical "stretched" exponential fitting ($N_{SC} = 2 \cdot 10^5$); (D): MC simulation fitting of "stretched" exponential decay ($N_{SC} = 6 \cdot 10^5$). $N_{IG} = 100$.

The GM properly restores the parameters of analytical multi-exponentials. The number $N_F`$ is considerably increased with increasing the number of exponentials. The method is badly applied for the analysis of the "stretched" exponential decay law where the χ^2 contours are the narrow ravines (see Fig. 1). Rather frequently the GM prematurely stopped or got into local minima. The convergence to a global minimum have only been performed from successfully generated initial guesses. Taking the results of the tests into account, the GM is expedient for applying at a

preliminary stage of the fitting and could be fruitful for the allocation of a global minimum that might further be used as initial guesses for a more powerful optimization method.

The HJM is slow in the convergence what might be due to the constant factor for the reduction of a search step h (usually 10 and too poor for the fast convergence). It has been observed that the constant factor should be reduced gradually, i.e. 10, 8, 6, 4, etc. In this case a relative acceleration of the search was reached. The HJM is ineffective for the multi-modal χ^2 contours yielded from the high values of the statistical noise (see Fig. 3).

The PM allows receiving steady parametric estimations for the analytical parameter fitting. Undoubtedly, the PM is one of the best search algorithms for the traditional fitting by an analytical expression as it can be concluded from the comparison of the N_F` values in Fig. 2. This method is also mobile for the analysis of the ET processes by a MC simulation fitting. The disadvantage is the poor application for multi-modal χ^2 surfaces.

The estimations by the RM are statistically steady for all kinds of parameter fittings. Drawbacks are the impossibility to analyze multi- modal χ^2 contours and nevertheless rather slow convergence as compared to gradient methods (see Fig. 1). For increasing the speed of convergence, so-called update of Davise, Swen, and Kemp [14] has been considered. This modification is a one-dimensional search on a method parameter λ. Testing of the updated algorithm has shown that such a reception could be justified. The N_F` values have been decreased to almost 80%. Thus, the RM and its updating could be used for the complex decay curve analysis.

The SM provides fast convergence only for simple fitting where the topological contours have a fundamental character and large gradients of heights are excluded. However, the method can successfully work for multi-modal fitting. On the other hand, the simplex method is one of the slowest methods considered in this chapter and therefore cannot be recommended for the experimental data analysis.

One of the most flexible and universal methods for fitting by MC simulation is the NMM. The method provides high accuracy avoiding ravine-like contours. However, the NMM is strongly declined down or even can stop into the local minima when χ^2 surface is multi-modal. Efficiency of the NMM depends on a choice of an initial simplex and, hence, the method is expedient for using at the finishing stage of the fitting procedure.
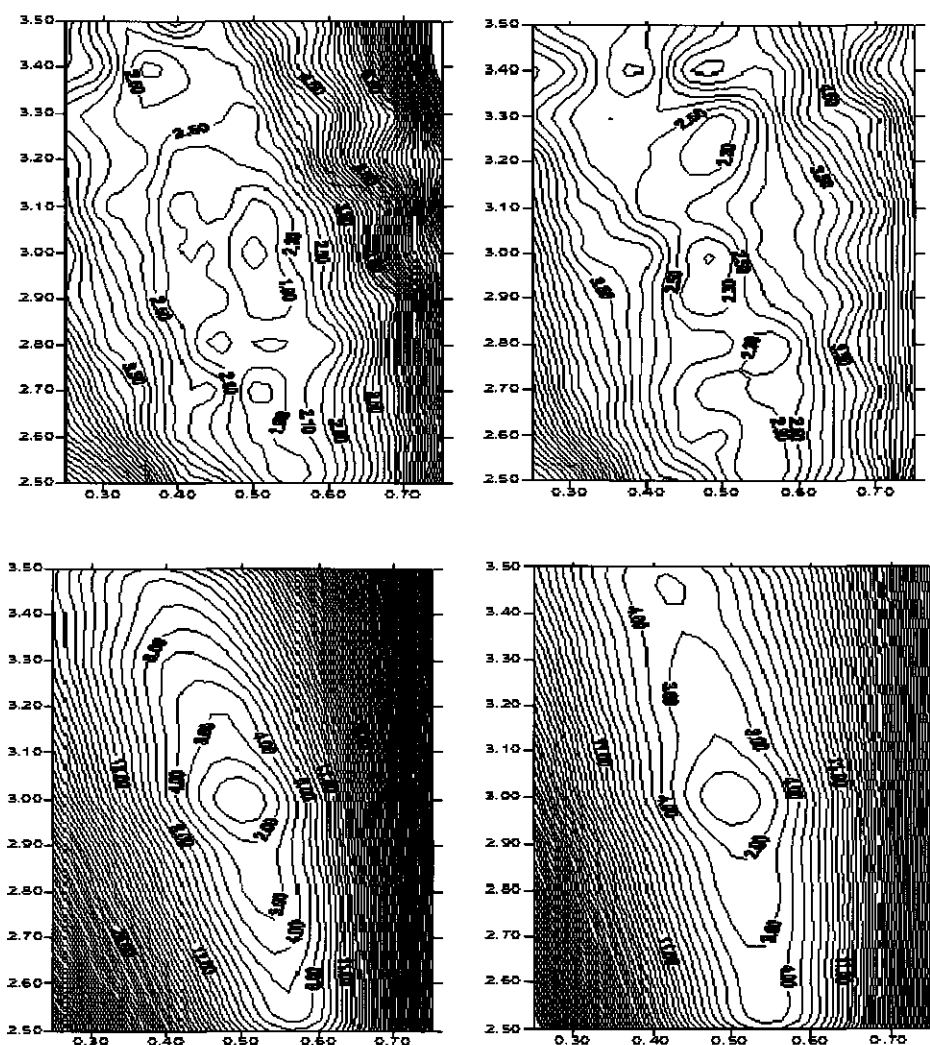
Fig. 3. The χ^2 contours built with the MC simulation of two exponential intensity decay. Simulated counts N_{SC}: (A) - 10^3; (B) - 10^4; (C) - 10^5; (D) - 10^6. The parameters $p_1 = 0.75$, $\tau_1 = 0.5$ and $p_2 = 0.25$, $\tau_2 = 3$ are correspond to the minimum.

Since the SAM only uses a random search procedure without any accelerating mechanisms, a slow convergence has always been registered. On the other hand, the SAM has provided practically a systematic exit from any local minimum. Thus, pure application of the SAM for simulation fitting is not effective and has resulted extremely large time for the fitting.

Acceptable results have been obtained for the combination of NMM and SAM. The number N_F` spent for the unimodal optimization is comparable to that for the NMM. However, for multmodal optimization the $N_T$` value is less than that from the NMM.

The BM requires rather large the N_F` but it is fully compensated by the steady convergence into a global minimum. The random formatting of an initial complex provides the covering of a large area in parameter space and, hence, the consequent tendency to converge to a global minimum. This method is very convenient for experimental data containing a substantial growth of the noise. The tests on the BM have shown that around 20 - 30% of t^{+}` has been served for localizing the area of the global minimum and the rest time (70 - 80 % of $t^{+}$`) the method specified restored parameters, being pulled in the region of a minimum. One of the accelerating mechanisms for the last stage of the optimization could be a variant of sharing with the NMM: the BM allocates the global minimum area, whereupon, the "fast" NMM specifies the parameter values. The second updating of the BM is which uses the square-law interpolation along a direct line connecting the reflected and central points of a complex. Using the square-law interpolation resulted in the N_T to be reduced by 30 - 40% compared to the standard BM. However, the updating method works incorrectly for unconvex χ^2 contours where the movement of a complex prematurely breaks and results in unpredictable consequences of the search procedure. Certainly, the given updating method represents large interest and could be used for MC simulation fitting.

The gradient fitting procedures have provided faster convergence than non-derivative methods especially for multi-parametric fitting (with two or tree exponentials). However, several methods (SDM and GNM) are still slow for processing the ravine-like χ^2 surfers. The second drawback of the gradient methods is often worse stability of the convergence from far S_{IG} regions (typically, [400%;500%], [500%;600%], etc.). The LMM and the MGNM are the favorites of the gradient methods as they use much less N_T and t^{+} then others.

Coming discussion is devoted to the comparative analysis of two fitting methods: the first one is from the non–derivative group, the NMM, and the second one is from the gradient group, the LMM. Both methods are the favorites of the respective method groups and their comparative analysis is rather interesting for practical application. The St`, $N_F$`, and t^{+}` for different segment regions S_{IG} are presented in Fig. 4.
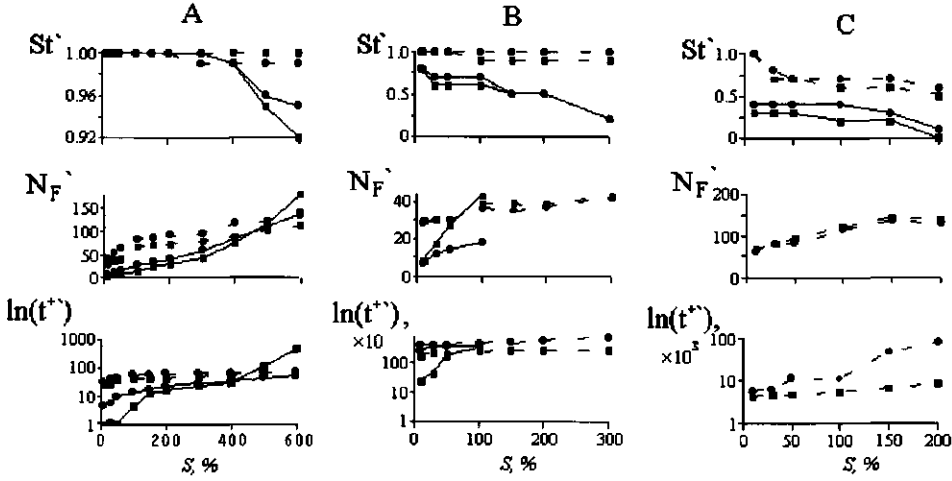
Fig. 4. The $St^`$, $N_F^`$, and $t^{+`}$ characteristics for different segment regions S_{IG} obtained for the LMM (solid line) and NMM (broken line). (A): analytical "stretched" exponential fitting (■: $N_{SC} = 10^4$, ●: $N_{SC} = 10^5$); (B): MC simulation fitting of "stretched" exponential intensity decay (■: $N_{SC} = 10^5$, ●: $N_{SC} = 5 \cdot 10^5$); (C): MC simulation fitting of two exponential intensity decay (■: $N_{SC} = 2 \cdot 10^5$, ●: $N_{SC} = 6 \cdot 10^5$). The $N_F^`$ and $t^+$ are omitted for the $St^` < 0.5$ since it is too poor for statistics sufficient for building confident estimators.

For the fits by the analytical and MC simulations, the LMM ensures better performance than the NMM. The problems in the LMM only arise when initial guesses are generated from the far segment regions S_{IG} (typically, [400%;500%], [500%;600%], etc.). For the analytical fits, when the number N_{SC} of simulated counts in the $F^E(t)$ histogram increases then the $N_F^`$ and $t^{+`}$ values for both methods become higher. Obviously, narrowing (the increase of ravine-likeness) of the χ^2 contours (see Fig. 1A and 1B) for the larger number of collected counts leads to the increase of the number of iterations in order to reach the optimum. In the case of MC simulation fitting, the increase of the number N_{SC} of simulated counts in the $F^E(t)$ or $F^T(a,t)$ histograms results in a faster convergence and higher stability for both methods. One can see in Fig. 1.C and 1D that the slope of the χ^2 contour for $5 \cdot 10^5$ simulated counts is much steeper than for the χ^2 contour with $2 \cdot 10^5$ simulated counts. Comparing the χ^2 contours built with the analytical and the MC simulations, one can conclude that in the latter case the shape of the global minimum region has been expanded and the slope becomes gentler. That is the explanation why the performance of the methods is better against increasing N_{SC} for the MC simulation fits. The increase of statistics in the $F^T(a,t)$ histogram will certainly provide better results. Due to the increased number of

parameters, provided by the MC simulation of the two exponential intensity decay, the stability St' of both methods essentially decreases.

3.6. Conclusions

- The χ^2 criterion is the best one for judging the goodness of the simulation-based fits as well as for parameter fitting. The other statistical tests can be used as support for χ^2 statistics;

- The accuracy of estimated parameters after simulation based fitting can be checked with the asymptotic standard errors method;

- A comparative analysis of the optimization algorithms for fluorescence decay fitting by both analytical and Monte Carlo simulations allows to select the Nealder and Mead method, Modification Nealder and Mead method, Powell method, Box method, Levenberg-Marquardt method and Modified Gauss-Newton method for the practical applications in data analysis, where the energy transfer processes are studied by Monte Carlo methods.

References

[1] J.R. Lakowicz (1999) *Principles of Fluorescence Spectroscopy* Kluwer Academic/Plenum Publishers, New York.

[2] J.N. Demas (1984) *Excited State Lifetime Measurement* Academic Press, New York.

[3] D.V. O'Connor, D. Phillips (1984) *Time-Correlated Single Photon Counting* Academic Press, London.

[4] D.V. O'Connor, W.R. Ware, J.C. Andre, *J. Phys. Chem.*, 83 (1979) 1333.

[5] V.V. Apanasovich, E.G. Novikov, *J. Appl. Spec.*, 56 (1992) 538.

[6] V.V. Apanasovich, E.G. Novikov, *Rev. Sci. Instrum.*, 67(1) (1996) 48.

[7] R. Rubinstein, A. Shapiro (1998) *Modern Simulation and Modelling* John Willey & Sons Inc., New York.

[8] K. Binder, D.V. Heerman (1992) *Monte Carlo Simulation in Statistical Physics* Springer-Verlag, Berlin.

[9] V.V. Apanasovich, E.G. Novikov, N.N. Yatskov, *Proc. SPIE*, 2980 (1997) 495.

[10] G.L. Nemhauser, A.H.G. Rinnooy Kan, M.J. Todd (1989) *Optimization* North -Holland, Amsterdam.

[11] D.P. Bertsekas (1996) *Constrained Optimization and Lagrange Multiplier Methods* Athena Scientific, Belmont.

[12] J.E. Dennis, R.B. Schnabel (1996) *Numerical Methods for Unconstrained Optimization and Nonlinear Equations* SIAM, Philadelphia.

[13] H.P. Schwefcl (1996) *Evaluation and Optimum Seeking* John Willey & Sons Inc., New York.

[14] D.M. Himmelblau (1970) *Process Analysis by Statistical Methods* John Willey & Sons Inc., New York.

[15] Y. Ermoliev, R.J.B. Wets (1992) *Numerical Techniques for Stochastic Optimization* Springer-Verlag, Berlin.

[16] P.R. Bevington (1969) *Data Reduction and Error Analysis for the Physical Sciences* McGraw-Hill, New York.

[17] W. Spendley, G.R. Hext, F.R. Himsworth, *Technometrics*, 4(4)(1962) 441.

[18] J.A. Nelder, R. Mead, *Comput. J.*, 8 (1965) 308.

[19] S.L. Shew and C.L. Olsen, *Analytical Chemistry*, 64 (1992) 1546.

[20] I.O. Bohachevsky, M.E. Johnson, M.L. Stein, *Technometrics*, 28 (1982) 209.

[21] R. Flecher (1987) *Practical Methods of Optimization* John Willey & Sons Inc., New York.

[22] M.J. Johanson, S.G. Frasier, *Methods Enzymol.*, 117 (1985) 301.

[23] D. M. Bates, D. G. Watts (1988) *Nonlinear Regression Analysis and Its Applications* John Wiley & Sons Inc., New York.

[24] P.E. Gill, W. Murray, M.A. Saunders, M.H. Wright (1989) *Practical Optimization* Academic Press, New York.

[25] D. M. Gay, *ACM Trans. Math. Software*, 9 (1983) 503.

[26] D.E. Knuth (1997 -2001) *The Art of Computer Programming* Reading Addison-Wesley, Massachusetts.

[27] V.E. Gmurman (1977) *Theory of Probability and Mathematical Statistics* Infra-M, Moscow (In Russian).

[28] V.A. Kolimaev, Ed. (1997) *Theory of Probability and Mathematical Statistics* High School, Moscow (In Russian).

[29] J.R. Lakowicz (1991) *Topics in Fluorescence Spectroscopy* V.1 Plenum Press, New York.

[30] M. Straume, M.J. Johanson, S.G. Frasier, *Methods Enzymol.*, 210 (1992) 117.

[31] M.J. Johanson, L.M. Faunt, *Methods Enzymol.*, 210 (1992) 1.

[32] M.J. Johanson, *Methods Enzymol.*, 240 (1994) 1.

[33] G.A. Korn, T.M. Korn (1961) *Mathematical Handbook for Scientists and Engineers* McGraw- Hill Book Company, New York.

[34] K.P. Giggino, T.A. Smith, *Prog. Reaction Kinetics.*, 18 (1993) 375.

[35] L. Andrews, A. Demidov (1999) *Resonance Energy Transfer* John Willey & Sons LtdInc., New York.

[36] M.N. Berberan-Santos, P. Choppinet, A. Fedorov, L. Jullien, B. Valeur, *J.Am.Chem.Soc.*, 121 (1999) 2526.

[37] Bratley P., Fox B.L., Schrage L.E. (1983) *A guide to simulation*: Springer, New York

[38] F.N. Chowdhury, Z.S. Kolber, M.D. Barkley, *Rev.Sci.Instrum.*, 62(1) (1991) 47

Chapter 4

Global analysis of energy relaxation and -transport processes

This Chapter describes a Monte Carlo simulation model for energy transport and -relaxation, affecting fluorescence- and fluorescence anisotropy decay. Equations for the χ^2 criterion and its weighting factors, used in a Monte Carlo simulation fitting procedure, are presented and modified for different types of time-resolved data analysis. Illustrative examples demonstrating several fits of the fluorescence- and fluorescence anisotropy decay using the Monte Carlo simulation fitting are presented. The concepts behind the simulations are discussed.

4.1. Simulation model of the processes of energy relaxation and transport

Non-isotropic Excitation Energy Transport in Organized Molecular Systems: Monte-Carlo Simulation-based Analysis of Fluorescence- and Fluorescence Anisotropy Decay

Mikalai M. Yatskou[a,b], Harry Donker[a], Eugene G. Novikov[b], Rob B.M. Koehorst[a], Arie van Hoek[a], Vladimir V. Apanasovich[b], Tjeerd J. Schaafsma[*a]

[a] Laboratory of Biophysics, Department of Agrotechnology and Food Sciences, Wageningen University, Dreijenlaan 3, 6703 HA Wageningen, The Netherlands

[b] Department of Systems Analysis, Belarusian State University, 4, F. Scoryna Ave., Minsk, 220050, Belarus

Abstract

A novel method for the analysis of time-resolved fluorescence data has been applied to organized molecular systems exhibiting a number of different, non-isotropic energy transfer processes. This work focuses on the analysis of the experimental fluorescence- and fluorescence anisotropy decays of two complex molecular systems, using Monte Carlo simulations by parameter fitting, employing physical models, developed for these systems. This procedure yields a final set of parameters, which characterizes the energy transfer processes in the investigated systems. The advantage of such a simulation-based analysis for global parametric fitting is discussed.

Energy transfer processes have been analyzed by this approach for two porphyrin model systems, i.e. spincoated films of zinc tetra-(octylphenyl)-porphyrins (ZnTOPP) and the tetramer of zinc mono(4-pyridyl)triphenylporphyrin (ZnM(4-Py)TrPP). For the ZnTOPP film energy transfer rate constants of $\sim 1\times10^{12}$ s^{-1} and $\sim 80\times10^{9}$ s^{-1} have been found, and are assigned to intra- and inter-stack transfer, respectively. For the tetramers, the transfer rate constants of

[*]Corresponding authors: Tel: +31-317482044; Fax: + 31-317482725; e-mail: Tjeerd.Schaafsma@mac.mf.wau.nl
Tel./Fax: + 375-172 789345; e-mail: yatskou@rfe.bsu.unibel.by

38×10^9 s^{-1} and 5×10^9 s^{-1} corresponding to transfer to nearest and next nearest neighbor molecules, respectively, are in agreement with a Förster type energy transfer mechanism.

1. Introduction

Energy transport, in the following denoted as ET, in organized molecular systems is one of the most important processes in photosynthesis, opto-electronic devices, artificial light harvesting systems, and solar cells [1,2,3,4,5]. The unique property of ET in photosynthetic complexes is its high efficiency even though this transfer occurs over relatively long distances. The reasons for this high efficiency are currently only partly understood.

ET processes in various natural pigment complexes and synthetic assemblies of chromophores have been widely studied through time-resolved fluorescence- and fluorescence anisotropy measurements [6,7,8,9]. Although a number of analytical expressions have been developed describing energy transfer phenomena observed *via* time-resolved fluorescence- and fluorescence anisotropy decay, mostly these expressions are unsuitable for complex, non-isotropic molecular systems, e.g. linear molecular aggregates in solution, liquid crystals, and solid films containing ordered domains [10,11,12,13,14]. One of the efficient non-analytical methods which in principle can describe the ET processes in complex systems, including non-isotropic ones, is the Monte Carlo (in the following denoted as MC) simulation method [7,15,16]. Although this method has been used extensively to test the validity of the approximations made in analytical theories [17,18,19,20], its possibilities stretch much further, as is demonstrated in this work.

Modeling ET processes in molecular assemblies using MC simulations has the advantage – among others - that it gives direct insight how various parameters of the model affect the experimental characteristics of the system, e.g. the time dependence of the anisotropy spectrum. Recently, MC algorithms have been applied to several types of ET mechanisms in non-isotropic molecular systems [10,12,19]. These algorithms need to assume *a priori* a particular type of ET, i.e. by a Förster-, higher multipole- or exchange mechanism [6,21,22]. Often, in systems with donor-acceptor distances comparable to the molecular dimensions such an *a priori* assumption cannot be made, however, since it is then unclear to what extent each mechanism contributes to

the observed ET rate constants. Another common problem concerns those systems where analytical expressions lead to undistinguishable results or are too complicated to provide clear evidence for a dominant energy transfer mechanism [14].

We propose a more general method to investigate ET processes in ordered, non-isotropic molecular systems, based on the parameter fitting *via* MC simulations [23,24], which does not require the type of ET mechanism to be known beforehand. There are three steps to be taken in this approach: i) create a physical model (which includes the geometry, dynamics, etc.) of the investigated molecular system; ii) develop and program a simulation model based on the physical model, with the model parameters corresponding to the various kinetic characteristics of the molecular system; iii) find through parametric fitting an optimum set of parameters of the simulation model corresponding to the experimental data.

This paper describes in detail how the kinetic constants for ET between the components of non-isotropic molecular systems, i.e. for two different porphyrins, can be determined using MC parameter fitting. Porphyrins belong to a widely studied class of compounds that can form ordered structures [25,26,27,28,29], and thereby should be expected to exhibit non-isotropic ET We consider two porphyrin systems, for which an analytical description of the ET process can hardly be derived from general principles and thus MC simulations might be useful.

The first porphyrin model system (further denoted as **system 1**) consists of ≤ 100 nm thick, spincoated films of a self-organizing porphyrin, ZnTOPP (Fig. 1A), on quartz substrates which have intentionally been doped with known amounts of an effective fluorescence quencher, i.e. copper tetra(-octylphenyl)-porphyrin (CuTOPP). A spectroscopic study of these films [30] has shown that the films consist of layers built from one-dimensional stacks of porphyrins with a "slipped deck of cards" configuration. The stacks are oriented with their short axes perpendicular to the substrate, whereas their long axes are distributed randomly in the plane parallel to the substrate, most likely in ordered domains. Time-resolved fluorescence measurements have shown that the fluorescence decay is not a single exponential, indicating ET inside the film. Analysis of the fluorescence decay using analytical models has also shown that the ET process (shown to be of the singlet type) is best
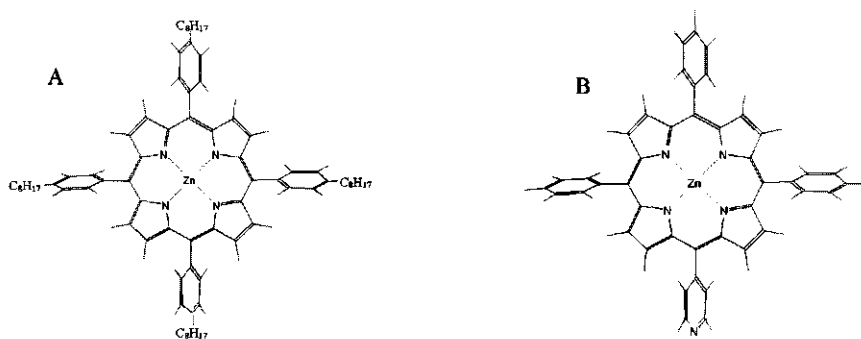
Figure 1. Structures of ZnTOPP (A) and Zn(4-Py)TrPP (B).

described by a quasi one-dimensional diffusion-limited model [31,32]. Such an analytical model only yields a rough estimate of the rate constant for intra-stack energy transfer but not for the inter-stack process. Finally, the application of the analytical model led to the conclusion that undoped ZnTOPP films contain a significant amount of non-intentional traps. Again, only a rough estimate could be given of the concentration of these traps. The present work demonstrates that more accurate and detailed information about the ET processes and the trap concentration can be obtained using MC simulations.

The second model system (further denoted as **system 2**) is the tetramer of Zn(4-Py)TrPP (Fig. 1B), in toluene solution [33]. Contrary to what has been observed for ZnTOPP films, the tetramer fluorescence decay of [Zn(4-Py)TrPP]$_4$ is a single exponential, which reflects the kinetics of the lowest singlet excited state S$_1$ of ligated Zn(4-Py)TrPP [33]. Since the porphyrin units in the tetramer are identical, energy transfer processes occurring between these units can only show up in the fluorescence anisotropy. Although the fluorescence anisotropy can in principle be analyzed by one of the proposed algorithms [19,34,35], the distances between the porphyrin units in the tetramer are comparable to the porphyrin diameter and therefore an *a priori* choice for a dominant mechanism of energy transfer is not justified. It could be argued that the exchange mechanism does not apply as a result of the perpendicular orientation of the porphyrin monomers. That may not be true, however, if the monomers in the tetramer are not perfectly flat, i.e. do not have D$_{4h}$, e.g. by distortion of the monomers as a result of the mutual ligation of the monomers in the tetramer. As is shown by this work the energy transfer rate constants as well as the transfer mechanism for the tetramer can be determined by MC simulation.

2. Simulation approach

2.1. Parametric fitting via MC simulations

Parametric fitting using MC simulations is schematically presented in Fig. 2.
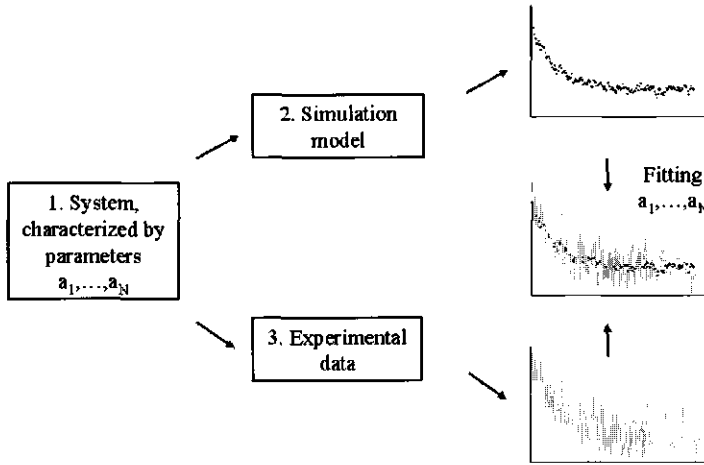

Figure 2. Simulation approach by parametric fitting.

The method approximates the experimental data (**block 3**) by the synthetic data (**block 2**) simulated using the MC methods [7,15,16]. Assuming that the theoretical model with the least number N of system parameters $\boldsymbol{a} = \{a_1,\ldots,a_N\}$ unambiguously describes the system (**block 1**), the best approximation of the experimental data yields the values of $\boldsymbol{a}$. The best approximation is defined by a criterion (or set of criteria), establishing how far the simulated theoretical function deviates from the experimental data. Generally, such a criterion is analytically represented by a function of the experimental and simulated data and is strongly dependent on the particular application area, the particular simulation method and the experimental conditions. In our numerical experiments we use the following criterion

$$\chi^2(\boldsymbol{a}) = \sum_{i=1}^{n} \frac{[F^E(t_i) - F^T(t_i,\boldsymbol{a})]^2}{w(t_i)}$$

(1)

where n is the number of channels of the multichannel analyzer ($N \ll n$), $w(t_i)$ is the weighting factor, $F^E(t_i)$ is the experimental fluorescence decay, represented by a number of detected counts per channel, $F^T(t_i,\boldsymbol{a})$ is the theoretical histogram, represented by the number of simulated counts per channel. According to this criterion the best approximation, corresponding to the set of

parameters a, is that which yields a minimum for $\chi^2(a)$. Although the criterion $\chi^2(a)$ in eqn. (1) is similar to that widely applied in statistics as the χ^2 criterion [36,37], the expression (1) differs from that commonly used, since both $F^T(t_i,a)$ and $F^E(t_i)$ contain statistical noise.

Fortunately, the statistical characteristics of the noise in the experimental data, as well as in the simulation model, are often known. For our case, all measurements were made using the time-correlated single photon counting method and streak camera detection, respectively, where the number of counts per channel of the multichannel analyzer is well approximated by Poisson statistics [38,39]. If the amount of experimental data is large enough (> ~30 counts per channel) the Poisson statistics transforms into Gaussian statistics [38,39]. Since the simulation model can be reproduced with an *a priori* statistical preciseness which is the same as, for instance, for the molecular behavior under the same conditions as in the experiments, the same statistics can be made to apply to the simulated data of $F^T(t_i,a)$.

Under the present conditions the statistical characteristics of the χ^2 criterion are directly applicable to eqn. (1). Indeed, the numerator $[F^E(t_i) - F^T(t_i,a)]$ of eqn. (1) is the difference between two Gaussian random variables. This difference itself is also the random variable of a Gaussian distribution with a zero mean value and a variance given by

$$w(t_i) = var[F^E(t_i) - F^T(t_i,a)] = var[F^E(t_i)] + var[F^T(t_i,a)]$$

(2)

where it is assumed that $F^E(t_i)$ and $F^T(t_i,a)$ are statistically independent and that $F^T(t_i,a)$ represents the best approximation for the experimental data $F^E(t_i)$. Using eqn. (2) as a weighting factor $w(t_i)$ in equation (1), the latter becomes a sum of squares of n independent standard Gaussian variates and can be discribed by a χ^2 density distribution function. Therefore, it should be expected that the mean value of a random variable of $\chi^2(a)$ equals the number of degrees of freedom $\nu = n - N - 1$, and the variance of a random variable of $\chi^2(a)$ equals ν. In the following we will use the normalised value $\chi^2(a)/\nu$ of $\chi^2(a)$.

If the number of counts per channel in the theoretical histogram approaches infinity, then the variance $var[F^T(t_i,a)]$ vanishes, and we arrive at the commonly used representation of the χ^2 criterion. In practice, we are able to increase the number of simulated counts as much as the computer facilities allow us to do, thus ensuring higher accuracy for the theoretical function.

Note that, although many papers nicely describe the application of the MC method to different molecular systems exhibiting ET [7,9,10,12,19], all of them require a set of *a priori* known parameters, which define the system structure and functionality. In our method we employ the same type of simulation models but with a set of unknown input parameter values. The correct values (or their estimates) are found through parametric fitting of the experimental data.

2.2. Global analysis

MC simulation monitored by the parametric fitting procedure opens the way for the application of the global analysis approach to a wide variety of research fields. The method commonly consists of fitting a set of measured responses by a corresponding set of theoretical models. Certain parameters of the theoretical models can be linked, for example, by forcing these parameters to be equal for all synthetic curves of the set.

In a more general approach a multi-dimensional experimental surface (for example, the fluorescence response, measured at different times, excitation/emission wavelengths, concentrations, temperatures, polarization angles, etc.) is fitted by the corresponding multi-dimensional theoretical model with a common set of unknown parameters. Such theoretical models are built on the basis of general physical laws. As a consequence there is no need to equalize particular parameters. This way of analysis ensures a consistent picture of the processes under investigation.

To build such a theoretical response in a multi-dimensional space is a rather tedious task using analytical techniques. The problems inherent to this approach are at least twofold: i) obtaining the analytical description of the processes, often represented by integral- or differential equations, and ii) technical problems of numerical implementation inherent to handling multi-dimensional arrays of numbers, which usually is very time- and memory- consuming even on modern computers. If, according to the model, one needs to solve integral or differential equations in multi-dimensional space, it most likely slows down the calculations considerably.

On the other hand, a MC simulation model operates by the elementary processes, which are easy to understand and to program. As a rule, no sophisticated mathematical methods are required: the simulation algorithm reproduces the physical processes occurring in the system almost directly. Moreover, the generation of a multi-dimensional theoretical function in the case of ET is rather straightforward. If, for example, one simulates the effects of ET in a time-resolved fluorescence experiment, each excitation photon is considered as an object having time- and space

coordinates, a polarization vector, an energy, etc. In the simulation procedure, those parameters can be introduced with the required preciseness. Simultaneously, the desired statistical characteristics can be recorded, thus resulting in a defined multi-dimensional response.

We finally note that the MC approach used in the experimental data analysis is somewhat similar to the MC methods, widely used in numerical analysis [15,16,40,41]. For example, multi-dimensional integration, performed using the methods of Monte-Carlo often allows one to save computer memory and, eventually, CPU time.

2.3. Simulation of the time-resolved fluorescence and anisotropy

In the following paragraphs we describe the basic principles underlying the simulation of fluorescence- and fluorescence anisotropy decay. Since each photon can be simulated as an object having a time coordinate and a polarization vector, the simulation model can generate simultaneously both the fluorescence- and the anisotropy decays.

The experimental procedure includes the determination of the components of the detected fluorescence, which are differently polarized w.r.t. the polarization direction of the excitation light. Fig.3 schematically represents the basic principles of the detection of the parallel ($I_\parallel$) and perpendicularly ($I_\perp$) polarized fluorescence components, corresponding to the detection using a polarizer oriented at 0° and 90° w.r.t. the polarization direction of the excitation light, denoted as the z-direction. A molecule can absorb an excitation photon with a probability that is proportional to the square of the cosines of the angle between the polarization vector of the excitation photon and one or more absorption transition moments of a molecule. Note that usually for isotropic systems a molecular coordinate system (x',y',z') is randomly oriented in a fixed laboratory coordinate system (x,y,z).
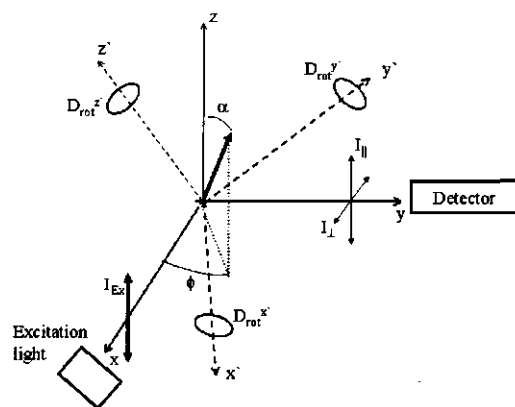
Figure 3. Schematic diagram for the measurement and simulation of parallel and perpendicularly polarized fluorescence components; α: angle between the transition moment for emission and the direction of the parallel detector; ϕ: angle between the projection of the emission transition moment onto the xy plane and the x axis.

This may be incorrect for non-isotropic molecular systems, however, since the molecular coordinate system can be either fixed or non-randomly distributed relative to the laboratory coordinate system. After being excited, a molecule remains in an excited state for a random time interval Δt_τ, defined by the exponential probability density function with a mean value equal to the fluorescence lifetime τ. Subsequently, a molecule can emit a photon in any direction, but we are interested in the x and z directions only, since $I_\parallel$ and $I_\perp$ are detected along these two axes. Detecting the x ($I_\parallel$) and z ($I_\perp$) components of the emitted photons, the total fluorescence and anisotropy can be represented by the following equations

$$I(t) = I_\parallel(t) + 2I_\perp(t)$$

(3)

$$r(t) = \frac{[I_\parallel(t) - I_\perp(t)]}{[I_\parallel(t) + 2I_\perp(t)]}$$

(4)

Fig. 4 shows a flow diagram of the algorithm for simulation of the $I_\parallel(t)$ and $I_\perp(t)$ components of the time-resolved fluorescence. The simulation procedure starts in **block 1** by setting the number N_R of simulation runs (or excitation photons) and generating the initial orientations $\Omega_0{}^a$ and $\Omega_0{}^e$ of the absorption and emission transition dipole moments, characterized by the azimuth and polar angles with respect to the laboratory system.
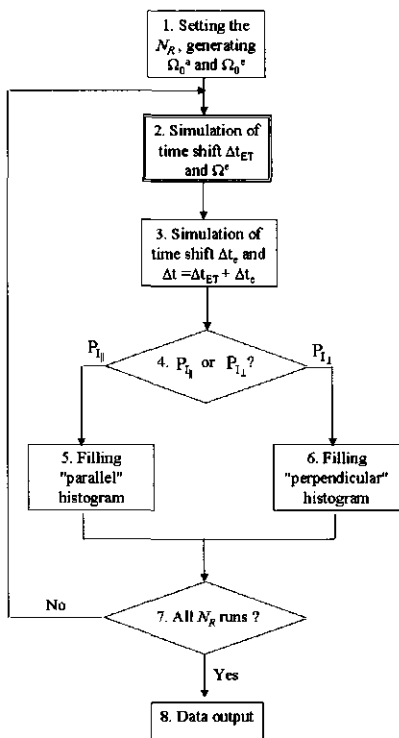
1. Setting the N_R, generating Ω_0^a and Ω_0^e

2. Simulation of time shift Δt_{ET} and Ω^e

3. Simulation of time shift Δt_e and $\Delta t = \Delta t_{ET} + \Delta t_e$

4. $P_{I_\parallel}$ or $P_{I_\perp}$?

$P_{I_\parallel}$

$P_{I_\perp}$

5. Filling "parallel" histogram

6. Filling "perpendicular" histogram

No

7. All N_R runs?

Yes

8. Data output

Figure 4. Flow diagram of the simulation algorithm for the $I_\parallel(t)$ and $I_\perp(t)$ components of the time-resolved fluorescence.

The full travel of a single photon, starting from the excitation of the molecular system and finishing by the photon emission, is considered as one simulation run. Employing an excitation-hopping model for the ET in **block 2** we simulate a time interval Δt_{ET} and the orientation $\Omega^e(\alpha,\phi)$ of the emission transition dipole moment after several transfer hops and diffusional rotations of the molecular system. Particular excitation-hopping models for **systems 1** and **2** will be considered in sections 4.1.2 and 4.2.2, respectively. A time shift Δt_e due to the finite width of the excitation pulse and delays in the detector is simulated in **block 3** using the experimentally measured instrumental impulse response function $E(t)$ representing the convolution of the shape of laser pulse and the detector response. The algorithm of generating a time shift Δt_e can be implemented in several ways [42,43,44].

Since $E(t)$ is an experimentally measured function we use the numerical algorithm based on the Neumann method [45]. To apply this algorithm we first normalize $E(t)$, so that $\int_0^{+\infty} E'(t)dt = 1$ where $E'(t) = E(t)/A$ and A is the normalization factor. After the normalization, the instrumental impulse response function $E'(t)$ represents a probability density function which can be directly used in the Neumann simulation procedure. In order to avoid possible fitting problems, caused by the different numbers of photon counts for the experimental and simulated decays, we apply the same normalization procedure for both experimental and simulated decays. Thus, after several simulation steps, the total time shift $\Delta t = \Delta t_{ET} + \Delta t_e$ is recorded in **blocks 5**

74

or **6** as belonging to either the "parallel component" ($P_{I_\parallel}$) or the "perpendicular component" ($P_{I_\perp}$) histograms, respectively, using the following equations [8]

$$P_{I_\parallel} \sim \cos^2 \alpha$$

(5)

$$P_{I_\perp} \sim \sin^2\phi \, \sin^2\alpha$$

(6)

The angles α and ϕ are determined by the density distribution function $f(\alpha,\phi)$ of the emission transition moment around the x, y, and z coordinate axes, by the molecular geometry as it affects the diffusion coefficients for rotation $D_{rot}{}^{x'}$, $D_{rot}{}^{y'}$, and $D_{rot}{}^{z'}$, by the angle between the absorption- and emission transition moments, and by the energy transfer process itself [46]. Simulation runs (**blocks 2 - 6**) are repeated N_R times (**block 7**). Finally, both histograms are used to calculate the simulated fluorescence- and anisotropy decays using eqns. (3) and (4).

The presented simulation model encompasses the case when the position of the detector in the laboratory system is not included into the eqns. (5) and (6). In principle, the detector can be oriented at any steric angle $\delta^{Det} = (\alpha^{Det}, \phi^{Det})$ with respect to the laboratory coordinate system. Then the probability to detect the emitted photon in the direction δ^{Det} is proportional to the radiation intensity in the δ^{Det} direction and equals $3/2 \sin^2\gamma$ [17], where γ is an angle between the emission dipole moment and the polarization angle of the detector. Then, eqns. (5) and (6) take the form:

$$P_{I_\parallel} \sim 3/2 \sin^2\gamma \cos^2 \alpha = 3/2 \, [1 - (\cos \alpha \cos \alpha^{Det} + \sin \alpha \cos \phi \sin \alpha^{Det} \cos \phi^{Det} + \sin \alpha \sin \phi \sin \alpha^{Det} \sin \phi^{Det})^2] \cos^2 \alpha$$

(7)

$$P_{I_\perp} \sim 3/2 \sin^2\gamma \sin^2\phi \, \sin^2\alpha = 3/2 \, [1 - (\cos \alpha \cos \alpha^{Det} + \sin \alpha \cos \phi \sin \alpha^{Det} \cos \phi^{Det} + \sin \alpha \sin \phi \sin \alpha^{Det} \sin \phi^{Det})^2] \sin^2\phi \, \sin^2\alpha$$

(8)

If the detector is oriented in the y- direction as in Fig. 3, i.e. $\alpha^{Det} = 90°$, $\phi^{Det} = 90°$, then eqns. (7) and (8) become

$$P_{I_\parallel} \sim 3/2 \, (1 - \sin^2 \alpha \sin^2 \phi) \cos^2 \alpha$$

(9)

$$P_{I_\perp} \sim 3/2 \, (1 - \sin^2 \alpha \sin^2 \phi) \sin^2\phi \, \sin^2\alpha$$

In general the shape of the optical spectra can be simulated as well using the above mentioned mathematical algorithms.

3. Experimental

3.1. Chemicals

Zinc tetraphenylporphyrin (ZnTPP), ZnTOPP and ZnM(4-Py)TrPP were prepared by metallization of free base tetraphenylporphyrin (H_2TPP) free base tetra-(octylphenyl)-porphyrin (H_2TOPP) and free base mono(4-pyridyl)-triphenylporphyrin (H_2M(4-Py)TrPP), respectively, by refluxing in DMF with $ZnCl_2$ (Merck, p.a.). CuTOPP was synthesized by the same procedure using $CuCl_2.2H_2O$ (Merck, p.a.). [47]. H_2TPP, H_2TOPP and H_2M(4-Py)TrPP were synthesized by condensation of benzaldehyde, 4-(n-octyl)benzaldehyde and a mixture of benzaldehyde and 4-pyridinecarbaldehyde, respectively, with pyrrole (Janssen Chimica, 99%) in refluxing propionic acid (Merck, z.s.) [48,49]. The porphyrins were purified by chromatography on silica (Merck, silica gel 60) with toluene (ZnTOPP, CuTOPP) or chloroform (ZnTPP, ZnM(4-Py)TrPP) as eluent. All porphyrins are estimated to be >99% pure as shown by thin-layer chromatography and absorption, fluorescence spectroscopy.

Preparation of porphyrin films for the system 1. Thin films of ZnTOPP doped with various concentrations of CuTOPP as well as undoped films on quartz plates (Suprasil, $\varnothing$ 15mm and 1 mm thickness) were prepared by spincoating from $5 \cdot 10^{-5}$ M toluene solutions. As the solutions already contained the appropriate amounts of ZnTOPP and CuTOPP, it may be assumed that in the films the CuTOPP molecules are distributed statistically among the ZnTOPP molecules. Before spincoating the quartz plates were subsequently rinsed with aqua regia, water, methanol and toluene and blown dry with nitrogen. For duplicate samples ZnTOPP purchased from Porphyrin Products were used. Results obtained with purchased or home-synthesized ZnTOPP were identical.

Preparation of solutions for system 2. Solutions of the 10^{-5} M ZnM(4-Py)TrPP in toluene were prepared after drying with sodium wire and storing over molecular sieves.

3.2. Time-correlated photon counting set-up

The experimental set-up for TCSPC has been described in detail elsewhere [30,50,51]. A mode-locked continuous wave Nd:YLF laser (Coherent model Antares 76-YLF, equipped with a LBO

frequency doubler (Coherent model 7900 SHGTC) and BBO frequency tripler (Coherent model 7950 THG) was used to synchronously pump a continuous wave dye laser (Coherent radiation model CR 590). As a dye Coumarin 460 was used for excitation at 465 nm. A set-up with electro-optic modulators in a dual pass configuration was used to reduce the pulse rate to 594 kHz [52]. The final pulse duration of the excitation pulses was ~ 4 ps FWHM and the maximum pulse energy was ~100 pJ. The spincoated samples were fixed on a thermostated, spring-loaded holder at an angle of 15° with respect to the direction of excitation.

Fluorescence light was collected at an angle of 90° with respect to the direction of the exciting light beam. Between the sample and the photomultiplier detector were placed: a set of single fast lenses with a rotatable sheet type polarizer in between, followed by a monochromator and a second set of single fast lenses focusing the output light of the monochromator on the photomultiplier cathode. All lenses were uncoated fused silica, F/3.0. The polarizer sheet was in a dc motor driven ball-bearing holder with mechanical stops, allowing computer controlled rotation (0.2 s). The sheet polarizer was Polaroid type HNP'B. The emission was detected, polarized under magic angle. The detection monochromator was a CVI model Digikröm 112 double monochromator (F/3.9) with the two gratings placed in a subtractive dispersion configuration. Due to the low intensity wide slits ($\Delta\lambda$ = 16 nm) were used. Detection electronics were standard time correlated single photon counting modules. The presented data were collected in a multichannel analyzer (MCA board from Nuclear Data model AccuspecB, in a PC) with a time window of 8192 channels at 3.125 ps/channel.

By reducing the intensity of the excitation pulses, a maximum photon frequency of 30 kHz ($\approx$5% of 594 kHz) was chosen [53] to prevent pile-up distortion. Also other instrumental sources for distortion of data were minimized [54] to below the noise level of normal photon statistics. Extreme care was taken to prevent artifacts from background luminescence. All substrates were carefully cleaned and checked for background luminescence prior to the measurements. For samples with a low fluorescence yield, the background luminescence of an uncoated substrate was recorded and subtracted from the sample data in analysis. For obtaining a dynamic instrumental response (~50 ps FWHM) for deconvolution purposes, the scatter of a rough-hewn, uncoated quartz substrate of 1 mm thickness was measured at the excitation wavelength.

3.3. Streak camera device

The experimental set-up for the streak camera has been described in [55]. The sample of ZnM(4-Py)TrPP in toluene was excited with 100 fs pulses of 565 nm, selected for the tetramers, at 10°C.

The pulses were generated at a 125 kHz repetition rate using a titanium: sapphire based oscillator (Coherent MIRA), a regenerative amplifier (Coherent REGA) and a double pass optical parametric amplifier (Coherent OPA-9400). The pulse energy was typically 25 nJ. The polarization of the exciting light was alternated between horizontal and vertical. The vertical component of the fluorescence was detected using a Hamamatsu C5680 synchroscan streak camera with a Chromex 250IS spectrograph. The full width at half of the maximum (FWHM) of the overall time response of this system was 3.5 ps and the spectral resolution was 8 nm. One streak image measured 315 nm in the spectral domain (1018 pixels) and 200 ps (1000 pixels) in the time-domain.

4. Analysis of porphyrin systems by MC simulations

4.1. System 1

4.1.1. Film structure

The porphyrin **system 1** consists of domains of ordered porphyrins on a quartz substrate as shown in Fig. 5. Within a particular domain the porphyrins are organized as a collection of stacks with their long axes oriented with respect to the domain axis [30]. There are two types of molecules in this system which are involved in energy transfer: (i) ZnTOPP which may act as an energy donor to (ii) CuTOPP acting as energy acceptor. The energy transport in this system can be studied through the donor fluorescence as CuTOPP acts as a dark energy trap, quenching the ZnTOPP fluorescence. Also the presence of non-intentional traps (non-eliminated impurity molecules) results in quenching of the ZnTOPP fluorescence. The molar fraction N_{CuTOPP} of CuTOPP was 0, 1×10^{-2}, 2×10^{-2}, 3×10^{-2}, and the fraction N_{imp} of non-intentional impurity molecules was constant under the experimental conditions. Under these conditions energy transfer between separated domains and singlet-singlet annihilation are assumed to be negligible.
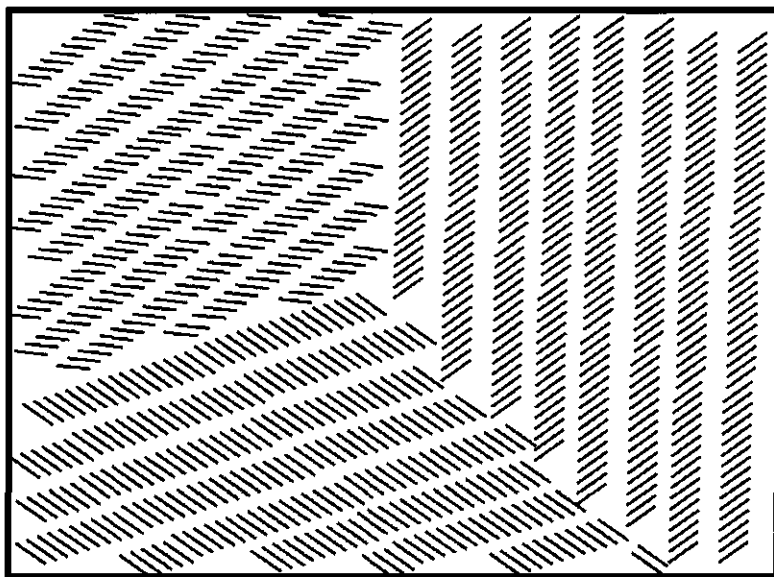
Figure 5. Molecular arrangement of ZnTOPP stacks spincoated from toluene solution on a quartz substrate.

4.1.2 Simulation model

The simulation model for **system 1** is built on the basis of a single domain model of porphyrin stacks approximated by the field of 1000×200 molecular sites in the (x,y) plane, parallel to the substrate surface, which is assumed to be atomically flat (Fig. 6). The parameters k^x_{ET} and k^y_{ET} represent the ET rate constants in the x and y directions, and τ is the fluorescence lifetime of monomeric ZnTOPP in the film. The parameters k^x_{ET}, k^y_{ET}, τ^{-1} are proportional to the probabilities P^x_{ET}, P^y_{ET}, and P_{τ}, where $P^x_{ET} + P^y_{ET} + P_{\tau} = 1$, to be used in the simulation model. We make the following assumptions: i) the probabilities of the "left" and "right" ET are equal in both x and y directions; ii) the probability of ET between non-neighboring molecules in a stack is at least one order smaller than that for transfer between neighboring porphyrin molecules; iii) the probability of the jump in the y direction covers all possible ways of the energy transfers in the y direction. Summarizing, the simulation model is now characterized by five parameters, i.e. k^x_{ET}, k^y_{ET}, N_{CuTOPP}, N_{imp}, and τ.

79

1000 molecules per stack

200 stacks
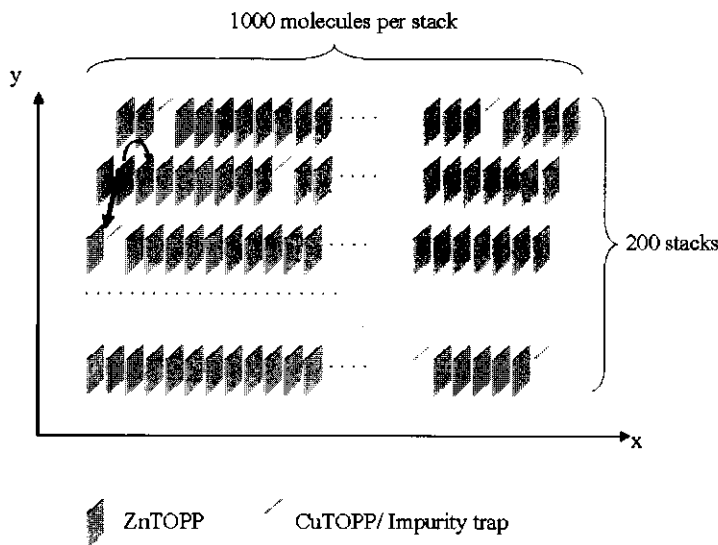
ZnTOPP   CuTOPP/ Impurity trap

Figure 6. Domain arrangement of porphyrins for **system 1**. The arrows indicate the directions of energy transfer.

A flow diagram for a single simulation run for **system 1** is presented in Fig. 7, and can be considered as a subroutine of **block 2** in Fig. 4. The molecular sites in the x and in y directions are counted by $i = 1,...,1000$ and $j = 1,...,200$, respectively. The position (i_0, j_0) of the first excited molecule, the positions (i^l, j^l), $l = 1,...,1000 \cdot N_{CuTOPP}$ of the N_{CuTOPP} dopant molecules and the positions (i^k, j^k), $k=1,..., 1000 \cdot N_{imp}$ of N_{imp} impurity molecules are randomly generated at the start of every simulation run (**block 1**). Subsequently, the fluorescence emission events and ET steps in the x and y directions are simulated in **block 3** using a discrete probability distribution, defined by P^x_{ET}, P^y_{ET}, P_τ, using a random number **R**, uniformly distributed in the interval [0;1]), and generated in **block 2**. The time required for a single of energy transfer step can be considered to be a continuous, random variable, distributed exponentially. Thus, the time Δt of ET from one molecule to another is given by [7]:

$$\Delta t = - (k^q_{ET})^{-1} \ln(\mathbf{R})$$

(11)

where q represents either x or y, depending on the direction of the hop. Random traveling of excitation energy through the system is simulated in **blocks 2 - 11** until it is emitted or trapped by the dopant or impurity molecule in **blocks 12-13** [7]. Upon trapping by an impurity, the

excitation energy walk stops without registering Δt_{ET} in **block 16**, i.e. without emission of the photon.
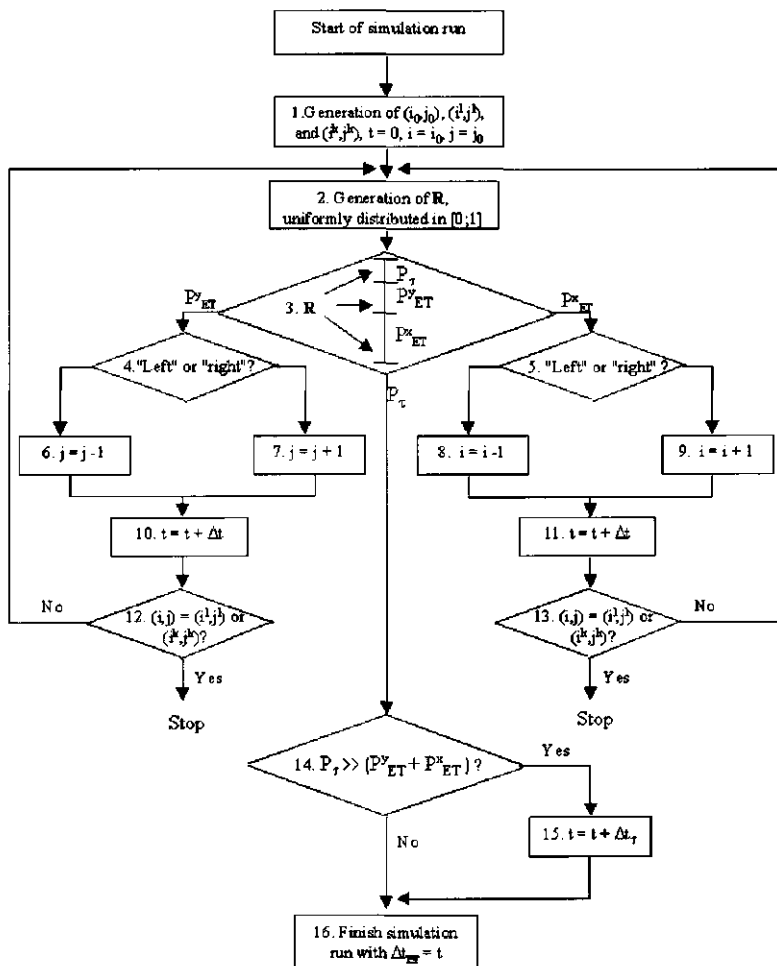

Figure 7. Flow diagram of one simulation run in **system 1**.

4.1.3 Results and discussion of computer simulations

The time-resolved fluorescence decays of ZnTOPP films (**system 1**) were analyzed using parametric fitting via Monte Carlo simulation models as described above. The number of channels in simulated histograms is 2048. For every simulation run a time shift Δt_e was simulated using the algorithm described in section 2.3.

Parametric fitting was applied based on the Nealder and Mead optimization method [56]. The fluorescence responses of films containing 1×10^{-2}, 2×10^{-2}, and 3×10^{-2} molar fractions of

CuTOPP were analyzed globally. Since the fluorescence decays measured for different concentrations of CuTOPP should have the same lifetime and percent of non-intentional impurity, these parameters were global parameters or linked through fluorescence decays of porphyrin **system 1**, measured at different concentrations.

The statistical χ^2 criterion as well as the plots of the weighted residuals and the autocorrelation function were used to judge the quality of fit. The 95% confidence intervals of the simulated decay parameters were calculated using the method of asymptotic standard errors [57]. All computer simulations were performed on the PC IBM Pentium III, 366 MHz.

Table 1. Parameters and their 95% confidence intervals[a] for simulation-based fits of experimental decays of **systems 1** and **2**.

Systems	τ^b (ns)	N_{Imp}^{b} ($\times 10^{-2}$)	N_{CuTOPP} ($\times 10^{-2}$)	k^x_{ET} ($\times 10^{12}$ s^{-1})/ k^N_{ET} ($\times 10^{9}$ s^{-1})	k^y_{ET}/k^A_{ET} ($\times 10^{9}$ s^{-1})
1	1.80 [1.76;1.84]	0.6 [0.5;0.7]	0.0 [0.0;0.0]	1.1 [0.9;1.3]	71 [63;79]
			1.0 [0.9;1.1]	1.0 [0.8;1.2]	83 [71;95]
			2.0 [1.9;2.1]	0.9 [0.8;1.0]	77 [67;87]
			3.0 [2.9;3.1]	0.9 [0.8;1.0]	83 [67;99]
2	1.50 [1.45;1.55]	-	-	38 [33;43]	5 [0;6]

[a] In square brackets
[b] Simultaneous fit of lifetime and impurity levels using global analysis

To build up theoretical fluorescence decay we used 10^8 simulation runs. This ensures, at one hand, an acceptable signal to noise ratio for the simulated decay, and on the other hand a reasonably short simulation time. All experimental fluorescence decays could be satisfactorily fitted by the simulated decays. Fig. 8 shows typical fits of the experimental decay of ZnTOPP using the parameters collected in Table 1.
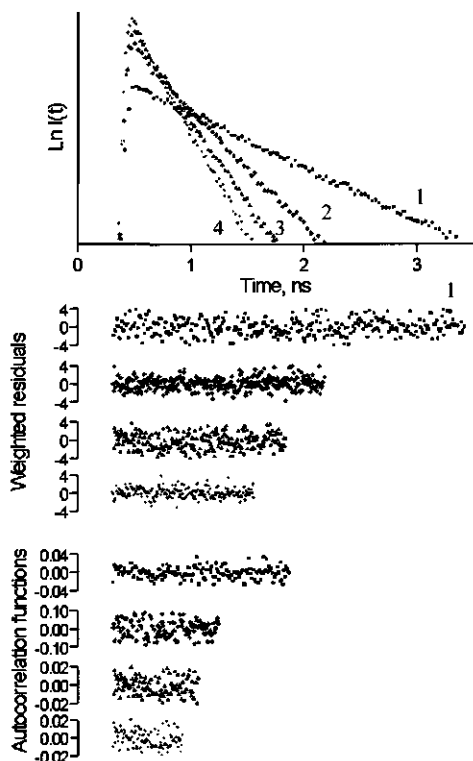
The intra-stack energy transfer rate constant k^x_{ET} is found to be almost one order larger than the inter-stack transfer k^y_{ET}. The molar fraction N_{CuTOPP} of CuTOPP in the film is found to be in the same range as that of the porphyrin solution used for spin coating. From the simulation results we found N_{imp} ~ 0.6×10^{-2} molar fraction of impurity molecules to be present in addition to the dopant. The ZnTOPP fluorescence lifetime τ is close to the value of 1.81 ± 0.03 ns found in toluene solution in the absence of dopant or impurity. Finally, all ET parameters obtained from the MC simulation-based analysis for **system 1** support previously reported results [30].
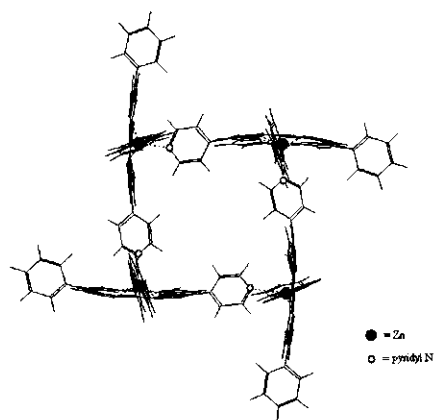
Figure 8. Parametric fit of fluorescence decays of ZnTOPP with 0 ((1):■, χ^2=1.18), 1×10^{-2} ((2):+, χ^2=1.10), 2×10^{-2} ((3):▲, χ^2=1.11), and 3×10^{-2} ((3):●, χ^2=1.08) molar fractions of doped CuTOPP. Experimental data are represented by solid lines. λ_{exc} = 465 nm; λ_{det} = 580 nm.

4.2. System 2

4.2.1. Structure

The porphyrin tetramer of **system 2** results from self-organization of Zn(4-Py)TrPP in toluene at 10°C [33] as shown in Fig. 9.

The porphyrin tetramer of **system 2** results from self-organization of Zn(4-Py)TrPP in toluene at 10°C [33] as shown in Fig. 9. Since energy transfer between the identical porphyrin units in the tetramer does not affect the fluorescence lifetime the only way to obtain information on ET within the tetramer is to analyze the time dependence of the fluorescence anisotropy, following a polarized excitation pulse.

Figure 9. The tetrameric structure of [ZnM(4-Py)TrPP]$_4$.

4.2.2 Simulation model

The simulation model of **system 2** assumes the [ZnM(4-Py)TrPP]$_4$ aggregate to consist of four mutually ligated porphyrns bound in such way that each molecule is perpendicular to the plane of a neighboring one. A schematic diagram of ET pathways in the tetramer is shown in Fig. 10.

The positions and relative orientations of the eight porphyrin transition dipole coordinate system of a monomer within the tetramer completely characterize the spectroscopic properties of the tetramer.

Figure 10. Schematic diagram of the energy transfer pathways in the [ZnM(4-Py)TrPP]$_4$ tetramer. For meaning of symbols, see text.

At the start of simulation run the coordinate system of the tetramer is randomly generated in the laboratory coordinate system. If the molecules in the tetramer are numbered as 1,2,3,4 then all possible molecular pairs involved in ET are labeled ij, where $i = 1,2,3,4$ and $j = 1,2,3,4$, $i \neq j$. The parameters k^{ij}_{ET} represent the rate constants for energy transfer between the i- and j- th molecules in the tetramer; and τ is the ZnM(4-Py)TrPP fluorescence lifetime. If we assume that $k^{ij}_{ET} = k^{ji}_{ET}$ then all possible ET steps in the tetramer can be reduced to two parameters: k^{N}_{ET}

84

for ET between nearest neighbors and k^A_{ET} for ET between next nearest neighbors, i.e. between a pair of molecules across the tetramer The parameters k^N_{ET}, k^A_{ET}, τ^{-1} are proportional to the probabilities P^A_{ET}, P^N_{ET}, P_τ (where $P^A_{ET} + P^N_{ET} + P_\tau = 1$), to be used in the simulation model.
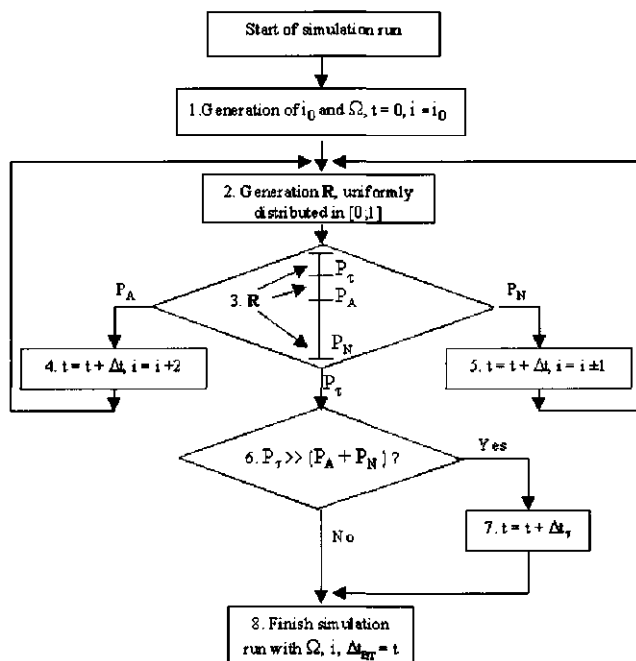

Figure 11. Flow diagram of one simulation run in **system 2**.

A flow diagram of the simulation model of ET in **system 2** is presented in Fig. 11. This diagram represents in fact a subroutine of **block 2** in Fig. 4. An ET walk starts (**block 1**) by generating the number i_0 of the initially excited molecules and their orientation $\Omega = (\alpha, \phi, \xi)$ with respect to the laboratory coordinate system. Note that for a given tetramer structure Ω also defines the orientation of the tetramer.

The emission transition dipoles of metallo-porphyrins are degenerate and mutually perpendicular, since the porphyrin macrocycle has D_{4h} symmetry. The orientation of the porphyrin monomer is then defined by three angles. For example, if α and ϕ are the spherical coordinates of either one of the degenerate emission moments with respect to the laboratory coordinate system, then ξ is a third angle defining the orientation of the molecular coordinate system with respect to that of the laboratory.

Following **block 2** the events of fluorescence emission or E.ET are simulated in **block 3** using a random number **R**, uniformly distributed in the interval [0;1], as generated in **block 2** and the probabilities P^A_{ET}, P^N_{ET}, P_τ. Again, the actual excitation event is considered to be instantaneous. The time Δt at which the excitation is localized on the i-th molecules is given by [7]:

$$\Delta t = - (k^q_{ET})^{-1} \ln(R)$$

(12)

where $q = N$ or A. Simulation of ET is repeated in **blocks 2 - 5** until the event of the fluorescence emission is generated. After each simulation run the total time Δt_{ET} after multiple hops is recorded as histograms of the "parallel component" ($P_{I_\parallel}$) or the "perpendicular component" ($P_{I_\perp}$), where "parallel" and "perpendicular" refer to the orientation of the last molecule participating in the ET chain. Then, for the initially excited and next nearest porphyrin within the tetramer, eqns. (9),(10) can be rewritten as

$$P_{I_\parallel} \sim 3/4 \ (1 - \sin^2 \alpha \sin^2 \phi) \ (\cos \phi \cos \alpha \cos \xi - \sin \phi \sin \xi + \cos \phi \sin \alpha)^2$$

(13)

$$P_{I_\perp} \sim 3/4 \ (1 - \sin^2 \alpha \sin^2 \phi) \ (- \sin \alpha \cos \xi + \cos \alpha)^2$$

(14)

and for the nearest neighbors to the left and right of the initially excited porphyrin unit, eqns. (9),(10) are

$$P_{I_\parallel} \sim 3/8 \ (1 - \sin^2 \alpha \sin^2 \phi) \ (\sqrt{3} \cos \phi \cos \alpha \cos \xi - \sqrt{3} \sin \phi \sin \xi + \cos \phi \sin \alpha)^2$$

(15)

$$P_{I_\perp} \sim 3/8 \ (1 - \sin^2 \alpha \sin^2 \phi) \ (-\sqrt{3} \sin \alpha \cos \xi + \cos \alpha)^2$$

(16)

4.2.3 Results and discussion of computer simulations

The monomer porphyrins were excluded from the simulation, as their fraction is negligibly small under the conditions of the experiment (10°C, $\lambda_{exc} = 565$ nm and $\lambda_{det} = 616$ nm). Energy transfer between the tetramers and singlet-singlet annihilation are not included in the simulations considering the low concentration (10^{-5} M) and excitation rate, respectively.
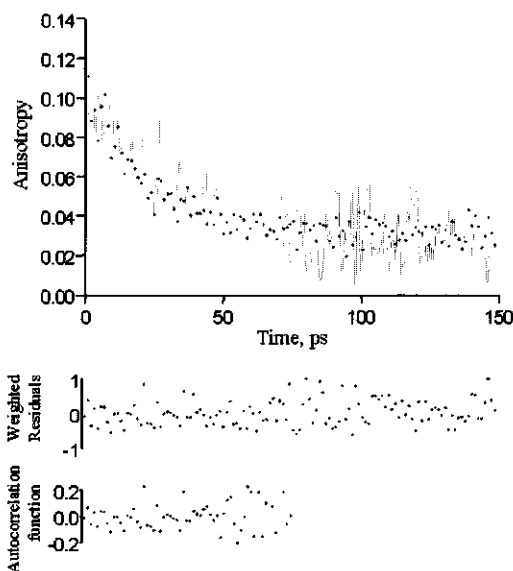
Figure 12. Example of simulation-based fit ($\bullet$, $\chi^2=1.01$) of the experimental [ZnM(4-Py)TrPP]$_4$ fluorescence anisotropy decay (—). $\lambda_{exc} = 565$ nm; $\lambda_{det} = 616$ nm.

Since the analysis uses a 160 ps time window and $(k^N_{ET})^{-1}$ and $(k^A_{ET})^{-1} \ll \phi_{tetr} \sim$ 1 ns [33] rotational diffusion of the tetramers is not taken into consideration. The experimental fluorescence anisotropy decay of the porphyrin tetramers was analyzed using parametric fitting by the MC simulation model for **system 2**, described above.

Using 999 channels with 0.2 ps per channel for the simulated histograms, the fluorescence anisotropy decay could be fitted well by the simulated decay using 10^7 simulation runs. Fig. 12 shows typical fits of the experimental anisotropy decay with the following parameters: $k^N_{ET} = 38 \times 10^9$ s^{-1}, $k^A_{ET} = 5 \times 10^9$ s^{-1}, and $\tau = 1.50$ ns (Table 1).

As expected, ET between neighboring porphyrins is much faster than across the tetramer, which explains the fast depolarization in the initial part of the anisotropy decay. The E.ET parameters obtained by the MC simulations agree with the values of $(31 \pm 2) \times 10^9$ s^{-1} and $(5.3 \pm 0.3) \times 10^9$ s^{-1} calculated from Förster theory using the point dipole-dipole model. The calculated value of 31×10^9 s^{-1} is close to that of the short component of $\sim 38 \times 10^9$ s^{-1} found by the MC simulations whereas the calculated value of 5.3×10^9 s^{-1} equals the longer one from the simulation. Note, however, that the lower boundary of the 95% confidence interval of k^A_{ET} is undefined between the upper boundary and zero in the detection window of 160 ps.

We have also checked the influence of monomer deformation in the tetramer on the ET rate constants by optimizing the angle between the degenerated absorption- and emission monomer transition dipole moments. Introducing the angle η as half of the angle between degenerate moments, eqns. (15) and (16) become

$$P_{I_\parallel} \sim 3/2 \, (1 - \sin^2 \alpha \sin^2 \phi) \, (\cos \phi \cos \alpha \cos \xi \sin \eta - \sin \phi \sin \xi \sin \eta + \cos \phi \sin \alpha \cos \eta)^2$$

(17)

$$P_{I_\perp} \sim 3/2 \, (1 - \sin^2 \alpha \sin^2 \phi) \, (-\sin \alpha \cos \xi \sin \eta + \cos \alpha \cos \eta)^2$$

(18)

Deformation of the monomers bound into the tetramer may influence the rate constants for both abovementioned ET processes by changing the relative contribution to these rate constants by the dipole-dipole and exchange mechanism. The best fit has been found when the porphyrins are completely flat in the tetramer, i.e. the angle between the degenerate moments is 90°. A ± 1° deviation of this angle leaves other parameters in the 95% confidence intervals of. The distortions of the tetramer, resulting from rotation of the monomers, are omitted since the steady state optical spectra of the tetramers indicate that the bound monomers are mutually perpendicular [33].

5. Conclusions

- A novel type of analysis of time-resolved fluorescence data by means Monte Carlo simulations, i.e. direct fitting the measured fluorescence and anisotropy decays, has been developed and demonstrated for two differently organized porphyrin systems;

- Two energy transfer constants, i.e. $\sim 1 \times 10^{12}$ s^{-1} and $\sim 80 \times 10^9$ s^{-1} assigned to intra- and inter-stack transfer, respectively, and a $\sim 0.6 \times 10^{-2}$ molar fraction of non-intentional impurity were found in thin, undoped films of zinc tetra-(octylphenyl)-porphyrin;

- Using the Monte Carlo method, the ET rate constants were calculated for porphyrin tetramers to be 38×10^9 s^{-1} and 5×10^9 s^{-1}. These values agree with Förster type of E.T, yielding 31×10^9 s^{-1} and 5.3×10^9 s^{-1} for transfer to nearest and next nearest neighbors and support the model of the symmetrical tetramer in which the porphyrins are not distorted from the D_{4h} symmetry and are perpendicularly oriented by intermolecular ligation, excluding exchange interactions.

References

[1] Michel-Beyerle, M. E., Ed. *Antennas and Reaction Centers in Photosynthetic Bacteria*; Springer-Verlag: Berlin, 1985.

[2] Breton, J.; Vermeglio, H. *The Photosynthetic Bacterial Reaction Center: Structure and Dynamics*; Plenum Press: New York, 1988.

[3] Quillec, M., Ed. *Materials for Optoelectronics*; Kluwer Academic Publishers: Boston, 1996.

[4] Donati, S. *Photodetectors, Devices, Circuits and Applications*; Prentice Hall: New Jersey, 2000.

[5] Chopra, K. L.; Das, S. R. *Thin Film Solar Cells*; Plenum Press: New York, 1983.

[6] Agranovich, V. M.; Galanin, M. D. *Electronic Excitation Energy Transfer in Condensed Matter*; North-Holland: New York, 1982.

[7] Andrews, L.; Demidov, A., Eds. *Resonance Energy Transfer*; John Wiley & Sons Ltd Inc: New York, 1999.

[8] Lakowicz, J. R. *Principles of Fluorescence Spectroscopy*, 4th ed.; Kluwer Academic/Plenum Publishers: New York, 1999.

[9] Giggino, K. P.; Smith, T. A. *Prog. Reaction Kinetics.* **1993**, *18*, 375.

[10] Markovitsi, D.; Germain, A.; Millié, P.; Lécuyer, P.; Gallos, L. K.; Argyrakis, P.; Bengs, H.; Ringsdorf, H. *J.Phys.Chem.* **1995**, *99*, 1005.

[11] Bacchiocchi, C.; Zannoni, C. *Chem.Phys.Lett.* **1997**, *268*, 541.

[12] Berberan-Santos, M. N.; Choppinet, P.; Fedorov, A.; Jullien, L.; Valeur, B. *J.Am.Chem.Soc.* **1999**, *121*, 2526.

[13] Sato, N.; Ito, S.; Sugiura, K.; Yamamoto, M. *J. Phys. Chem. A* **1999**, *103*, 3402.

[14] Loura, L. M. S.; Prieto, M. *J.Chem.Phys. B* **2000**, *104*, 6911.

[15] Rubinstein, R.; Shapiro, A. *Modern Simulation and Modeling*; John Wiley & Sons Ltd Inc: New York, 1998.

[16] Binder, K.; Heerman, D. V. *Monte Carlo Simulation in Statistical Physics*; Springer-Verlag: Berlin, 1992.

[17] Harvey, S. C.; Cheung, H. C. *Proc. Nat. Acad. Sci. USA* **1972**, *69*, 3670.

[18] Berberan-Santos, M. N.; Valeur, B. *J. Chem. Phys.* **1991**, *95*, 8049.

[19] Johansson, L. B. Å.; Engström, S.; Lindberg, M. *J.Phys.Chem.* **1992**, *96*, 3845.

[20] Hussey, D. M.; Matzinger, S.; Fayer, M. D. *J.Chem.Phys.* **1998**, *109*, 8708.

[21] Förster, T. *Ann. Physik.* **1948**, *2*, 55.

[22] Dexter, D. L. *J. Chem. Phys.* **1953**, *21*, 836.

[23] Apanasovich, V. V.; Novikov, E. G.; Yatskov, N. N. *Proc. SPIE* **1997**, *2980*, 495.

[24] Apanasovich, V. V.; Novikov, E. G.; Yatskou, M. M. *J. Appl. Spec.*, in press.

[25] Kerp, H. R.; Donker, H.; Koehorst, R. B. M.; Schaafsma, T. J.; van Faassen, E. E. *Chem. Phys. Lett.* **1998**, *298*, 302.

[26] Lawrence, D.; Jiang, I.; Levett, M. *Chem. Rev.* **1995**, *95*, 2229.

[27] Prodi, A.; Indelli, M. T.; Kleverlaan, C. J.; Scandola, F.; Alessio, E.; Gianferrara, T.; Marzilli, L. G. *Chem. Eur. J.* **1999**, *5*, 2668.

[28] Li, F.; Gentemann, S.; Kalsbeck, W. A.; Seth, J.; Lindsey, J. S.; Holten, D.; Bocian, D. F. *J. Mater. Chem.* **1997**, *7*, 1245.

[29] Cho, H. S.; Song, N. W.; Kim, Y. H.; Jeoung, S. C.; Hahn, S.; Kim, D.; Kim, S. K.; Yoshida, N.; Osuka, A. *J.Phys.Chem. A* **2000**, *104*, 3287.

[30] Donker, H.; Koehorst, R. B. M.; van Hoek, A.; van Schaik, W.; Schaafsma, T. J. *J.Phys.Chem.*, submitted.

[31] Dlott, D. D.; Fayer, M. D.; Wieting, R. D. *J.Chem.Phys.* **1977**, *67*, 3808.

[32] Wieting, R. D.; Fayer, M. D.; Dlott, D. D. *J.Chem.Phys.* **1978**, *69*, 1996.

[33] Yatskou, M. M.; Donker, H.; Koehorst, R. B. M.; van Hoek, A.; Schaafsma, T. J. to be submitted.

[34] Engström, S.; Lindberg, M.; Johansson, L. B. Å. *J.Phys.Chem.* **1988**, *89*, 204.

[35] Baumann, J.; Fayer, M. D. *J.Chem.Phys.* **1986**, *85*, 4087.

[36] Enrenberg, A. S. C. *Data Reduction*; John Wiley & Sons Ltd Inc: New York, 1975.

[37] Korn, G. A.; Korn, T. M. *Mathematical Handbook for Scientists and Engineers*; McGraw- Hill Book Company: New York, 1961.

[38] O'Connor, D. V.; Phillips, D. *Time-Correlated Single Photon Counting*; Academic Press: London, 1984.

[39] Demas, J. N. *Excited State Lifetime Measurements*; Academic Press: New York, 1983.

[40] Barlow, R. *J. Comp. Phys.* **1987**, *72*, 202.

[41] Barlow, R.; Beeston, C. *Comp. Phys. Comm.* **1993**, *77*, 219.

[42] Ameloot, M.; Hendrix, H. *J. Chem. Phys.* **1982**, *76*, 4419.

[43] Chowdhury, F. N.; Kolber, Z. S.; Barkley, M. D. *Rev.Sci.Instrum.* **1991**, *62*, 47.

[44] Beechem, J.; Ameloot, M.; Brand L. *Chem.Phys.Lett.* **1985**, *120*, 446.

[45] Bratley, P.; Fox, B. L.; Schrage, L. E. *A Guide to Simulation*; Springer: New York, 1983.

[46] Lakowicz, J. R., Ed. *Topics in Fluorescence Spectroscopy*, Vol.2; Plenum Press: New York, 1991.

[47] Adler, A. D.; Longo, F. R.; Kampas, F.; Kim, J. *J. Inorg. Nucl. Chem.* **1970**, *32*, 2443.

[48] Adler, A. D.; Longo, F. R.; Shergalis, W. J. *Am. Chem. Soc.* **1964**, *86*, 3145.

[49] Little, R. G.; Anton, J. A.; Loach, P. A.; Ibers, J. A. *J. Heterocycl. Chem.* **1975**, *12* 343.

[50] Visser, A. J. W. G; van den Berg, P. A. W.; Visser, N. V.; van Hoek, A.; van den Burg, H. A.; Parsonage, D.; Claiborne, A. *J. Phys. Chem. B* **1998**, *102*, 10431.

[51] van den Berg, P. A. W.; van Hoek, A.; Walentas, C. D.; Perham, R. N.; Visser, A. J. W. G. *Biophys. J.* **1998**, *74*, 2046.

[52] van Hoek, A.; Visser, A. J. W. G. *Rev. Sci. Instruments* **1981**, *52*, 1199.

[53] Vos, K.; van Hoek, A.; Visser, A. J. W. G. *Eur. J. Biochem.* **1187**, *165*, 55.

[54] van Hoek, A.; Visser, A. J. W. G. *Analytical Instrumentation* **1985**, *14*, 359.

[55] Gobets, B.; van Stokkum, I. H. M.; Rögner, M.; Kruip, J.; Kleima, F. J.; Schlodder, E.; Karapetyan, N. V.; Dekker, J. P.; van Grondelle, R. *Biophys. J.*, submitted.

[56] Nealder, J. A.; Mead, R. *Comput. J.* **1965**, *8*, 308.

[57] Johanson, M. J. *Methods Enzymol.* **1994**, *240*, 1.

4.2. Simulation-based fitting of the time-resolved fluorescence- and anisotropy decays

This Section describes several approaches for MC simulation-based fitting of fluorescence and anisotropy decays detected through TCSPC and streak camera measurements. Attention is focused on the χ^2 criterion and its weighting factors since it has been shown in Chapter 3 that this criterion is one of the best tests for fluorescence decay fitting using MC simulations.

Simulation-based fitting against scatter decay.

Fluorescence. If the fluorescence intensity is measured at the position of the polarization detector at the magic angle (54.7°), then eqn. (1) of Section 4.1. can be straightforwardly used for simulation-based fitting of the experimental data. With the parallel ($F^E_\parallel(t)$) and perpendicularly ($F^E_\perp(t)$) polarized components of the fluorescence decay $F^E(t)$ are measured, the weighting factor for eqn. (1) becomes

$$w(t_i) = \text{var}[F^E_\parallel(t_i)] + 4\,\text{var}[F^E_\perp(t_i)] + \text{var}[F^T_\parallel(t_i,\boldsymbol{a})] + 4\,\text{var}[F^T_\perp(t_i,\boldsymbol{a})]$$

(1a)

where $F^T_\parallel(t,\boldsymbol{a})$ and $F^T_\perp(t,\boldsymbol{a})$ are the parallel and perpendicular components of the simulated fluorescence $F^T(t,\boldsymbol{a})$. Note that eqn. (1) of Section 4.1. contains a so-called G – factor, or geometry factor. which for a properly designed detection system equals 1. In this Section all equations have $G = 1$.

Assuming Poissonian statistics of the TCSPC experimental data, the variances of the experimental and simulated decays can be approximated as

$$\text{var}[F^E_\parallel(t)] = F^E_\parallel(t),$$
$$\text{var}[F^E_\perp(t)] = F^E_\perp(t),$$
$$\text{var}[F^T_\parallel(t,\boldsymbol{a})] = F^T_\parallel(t,\boldsymbol{a}),$$
$$\text{var}[F^T_\perp(t,\boldsymbol{a})] = F^T_\perp(t,\boldsymbol{a}).$$

(1b - d)

Anisotropy. The observed fluorescence anisotropy decay $r^E(t)$ can be fitted in several ways.

The direct approach is to fit the anisotropy

$$r^E(t) = [F^E_\parallel(t) - F^E_\perp(t)]/\,[F^E_\parallel(t) + 2\,F^E_\perp(t)]$$

(2a)

by the simulated one

$$r^T(t,\boldsymbol{a}) = [F^T_{\parallel}(t,\boldsymbol{a}) - F^T_{\perp}(t,\boldsymbol{a})]/[F^T_{\parallel}(t,\boldsymbol{a}) + 2F^T_{\perp}(t,\boldsymbol{a})].$$

(2b)

Then the χ^2 criterion that should be minimized takes the form

$$\chi^2(\boldsymbol{a}) = \sum_{i=1}^{n} \frac{[r^E(t_i) - r^T(t_i,\boldsymbol{a})]^2}{w(t_i)}$$

(2c)

Using the principles of error propagation, the weighting factor $w(t_i)$ for the χ^2 criterion is given by

$$w(t_i) = [r^E(t_i)]^2 \left(\frac{\mathrm{var}[F^E_{\parallel}(t_i)] + 4\,\mathrm{var}[F^E_{\perp}(t_i)]}{[F^E_{\parallel}(t_i) + 2F^E_{\perp}(t_i)]^2} + \frac{\mathrm{var}[F^E_{\parallel}(t_i)] + \mathrm{var}[F^E_{\perp}(t_i)]}{[F^E_{\parallel}(t_i) - F^E_{\perp}(t_i)]^2} + \right.$$

$$\left. \frac{\mathrm{var}[F^E_{\parallel}(t_i)] + 2\,\mathrm{var}[F^E_{\perp}(t_i)]}{[F^E_{\parallel}(t_i) + 2F^E_{\perp}(t_i)][F^E_{\parallel}(t_i) - F^E_{\perp}(t_i)]} \right) +$$

$$[r^T(t_i,\boldsymbol{a})]^2 \left(\frac{\mathrm{var}[F^T_{\parallel}(t_i,\boldsymbol{a})] + 4\,\mathrm{var}[F^T_{\perp}(t_i,\boldsymbol{a})]}{[F^T_{\parallel}(t_i,a) + 2F^T_{\perp}(t_i,\boldsymbol{a})]^2} + \frac{\mathrm{var}[F^T_{\parallel}(t_i,\boldsymbol{a})] + \mathrm{var}[F^T_{\perp}(t_i,\boldsymbol{a})]}{[F^T_{\parallel}(t_i,\boldsymbol{a}) - F^T_{\perp}(t_i,\boldsymbol{a})]^2} + \right.$$

$$\left. \frac{\mathrm{var}[F^T_{\parallel}(t_i,\boldsymbol{a})] + 2\,\mathrm{var}[F^T_{\perp}(t_i,\boldsymbol{a})]}{[F^T_{\parallel}(t_i,\boldsymbol{a}) + 2F^T_{\perp}(t_i,\boldsymbol{a})][F^T_{\parallel}(t_i,\boldsymbol{a}) - F^T_{\perp}(t_i,\boldsymbol{a})]} \right)$$

(2d)

The second method is that of parametric estimation of $r^E(t)$, since it actually fits the parallel $F^E_{\parallel}(t)$ and perpendicular $F^E_{\perp}(t)$ fluorescence components. Then, using eqn. (1) of Section 4.1., the minimizing χ^2 equation can be written as

$$\chi^2(\boldsymbol{a}) = \frac{1}{2} \left(\sum_{i=1}^{n} \frac{[F^E_{\parallel}(t_i) - F^T_{\parallel}(t_i,\boldsymbol{a})]^2}{w_{\parallel}(t_i)} + \sum_{i=1}^{n} \frac{[F^E_{\perp}(t_i) - F^T_{\perp}(t_i,\boldsymbol{a})]^2}{w_{\perp}(t_i)} \right)$$

(3a)

with

$$w_{\parallel}(t_i) = \mathrm{var}[F^E_{\parallel}(t_i)] + \mathrm{var}[F^T_{\parallel}(t_i,\boldsymbol{a})]$$

(3b)

$$w_{\perp}(t_i) = \mathrm{var}[F^E_{\perp}(t_i)] + \mathrm{var}[F^T_{\perp}(t_i,\boldsymbol{a})]$$

(3c)

Simulation-based fitting using the decay of a reference compound.

Fluorescence. In general, the simulation fitting can hardly be applied to the analysis of fluorescence decay data using the previously proposed [1] reference compound method.

According to this method the observed fluorescence $F^E(t)$ is approximated by a function $F^T(t,a)$ calculated with following equation

$$F^T(t,a) = F_r(t) \cdot i(0,a) + F_r(t) \otimes [i(t,a) \cdot \tau_{ref}^{-1} + \frac{d}{dt} i(t,a)]$$

(4)

where $F_r(t)$ and τ_{ref} are the observed fluorescence decay and the *a priory* known lifetime of the reference fluorophore, and $i(t,a) = i_\parallel(t,a) + 2\ i_\perp(t,a)$ is a histogram of the fluorescence impulse response function obtained from a simulation model. Since $i(t)$ is statistically distorted for MC simulation, the derivative $\frac{d}{dt} i(t,a)$ in eqn. (4) cannot be accurately calculated, and this normally results in significant numerical distortions in the function approximating the fluorescence.

Chowdhury at al. [2] proposed an algorithm which can be used in a reference deconvolution method with MC convolution. This approach can also be applied for MC simulation fitting. The idea of the algorithm consists of an additional convolution of the sample decay with a reference compound decay, i.e. convoluting both sides of eqn. (23) of Chapter 1 with the known impulse function of the reference fluorophore $i_r(t)$, yielding

$$i_r(t) \otimes F^E(t) = i_r(t) \otimes e(t) \otimes i(t,a)$$

(5)

Denoting

$$F_r(t) = e(t) \otimes i_r(t)$$

(6)

eqn. (5) becomes

$$F^E(t) \otimes i_r(t) = F_r(t) \otimes i(t,a)$$

(7)

and the χ^2 criterion for the fluorescence decay fitting transforms to the form

$$\chi^2(a) = \sum_{i=1}^{n} \cdot \frac{[F^E(t_i) \otimes i_r(t_i) - F_r(t_i) \otimes i(t_i, a)]^2}{w(t_i)}$$

(8a)

with the weighting factor $w(t_i)$ given by

$$w(t_i) = var[F^E(t_i)] \otimes [i_r(t_i)]^2 + var[F_r(t_i)] \otimes [i(t_i, a)]^2 + [F_r(t_i)]^2 \otimes var[i(t_i, a)]$$

(8b)

Anisotropy. The fluorescence anisotropy parameters can be obtained in the same way as the parameters obtained from the fluorescence decay and using parameter fitting for $r^E(t)$ as in eqn (3a). Rewriting eqn. (7) for the polarized fluorescence components $F^E_{\parallel}(t)$ and $F^E_{\perp}(t)$ and substituting them into eqn. (3a), χ^2 can be written as

$$\chi^2(a) = \frac{1}{2}\left(\sum_{i=1}^{n} \frac{[F^E_{\parallel}(t_i) \otimes i_{r\parallel}(t_i) - F_{r\parallel}(t_i) \otimes i_{\parallel}(t_i, a)]^2}{w_{\parallel}(t_i)} + \sum_{i=1}^{n} \frac{[F^E_{\perp}(t_i) \otimes i_{r\perp}(t_i) - F_{r\perp}(t_i) \otimes i_{\perp}(t_i, a)]^2}{w_{\perp}(t_i)} \right)$$

(9a)

with

$$i_{r\parallel}(t) = (1/3)\, i_r(t)[1 + 2r_r(t)]$$

(9b)

$$i_{r\perp}(t) = (1/3)\, i_r(t)[1 - r_r(t)]$$

(9b)

where $r_r(t)$ is the known fluorescence anisotropy of the reference fluorophore. The weighting factors $w_{\parallel}(t_i)$ and $w_{\perp}(t_i)$ for the eqn. (9a) are

$$w_{\parallel}(t_i) = var[F^T_{\parallel}(t_i)] \otimes [i_{r\parallel}(t_i)]^2 + var[F_{r\parallel}(t_i)] \otimes [i_{\parallel}(t_i, a)]^2 + [F_{r\parallel}(t_i)]^2 \otimes var[i_{\parallel}(t_i, a)]$$

(9c)

$$w_{\perp}(t_i) = var[F^T_{\perp}(t_i)] \otimes [i_{r\perp}(t_i)]^2 + var[F_{r\perp}(t_i)] \otimes [i_{\perp}(t_i, a)]^2 + [F_{r\perp}(t_i)]^2 \otimes var[i_{\perp}(t_i, a)]$$

(9d)

Simulation-based fitting using multi-exponential deconvolution.

Fluorescence. In this approach the observed fluorescence $F^E(t)$ is approximated by a multi-exponential function $\widetilde{i}(t,\widetilde{a})$, with $\widetilde{a} = \{p_{1,...}, p_{n1}; \tau_1,..., \tau_{n1}\}$ and n1 the number of fluorescence exponentials using multi-exponential fitting [3]. Then the deconvolution of the measured decay $F^E(t)$ consists of the calculation of the parameters $\widetilde{a}$ of that multi-exponential response. Once the approximated decay function $\widetilde{i}(t,\widetilde{a})$ is known it can be fitted by a MC simulated decay $i(t,a)$, yielding the real physical parameters of the system. In this case the χ^2 equation takes the form

$$\chi^2(a) = \sum_{i=1}^{n} \frac{\left[\widetilde{i}(t_i,\widetilde{a}) - i(t_i,a)\right]^2}{w(t_i)}$$

(10a)

with

$$w(t_i) = \text{var}[i(t_i,a)]$$

(10b)

and

$$\text{var}[i(t,a)] = i_\parallel(t,a) + 4F^T_\perp(t,a).$$

(10c)

Anisotropy. The same approach can be applied to multi-exponential anisotropy decay $\widetilde{r}(t_i,\widetilde{a})$, with $\widetilde{a} = \{\beta_{1,...}, \beta_{n2}; \varphi_1,..., \varphi_{n2}\}$, and n2 the number of anisotropy exponentials resulting from the best fit of the experimental anisotropy decay $r^E(t)$. Then the multi-exponential anisotropy decay $\widetilde{r}(t_i,\widetilde{a})$ is fitted by the simulated anisotropy decay $r^T(t,a) = [i_\parallel(t,a) - i_\perp(t,a)]/ [i_\parallel(t,a) + 2i_\perp(t,a)]$ using eqns. (2) or (3a). The weighting factor for eqn. is

$$w(t_i) = [r^T(t_i,a)]^2 \left(\frac{\text{var}[i_\parallel(t_i,a)] + 4\text{var}[i_\perp(t_i,a)]}{[i_\parallel(t_i,a) + 2i_\perp(t_i,a)]^2} + \frac{\text{var}[i_\parallel(t_i,a)] + \text{var}[i_\perp(t_i,a)]}{[i_\parallel(t_i,a) - i_\perp(t_i,a)]^2} + \frac{\text{var}[i_\parallel(t_i,a)] + 2\text{var}[i_\perp(t_i,a)]}{[i_\parallel(t_i,a) + 2i_\perp(t_i,a)][i_\parallel(t_i,a) - i_\perp(t_i,a)]} \right)$$

(11a)

The weighting factors for eqn. (3a) are

$$w_{\parallel}(t_i) = var[i_{\parallel}(t_i, \boldsymbol{a})]$$

(11b)

$$w_{\perp}(t_i) = var[i_{\perp}(t_i, \boldsymbol{a})]$$

(11c)

4.3. Testing the computer simulation approach for fitting of the processes of energy relaxation and -transport using TCSPC data

Tests of the computer simulation approach for fitting of the energy relaxation- and transport processes for different molecular systems are presented in Section 4.1. In this Section several examples of test results of the techniques mentioned in Section 4.2. are presented as applied to the TCSPC and streak camera experimental data.

Testing of simulation-based fitting against scatter decay. The result of fitting of the fluorescence decay of spin coated ZnTOPP films using scatter decays are described in detail in Section 4.1. An example of the fitting of the [Zn(4-Py)TrPP]$_4$ fluorescence anisotropy decay using eqn. (2) is shown in Section 4.1, Fig. 12. The number of simulation runs N_R (or simulation counts) is of critical importance in simulation-based fitting because it determines the signal to noise ratio. Fitted fluorescence decays of spin coated ZnTOPP films for $N_R = 10^5$, 10^6, and 10^7 simulation runs are shown in Fig. 1.

Since it is significant to minimize the computer simulation time and at the same time to reach acceptable statistics of the simulated data, the number N_R of simulation runs should be carefully chosen. The χ^2 value vs. N_R for simulation-based fits of the fluorescence decay of ZnTOPP films and the fluorescence anisotropy decay of [Zn(4-Py)TrPP]$_4$ is presented in Fig. 2.

For $N_R < 10^4$, χ^2 approaches a value < 1 corresponding to poor statistics of the simulated data. For $10^4 < N_R \leq 10^6$ $\chi^2 > 1$, i.e. the signal to noise ratio is still close to the critical margin. For $N_R \approx 10^6 \rightarrow +\infty$ χ^2 approaches 1. As can be seen in Fig. 2, the change of χ^2 with N_R for the data of the ZnTOPP films is more pronounced than for [Zn(4-Py)TrPP]$_4$. This is due to the specifications of the simulation model in both cases, in particular the global set of the parameters.
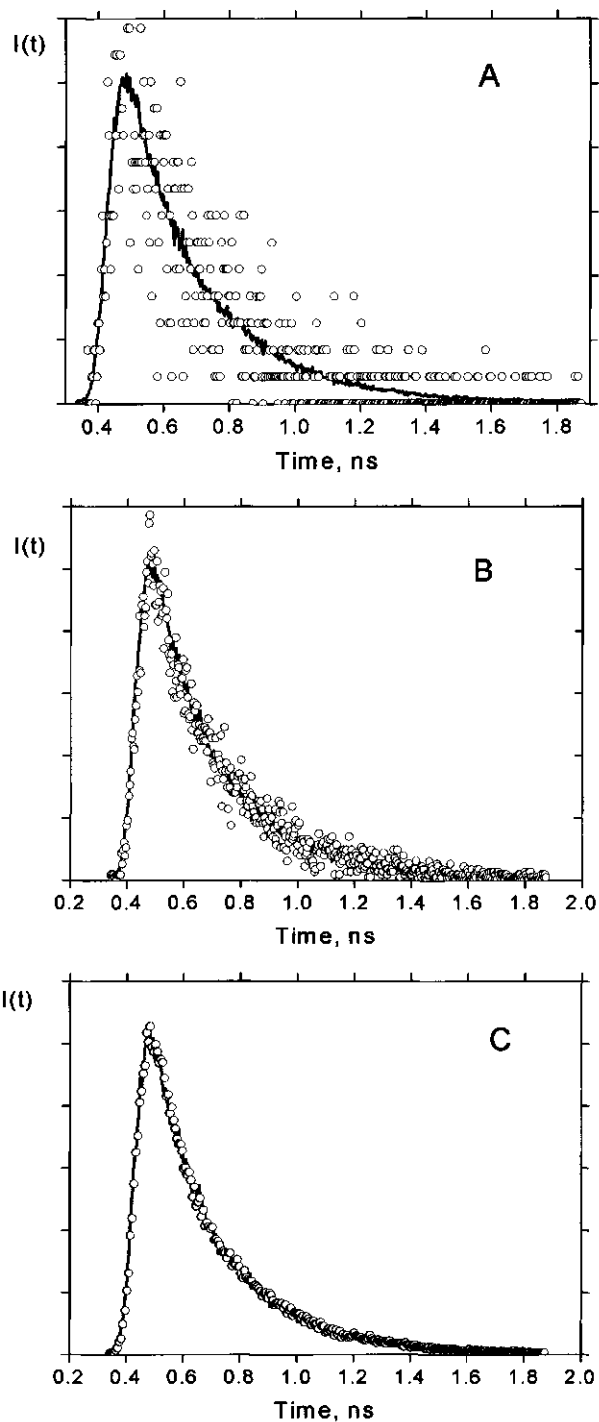
Fig.1. Examples of MC simulation fluorescence decay fits of spin coated ZnTOPP films doped with 1×10^{-2} molar fraction of CuTOPP; $N_R = 10^5$ (A), 10^6 (B), and 10^7 (C); —: experimental data; o: simulated data; $\lambda_{exc} = 465$ nm; $\lambda_{det} = 580$ nm.
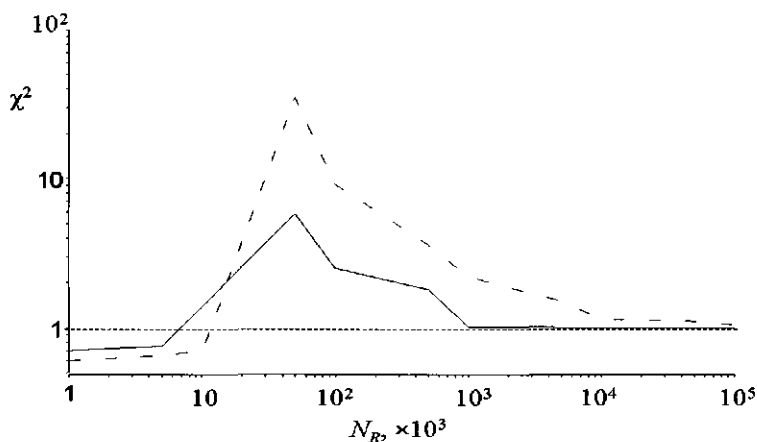
Fig. 2. χ^2 vs. N_R for simulation-based fits. — — — — : fluorescence decay of ZnTOPP films doped with 1×10^{-2} molar fraction of H_2TOPP; ———: fluorescence ansiotropy decay of $[Zn(4\text{-Py})TrPP]_4$ in toluene, 10°C.

Simulation-based fitting using the decay of a reference compound.

The example of the fluorescence decay fit of $[Zn(4\text{-Py})TrPP]_4$ in toluene at 10°C, using eqns. (8a),(8b), is shown in Fig. 3.
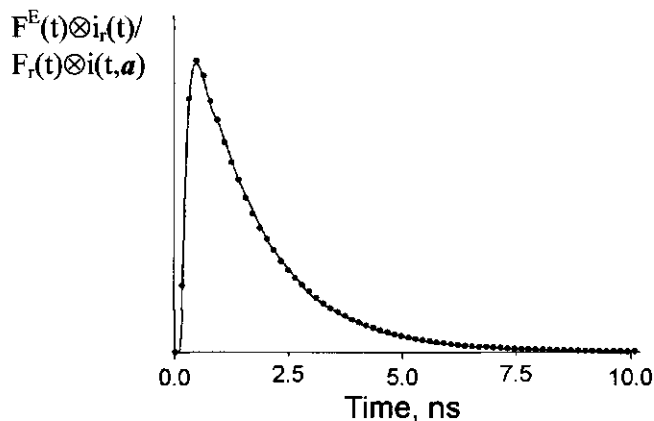

Fig. 3. Fluorescence decay fit of $[Zn(4\text{-Py})TrPP]_4$ in toluene at 10°C; $N_R = 10^6$; ——: $F^E(t)\otimes i_r(t)$; •: $F_r(t)\otimes i(t,a)$. $\lambda_{exc} = 435$ nm; $\lambda_{det} = 625$ nm.

Simulation-based fitting using multi-exponential deconvolution. Fig. 4 shows several typical examples of the fluorescence decay fits for spin coated ZnTOPP films using eqns. (10a) - (10c).
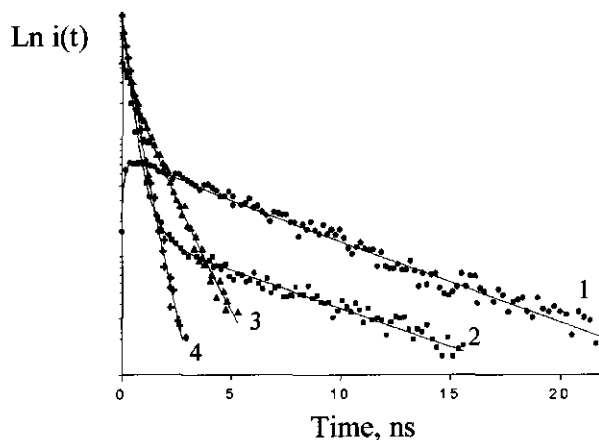
Fig. 4. Examples of parametric fits of the fluorescence decays of ZnTOPP films. ■,(1): doped with 1×10^{-2} molar fraction of H_2TOPP, $\lambda_{det} = 725$ nm; ●,(2): same dopant concentration, $\lambda_{det} = 580$ nm; ▲,(3): undoped ZnTOPP films, $\lambda_{det} = 580$ nm; +,(4): doped with 1×10^{-2} molar fraction of CuTOPP, $\lambda_{det} = 580$ nm. Experimental data are represented by solid lines. For all examples $\lambda_{exc} = 465$ nm.

The advantage of this method is that the deconvolution for the multi-exponential decay function can be done rather accurately and reasonably fast. In addition, further parametric fit of the multi-exponential decay $\tilde{i}(t,\tilde{a})$ does not require convolution at each iteration, which considerably slows down the whole calculation procedure.

4.4. Conclusions

- A successful Monte Carlo simulation model for energy transport and -relaxation has been developed, yielding excellent fits of the fluorescence- and fluorescence anisotropy decays

- Several approaches for the simulation-based fitting of the fluorescence- and fluorescence anisotropy decay have been critically reviewed. A number of illustrative examples demonstrate the effects of the simulation parameters on the quality of the fits for the experimental data of the time-correlated single photon counting and streak camera methods.

References

[1] K. Vos, A. van Hoek, A.J.W.G. Visser, *Biochemistry*, 165 (1987) 55.

[2] F.N. Chowdhury, Z.S. Kolber, M.D. Barkley, *Rev.Sci.Instr.*, 62 (1991) 47.

[3] J.R. Lakowicz (1999) *Principles of Fluorescence Spectroscopy* Kluwer Academic/Plenum Publishers, New York.

Chapter 5

The Analysis of the Photophysics of Self-organized Porphyrin Systems

This Chapter describes the photophysics of organized porphyrin systems. Steady state spectra are explained by simple exciton theory and a non-calorimetric thermodynamic method. Computer simulations of energy transfer processes in self-organized porphyrin tetramer and ordered porphyrin domains on a solid substrate of the quartz films are presented. The results of computer simulations are discussed and compared with the predictions of Förster theory.

5.1. Introduction to the simulation of photophysical processes in organized porphyrin systems

Understanding the photophysics of self-organized porphyrin structures is extremely important since it opens the way to manipulate and construct molecular structures for a variety of practical applications (see Preface). For example, for artificial antennas in organic solar cells, a self-organized porphyrin system should be i) an effective harvesting system for absorbing visible light; ii) an effective ET system, i.e. the ET rate constant should be much larger than those for other energy relaxation processes; and iii) photochemically stable over a prolonged period of time and insensitive to temperature changes. These properties of self-organized porphyrin systems should first be studied in liquid solution, the results being used as a guideline for subsequent solid films studies. Furthermore, in studies of the films the properties of self-organized porphyrin systems can be combined with knowledge of the film structure, its spectroscopic properties, and the nature and strength of the intermolecular interactions. This combination is a promising approach to investigate which self-organized aggregates are most suitable as candidates for artificial antennas, e.g. for organic solar cells.

Self-assembled [ZnM(4-Py)TrPP]$_4$ tetramers and ZnTOPP ordered domains are typical examples of self-organized porphyrin systems for artificial antennas. Both systems have been investigated using steady state and time-resolved fluorescence spectroscopy. In solution the photophysical processes of these self-organized ZnM(4-Py)TrPP and ZnTOPP molecular systems can be investigated in great detail by a number of methods:

- applying simple exciton theory to explain the optical spectra [1],

- using the non-calorimetric thermodynamic method [2] to determine the enthalpy and -entropy changes upon tetramer formation,

- using fluorescence and anisotropy decay parameters to study excited states involved in ET processes and the relevant geometrical distances by application of Förster theory [3]

- MC simulations presented in various parts of this Thesis.

The optical spectra and fluorescence decays of solid dye films obey the same basics as the same dyes in solution but are in addition affected by the environment of the dye molecules and their close packing in the solid layer. Noting that the optical properties of solid films, such as the refractive index or the permittivity coefficient, are not well defined at the molecular level, the optical spectra for self-organized porphyrin systems can only qualitatively be analyzed by comparison with these spectra in solution or systems which are much better understood, e.g. films of monomers. The fluorescence decay of the organized porphyrin films is multi-exponential due to close packing of the porphyrins resulting in energy transfer to energy traps formed by physical defects or non-intentional impurity molecules. For the same reasons as mentioned before for optical spectra the fluorescence and fluorescence anisotropy decay can not be analyzed by the traditional approach of using analytical expressions for ET of the Förster- or exchange type. The ET process(es) giving rise to the optical spectra and the fluorescence- and fluorescence anisotropy decay can be successfully analyzed using Monte Carlo simulations, specifically developed for that purpose.

5.2. Photophysics of porphyrin systems in solution and solid films

5.2.1. Energy levels and the Kasha model

A general theory for excitonic interactions in molecular aggregates has been developed by Kasha [1] and subsequently adapted to explain the optical spectra of different porphyrin structures [4]. The basic assumption of the exciton model theory is that the interaction between an excited molecule and a neighboring ground state molecule can be described as a dipole-dipole interaction. The application of the Kasha model is only justified when the overlap between the electronic wavefunction of the energy donor is small so that interacting molecules preserve their individuality in an aggregate. A typical example of a calculation of wave-functions and energy

levels applying Kasha theory to the [ZnM(4-Py)TrPP]₄ tetramer in toluene is given in Section 5.2.2.

Using the molecular exciton model the energy levels of [ZnM(4-Py)TrPP]₄ tetramer in toluene solution can be calculated by taking into account the interactions between the parallel and perpendicular transition dipole moments (see Section 5.2.2.). For the dimer, cyclic trimer and higher aggregates, as well for linear polymers the pattern of the energy levels is expected to be more complicated than for the cyclic tetramer. For example, two bands should be present in the absorption spectrum of larger cyclic aggregates: one band, centered at the lowest, unshifted position w.r.t. that of the ligated ZnM(4-Py)TrPP monomer, resulting from the interactions between parallel oriented transition dipole moments in the aggregate, and a second one red-shifted w.r.t. the position of the ligated monomer and broadened, as a result of interactions of non-parallel transition dipole moments. For linear polymers only a single, strongly broadened band is predicted, unshifted w.r.t. the position of ligated monomer. The width of this broadened band is determined by the steric structure of the linear polymer.

The application of the Kasha exciton model to explain the absorption spectra of porphyrin aggregates in the films can be criticized for two reasons: i) there is no clear evidence for applicability of Kasha theory since the electron overlap can be significant and therefore the dipole-dipole approximation may not be valid; ii) the properties of the molecular environment of the film at a solid substrate are not well-defined and thus the energy levels and the transition dipole values, for example, can not be calculated with accuracy. By consequence, the optical spectra of the porphyrin aggregates in the films can only be analyzed by qualitative comparison with those in solutions.

References

[1] Kasha, M.; Rawls, H.R.; El-Bayoumi, M. A. *Pure Appl. Chem.* **1965**, *11*, 371.

[2] Atkins, P.W. *Physical Chemistry*; Oxford University Press: Oxford, 1998.

[3] Förster, T. *Ann. Physik.* **1948**, *2*, 55.

[4] Stomphorst, R. G.; Koehorst, R. B. M.; van der Zwan, G.; Benthen, B.; Schaafsma, T. J. *J. Porph. Phtalocyanins* **1999**, *3*, 346.

5.2.2. Spectroscopic Properties of a Self-assembled Zinc Porphyrin Tetramer

I. Steady State Optical Spectroscopy

Mikalai M. Yatskou[#], Rob B.M. Koehorst, Harry Donker, and Tjeerd J. Schaafsma[*]

Laboratory of Biophysics, Department of Agrotechnology and Food Sciences, Wageningen University, Dreijenlaan 3, 6703 HA Wageningen, The Netherlands

Abstract

Aggregation of zinc mono-(4-pyridyl)-triphenylporphyrin (ZnM(4-Py)TrPP) in toluene and polystyrene/toluene mixtures has been investigated by steady state optical spectroscopy. The Q-band absorption spectra as well as the fluorescence spectra show a temperature-dependent red shift as a result of ligation of the porphyrin zinc center. The smallest aggregate that can account for the optical spectra and their concentration dependence is a symmetrical tetramer in which each zinc atom is ligated to a pyridyl substituent of a neighboring porphyrin molecule. The Soret band shows a splitting which can be explained by applying simple exciton theory to the tetramer. The equilibrium constant and thermodynamic parameters for the monomer-tetramer equilibrium have been determined as $K = 6.2 \pm 0.8 \ 10^{13} \ M^{-3}$, $\Delta H = 40 \pm 2 \ kCalM^{-1}$, $\Delta S = 150 \pm 10 \ CalK^{-1}M^{-1}$, in agreement with tetramer formation.

Introduction

Thin porphyrin films have been widely studied by optical spectroscopy for several reasons, one of them being their potential application in organic solar cells [1,2,3]. Photovoltaic cells have been constructed using two photoactive porphyrin layers acting as an electron donor and – acceptor, respectively [4,5,6]. The efficiency of these cells may be improved by making use of a light-collecting antenna transferring the excitation energy to the photoactive region of the cell, where charge separation takes place.

[#] On leave from Department of Systems Analysis, Belarusian State University, 4, F. Scoryna Ave., Minsk, 220050, Belarus

[*] Corresponding author: Tel: +31-317482044; Fax: + 31-317482725; e-mail: Tjeerd.Schaafsma@mac.mf.wau.nl

As in natural photosynthetic antenna complexes [7,8,9], the efficiency of energy transfer relative to other photophysical processes in porphyrin complexes is expected to depend on the relative position and orientation of the porphyrins involved. Various porphyrin assemblies, both covalently as well as non-covalently bound, have been studied to obtain a better understanding of their photophysical properties, including internal energy transfer [10,11,12,13,14]. Although much progress has been made in understanding the excited state kinetics in these porphyrin assemblies, the current understanding of the steady state and time-dependent properties of their excited state(s) is still incomplete.

This paper (I) reports the steady state absorption- and fluorescence properties of a model system of a self-assembled symmetric porphyrin tetramer in toluene solution, using zinc mono (4-pyridyl)-triphenylporphyrin (ZnM(4-Py)TrPP, Fig. 1) as a good candidate for self-assembled aggregates [15,16,17].
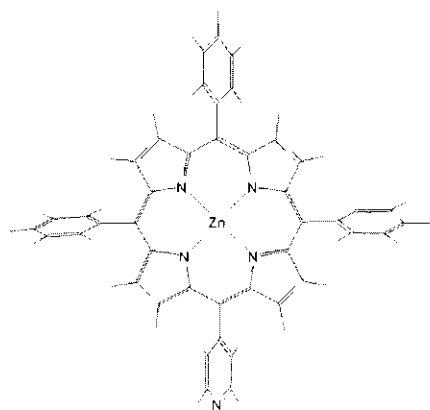

Figure 1. Zinc mono-(4-pyridyl)-triphenylporphyrin (ZnM(4-Py)TrPP).

The ground state structure of the tetramer cannot be determined from ^{1}H NMR ring current shifts [16,18,19,20] due the low solubility of the tetramer in toluene, and therefore has been calculated using a Chem-X program [21]. The thermodynamic parameters of the tetramer ground state are reported, whereas its excited state properties are explained by simple exciton theory. The subsequent paper (II) presents the quantitative kinetics of the tetramer excited state using time-resolved fluorescence spectroscopy and anisotropy measurements.

Both papers are part of a program, starting with a description of the photophysical processes in a well-defined porphyrin aggregate, to elucidate these processes in more complicated disordered and ordered solid porphyrin films, which may for instance serve as light-collecting antenna's in organic solar cells.

In the experiments reported in this and the following paper II a solution of zinc tetraphenylporphyrin (ZnTPP) in dry toluene and in toluene/pyridine 1:10 v/v is used as a reference for the non-ligated and ligated species, respectively. For the same reasons as mentioned before, similar studies as reported in this work have been carried out on a number of

other tetra-phenyl-porphyrin derivatives including zinc tetra-(octylphenyl)-porphyrin (ZnTOPP) [22].

Experimental

Chemicals

Meso-tetraphenylporphyrin free base (H_2TPP) and a derivative with one meso-phenyl group substituted by a meso-(4-pyridyl) group, mono(4-pyridyl)-triphenylporphyrin free base (H_2M(4-Py)TrPP), were synthesized from pyrrole and benzaldehyde, and from pyrrole and a mixture of benzaldehyde and 4-pyridinecarbaldehyde, respectively, by standard procedures [23]. Zinc was inserted into the free base by refluxing a solution in dimethylformamide (DMF) in the presence of excess zinc(II)chloride [24] yielding ZnTPP and ZnM(4-Py)TrPP, respectively. The zinc porphyrins were purified by chromatography over silica gel (Merck) with chloroform (Merck p.a.) as the eluent. The porphyrins were estimated to be >99% pure by thin-layer chromatography, absorption- and fluorescence spectroscopy. All reagents (Merck) were synthetic grade.

For optical measurements solutions were prepared in toluene (Merck, p.a.) after drying with sodium wire and storing over molecular sieve. Anhydrous pyridine (Aldrich) was used without additional drying or purification. For measuring polarization steady state fluorescence anisotropy the porphyrins were dissolved in viscous solutions of polystyrene (PS) in toluene (further denoted as PS/Tol). All solvents used were p.a. grade, unless stated otherwise.

Steady-State Absorption and Emission Measurements

A Cary 5E spectrophotometer and a Perkin Elmer LS5 fluorimeter or a Fluorolog 3-22 Jobin Yvon spectrophotometer were used to record the electronic absorption- and fluorescence spectra. The Fluorolog spectrophotometer was equipped with 2 electronically actuated Glann-Thompson UV polarizers (Model 1008 Dual Auto Polarizer) to measure the steady state anisotropy spectra. To study the effect of pyridine ligation, absorption - and fluorescence spectra were recorded of $\approx$ $2.2 \cdot 10^{-5}$ and $1.6 \cdot 10^{-5}$ M ZnTPP solutions in neat toluene and in toluene/10^{-4} M pyridine, respectively. Complexation of ZnM(4-Py)TrPP via intermolecular ligation of the zinc center of one porphyrin to a pyridyl substituent of a neighboring porphyrin was studied by measuring the absorption- and fluorescence spectra of $2.2 \cdot 10^{-6}$ - $8.0 \cdot 10^{-5}$ M solutions in toluene over a 10-55°C temperature range. Steady state absorption- and fluorescence anisotropy spectra of ZnM(4-Py)TrPP in PS/Tol were recorded to study energy transfer processes within an aggregate.

107

Results

Temperature-dependent absorption spectra are shown in Fig. 2 for solutions of (A): $\approx 2.2 \cdot 10^{-5}$ M ZnTPP in toluene, (B): $\approx 1.6 \cdot 10^{-5}$ M ZnTPP in toluene/10^{-4} M pyridine, and (C): $\approx 4.0 \cdot 10^{-5}$ M ZnM(4-Py)TrPP in toluene.
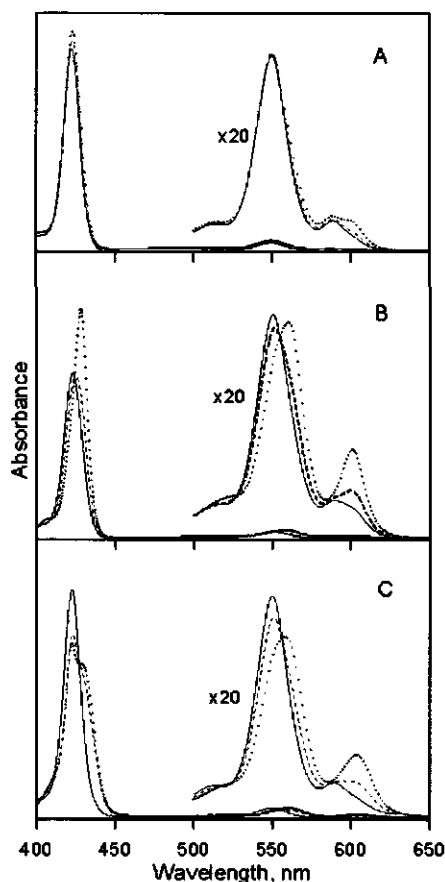

Figure 2. Effect of temperature on the absorption spectrum of (A) a $\approx 2.2 \cdot 10^{-5}$ M solution of ZnTPP in toluene, (B) a $\approx 1.6 \cdot 10^{-5}$ M solution of ZnTPP in a toluene/10^{-4} M pyridine mixture, (C) a $\approx 4.0 \cdot 10^{-5}$ M solution of ZnM(4-Py)TrPP in toluene. Solid line: 55°C; broken line: 35°C; dotted line: 10°C.

All spectra show similar absorption spectra at 55°C, with maxima at 550 and 595 nm for the Q(0,1) and Q(0,0) bands, respectively, and at 423 nm for the Soret band. However, the absorption spectra of (A), (B), and (C) change differently with decreasing temperature. Decreasing the temperature from 55 to 10°C results for (A) in only small changes of the absorption spectrum (Fig. 2A). Obviously, despite drying on sodium wire still a trace amount of water is present in the dried toluene, giving rise to a small, temperature dependent, ligation shift, as can be concluded by comparison with the spectrum of ZnTPP in non-dried toluene. Since the ligation strength of the oxygen donor of water is much smaller than that of pyridine the ligation shift was accordingly much smaller [25,26].For the same temperature range the maxima of the Q(0,0), Q(0,1) and Soret absorption bands of (B) shift from 589 to 601 nm, from 550 nm to 561 nm, and from 423 to 428 nm, respectively (Fig. 2B), whereas for (C) shifts were found from 589 to 604 nm and 550 to 560 nm for the Q(0,0) and Q(0,1) bands, respectively.
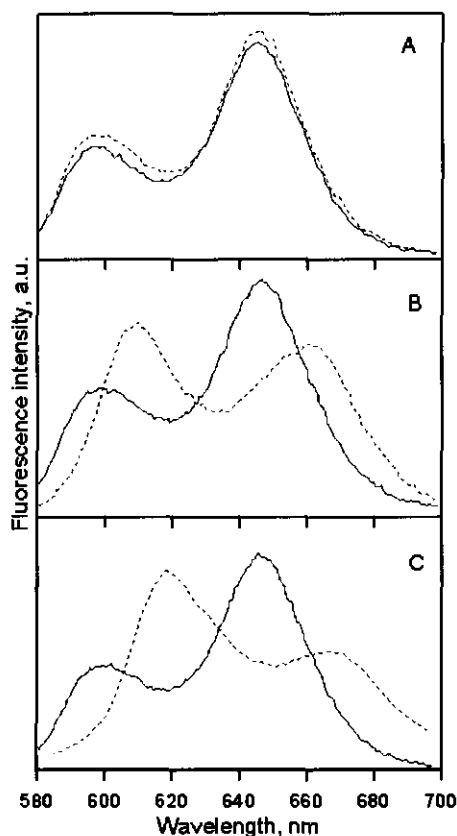
At 10°C the Soret band is split into two components, of which one is red-shifted from 422 to 430 nm and the other is practically not shifted with respect to the monomer wavelength of 423 nm at 55°C.
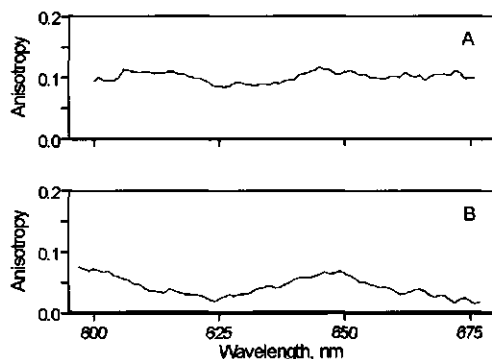
Figure 4. Steady state anisotropy detected at 10°C of (A) $\approx 1.6 \cdot 10^{-5}$ M ZnTPP; (B) $\approx 1.6 \cdot 10^{-5}$ M ZnM(4-Py)TrPP both in PS/Tol. Excitation at the Q(0,1) maximum.

Fluorescence emission spectra of the same porphyrin samples at 10 and 55°C are presented in Fig. 3. All emission spectra were recorded using excitation at the maximum of the Q(0,1) band. At 10°C the fluorescence spectrum of (B) is red-shifted with respect to that of (A) (Fig. 3A,B) and the intensity of the Q(0,0) band is higher than that of Q(0,1) typical for ligated metalloporphyrins [27]. For (C) at 10°C (Fig. 3C) the fluorescence spectrum looks similar to that of (B), but somewhat less resolved (Fig. 3B).

Figure 3. Effect of temperature on the fluorescence spectrum of (A) a $\approx 2.2 \cdot 10^{-5}$ M solution of ZnTPP in toluene, (B) a $\approx 1.6 \cdot 10^{-5}$ M solution of ZnTPP in a toluene/10^{-4} M pyridine mixture, (C) a $\approx 4.0 \cdot 10^{-5}$ M solution of ZnM(4-Py)TrPP in toluene. Solid line: 55°C; broken line: 10°C. Excitation of all samples at the Q(0,1) maximum.

Steady state fluorescence anisotropy spectra of $\approx 1.6 \cdot 10^{-5}$ M ZnTPP and the same concentration of ZnM(4-Py)TrPP in PS/Tol at 10°C are presented in Fig. 4. The steady state anisotropy spectrum of ZnTPP (Fig. 4A) varies around a mean value of 0.1. The average anisotropy of ZnM(4-Py)TrPP (Fig. 4B) is lower than that of ZnTPP and has two minima at 625 and 675 nm, and two maxima at 600 and 650 nm.

Discussion

The changes observed for the Soret- and Q-bands, presented in Fig. 2B, are attributed to ligation of the metal center of ZnTPP to pyridine at 10°C. From the shifts in both the Q - and the Soret

109

bands we can conclude that at 10°C ligation of ZnTPP with pyridine is almost complete [28], whereas at 55°C the equilibrium constant K for the equilibrium ZnP + L = ZnP·L is much smaller. With the coordinating ligand covalently linked to the porphyrin as for ZnM(4-Py)TrPP, a decrease of temperature of the solution is expected to result in porphyrin complexation via zinc-pyridyl ligation. Indeed we observe Q-band shifts in the absorption spectrum upon a 55 to 10°C temperature decrease (Fig. 2C) [16,25]. The Q-bands shifts are very similar to those in Fig. 2B, and can therefore be ascribed to a high percentage of the ligated zinc porphyrin at 10°C. Previously, the Soret band splitting was not observed for the same compound in CHCl₃ [16] or just reported to be broadened [3] at 25°C for toluene and CH₂Cl₂ as a solvent. The split Soret band observed at 10°C might suggest that only half of the ZnM(4-Py)TrPP molecules are internally ligated in agreement with a dimer model as previously proposed [3], but contradicting the observation that the entire Q-band is shifted. A polymeric structure for ZnM(4-Py)TrPP in CHCl₃ at concentrations up to 10^{-2} M [16] is unlikely to explain our results in view of the low concentration ($\approx 4.0 \cdot 10^{-5}$ M) which we have used.
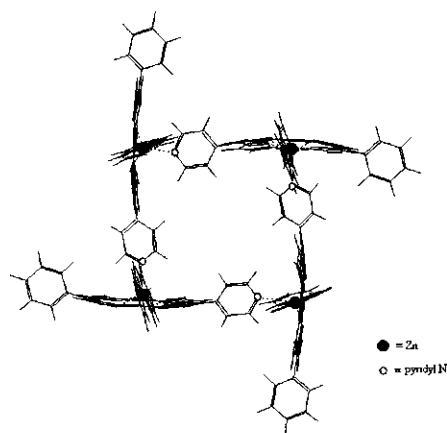

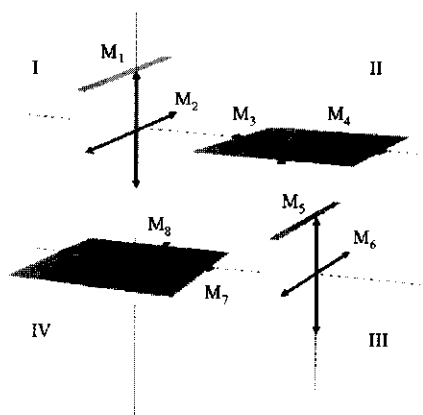**Figure 5.** ZnM(4-Py)TrPP tetramer structure, calculated by the Chem X program.

Figure 6. The structural arrangements of the transition moments (M_i, i=1,..,8) in the ZnM(4-Py)TrPP tetramer. The porphyrins in the aggregate are numbered I - IV.

A symmetrical tetramer in which each zinc atom is ligated to a pyridyl substituent of one of the neighboring porphyrin molecules is the smallest complex, which can account for the shift of the entire Q-band (Fig. 5). The formation of a tetrameric complex also explains the splitting of the Soret band, invoking simple dipole-dipole excitonic interactions [29,30,31] in the S_2-state between four mutually perpendicular porphyrin molecules for which the spatial arrangement of the transition dipole moments for the cyclic tetrameric complex is shown in Fig. 6.

The ground state wavefunction of the tetramer is:

$$\Psi_G = \psi_I \psi_{II} \psi_{III} \psi_{IV}$$

(1)

where ψ_I, ψ_{II}, ψ_{III}, ψ_{IV} are the ground state wavefunctions of molecules I, II, III, and IV, respectively. The Hamiltonian operator for the tetramer is

$$H = H_I + H_{III} + H_{III} + H_{IV} + \frac{1}{2}\sum_{i=1}^{8}\sum_{j=1}^{8} V_{ij}$$

(2)

where H_I, H_{II}, H_{III}, H_{IV} are the Hamiltonians for the isolated molecules I, II, III, and IV; V_{ij} for $i=1,\ldots,8$ and $j=1,\ldots,8$ are the intermolecular perturbation potentials.

The wavefunction for the tetramer excited state can be written as

$$\Psi_E = a\psi_I^{*1}\psi_{II}\psi_{III}\psi_{IV} + b\psi_I^{*2}\psi_{II}\psi_{III}\psi_{IV} + c\psi_I\psi_{II}^{*3}\psi_{III}\psi_{IV} + d\psi_I\psi_{II}^{*4}\psi_{III}\psi_{IV}$$
$$+ e\psi_I\psi_{II}\psi_{III}^{*5}\psi_{IV} + f\psi_I\psi_{II}\psi_{III}^{*6}\psi_{IV} + g\psi_I\psi_{II}\psi_{III}\psi_{IV}^{*7} + h\psi_I\psi_{II}\psi_{III}\psi_{IV}^{*8}$$

(3)

where $\psi_I^{*1}, \psi_I^{*2}, \psi_{II}^{*3}, \psi_{II}^{*4}, \psi_{III}^{*5}, \psi_{III}^{*6}, \psi_{IV}^{*7}, \psi_{IV}^{*8}$ are excited state wavefunctions for the excited states corresponding to 1-, 2-, 3-, 4-, 5-, 6-, 7-, 8-th transition dipole moments of molecule # I, II, III, and IV; a, b, c, d, e, f, g, h are coefficients to be determined.

Solving for the energies $\overline{E}_E$ and coefficients of the eight excited state tetramer [30] eigenfunctions $\overline{\Psi}_E$ yields

$$\overline{E}_E = \begin{bmatrix} \widetilde{\varepsilon} - \varepsilon_{15} \\ \widetilde{\varepsilon} - \varepsilon_{15} \\ \widetilde{\varepsilon} + \varepsilon_{15} \\ \widetilde{\varepsilon} + \varepsilon_{15} \\ \widetilde{\varepsilon} - \varepsilon_{48} \\ \widetilde{\varepsilon} - \varepsilon_{48} \\ \widetilde{\varepsilon} - 2\varepsilon_{24} + \varepsilon_{48} \\ \widetilde{\varepsilon} + 2\varepsilon_{24} + \varepsilon_{48} \end{bmatrix} \quad \overline{\Psi}_E = \begin{bmatrix} 0 & 0 & -1 & 0 & 0 & 0 & 1 & 0 \\ -1 & 0 & 0 & 0 & 1 & 0 & 0 & 0 \\ 0 & 0 & 1 & 0 & 0 & 0 & 1 & 0 \\ 1 & 0 & 0 & 0 & 1 & 0 & 0 & 0 \\ 0 & 0 & 0 & -1 & 0 & 0 & 0 & 1 \\ 0 & -1 & 0 & 0 & 0 & 1 & 0 & 0 \\ 0 & -1 & 0 & 1 & 0 & -1 & 0 & 1 \\ 0 & 1 & 0 & 1 & 0 & 1 & 0 & 1 \end{bmatrix}$$

(4)

With $\varepsilon_{ij} = \varepsilon_{ji}$, $i = 1,\ldots,8$ and $j = 1,\ldots,8$, the non-zero values of $\varepsilon_{15} = \varepsilon_{37}$, $\varepsilon_{48} = \varepsilon_{26}$, $\varepsilon_{28} = \varepsilon_{24} = \varepsilon_{46} = \varepsilon_{68}$ are

$$\varepsilon_{15} = \iiint \psi_I^{*1} \psi_{II} \psi_{III} \psi_{IV} V_{15} \psi_I \psi_{II} \psi_{III}^{*5} \psi_{III} \psi_{IV} d\tau_I d\tau_{II} d\tau_{III} d\tau_{IV}$$

$$\varepsilon_{24} = \iiint \psi_{II}^{*2} \psi_{II} \psi_{III} \psi_{IV} V_{24} \psi_I \psi_{II}^{*4} \psi_{III} \psi_{IV} d\tau_I d\tau_{II} d\tau_{III} d\tau_{IV}$$

$$\varepsilon_{48} = \iiint \psi_I \psi_{II}^{*4} \psi_{III} \psi_{IV} V_{48} \psi_I \psi_{II} \psi_{III} \psi_{IV}^{*8} d\tau_I d\tau_{II} d\tau_{III} d\tau_{IV}$$

(5)

where $\widetilde{\varepsilon} = E^* + 3E_G + D^*$; E^* is the isolated monomer excited state energy; E_G is the monomer ground state energy, and D^* represents the van der Waals interaction energy in the excited state, defined as

$$D^* (= \varepsilon_{ii} = \varepsilon_{11}) = \iiint \psi_I^{*1} \psi_{II} \psi_{III} \psi_{IV} V_{11} \psi_I^{*1} \psi_{II} \psi_{III} \psi_{IV} d\tau_I d\tau_{II} d\tau_{III} d\tau_{IV}, \quad i = 1,\ldots,8$$

(6)

Eqn. (4) yields two allowed transitions of which one is twofold degenerate with energy $\widetilde{\varepsilon} + \varepsilon_{15}$ and one non-degenerate with energy $\widetilde{\varepsilon} + 2\varepsilon_{24} + \varepsilon_{48}$. Now we would calculate the energy splitting ΔE between the two allowed transitions. From the optical spectrum of the ZnM(4-Py)TrPP monomer in toluene [32], the dipole strength of the Soret band is calculated to be 9.5±0.5 D. Using the point-dipole point-dipole approximation for the intermolecular perturbation potentials* the energy splitting ΔE between the two allowed transitions of the tetramer is calculated to be 480±50 cm^{-1}, in good agreement with the experimental splitting ~ 440 cm^{-1}. Relative energy levels and transitions for monomer, ligated monomer, and tetramer dipole arrangements are shown in Fig. 7.

---

*From the tetramer structure in vacuum, calculated using the Chem-X program the center-to-center distances are found to be ≈ 10 Å for nearest neighbor porphyrins and ≈ 14 Å for the next nearest neighbor ones.
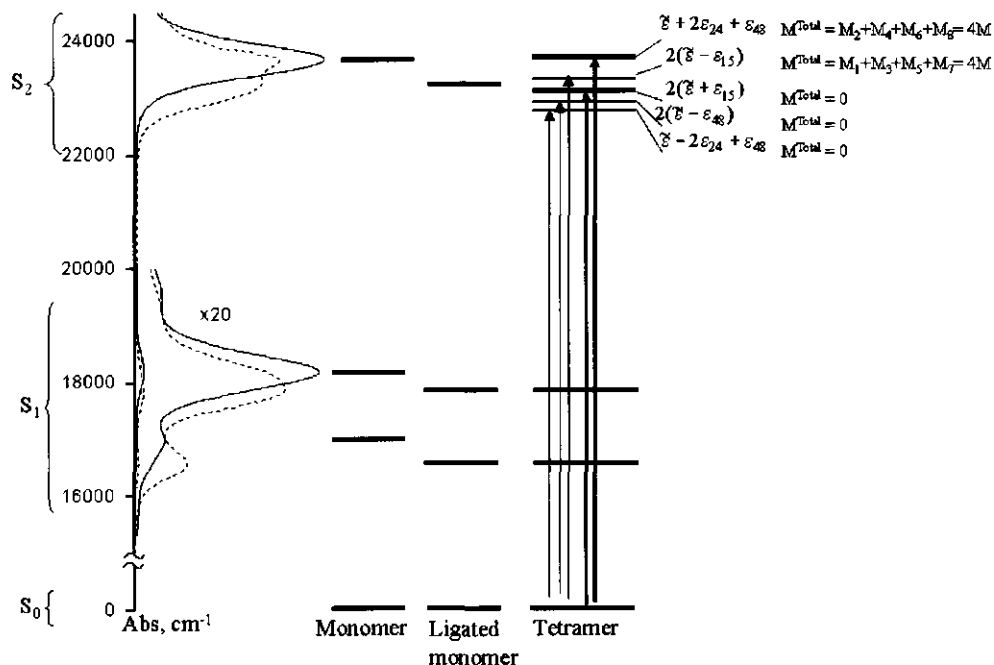
Figure 7. The tetramer energy level scheme, calculated using the exciton model (see text), and relative non-ligated and ligated monomer energy levels. Thick and thin arrows represent allowed and forbidden transitions, respectively.

According to the exciton model the component of the Soret band, which is red shifted w.r.t. the non-ligated monomer position, results from a superposition of two transition dipole-dipole interactions, i.e. M_1/M_5 and M_3/M_7. The total transition moment of the redshifted band is $M_{Shift}^{Total} = M_1 + M_3 + M_5 + M_7 = 4M$. The band is 32 ± 4 cm^{-1} red-shifted w.r.t. position of the ligated monomer, too small a shift to be resolved in the absorption spectrum. In view of the discussion above, the component which is unshifted w.r.t. the non-ligated monomer position, is the result of excitonic interaction between four parallel transition dipole moments (M_2, M_4, M_6, and M_8) with the same directions and the total transition dipole moment of this band is again $M_{Unshift}^{Total} = M_2 + M_4 + M_6 + M_8 = 4M$. This band is significantly blue-shifted ($\Delta E \sim 480$ cm^{-1}) w.r.t. the position of the ligated monomer. The total calculated dipole strengths are in agreement with those calculated from the experimental splitting of the Soret bands. The red-shift of the Q-bands only results from axial ligation of the zinc porphyrins, since exciton interaction between the S_1 states is negligibly small due to the much smaller transition moments involved. It is important to note that application of the extended dipole-dipole model [33] does not significantly change the abovementioned conclusions and changes the results of calculations with less then 10%.

The isosbestic points at 560 and 580 nm in the absorption spectra of Fig. 2C indicate a shift in the equilibrium between two and only two species absorbing at different wavelengths at constant total concentration. The $2.2 \cdot 10^{-6}$ M ZnTM(4-Py)TrPP spectrum measured at 55°C and the $8.0 \cdot 10^{-5}$ M ZnTM(4-Py)TrPP spectrum measured at 15°C can be assigned to the non-ligated and the ligated ZnM(4-Py)TrPP* monomers, respectively. This conclusion is supported by the observation that the emission spectra for both abovementioned concentrations and temperatures do not change with excitation at $\lambda = 415$, 420, 425,430, and 435 nm. This implies that the spectra at an arbitrary, intermediate concentration can be described as a linear combination of the spectra of the abovementioned two species. Using the total concentration of the porphyrin in solution the concentration of non-ligated - and ligated ZnM(4-Py)TrPP at different temperatures can then be determined. Applying Lambert-Beer's law to the absorption of non-ligated - and ligated species, the absorption spectrum for a given total concentration $C_{tot} = C^T_{ZnP} + C^T_{ZnP \cdot L}$ at different wavelengths and temperatures is given by:

$$A_{tot}^T(\lambda) = \{C^T_{ZnP} \cdot \varepsilon_{ZnP}(\lambda) + C^T_{ZnP \cdot L} \cdot \varepsilon_{ZnP \cdot L}(\lambda)\} \cdot l$$

(7)

where $A_{tot}^T(\lambda)$ is the total absorbance at a temperature T (°C) and wavelength λ (nm); C_{tot} is the total ZnM(4-Py)TrPP molar concentration, and C_{ZnP}, $C_{ZnP \cdot L}$ are the monomer concentration of non-ligated porphyrin and that of ligated porphyrin, respectively; ε_{ZnP} and $\varepsilon_{ZnP \cdot L}$ are the corresponding molar extinction coefficients ($lM^{-1}cm^{-1}$), assumed to be constant over the experimental temperature range, and l is the optical pathlength of the cuvette (1 cm). With data taken from absorption spectra, i.e. $A^{55°C}_{2.2 \cdot 10^{-6} M}(\lambda), A^{15°C}_{8.0 \cdot 10^{-5} M}(\lambda)$ of the $2.2 \cdot 10^{-6}$ and $8.0 \cdot 10^{-5}$ M ZnTM(4-Py)TrPP solutions measured at 55 and 15°C, respectively, and using $\varepsilon_{ZnP}(550 \text{ nm}) = 22.000 \, lM^{-1}cm^{-1}$ and $\varepsilon_{ZnP \cdot L}(560 \text{ nm}) = 20.000 \, lM^{-1}cm^{-1}$ [3], eqn. (7) can be written as

$$A_{tot}^T(\lambda) = C^T_{ZnP} \cdot \frac{A^{55°C}_{2.2 \cdot 10^{-6} M}(\lambda) \cdot \varepsilon_{ZnP}(550nm)}{A^{55°C}_{2.2 \cdot 10^{-6} M}(550nm)} + C^T_{ZnP \cdot L} \cdot \frac{A^{15°C}_{8.0 \cdot 10^{-5} M}(\lambda) \cdot \varepsilon_{ZnP \cdot L}(560nm)}{A^{15°C}_{8.0 \cdot 10^{-5} M}(560nm)}$$

(8)

---

*In this context ligated ZnM(4-Py)TrPP monomer refers to the absorption spectrum of $8.0 \cdot 10^{-5}$ M ZnTM(4-Py)TrPP recorded at 15°C.

Thus, the concentrations $C_{ZnP}^{T}, C_{ZnP \cdot L}^{T}$ of non-ligated and ligated porphyrins can now be calculated from eqn.(8). The results calculated for the three ZnM(Py-4)TrPP concentrations are plotted in Figure 8 and summarized in Table 1.
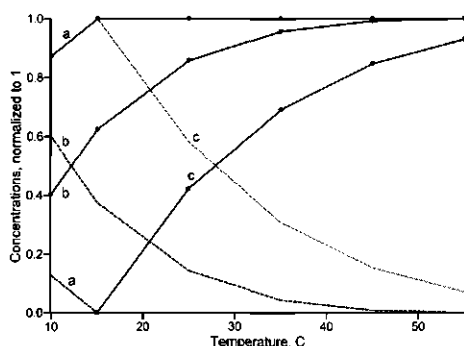

Figure 8. Concentrations of the non-ligated monomers $\widetilde{C}_{ZnP}$ (solid curves) and ligated monomers $\widetilde{C}_{ZnP \cdot L}$ (broken lines) of (set a) $2.2 \cdot 10^{-6}$ M, (set b) $2.2 \cdot 10^{-5}$ M, and (set c) $8.0 \cdot 10^{-5}$ M ZnM(4-Py)TrPP *vs* temperature. $\widetilde{C}_{ZnP} + \widetilde{C}_{ZnP \cdot L}$ is normalized to 1.

Because of considerable overlap between the fluorescence- and absorption spectra of non-ligated – and ligated ZnM(4-Py)TrPP and the energy difference between their lowest excited singlet-states (corresponding to 589 and 604 nm, respectively) in non-cyclic complexes (e.g. dimers, trimers and oligomers) unidirectional energy transfer can take place from an excited, non-ligated porphyrin to a neighboring, ligated one. Consequently, incorporating non-ligated monomers into these structures should result in a decrease of the fluorescence yield of the non-ligated species due to the energy transfer to ligated species in the chain and a simultaneous increase of the yield of ligated species. The temperature dependence of the fluorescence spectrum (excitation at 550) fits to a different model, however, as will be demonstrated below. The temperature-dependent fluorescence spectra of the $2.2 \cdot 10^{-5}$ M ZnTM(4-Py)TrPP can be simulated in the same way as their absorption spectra, calculating the total porphyrin fluorescence intensity $I_{tot}^{T}(\lambda)$ at temperature T, from that of the separate non-ligated- and ligated zinc porphyrins (eqn. (9)):

$$I_{tot}^{T}(\lambda) = I_{ZnP}^{T}(\lambda) + I_{ZnP \cdot L}^{T}(\lambda)$$

(9)

We note that for $2.2 \cdot 10^{-6}$ M solutions the fluorescence spectrum at 55°C ($I_{2.2 \cdot 10^{-6} M}^{55°C}(\lambda)$ in eqn.(10)), originates from 100% non-ligated monomers. Likewise, for $8.0 \cdot 10^{-5}$ M solutions the fluorescence spectrum at 10°C ($I_{8.0 \cdot 10^{-5} M}^{10°C}(\lambda)$ in eqn. (11)), corresponds to the 100% ligated species (see above).

The simulated spectra were calculated making the reasonable assumption that the fluorescence intensity of both species varies linearly with their relative concentrations. Then:

$$I^T_{ZnP}(\lambda) = (C^T_{ZnP}/2.2 \cdot 10^{-6}) \cdot I^{55°C}_{2.2 \cdot 10^{-6} M}(\lambda)$$

(10)

$$I^T_{ZnP \cdot L}(\lambda) = (C^T_{ZnP \cdot L}/8.0 \cdot 10^{-5}) \cdot I^{10°C}_{8.0 \cdot 10^{-5} M}(\lambda)$$

(11)

where C^T_{ZnP} and $C^T_{ZnP \cdot L}$ are the estimated contributions of non-ligated and ligated species expressed as monomer concentrations.

Combining eqns. (9)-(11) yields:

$$I^T_{tot}(\lambda) = (C^T_{ZnP}/2.2 \cdot 10^{-6}) \cdot I^{55°C}_{2.2 \cdot 10^{-6} M}(\lambda) + (C^T_{ZnP \cdot L}/8.0 \cdot 10^{-5}) \cdot I^{10°C}_{8.0 \cdot 10^{-5} M}(\lambda)$$

(12)

The simulated spectra contain the same contribution of ZnP and ZnP·L as experimentally found from the temperature dependence of the absorption spectra. This result contradicts a model that includes formation of non-cyclic structures but is in agreement with the proposed tetramer formation.

The steady state anisotropy of ZnM(4-Py)TrPP is at least two times lower at the maximum of the Q(0,1) transition as compared to that of the ZnTPP spectrum (Fig. 4A). Using the Perrin equation for the steady state anisotropy

$$r = \beta_0/(1+(\tau/\phi))$$

(13)

with β_0 - the magnitude of the initial anisotropy, τ - the fluorescence lifetime, and ϕ - the effective rotational volume of the molecule. Note that for zinc porphyrins in viscous PS/Tol solution $\tau/\phi \ll 1$ as will be shown in Part II, so that the estimated value of the steady state anisotropy can be approximated as $r = \beta_0$. It is seen from Fig. 4 that for monomers β_0 is ~ 0.1 and for tetramers ~ 0.025 at the maximum of the Q(0,1) transitions. The decreased magnitude of the initial anisotropy is a clear indication of an additional depolarization channel in the tetramer, as is expected for one or more energy transfer processes within the tetramer. The increase of the steady state anisotropy around 600 nm and 650 nm indicates the presence of a fraction of non-ligated monomers. The effects of energy transfer on the time dependence of the fluorescence anisotropy are analyzed in more detail in Part II.

The changes in the absorption spectra resulting from tetramer formation may be utilized to quantitatively study the equilibrium reaction by the non-calorimetric thermodynamic method [34]. Although this method has limited accuracy it provides an additional argument for the

proposed monomer-tetramer equilibrium. Generally, the equilibrium constants $K_{[M_n]}$ for the reactions: $n \cdot [M] = [M_n]$ can be calculated using the equation [34]:

$$K_{[M_n]} = [M_n]/[M]^n$$

(14)

where $[M]$ and $[M_n]$ are the molar concentrations of the monomer and an aggregate of n ligated molecules in the aggregate, respectively. Taking the monomer concentration of non-ligated and ligated porphyrins from Table 1 and using eqn. (14), the enthalpy ΔH and entropy ΔS with n can be calculated from the slopes of the van 't Hoff plots [34].
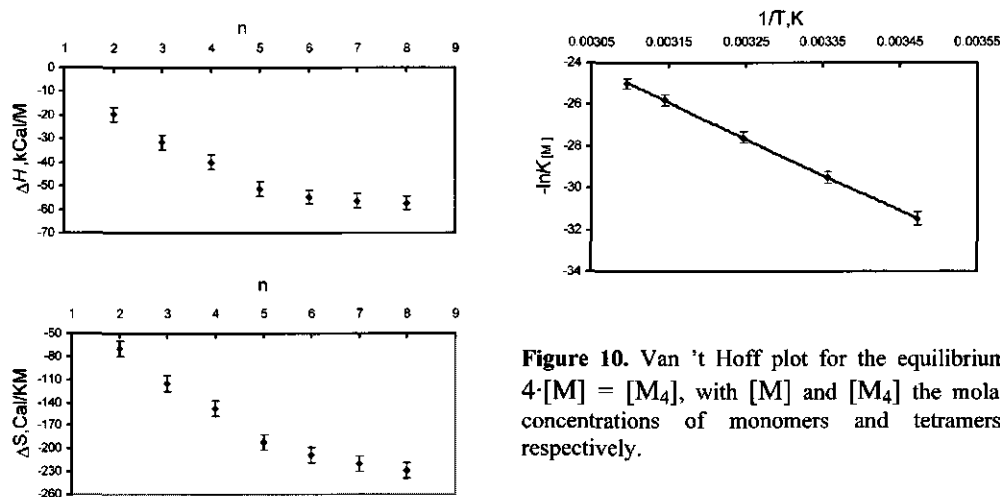

Figure 10. Van 't Hoff plot for the equilibrium $4 \cdot [M] = [M_4]$, with $[M]$ and $[M_4]$ the molar concentrations of monomers and tetramers, respectively.

Figure 9. The enthalpy ΔH and entropy ΔS for the equilibrium between n molecules M and the aggregate M_n.

Fig. 9 presents ΔH and ΔS for the aggregates formed by $n = 2,...,8$ ligated molecules. The values for $n = 2,3,7,8$ need not be considered as their van 't Hoff plots are distinctly non-linear, implying an equilibrium between more then two species, contradicting the finding of an isosbestic point of the optical spectra. Also, ΔS values do not change much starting from $n \geq 6$, indicating that large aggregates ($n \geq 6$) can also be rejected, leaving aggregates with $n = 4$ and 5 to be considered. The smallest aggregate has $n = 4$ which agrees with the result of the calculation of the excitonic splitting of the Soret band. The same calculations for the pentamer ($n = 5$) and hexamer ($n = 6$) result in more complicated spectra. For tetramers involved in the reaction, $K_{[M_n]}$, ΔH, and ΔS are calculated to be $6.2 \pm 0.8 \ 10^{13} \ M^{-3}$, $40 \pm 2 \ kCalM^{-1}$, and $150 \pm 10 \ CalK^{-1}M^{-1}$, respectively. The van 't Hoff plot is shown in Fig. 10. ΔH for insertion of one ZnM(4-Py)TrPP

molecule into the tetrameric complex is ~10 kcalM^{-1} in good agreement with values calculated for the ZnTPP/pyridine equilibrium [35,36]. ΔS is almost one order larger than for ZnTPP ligated to pyridine [35,36], that also supports the formation of a relatively large closed structure.

Conclusions

This work clearly demonstrate that

- the effects of lowering the temperature or increasing the concentration of a ZnM(4-Py)TrPP/toluene solution on the absorption- and fluorescence spectra are the result of porphyrin aggregation;

- the shifts, found in both the Q-band region of the absorption spectrum and in the fluorescence spectrum, can be ascribed to coordination of the metal center of one ZnM(4-Py)TrPP molecule to the pyridyl substituent of a second, neighboring molecule. Excitonic interactions can be neglected for the S_1 state;

- the splitting of the Soret band in the absorption spectrum can be readily explained by an excitonic interaction in the S_2-state between four perpendicularly oriented ZnM(4-Py)TrPP molecules in a structure in which each zinc atom is ligated to a pyridyl substituent of a neighboring molecule;

- a symmetrical tetramer is the smallest complex that can account for all of the observed shifts in the optical spectra;

- the estimated thermodynamic parameters are in good agreement with those expected for a tetramer.

The abovementioned conclusions outlined here are supported and extended in part II of this paper using time-resolved fluorescence and fluorescence anisotropy measurements.

References

[1] Schaafsma, T. J. *Sol. Energy Mat. Sol. Cells* **1995**, *38*, 349.

[2] Leray, I.; Verniéres, M. C.; Pansu, R.; Bied-Charreton, C.; Faure, J. *Thin Solid Films* **1997**, *303*, 295.

[3] Takahashi, K.; Komura, T.; Imanaga, H. *Bull. Chem. Soc. Jpn.* **1989**, *62*, 386.

[4] Savenije, T. J.; Koehorst, R. B. M.; Schaafsma, T. J. *Chem. Phys. Lett.* **1995**, *244*, 363.

[5] Günster, S.; Siebentritt, S.; Meissner, D. *Mol. Cryst. Liq. Cryst. A* **1993**, *230*, 351.

[6] Wöhrle, D.; Tennigkeit, B.; Elbe, J.; Kreienhop, L.; Schnurpfeil, G. *Mol. Cryst. Liq. Cryst. A* **1993**, *230*, 221.

[7] Larkum, A. W. D.; Barrett, J. *Adv. Bot. Res.* **1983**, *10*, 1.

[8] Scheer, H.; Siegried, S.; de Gruyter, W. *Photosynthetic Light-Harvesting Systems*; Springer: Berlin, 1988.

[9] Karrasch, S.; Bullough, P.A.; Ghosh, R. *EMBO J.* **1995**, *14*, 631.

[10] Prodi, A.; Indelli, M. T.; Kleverlaan, C. J.; Scandola, F.; Alessio, E.; Gianferrara, T.; Marzilli, L. G. *Chem. Eur. J.* **1999**, *5*, 2668.

[11] Rubtsov, I. V.; Kobuke, Y.; Miyaji, H.; Yoshihara, K. *Chem. Phys. Lett.* **1999**, *308*, 323.

[12] Lawrence, D.; Jiang, I.; Levett, M. *Chem. Rev.* **1995**, *95*, 2229.

[13] Li, F.; Gentemann, S.; Kalsbeck, W. A.; Seth, J.; Lindsey, J. S.; Holten, D.; Bocian, D. F. *J. Mater. Chem.* **1997**, *7*, 1245.

[14] van Patten, P. J.; Shreve, A. P.; Lindsey, J. S.; Donohoe, R. J. *J. Phys. Chem. B* **1998**, *102*, 4209.

[15] Alessio, E.; Gremia, S.; Mestroni, S.; Iengo, E.; Srnova, I.; Slof, M. *Inorg. Chem.* **1999**, *38*, 869.

[16] Fleiscer, E. B.; Shachter, A. M. *Inorg. Chem.* **1991**, *30*, 3763.

[17] Shachter, A. M.; Fleiscer, E. B.; Haltiwanger, R. C. *J. Chem. Soc. Chem. Commun.* **1998**, 60.

[18] Abraham, R. J. *J. Mol. Phys.* **1961**, *4*, 145.

[19] Hofstra, U.; Koehorst, R. B. M.; Schaafsma, T. J. *Magn. Reson. Chem.* **1987**, *25*, 1069.

[20] Koehorst, R. B. M.; Hofstra, U.; Schaafsma, T. J. *Magn. Reson. Chem.* **1988**, *26*, 167.

[21] *Chem-X*; Chemical Design Ltd: Oxon, England, 1993.

[22] Donker, H.; Koehorst, R. B. M.; van Hoek, A.; van Schaik, W.; Yatskou, M. M.; Schaafsma, T. J. *J. Phys. Chem. B*, submitted.

[23] Adler, A. D.; Longo, F. R.; Finarelli, J. D.; Goldmacher, J.; Assour, J.; Korsakoff, L. *J. Organic Chem.* **1967**, *32*, 476.

[24] Adler, A. D.; Longo, F. R.; Kampas, F.; Kim, J. *J. Inorg. Nucl. Chem.* **1970**, *32*, 2443.

[25] Nardo; J. V.; Dawson, J. H. *Inorg. Chem. Acta.* **1986**, *123*, 9.

[26] Datta-Gupta, N.; Malakar, D.; Ramcharan, R.G. *J. Inorg. Nucl. Chem.* **1981**, *43*, 2079.

[27] Selensky, R.; Holten, D.; Windsor, M. W.; Paine III, J.B.; Dolphin, D.; Gouterman, M.; Thomas, J. C. *Chem. Phys.* **1981**, *60*, 33.

[28] Humphry-Baker, R.; Kalyanasundaram, K. *J. Photochemistry* **1985**, 31, 105.

[29] McRae, E.G.; Kasha, M. *J. Chem. Phys.* **1958**, *28*, 721.

[30] Kasha, M.; Rawls, H.R.; El-Bayoumi, M. A. *Pure Appl. Chem.* **1965**, *11*, 371.

[31] Stomphorst, R. G.; Koehorst, R. B. M.; van der Zwan, G.; Benthen, B.; Schaafsma, T. J. *J. Porph. Phtalocyanins* **1999**, *3*, 346.

[32] Michl, T.; Thulstrup, E. W. *Spectroscopy with Polarized Light*; VCH: New York, 1986.

[33] Czikklely, V.; Forsterling, H. D.; Kuhn, H. *Chem. Phys. Lett.* **1970**, *6*, 207.

[34] Atkins, P.W. *Physical Chemistry*; Oxford University Press: Oxford, 1998.

[35] Miller, J.R.; Dorought, G. D. *J. Am. Chem. Soc.* **1952**, *74*, 3977.

[36] Datta-Gupta, N.; Malakar, D.; Ramcharan, R. G. *J. Inorg. Nucl. Chem.* **1981**, *43*, 2079.

5.2.3. Spectroscopic Properties of a Self-assembled Zinc Porphyrin Tetramer II. Time-Resolved Fluorescence Spectroscopy

Mikalai M. Yatskou[#], Rob B.M. Koehorst, Arie van Hoek, Harry Donker

and Tjeerd J. Schaafsma[*]

Laboratory of Biophysics, Department of Agrotechnology and Food Sciences,

Wageningen University, Dreijenlaan 3, 6703 HA Wageningen, The Netherlands

Bas Gobets, Ivo van Stokkum and Rienk van Grondelle

Faculty of Sciences, Division of Physics and Astronomy, Vrije Universiteit,

De Boelelaan 1081, 1081 HV Amsterdam, The Netherlands

Abstract

Excited state kinetics of complexes of a functionalised zinc tetraphenylporphyrin (ZnTPP) derivative, zinc mono(4-pyridyl)triphenylporphyrin (ZnM(4-Py)TrPP) in toluene and polystyrene/toluene mixtures have been investigated by time-resolved fluorescence spectroscopy. In addition to the ~ 2.0 ns monomer fluorescence lifetime a ~ 1.5 ns component was found by applying global analysis to the time-resolved fluorescence decay. The 1.5 ns component is assigned to a cyclic porphyrin tetramer [see Part I], with a ≈ 1 ns rotational correlation time at $10°$ C. The initial fluorescence anisotropy of the monomer is found to be 0.1. In the tetramer an additional depolarization process occurs with a correlation tiume of ~ 31 ps, resulting in a further decrease of the anisotropy from 0.1 to 0.025. This additional depolarization is ascribed to singlet energy transfer between the porphyrin units that constitute the tetramer.

The intramolecular energy transfer processes have been simulated using the Monte Carlo method, yielding rate constants of $(26 \pm 4 \text{ ps})^{-1}$ and $\leq (180 \text{ ps})^{-1}$ for energy transfer between nearest neighbor and next nearest neighbor porphyrins in the tetramer.

[#]On leave from Department of Systems Analysis, Belarusian State University, 4, F. Scoryna Ave., Minsk, 220050, Belarus

[*]Corresponding author: Tel: +31-317482044; Fax: + 31-; e-mail: Tjeerd.Schaafsma@mac.mf.wau.nl

Introduction

Energy transfer in photosynthetic light-harvesting complexes is extremely efficient even over long distances [1,2]. Although much progress has been made in describing the photophysics of such complex systems, the understanding of their excited state dynamics is still far from complete. Many synthetic model systems have been synthesized to obtain a better insight in the energy transfer processes in natural systems [3,4,5,6,7,8,9,10,11,12]. In particular self-assembled aggregates of metalloporphyrin arrays have been used as building blocks for artificial light harvesting systems and various molecular electronic devices [13,14,15,16].

This work focuses on porphyrin tetramers as models for plant pigments, such as chlorophyll organized in various protein complexes, since similarly to these complexes the tetramers have a fixed, defined structure and show fast energy transfer from a particular excited porphyrin to one or more of its neighbors and loss of excitation energy by relaxation to the ground state [Part I]. Differently from photosynthetic pigment complexes, in porphyrin tetramers these processes can be studied in isolated units in a time domain, which is experimentally much better accessible than in the natural systems, which often exhibit extremely fast excited state dynamics in response to optical excitation [17,18,19].

This study is part of a research program aimed at understanding how the concepts of the molecular basis of photosynthesis can be used to construct artificial devices, in particular solar cells with a high photovoltaic efficiency.

From the steady state absorption- and fluorescence spectra (Part I) it could be concluded, that at low temperature a self-assembled aggregate of ZnM(4-Py)TrPP is formed in toluene and viscous polystyrene/ toluene mixtures (PS/Tol) with a cyclic, tetrameric structure (Fig. 1). This Part II reports the kinetics of the processes involving the first excited singlet state of the tetramer using time-correlated single photon counting as well as streak camera detection [20]. The latter method has some distinct advantages, i.e. a time-resolution almost 10 times as high as the TCSPC method, which allows resolving fluorescence- and fluorescence anisotropy decay times of less than 1 ps. Also, the kinetics of the whole spectrum is detected instead of at a single wavelength, as with TCSPC. For streak camera measurements, the solution needs to be circulated limiting the experiments to non-viscous and non-inertial solvents (e.g. toluene) and excluding viscous solvents. For this reason, all measurements on viscous PS/Tol solutions had to be done using the TCSPC method.
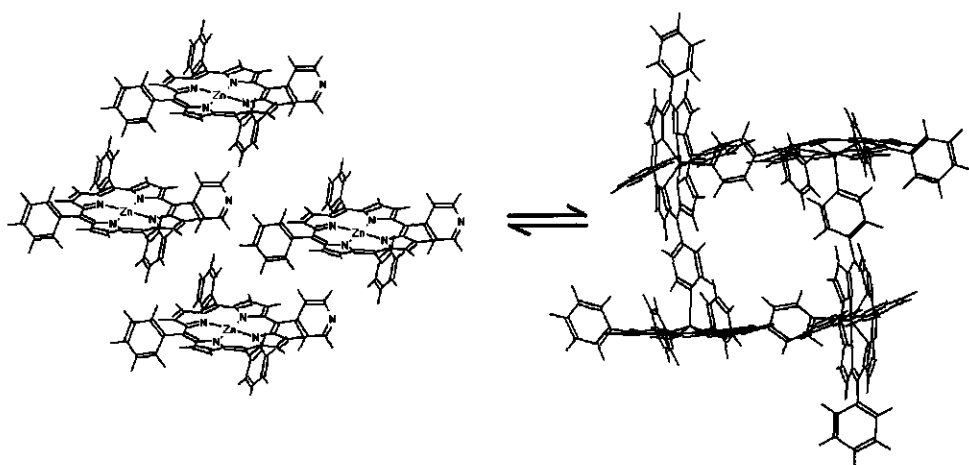
Figure 1. Self-organization of ZnM(4-Py)TrPP into the tetramer.

To understand the photophysical properties of ZnM(4-Py)TrPP tetramers, resulting from time-resolved fluorescence- and fluorescence anisotropy measurements we also investigated unsubstituted zinc tetra(*p*-phenyl)porphyrin (ZnTPP) and its pyridine-ligated analog as reference compounds under the same experimental conditions, but without forming aggregates. In view of its structure (Fig.1) the fluorescence lifetime of the cyclic tetramer should be close to that of pyridine ligated ZnTPP. Furthermore, note that energy transfer between the porphyrin units of the tetramer does not affect this lifetime since all monomer units of the tetramer are identical. Thus, energy transfer processes within the porphyrin tetramer can only be studied by investigating the fluorescence anisotropy decay.

For porphyrin monomers the time dependent fluorescence anisotropy $r(t)$ is only determined by rotational diffusion:

$$r(t) = r_M^{RD}(t)$$

(1)

where $r_M^{RD}(t)$ is the rotational diffusion anisotropy of the monomer. On the other hand, for a porphyrin complex in solution the time dependent fluorescence anisotropy $r(t)$ can be written as a product of two independent depolarization processes

$$r(t) = r^{ET}(t) \cdot r_T^{RD}(t)$$

(2)

where $r^{ET}(t)$ and $r_T^{RD}(t)$ represent energy transfer within the complex and rotational diffusion of the complex itself.

The steady state fluorescence anisotropy $r^{ET}(\infty) = \lim_{t \to \infty} r^{ET}(t) = c$ = constant and equals

0.025 for the tetramer in PS/Tol solution [see Part I]; $r_T^{RD}(t)$ in eqn. (2) represents the fluorescence anisotropy decay resulting from fully spherical rotational diffusion of the tetramer, which decays to zero in toluene solution for $t \to \infty$. Considering the size of the tetramer, for high viscosity solvents such as PS/Tol we may safely assume that the energy transfer in the tetramer is much faster than rotational diffusion. Then, for $t \to \infty$ the fluorescence anisotropy of the tetramer is given by $r(t) = c \cdot r_T^{RD}(t)$.

We applied global analysis to the TCSPC fluorescence decay components of ZnM(4-Py)TrPP in the 10°C – 55°C temperature range. The monomer and tetramer fluorescence lifetime components were associated with their corresponding anisotropies, yielding $r_M^{RD}(t)$ and $c \cdot r_T^{RD}(t)$ of the monomers and tetramers, respectively. Global analysis has also been applied to streak camera data, yielding a time constant that describes the depolarization due to energy transfer within the tetramer. By associating the fluorescence anisotropy with the spectral properties of the tetramer, its anisotropy decay $r^{ET}(t)$ could be resolved in two time domains: one with a short decay time due to energy transfer within the tetramer and a second one with a relatively long decay time due to the rotational diffusion of the tetramer. The rate constants for singlet energy transfer within the tetramer were extracted from the fluorescence anisotropy decay $r^{ET}(t)$ using Monte Carlo simulation, yielding the rate constants for energy transfer and – relaxation processes in a rather straightforward manner [11,21,21,22].

The application of the Monte Carlo method is of course not limited to porphyrin tetramers in solution as has been demonstrated for ordered, spin coated solid organic films of zinc tetra-(octylphenyl)-porphyrin (ZnTOPP) [23,24].

Experimental

Materials

ZnM(4-Py)TrPP and ZnTPP were prepared following standard procedures [25,26]. The porphyrins were chromatographically purified over silica gel (Merck) using chloroform (Merck p.a.) as the eluent. The porphyrins were estimated to be >99% pure by thin-layer chromatography, absorption- and fluorescence spectroscopy. Approximately $2 \cdot 10^{-5}$ M solutions

of ZnM(4-Py)TrPP and ZnTPP were prepared in dry toluene, viscous solutions of PS/Tol, and a toluene/10^{-4} M pyridine mixture.

Time-resolved methods

TCSPC instrumentation. The experimental set-up for TCSPC has previously been described [24,27,28]. A mode-locked continuous wave Nd:YLF laser (Coherent model Antares 76-YLF, equipped with a LBO frequency doubler (Coherent model 7900 SHGTC) and BBO frequency tripler (Coherent model 7950 THG) was used to synchronously pump a continuous wave dye laser (Coherent radiation model CR 590). As a dye Coumarin 460 (Exciton Inc.) was used for excitation at 465 nm. A set-up with electro-optic modulators in a dual pass configuration was used to reduce the pulse rate to 594 kHz [29]. The final pulse duration of the excitation pulses was ~ 4 ps FWHM and the maximum pulse energy was ~100 pJ. To obtain a dynamic instrumental response (~ 50 ps FWHM) for deconvolution purposes, the fast single exponential fluorescence decay of Erythrosin B in water was used as a reference. The presented data were collected in a multichannel analyzer (MCA board from Nuclear Data model AccuspecB, in a PC) with a time window of 4096 channels at 2.5 ps/channel. The excitation wave-length was 435 nm and the emission wavelengths were selected by a cut-off filter (Schott KV 500) and line filters of 595 and 625 nm with a 16 nm band width.

The TCSPC method has been applied to ZnTPP in toluene, toluene/pyridine, and PS/Tol, and to ZnM(4-Py)TrPP in toluene and PS/Tol. The sample temperature was adjusted to 10, 15, 25 and 55°C, using a cold nitrogen gas flow from an Oxford ITC4 temperature controller.

Streak camera detection. The experimental set-up for streak camera detection has been previously described [30]. Solutions of ZnM(4-Py)TrPP in toluene were contained in a 1 cm path length glass cuvette, and were thermostated either at 10 or 55 °C. The sample was refreshed using a small magnetic stirrer. The sample was excited with 100 fs pulses at 565 nm (10 °C, relatively selective for tetramers) or 550 nm (55 °C, relatively selective for monomers), which were generated at a 125 kHz repetition rate using a Titanium: sapphire based oscillator (Coherent, MIRA), a regenerative amplifier (Coherent, REGA) and a double pass optical parametric amplifier (Coherent, OPA-9400). The pulse energy was typically 25 nJ. The polarization of the exciting light was alternated between horizontal and vertical. The vertically and horizontally polarized fluorescence components were detected using a Hamamatsu C5680 synchroscan streak camera equipped with a Chromex 250IS spectrograph. The instrument response function (IRF) was Gaussian shaped with a FWHM width of ≈ 3.5 ps. The spectral

resolution was 8 nm. One streak image measured 315 nm in the spectral domain (1018 pixels) and 200 ps or 2.2 ns (1000 pixels) in the time-domain.

Time-resolved Decay Analysis

TCSPC. The experimental time-resolved fluorescence- as well as the anisotropy decay results from the convolution of the instrumental and sample response functions. The fluorescence- and anisotropy decays $I(t)$ and $r(t)$ were fitted to a sum of exponentials

$$I(t) = \sum_{i=1}^{N} p_i \exp(-t/\tau_i)$$

(3)

$$r(t) = \sum_{i=1}^{M} \beta_i \exp(-t/\phi_i)$$

(4)

by the iterative nonlinear least squares method using the Marquardt algorithm [31]; p_i and τ_i are the amplitude and lifetime of the i-th fluorescence component, respectively; β_i and ϕ_i are the amplitude and the rotational correlation time of the i-th exponential of the fluorescence anisotropy component, and $\beta_0 = \sum_{i=1}^{M} \beta_i$ is the initial fluorescence anisotropy; N and M are the numbers of the fluorescence and anisotropy exponentials.

The abovementioned parameters were obtained by global analysis [32] of the fluorescence decay measured over a 10°C - 55°C temperature range and detection at 597 nm and 625 nm, simultaneously fitting the fluorescence decays at different temperatures as well as wavelengths. The parameters of the anisotropy decays were retrieved using a non-associative as well as an associative model for the time-resolved fluorescence anisotropy.

For the non-associative model the $I_{\parallel}(t)$ and $I_{\perp}(t)$ intensity components take the form

$$I_{\parallel}(t) = I(t)[1 + 2r(t)]$$

(5)

$$I_{\perp}(t) = I(t)[1 - r(t)]$$

(6)

where $I(t)$ and $r(t)$ are given by eqns. (3) and (4), respectively. For the associative model applied to the anisotropy decay, the fluorescence intensities $I_{\parallel}(t)$ and $I_{\perp}(t)$ contributing to the anisotropy can be written as

$$I_{\parallel}(t) = \sum_{i=1}^{N} A_i \exp(-t/\tau_i)[1 + 2\sum_{j=1}^{M_i} \beta_{ij} \exp(-t/\phi_{ij})]$$

$$(7)$$

$$I_{\perp}(t) = \sum_{i=1}^{N} A_i \exp(-t/\tau_i)[1 - \sum_{j=1}^{M_i} \beta_{ij} \exp(-t/\phi_{ij})]$$

$$(8)$$

where M_i is the number of anisotropy exponentials contributed by the i-th fluorescence component, and ϕ_{ij} is the rotational correlation time of the j-th exponential of the fluorescence anisotropy contributed by the i-th fluorescence component. The total initial anisotropy is $\beta_0 = \sum_{i=1}^{N} \beta_{0i}$, with $\beta_{0i} = \sum_{j=1}^{M_i} \beta_{ij}$ the initial anisotropy of the i-th fluorescence component. The total time-dependent anisotropy can then be written as

$$r(t) = \frac{\sum_{i=1}^{N}\sum_{j=1}^{M_i} p_i \beta_{ij} \exp(-t/\tau_i) \exp(-t/\phi_{ij})}{\sum_{i=1}^{N} p_i \exp(-t/\tau_i)}$$

$$(9)$$

Global analysis was applied to the TCSPC data using Fluorescence Data Processor Software [33]. The accuracy of the fluorescence and anisotropy decay parameters from this analysis was estimated by the exhaustive search method [32]. The quality of the fit was judged by the χ^2 statistical criterion and by visual inspection of the time-dependent weighted residuals and their autocorrelation functions [34].

Streak camera. The data were globally analyzed using an associative model with two components decaying independently, each possessing its own anisotropy [35] Thus, the data for parallel and perpendicular detection are described by:

$$I_{\parallel}(t) = \sum_{l=1}^{2} \varepsilon_l(\lambda)(1 + 2\beta_{0l} \exp(-t/\phi_l)) \exp(-t/\tau_l) \otimes IRF(t)$$

$$(10)$$

$$I_{\perp}(t) = \sum_{l=1}^{2} \varepsilon_l(\lambda)(1 - \beta_{0l} \exp(-t/\phi_l)) \exp(-t/\tau_l) \otimes IRF(t)$$

$$(11)$$

where ε_l, β_{0l}, ϕ_l and τ_l represent the species associated spectra, the initial anisotropy, the anisotropy decay time constant and the fluorescence lifetime of component l, respectively; $\otimes$ indicates the convolution with a Gaussian shaped instrument response function $IRF(t)$.

Results

TCSPC measurements

Monomers. For ZnTPP a single fluorescence lifetime of 1.95 ns in toluene and 2.05 ns in PS/Tol was found. The best fit of the anisotropy decay of ZnTPP is found with a single exponential with ϕ_1 = 70 ps/90 ps at 55°C/10°C for toluene as a solvent; for PS/Tol as a solvent there are two exponentials at 55°C with ϕ_1 = 1.44 ns, ϕ_2 = 16.00 ns and a single exponential at 10°C with ϕ_1 = 21.00 ns. The initial fluorescence anisotropy of ZnTPP monomers (which do not aggregate in the temperature and concentration range of our experiments) is ∼ 0.07 in toluene and ∼ 0.1 in PS/Tol. The fits of the anisotropy decays of ZnTPP in toluene and PS/Tol at 10 and 55°C are shown in Figs. 3A and 3C. The lifetime τ, the initial anisotropies β_1 and β_2, and the rotational correlation times ϕ_1 and ϕ_2 for the ZnTPP monomers in toluene and PS/Tol are collected in Table 1.

Table 1. Fluorescence and anisotropy decay parameters of zinc porphyrin monomers in toluene (Tol) and PS/Tol solvents at different temperatures using eqns. (1) - (4).

Sample / λ_{det}	τ, ns	Temperature, 55°C				Temperature, 10°C	
		β_1	ϕ_1, ns	β_2	ϕ_2, ns	β_1	ϕ_1, ns
ZnTPP/Tol 597 nm	1.95 [1.94;1.97]	0.070 [0.068;0.072]	0.07 [0.06;0.09]	---	---	0.073 [0.071;0.078]	0.09 [0.08;0.11]
ZnTPP/Tol with Pyridine 625 nm	1.58 [1.55;1.62]	0.068 [0.067;0.071]	0.07 [0.06;0.08]	---	—	0.075 [0.073;0.079]	0.09 [0.08;0.10]
ZnTPP/PS/Tol 597 nm	2.05 [2.04;2.07]	0.072 [0.071;0.073]	1.44 [1.38;1.52]	0.022 [0.021;0.023]	16.00 [14.00;~]	0.101 [0.094;0.108]	21.00 [20.00;~]
ZnTPP/PS/Tol with Pyridine 625 nm	1.61 [1.60;1.62]	0.076 [0.075;0.077]	1.62 [1.46;1.74]	0.024 [0.023;0.025]	17.00 [16.00;~]	0.098 [0.092;0.105]	24.00 [22.00;~]

The confidence intervals of the parameters, shown in square brackets, are estimated at the 95% level.
The marker "~" indicates undefined upper values of the anisotropy decay parameters.
The marker "---" indicates the absence of a calculated parameter.

Ligated monomers. The same analysis of ZnTPP in the presence of excess pyridine as a ligand yielded a lifetime of 1.58 ns in toluene and 1.61 ns in PS/Tol. A fit of the anisotropy decay of ZnTPP/pyridine shows a single exponential with ϕ_1 = 70 ps /90 ps at 55°C/10°C in toluene as a

solvent and with two exponentials at 55°C with $\phi_1 = 1.62$ ns, $\phi_2 = 17.00$ ns; a single exponential was found at 10°C with $\phi_1 = 24.00$ ns in PS/Tol as a solvent. As expected, the initial anisotropy value of ZnTPP/pyridine is temperature-independent, and equals ~ 0.07 in toluene and ~ 0.1 in PS/Tol. The lifetime τ, the initial anisotropy values β_1 and β_2, and the rotational correlation times ϕ_1 and ϕ_2 for ZnTPP/pyridine in toluene and PS/Tol are collected in Table 1.

Tetramers. Assuming that the lifetime of the lowest singlet excited state of both ligated and non-ligated ZnM(4-Py)TrPP is independent of temperature in the 10°C - 55°C range, the fluorescence decay parameters of the mixture of monomers and tetramers were determined by global analysis. Two fluorescence exponentials were found to nicely fit to all temperature-dependent ZnM(4-Py)TrPP experimental decay curves. A fit to a single exponential gave less satisfactory results and fitting with more than two exponentials did not lead to significant improvement either.
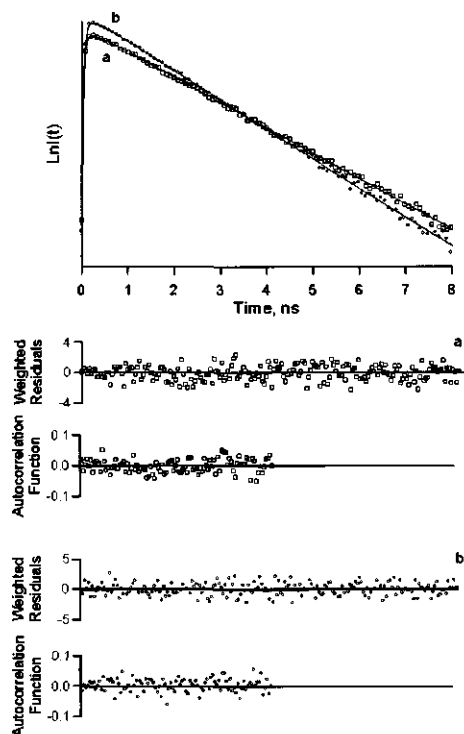

Figure 2. Experimental total fluorescence decays measured at 55°C (a, □) and 10°C (b, ○), and fitted (solid lines) curves for ZnM(4-Py)TrPP; $\lambda_{exc} = 435$ nm and $\lambda_{det} = 625$ nm.

The two global fluorescence components of ZnM(4-Py)TrPP in toluene have 1.97 ns and 1.53 ns lifetimes, and 2.22 ns and 1.56 ns for PS/Tol as a solvent. In toluene and PS/Tol the relative contribution of the 1.53 - 1.56 ns fluorescence component to the total fluorescence reaches 90% and 84% at 10°C and 39% and 48% at 55°C, respectively. Fig.2 shows two experimental fluorescence decays detected at 625 nm at 10°C and 55°C, and the result of the global analysis using two exponentials. The ZnM(4-Py)TrPP anisotropy associated with the different fluorescence components measured at 10°C could be appropriately analyzed using single exponentials with rotational correlation times $\phi_{11} = 100$ ps/26.00 ns and $\phi_{21} = 1.00/90.00$ ns in toluene and PS/Tol for the 1.97 - 2.22 ns and 1.53 - 1.56 ns lifetime components, respectively.
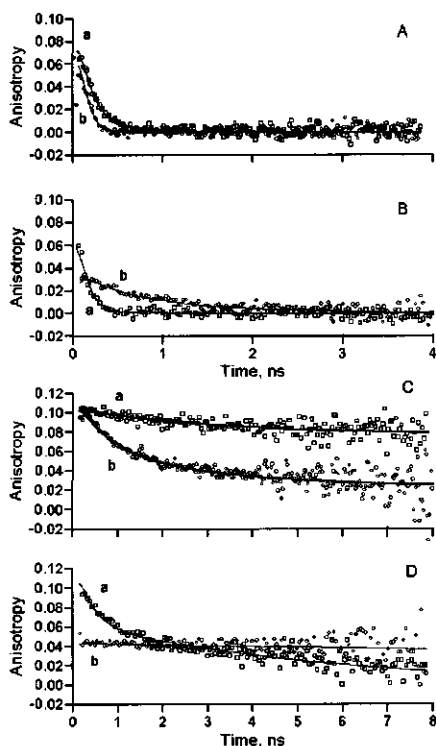
Table 2. Fluorescence- and fluorescence anisotropy decay parameters of ZnM(4-Py)TrPP in toluene (Tol) and PS/Tol solvents at different temperatures. Fluorescence decay parameters have been obtained using global analysis approach. The anisotropy decay parameters have been retrieved non-associatively (eqns. (3), (4)) at 55°C and associatively (eqns. (5), (6)) at 10° C. The relative contributions p_i', i = 1,2, to the total fluorescence introduced by different fluorescence components are calculated using equation $p_i' = \dfrac{p_i\tau_i}{p_1\tau_1 + p_2\tau_2}$, i = 1, 2. The standard deviations of the p_i' values do not exceed 5% of their values.

Sample / λ_det	τ1, ns	τ2, ns	Temperature, 55°C						Temperature, 10°C					
			p'1,%	p'2,%	β1	φ1, ns	β2	φ2, ns	p'1,%	β11	φ11, ns	p'2,%	β21	φ21, ns
ZnM(4-Py)TrPP in Tol 625 nm	**1.97** [1.93;2.03]	**1.53** [1.50;1.56]	61	39	0.067 [0.065;0.070]	**0.08** [0.06;0.09]	—	—	7	0.075 [0.071;0.082]	**0.10** [0.09;0.12]	93	0.020 [0.010;0.030]	**1.00** [0.95;1.42]
ZnM(4-Py)TrPP in PS/Tol 625 nm	**2.22** [2.05;2.37]	**1.56** [1.48;1.61]	48	52	0.076 [0.075;0.077]	**1.05** [0.97;1.48]	0.025 [0.025;0.026]	**21.00** [18.00;~]	16	0.100 [0.090;0.110]	**26.00** [24.00;~]	84	0.025 [0.023;0.025]	**90.00** [80.00;~]

The confidence intervals of the parameters, shown in square brackets, are estimated at the 95% level.
The marker "~" indicates undefined upper values of the anisotropy decay parameters.
The marker "—" indicates the absence of a calculated parameter.

Figure 3. Experimental ($\square$,$\circ$) and fitted (solid) curves of (A, C): ZnTPP and (B, D): ZnM(4-Py)TrPP fluorescence anisotropy in toluene (A, B) and PS/Tol (C, D) detected at 55°C (a, $\square$) and 10°C (b, $\circ$); λ_{exc} = 435 nm; λ_{det} = 595 nm and λ_{det} = 625 nm.

The ZnM(4-Py)TrPP anisotropy decay at 55°C was analyzed using an associative as well as a non-associative model, of which only the latter gave reliable results, yielding a single exponential (ϕ_1 = 80 ps) in toluene and two exponentials (ϕ_1 = 1.05 ns and ϕ_2 = 21.00 ns) in PS/Tol. The initial anisotropy value of the 1.97 - 2.22 ns fluorescence component is 0.076 and 0.1 in toluene and PS/Tol, respectively, whereas the initial anisotropy value of the 1.53 - 1.56 ns fluorescence component was considerably lower, i.e. 0.020 and 0.025 in toluene and PS/Tol, respectively. The results of the fits of the anisotropy decay of the ZnM(4-Py)TrPP in toluene and PS/Tol at 10 and 55°C are shown in Figs. 3B and 3D. The results of the fluorescence global analysis with associative as well as non-associative anisotropy for ZnM(4-Py)TrPP in toluene and PS/Tol are presented in Table 2.
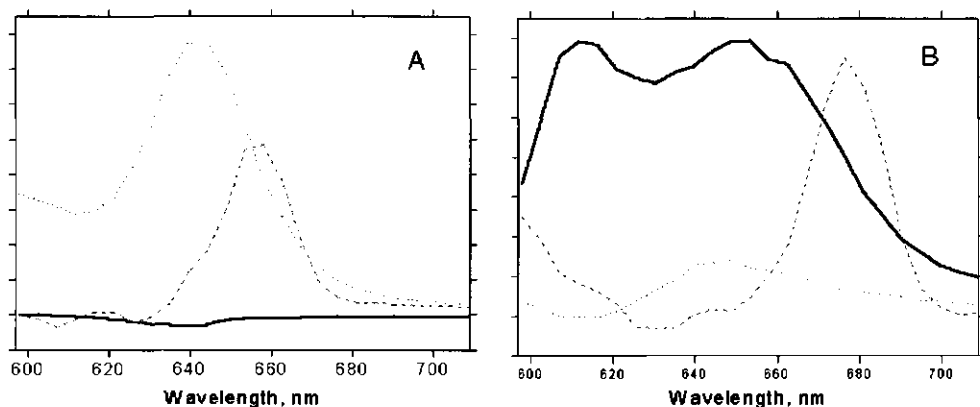
Streak camera measurements

Using the streak camera faster kinetics of the tetramer is accessible than with the TCSPC method, including energy transfer within the tetramer. Since the streak camera measures the time evolution of the whole fluorescence spectrum rather than at single wavelengths, the monomer and tetramer spectra associated with different fluorescence- and fluorescence anisotropy lifetimes could be resolved. These species-associated fluorescence spectra for ZnM(4-Py)TrPP in toluene at 10°C and 55°C are shown in Fig. 4.

Monomers. Fig. 4A shows the results of the measurements at 55°C. The dominating contribution has a spectrum (dotted curve) which peaks at 642 nm. The fluorescence lifetime of this

Figure 4. Species associated spectra resulting from the global analysis of the polarized streakcamera datasets applying an associative model (see text). A) Temperature 55 °C, excitation wavelength 550 nm. Solid line: component of unclear origin with 83 ps isotropic lifetime; dotted line: monomers, with a 1.9 ns fluorescence lifetime and a 67 ps (amplitude 0.08) fluorescence anisotropy lifetime; dashed line: IRF-limited contribution representing Raman scattering by the solvent. B) Temperature 10 °C, excitation wavelength 565 nm. Solid line: tetramers, with a 1.6 ns fluorescence lifetime and a 31 ps (amplitude 0.07) fluorescence anisotropy lifetime; dotted line: monomers, with a 2.1 ns fluorescence lifetime and a 0.61 ns (amplitude 0.13) fluorescence anisotropy lifetime; dashed line: IRF-limited contribution representing Raman scattering by the solvent.

component is 1.9 ± 0.2 ns, whereas the rotational correlation time is 67 ± 7 ps. These combined data are a clear indication that this component represents the monomers. A small ~ 83 ps rising component (solid curve) was also necessary to obtain a good fit of the data, the nature of which is presently unknown.

The monomer species, corresponding to the spectrum in Fig 4B, detected at 10°C (dotted curve) with a peak around 645 nm, has a fluorescence lifetime of 2.1 ± 0.2 ns and a rotational correlation time of 0.61 ± 0.06 ns, with an amplitude of 0.13 ± 0.01. The dashed component in Figs. 4A and -B, which peaks at 656 and 677 nm, respectively, represents a pulse-limited contribution, assigned to a Raman scattering line of toluene 2900 cm^{-1} red shifted with respect to the excitation wavelength.

Tetramers. Fig. 4B shows the species-associated spectra for ZnM(4-Py)TrPP in toluene at 10°C, at which temperature monomers and tetramers co-exist. To record intramolecular energy transfer in the tetramers 565 nm was used for excitation, which is relatively selective for this species. The solid line in Fig. 4B represents a spectrum with maxima around 612 nm and 652 nm of a species with a 1.6 ± 0.2 ns fluorescence lifetime and a ~ 31 ps rotational correlation time with a 0.07 ± 0.01 relative amplitude. The fluorescence spectrum and -lifetime of this species were basically identical to those found in the TCSPC measurements, indicating that this species is the tetramer.

We therefore conclude that the 31 ps anisotropy decay reflects energy transfer within the tetramer. The relative amplitude of this decay component agrees with the expected initial anisotropy of 0.1. The small contribution with ~ 0.02 relative amplitude of the anisotropy decay in the nanosecond region due to rotational diffusion, that was observed in the TCSPC measurements, was not resolved by the streak-camera measurements.

Discussion

TCSPC results

ZnTPP monomers. The 1.95 - 2.05 ns lifetimes for monomeric, non-ligated ZnTPP collected in Table 1 are in good agreement with literature [36,37,38,39]. The slight increase of the lifetime in PS/Tol as compared to that in toluene is considered to be a medium effect. The fluorescence anisotropy decay r(t) of ZnTPP in toluene is a single exponential (Table 1), in agreement with published results [36,40,41,42]. However, the fluorescence anisotropy r(t) of ZnTPP monomers in PS/Tol cannot be fitted to a single exponential at 55°C. In viscous solutions the fluorescence anisotropy r(t) of a planar molecule such as the ZnTPP monomer is given by [36]

$$r(t) = \beta_0 \, [0.25 \cdot \exp(-6 \cdot D_\perp \cdot t) + 0.75 \cdot \exp(-(2 \cdot D_\parallel + 4 \cdot D_\perp) \cdot t)]$$

$$(12)$$

where $D_\parallel$ and $D_\perp$ are the in-plane and out-of-plane rotational diffusion coefficients. Eqn. (12) is a double exponential and fits the experimental data of ZnTPP in PS/Tol at 55°C very well. The best fitted parameters collected in Table 1 show that the pre-exponential factors β_1 and β_2 are close to those in eqn. (12). The upper limits of the 95% confidence intervals of the rotational correlation times corresponding to the largest β_2 value cannot be determined with sufficient accuracy because in viscous solution the correlation times are longer than the 8 ns experimental time window. The ZnTPP anisotropy decay measured in PS/Tol solution at 10°C can be approximated by a single exponential. The second slower anisotropy component is not found at 10°C presumably again due to the 8 ns experimental time window and the slowing down of the rotation at this temperature. The initial anisotropy value β_0 for the ZnTPP in PS/Tol is ~ 0.1 in good agreement with both the predicted values [43,44] and published data [7,45]. We found a somewhat lower value of 0.07 - 0.08 for β_0 for the porphyrin monomers in the non-viscous solvent toluene, resulting from the relatively fast rotational diffusion with a 80 - 100 ps correlation time in this solvent.

Ligated ZnTPP monomers. Ligation of ZnTPP to pyridine results in shortening of the fluorescence lifetime to 1.58 - 1.61 ns in both solvents. The slight increase of the lifetime in PS/Tol as compared to that in toluene is again ascribed to a medium effect. Ligation of ZnTPP with pyridine does not significantly change the anisotropy decay parameters (Table 1), so that the previous discussion of the results for non-ligated ZnTPP also applies to its ligated analog.

ZnM(4-Py)TrPP monomers and tetramers. Following the previous analysis of the monomer fluorescence- and fluorescence anisotropy decay of ZnTPP monomers in toluene and PS/Tol, we now apply the same method to the porphyrin tetramer. Note that the anisotropy decays in both solvents are expected to be affected by the energy transfer processes within the tetramer, and thus by the porphyrin aggregate structure.

Using global analysis to retrieve the ZnM(4-Py)TrPP fluorescence components, we attribute the 1.97 - 2.22 ns lifetime to the non-ligated monomers in view of the results for ZnTPP in Table 1. The 1.53 - 1.56 ns fluorescence lifetime is close to the 95% confidence interval of the lifetime of pyridine-ligated ZnTPP, and thus likely corresponds to the ligated ZnM(4-Py)TrPP unit in the tetramer. Similarly, the increase of the relative contribution of the 1.53 - 156 ns fluorescence component to 84% and 93% in toluene and PS/Tol, respectively, by lowering the temperature to 10°C can be explained by the temperature-dependent intramolecular ligation of the porphyrin units resulting in formation of a cyclic tetramer as shown in Fig. 1 (*cf.* paper I). At 55°C ligated porphyrins in toluene and PS/Tol still contribute 39% and 52%, respectively, to the total fluorescence. This relatively large contribution, even at 55°C, results from the fact that the excitation was around 435 nm, closest to the Soret band maximum of the ligated species at 430 nm, whereas the fluorescence was detected at 625 nm, again corresponding to the ligated species. The different fractions of the ligated species at 10°C and 55°C in toluene and PS/Tol, respectively, are caused by the lower solubility of porphyrins in Ps/Tol than in toluene.

The ZnM(4-Py)TrPP rotational correlation time $\phi_{11} = 100$ ps in toluene at 10°C associated with the 1.97 ns lifetime is of the same order as that of ZnTPP under the same experimental conditions and therefore is assumed to reflect the monomer anisotropy. The anisotropy associated with the 1.53 ns lifetime is also a single exponential in toluene at 10°C but now with a long $\phi_{21} = 1.00$ ns rotational correlation time, which is characteristic for rotation of the aggregate, assuming that the energy transfer is much faster then rotational diffusion (*cf.* eqns. (3) and (4)). From the associative analysis of the anisotropy decay of ZnM(4-Py)TrPP in toluene at 10°C we conclude that ϕ_{21}, associated with the 1.53 ns fluorescence component, is about ten

times longer than ϕ_{11} of the monomer at the same temperature (Table 1). Describing the rotational dynamics of porphyrin monomers and -tetramers in toluene by single ϕ_{11} and ϕ_{21} values and approximating the tetramer as a sphere, its effective rotational radius ρ_{Tetr} can be related to that of the monomer ρ_M as follows from the Stokes-Einstein-Debye-Perrin relation [46]:

$$\rho_{Tetr} = (\phi_{11}/\phi_{21})^{-1/3} \cdot \rho_M$$

(13)

The radius of the solvent cavity in which the tetramer rotates is calculated to be almost twice that of the porphyrin monomer and quite close to the radius calculated from the tetramer vacuum structure using the Chem-X program [47]. Although this finding may not be considered as unambiguous evidence for a tetrameric aggregate, it certainly points to a cyclic, closed structure. The same conclusions as for ZnM(4-Py)TrPP in toluene apply to the PS/Tol solution, i.e. that (i) the anisotropy decay parameters of ZnM(4-Py)TrPP associated with the 2.22 fluorescence component closely agree with those for ZnTPP; (ii) the rotational correlation time associated with the 1.56 fluorescence component is longer than that for ZnTPP monomers; (iii) the rotational correlation time of the tetramer in PS/Tol solution is less accurate than in toluene as a result of the 8 ns experimental time window. The ZnM(4-Py)TrPP anisotropy at 55°C analyzed with a non-associative model reflects almost the same anisotropy parameters as for the ZnTPP monomers in both solvents (cf. Tables 1 and 2).

The initial β_{11} anisotropy value of the ZnM(4-Py)TrPP monomer in PS/Tol at 10°C, associated with the 1.97 - 2.22 ns fluorescence component is ~ 0.075 - 0.100 in both solvents, in good agreement with the ZnTPP monomer values (cf Tables 1, 2 and Fig. 3). The β_{21} value of 0.025, associated with the 1.53 - 1.56 ns fluorescence component at 10°C, is approximately four times smaller than for the porphyrin monomer in toluene and PS/Tol (cf Tables 1,2 and Fig. 3). From this finding we may conclude that fast internal energy transfer occurs between the porphyrin units within the tetramer, resulting in effective fluorescence depolarization. This is also noticeable for toluene as a solvent but less accurate than for PS/Tol, since rotational motion may also affect the anisotropy decay. Taking into account that energy transfer processes are at least one order faster than the 1.58 ns lifetime and its associated rotational correlation time, then the observed initial anisotropy β_{21} is expected to reflect the relative orientations of the porphyrin molecules in the aggregate. Following Fig. 6 of Part I the theoretical value for β_{21} is calculated

to be 0.025, in very good accordance with the experimental results (Table 2) and the steady state anisotropy (Part I, Fig. 4B).

Streak camera results

Having collected the tetramer fluorescence- and anisotropy data in an 8 ns time window using the TCSPC method, subsequently a streak camera with a higher time resolution was used. The time-resolved fluorescence- and anisotropy decays for $2.2 \cdot 10^{-5}$ M ZnM(4-Py)TrPP in toluene were analyzed in a 200 ps time window at the same temperature as in the TCSPC measurements.

Zn(4-Py)TrPP monomers and tetramers. Just as with the TCSPC method, lifetimes of 1.6 and 1.95 - 2.10 ns were found for the Zn(4-Py)TrPP tetramer and the monomer by applying the global analysis to the fluorescence decays. The 67 ps rotational correlation time associated with the monomer spectrum at 55°C agrees with that previously observed for the monomers using the TCSPC method. At 10°C a 0.61 ns rotational correlation time is found, definitely higher than the 100 ps value from TCSPC measurement. This long anisotropy component is most likely resulting from a less accurate resolution of the associated long rotational correlation times. Taking into account that at 10°C the tetramer concentration is much higher than that of the monomers and noting the relation $\beta^{Mon}\phi_{rot}^{Mon} \approx \beta^{Tetr}\phi_{rot}^{Tetr}$ for the anisotropy parameters, the 0.61 ns correlation time actually constitutes the mean value of the monomer and tetramer rotational correlation times weighted with their relative contributions, basically in agreement with the results of TCSPC data analysis. The 31 ps component, that only could be observed at the higher time resolution of the streak camera, obviously must be assigned to energy transfer within the tetramer.

Following this critical evaluation of the various TCSPC- and streak camera results, now the rate constants for energy transfer processes within the tetramer can be quantitatively determined. This is done by analyzing the experimental time-resolved fluorescence anisotropy decay detected at 612 nm making use of Monte Carlo simulations and adopting a hopping model for energy transfer within the tetramer.

Monte Carlo simulations

The Monte Carlo algorithm for generating the fluorescence- as well as the anisotropy decay closely follows previously developed procedures [22,48]. Fig. 5 schematically presents the basic principles for collecting the parallel and perpendicularly polarized components of the porphyrin
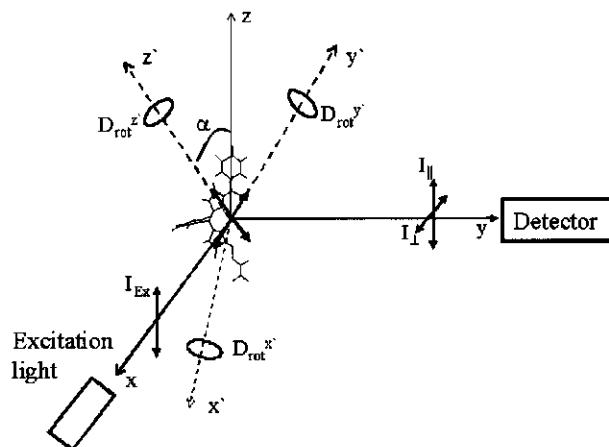
Figure 5. Schematic diagram for the measurement and simulation of parallel and perpendicular fluorescence components. The molecular coordinate system (x`,y`,z`) has a random orientation with respect to the laboratory system (x,y,z).

monomer fluorescence. It is important to note that this monomer scheme can be extended to that for the tetramer by assuming four connected porphyrin monomers fixed in a molecular coordinate system attached to one of the monomers in the aggregate. The contributions of the tetramer to the fluorescence intensities $I_∥$ and $I_⊥$ are given by [48]

$$P_{I_∥} \sim \cos^2 \alpha$$

(14)

$$P_{I_⊥} \sim 0.5\sin^2 \alpha$$

(15)

where $P_{I_∥}$ and $P_{I_⊥}$ denote the probabilities of the $I_∥$ and $I_⊥$ fluorescence components; α is the angle between the emission transition moment and the detecting polarizer which is oriented parallel to the polarization of the excitation light. Eqns. (14) and (15) correspond to detection with the polarizer oriented at 0° and 90° w.r.t the polarization of the excitation light. The angle α is determined by the geometry of the tetramer by the rotational diffusion coefficients $D_{rot}^{x'}$, $D_{rot}^{y'}$, $D_{rot}^{z'}$ and the energy transfer rate constants. For the monomer porphyrin $D_{rot}^{x'} = D_{rot}^{y'} = D_⊥$, and $D_{rot}^{z'} = D_∥$ for rotational diffusion around the x`, y`, z` molecular coordinate axes.

The simulation of the energy transfer processes in the tetramer is based on random hopping of the excitation energy. Starting from an initially excited molecule, the excitation visits the porphyrin monomer units in the tetramer until the event of emission. The time spent by the

hopping excitation from the moment of initial excitation till emission is considered as one run in the simulation procedure.
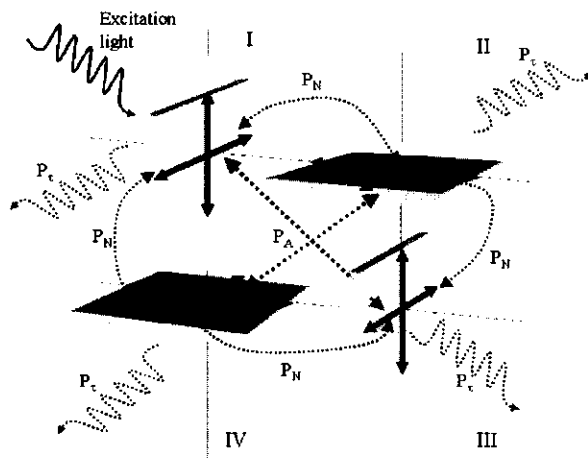
Figure 6. Schematic illustration for the kinetic processes within the arrangement of the porphyrins (grey squares) and their transition moments (bold arrows).

The schematic diagram of excitation hopping in the tetramer is shown in Fig. 6. To simplify the discussion we number the molecules in the tetramer by I, II, II, and IV. Then all possible molecular pairs which are the sites for excitation hops are labeled as ij, with $i \neq j$ = I, II, III, IV. The probabilities for clockwise and anti-clockwise excitation hopping are assumed to be equal, i.e. $P_{ij} = P_{ji}$. The probabilities for excitation hopping between neighboring units are denoted P_N = P_{I-II} = P_{II-III} = P_{II-IV} = P_{IV-I}, and between units at opposite sides of the tetramer P_A = P_{I-III} = P_{II-IV}. With P_τ the probability for fluorescence emission, P_N, P_A, P_τ are related by $P_N + P_A + P_\tau = 1$. The Monte Carlo random walk starts by generating an initial orientation of the tetramer, in particular an orientation of the initially excited molecule i with its coordinate system $(x`,y`,z`)_i$ [48] in the laboratory coordinate system (x,y,z). Next, excitation hopping is simulated using a random numbers generator and introducing starting values for the probabilities P_N, P_A, P_τ [22]. The procedure is repeated until the event of fluorescence emission. At the last step of the simulation run the total time Δt elapsed after a number of energy transfer hops following one excitation is stored either as the "parallel" or the "perpendicular" component using eqns. (14) and (15) [48], yielding two histograms, which are the source for the simulated anisotropy decay using

138

$$r(t) = \frac{I_{\parallel}(t) - I_{\perp}(t)}{I_{\parallel}(t) + 2I_{\perp}(t)}$$

(16)

Finally we note that the probabilities P_N, P_A, P_τ are inversely proportional to the corresponding energy transfer hopping times τ^{ET}_N, τ^{ET}_A, and the tetramer fluorescence lifetime τ^{tetr}, respectively. We simulated 10^7 excitation runs, which ensured a combination of an acceptable signal to noise ratio, stable values of χ^2, and a reasonably short simulation time. Isolated monomer porphyrins were excluded from the simulations, since associative anisotropy analysis showed a negligible contribution of the monomers to the total emission under the experimental conditions (10°C, λ_{exc} = 565 nm; λ_{det} = 612 nm). Energy transfer between the tetramers and singlet-singlet annihilation are also not considered because of the low molar porphyrin concentration and excitation rates. Since the analysis is limited to a 200 ps time window rotational diffusion of the tetramers need not be considered since both τ^{ET}_N and presumably $\tau^{ET}_A \ll \phi_{tetr} \approx 1$ ns (Table 2).

The lifetimes τ^{ET}_N, τ^{ET}_A, and τ^{Tetr} were used to fit the simulated anisotropy decay to the experimental decay curve, employing a published fitting algorithm [49,50]. The 95% confidence intervals of the simulated decay parameters were estimated using the method of asymptotic standard errors [34].
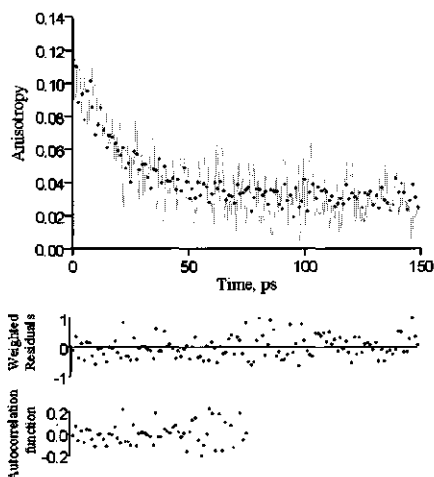
Figure 7. Examples of simulation-based fit (●) of the tetramer fluorescence anisotropy decay (—); λ_{exc}= 465 nm, λ_{det}= 612 nm; $D_{\parallel}$ = $D_{\perp}$ = 0.

As shown in Fig. 7 the experimental tetramer anisotropy decay at 612 nm could be nicely fitted with the following set of parameters: τ^{ET}_N = 26 ± 4 ps, τ^{ET}_A = 190 ps, implying that the rate constant for energy transfer across the tetramer is bounded as $0 \leq k^{ET}_A \leq (180$ ps$)^{-1}$, and τ^{tetr} = 1.5 ± 0.1 ns. Note, however, that the value of (190 ps)$^{-1}$ for the $(\tau^{ET}_A)^{-1}$ rate constant may have an uncertainty due to cross-correlation with the rotational correlation time ϕ_{tetr} of the tetramer. As expected, the rate constant for energy transfer between neighboring porphyrins is found to be much

larger than across the tetramer, explaining the fast depolarization in the initial part of the anisotropy decay.

As an additional test of the simulations we calculate the anisotropy of a non-rotating tetramer in the 8 ns time window, implying $D_\parallel = D_\perp = 0$. The Monte Carlo simulations of experiments under these conditions result in an initial anisotropy value of 0.025, in close agreement with the experimental initial anisotropy β_{21} (Table 1).

If all four porphyrin planes in the tetramer are indeed perpendicular, as shown in Fig.1, then there is no overlap between the π-orbitals of any two porphyrin monomers, and consequently no energy transfer by the exchange mechanism. Then the rate constants for energy transfer coming out of the Monte Carlo simulations should agree with those calculated with a Förster type of energy transfer [51]. Using a point dipole model the energy transfer rate constant k_{ET} follows from

$$k_{ET} = \kappa^2 \cdot k_{rad} \cdot (R_0/R)^6$$

(17)

with

$$R_0^6 = 9 \cdot 10^{-25} \cdot Q \cdot n^{-4} \cdot J$$

(18)

where κ is the orientation factor, k_{rad} is the rate constant for radiative decay of the energy donor, R_0 is the critical transfer distance (Förster radius), R is the center-to-center distance between energy donor and - acceptor, Q is the absolute excitation yield of the unquenched energy donor, n is the solvent refractive index, and J is the overlap integral of the donor fluorescence spectrum with the acceptor absorption spectrum. Using the absorption - and emission spectra of ZnM(4-Py)TrPP at 10°C, the overlap integral was calculated to be $\sim 8.5 \cdot 10^{-15}$ $M^{-1}cm^{-1}$. With $Q = 0.04$ [52], and $n_{toluene} = 1.49$ [53] in eqn. (18) it follows that $R_0 \approx 19$ Å. The center-to-center distances R between neighbor and next nearest neighbor molecules in the tetramer were determined from a molecular model to be 10 Å and 14 Å. Substituting these data in eqn. (17) and using $\kappa = 1$ for parallel transition moments and $\kappa = 0.5$ for those across the tetramer (Fig. 8), the Förster rate constants k_{ET} are calculated to be $\sim (32 \text{ ps})^{-1}$ and $\sim (190 \text{ ps})^{-1}$ for energy transfer between molecules I-II/I-IV and I-III, respectively. Note that the $(190 \text{ ps})^{-1}$ rate constant is the result of

the sum of two rate constants $(240 \text{ ps})^{-1}$ and $(960 \text{ ps})^{-1}$ calculated with orientation factors $\kappa = 1$ and $\kappa = 0.5$, respectively (Fig. 8) for the transition moments of molecules I and III.
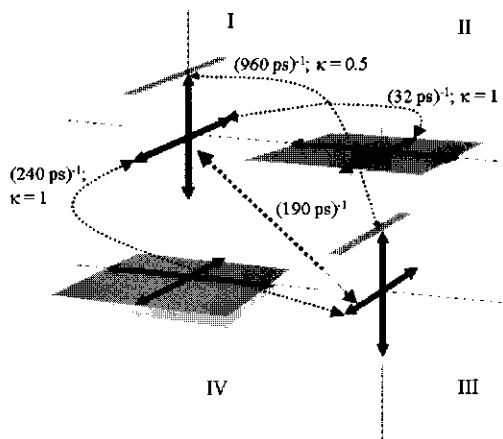

Figure 8. Energy transfer pathways in the porphyrin tetramer and the corresponding rate constants calculated using eqns. (15) and (16).

The $\sim (32 \text{ ps})^{-1}$ rate constant is close to that of the Monte Carlo simulations, whereas the $(190 \text{ ps})^{-1}$ calculated using eqn. (17), equals the abovementioned simulated upper limit (*cf.* Fig. 8). The total rate constant for energy transfer from a particular excited porphyrin in the tetramer to any of the other porphyrins, is calculated to be $(23 \pm 3 \text{ ps})^{-1}$ using the Monte Carlo simulations. This result is in fair agreement with the averaged $(31 \text{ ps})^{-1}$ rate constant, which we already calculated by global fitting of the experimental anisotropy decays at $10°C$.

The porphyrin units in the tetramer structure of Fig. 1 are in fact so close, that one may wonder whether the point dipole model, used to calculate the Förster rate constants is justified at all. We found that the use of the extended-dipole model [54] does not significantly alter the conclusions of this work and changes the abovementioned results by no more than 10%. The good agreement between the experimental and calculated Förster energy transfer rate constants nicely confirms the tetramer structure presented in Fig. 1.

Conclusions

- Lowering the temperature of solutions of ZnM(4-Py)TrPP in toluene and polymer/toluene results in formation of cyclic tetramers *via* zinc-pyridyl ligation as can be concluded from the ligation shifts and splitting of the Soret band in the visible absorption spectra (Part I). Consistent with this observation the monomer fluorescence

with a 1.95 - 2.22 ns lifetime is accompanied by a 1.53 - 1.56 ns lifetime component, assigned to ligated porphyrin units. The 1.5 ns fluorescence component is associated with a rotational correlation time of ~1 ns, as compared to ~100 ps for the monomer, in agreement with the tetramer/monomer size ratio.

- Both the steady state anisotropy spectrum and the fluorescence anisotropy decay of ZnM(4-Py)TrP at 10°C are in agreement with internal energy transfer resulting in fluorescence depolarization and a static value of 0.025 for the fluorescence anisotropy. The anisotropy decay parameters are shown to be in accordance with a tetrameric structure of the aggregate.

- It follows from Monte Carlo simulations, that the rate constants for energy transfer between nearest and next nearest neighbors are $\sim (26 \text{ ps})^{-1}$ and $\sim (190 \text{ ps})^{-1}$, respectively. These rate constants are in agreement with a Förster energy transfer mechanism and confirm a tetramer structure with all four porphyrin monomers mutually perpendicular.

- This work demonstrates that Monte Carlo simulation of time-resolved fluorescence and anisotropy data is powerful tool to determine the structure and the excited state kinetics of self-assembled porphyrin aggregates in solution. Since this method is not limited to solutions, it is expected to be generally applicable to interacting dyes including solid dye films.

Acknowledgments

References

[1] van Grondelle, R.; Dekker, J. P.; Gillbro, T.; Sundström, V., *Biochem. Biophys. Acta* **1994**, *1187*, 1.

[2] Sundström, V.; Pullerits, T.; van Grondelle, R. *J. Phys. Chem. B* **1999**, *103*, 2327.

[3] Prodi, A.; Indelli, M. T.; Kleverlaan, C. J.; Scandola, F.; Alessio, E.; Gianferrara, T.; Marzilli, L. G. *Chem. Eur. J.* **1999**, 5, 2668.

[4] van Patten, P. J.; Shreve, A. P.; Lindsey, J. S.; Donohoe, R. J. *J. Phys. Chem. B* **1998**, *102*, 4209.

[5] Li, F.; Gentemann, S.; Kalsbeck, W. A.; Seth, J.; Lindsey, J. S.; Holten, D.; Bocian, D. F. *J. Mater. Chem.* **1997**, *7*, 1245.

[6] Lawrence, D.; Jiang, I.; Levett, M. *Chem. Rev.* **1995**, *95*, 2229.

[7] Maiti, N. C.; Mazumdar, S.; Periasamy, N. *J. Phys. Chem. B* **1998**, *102*, 1528.

[8] Alessio, E.; Gremia, S.; Mestroni, S.; Iengo, E.; Srnova, I.; Slof, M. *Inorg. Chem.* **1999**, *38*, 869.

[9] Shachter, A. M.; Fleischer, E. B.; Haltiwanger, R. C. *J. Chem. Soc. Chem. Commun.* **1998**, 60.

[10] Leray, I.; Verniéres, M. C.; Pansu, R.; Bied-Charreton, C.; Faure, J. *Thin Solid Films* **1997**, *303*, 295.

[11] Sato, N.; Ito, S.; Sugiura, K.; Yamamoto, M. *J. Phys. Chem. A* **1999**, *103*, 3402.

[12] Kerp, H. R.; Donker, H.; Koehorst, R. B. M.; Schaafsma, T. J.; Van Faassen, E. E. *Chem. Phys. Lett.* **1998**, *298*, 302.

[13] Barbara, P. F.; Meyer, T. J.; Ratner, M. A. *J. Phys. Chem.* **1996**, *100*, 13148.

[14] Yamazaki, I.; Tamai, N.; Yamazaki, T.; Marakami, A.; Mimuro, M.; Fujita, Y. *J. Phys. Chem.* **1988**, *92*, 5035.

[15] Wasielewski, M. R. *Chem. Rew.* **1992**, *92*, 435.

[16] Wasielewski, M. R.; Gaines III, G. L.; Weiderrecht, G. P.; Svec, W. A.; Niemczyk, M. P. *J. Am. Chem. Soc.* **1993**, *115*, 10442.

[17] Gradinaru, C. C.; Pascal, A. A.; van Mourik, F.; Robert, B.; Horton, P.; van Grondelle, R.; van Amerongen, H. *Biochemistry* **1998**, *37*, 1143.

[18] Gradinaru, C. C.; Özdemir, S.; Gülen, D.; van Stokkum, I. H. M.; van Grondelle, R.; van Amerongen, H. *Biophys. J.* **1998**, *75*, 3064.

[19] Gradinaru, C. C.; van Stokkum, I. H. M.; Pascal, A. A.; van Grondelle, R.; van Amerongen, H. *J. Phys. Chem. B* **2000**, *104*, 9330.

[20] Lakowicz, J. R., Ed., *Topics in Fluorescence Spectroscopy*, Vol. 1; Plenum Press: New York, 1991.

[21] Johansson, L. B. -Å.; Engström, S.; Lindberg, M. *J. Phys. Chem.* **1992**, *96*, 3845.

[22] Andrews, L.; Demidov, A., Eds., *Resonance Energy Transfer*; John Willey & Sons Ltd Inc: New York, 1999.

[23] Yatskou, M. M.; Donker, H.; Koehorst, R. B. M.; van Hoek, A.; Schaafsma, T. J. *Chem. Phys. Lett.*, submitted.

[24] Donker, H.; Koehorst, R. B. M.; van Hoek, A.; van Schaik, W.; Yatskou, M. M.; Schaafsma, T. J. *J. Phys . Chem. B*, submitted.

[25] Adler, A. D.; Longo, F. R.; Finarelli, J. D.; Goldmacher, J.; Assour, J.; Korsakoff, L. *J. Organic Chem.* **1967**, *32*, 476.

[26] Adler, A. D.; Longo, F. R.; Kampas, F.; Kim, J. *J. Inorg. Nucl. Chem.* **1970**, *32*, 2443.

[27] Visser, A. J. W. G.; van den Berg, P. A. W.; Visser, N. V.; van Hoek, A.; van den Burg, H. A.; Parsonage, D.; Claiborne, A. *J. Phys. Chem. B* **1998**, *102*, 10431.

[28] van den Berg, P. A. W.; van Hoek, A.; Walentas, C. D.; Perham, R. N.; Visser, A. J. W. G. *Biophys. J.* **1998**, *74*, 2046.

[29] van Hoek, A.; Visser, A. J. W. G. *Rev. Sci. Instruments* **1981**, *52*, 1199.

[30] Gobets, B.; van Stokkum, I. H. M.; Rögner, M.; Kruip, J.; Kleima, F. J.; Schlodder, E.; Karapetyan, N. V.; Dekker, J. P.; van Grondelle, R. *Biophys. J.*, submitted.

[31] Marquardt, D. W. *J. Soc. Ind. Appl. Math.* **1963**, *11*, 431.

[32] Beechem, J. M. *Methods Enzymol.* **1992**, *210*, 37.

[33] Digris, A. V.; Skakun, V. V.; Novikov, E. G.; van Hoek, A.; Claiborne, A.; Visser, A. J. W. G. *Eur. Biophys J.* **1999**, *28*, 526.

[34] Bevington, P. R. *Data Reduction and Error Analysis for the Physical Sciences*; McGraw-Hill: New York, 1969.

[35] Kleima, F. J.; Hofmann, E.; Gobets, B.; van Stokkum, I. H. M.; van Grondelle, R.; Diederichs, K.; van Amerongen, H.; *Biophys. J.* **2000**, *78*, 344.

[36] Maiti, N. C.; Mazumdar, S.; Periasamy, N. *J. Phys. Chem.* **1995**, *99*, 10708.

[37] Lindsey, J. S.; Delaney, J. K.; Mauzerall, D. C.; Linschitz, H. *J. Am. Chem. Soc.* **1988**, *110*, 3611.

[38] López-Cornejo, P.; Costa, S. M. B. *Langmuir* **1998**, *14*, 2042.

[39] Fonda, H. N.; Gilbert, J. V.; Cormier, R. A.; Sprague, J. R.; Kamioka, K.; Connoly, J. S. *J. Phys. Chem.* **1993**, *97*, 7024.

[40] Millar, D. P.; Shah, R.; Zewail, A. H. *Chem. Phys. Lett.* **1979**, *66*, 435.

[41] Dutt, G. B.; Doraiswamy, S.; Periasamy, N.; Venkataraman, B. *J. Chem. Phys.* **1990**, *93*, 8498.

[42] Roy, M.; Doraiswamy, S. *J. Chem. Phys.* **1991**, *94*, 5360.

[43] Knox, R. S.; Gülen, D. *Photochem. Photobiol.* **1993**, *57*, 40.

[44] Wynne, K.; Hochstrasser, R. M. *Chem. Phys.* **1993**, *171*, 179.

[45] Gouterman, M.; Stryer, L. *J. Phys. Chem.* **1962**, *37*, 2260.

[46] Atkins, P. W. *Physical Chemistry* Oxford University Press: Oxford, 1998.

[47] *Chem-X* Chemical Design Ltd: Oxon, England, 1993.

[48] Harvey, S. C.; Cheung, H. C. *Proc. Nat. Acad. Sci. USA* **1972**, *69*, 3670.

[49] Apanasovich, V. V.; Novikov, E. G.; Yatskou, M. M. *J. Appl. Spec.*, in press.

[50] Apanasovich, V. V.; Novikov, E. G.; Yatskov, N. N. *Proc. SPIE*, Advances in Fluorescence Sensing Technology III **1997**, *2980*, 495.

[51] Förster, T. *Ann. Physik.* **1948**, *2*, 55.

[52] Harriman, A.; Porter, G.; Searle, N. *J. Chem. Soc., Faraday Trans. II* **1979**, *75*, 1515.

[53] *Handbook of Chemistry and Physics*; CRC Press: Cleveland, Ohio44128, USA, 1974.

[54] Czikklely, V.; Forsterling, H. D.; Kuhn, H. *Chem. Phys. Lett.* **1970**, *6*, 207.

5.3. A Study of Energy Transfer Processes in Zinc-Porphyrin Films Using Monte Carlo Simulation of Fluorescence Decay

Mikalai M. Yatskou[#], Harry Donker, Rob B.M. Koehorst, Arie van Hoek, Tjeerd J. Schaafsma[*]

Laboratory of Biophysics, Department of Agrotechnology and Food Sciences, Wageningen University, Dreijenlaan 3, 6703 HA Wageningen, The Netherlands

Abstract

Energy transfer processes in spin coated, thin films of zinc tetra(-octylphenyl)-porphyrin (ZnTOPP) doped with copper tetra(-octylphenyl)-porphyrin (CuTOPP) or free-base tetra(-octylphenyl)-porphyrin (H$_2$TOPP) were investigated by time-resolved fluorescence measurements and analyzed by means of Monte Carlo simulations. The simulations have been applied to a single domain model of parallel porphyrin stacks, yielding two energy transfer pathways i.e. the intra- and inter-stack energy transfer within each domain, with rate constants $(0.8 - 1.1) \times 10^{12}$ s^{-1} and $(71 - 91) \times 10^{9}$ s^{-1}, respectively. The fluorescence lifetimes for the ZnTOPP and H$_2$TOPP films are $(1.80 - 1.88) \times 10^{-9}$ s and $(6.8 - 7.3) \times 10^{-9}$ s, respectively. In addition a rate constant for H$_2$TOPP to ZnTOPP back transfer was found to be $(8.8 - 9.4) \times 10^{6}$ s^{-1}. These results are in perfect agreement with those of a previous analytical analysis [1].

Key words: Spincoated film, ZnTOPP, CuTOPP, H$_2$TOPP, fluorescence decay, energy transfer, Monte Carlo simulation.

Introduction

Recently, dye films have gained much interest since these are promising materials for constructing organic solar cells [2,3,4,5]. For such cells to be efficient, energy transfer, further

---

[#] On leave from the Department of Systems Analysis, Belarusian State University, 4, F. Scoryna Ave., Minsk, 220050, Belarus

[*]Corresponding author: Tel: +31-317482044; Fax: + 31-317482725; e-mail: Tjeerd.Schaafsma@mac.mf.wau.nl

denoted as E.T., through the film must be optimized [6,7,8]. There are at least two reasons why the analysis of E.T. in molecular films is far from simple since: (i) the films may contain different types of aggregates, e.g. linear or cyclic chains or ordered domains [1,9,10,11] with different spectroscopic properties, and (ii) the E.T. rate constants depend on the nature and strength of the intermolecular interactions at the aggregate and domain level [12,13,14]. These interactions depend again on the detailed film structure.

This paper reports and discusses the results of a study of E.T. processes in thin, spincoated films of a self-organizing porphyrin, ZnTOPP (Fig. 1) on quartz substrates.
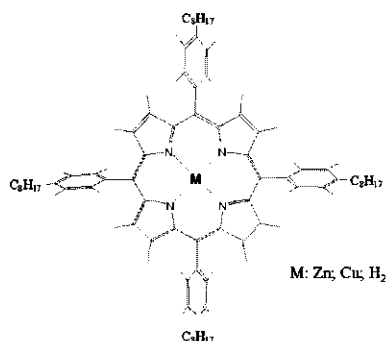
Figure 1. Molecular structure of Zn-, Cu-, and H₂TOPP.

The films have been intentionally doped with known amounts of effective fluorescence quenchers, i.e. CuTOPP or H$_2$TOPP (Fig. 1). Optical spectroscopy of these films [1] has shown that they consist of layers of one-dimensional stacks in a "slipped deck of cards" configuration. The porphyrin planes within the stacks are oriented perpendicular to the substrate. The long axes of the stacks, which form ordered domains, are parallel to the substrate.

The domain orientations are randomly distributed in the substrate plane. The fluorescence decay of these films cannot be described by a single exponential, most likely indicating energy transfer/ migration within the domains. Analysis of the fluorescence decay of the ZnTOPP films using analytical models has shown that the spectroscopic properties of the films are best described by quasi one-dimensional, diffusion limited energy transfer [1]. This analysis yields a rough estimate of $((0.1 - 1.0) \times 10^{12}$ s$^{-1})$ and 0.07×10^{12} s^{-1} for the inter- and intra-stack energy transfer rate constants, respectively. The results of that study also showed that the undoped films contain a considerable fraction of non-intentionally incorporated traps, but again only an estimate could be given.

An alternative and effective approach for retrieving the energy transfer characteristics from the fluorescence decay is the Monte Carlo (further denoted as MC) simulation method [15,16,17]. We applied MC simulation to the fluorescence data of the film using a model of the porphyrin film, which assumes that the film consists of domains containing a number of parallel porphyrin stacks. In principle for this model at least two E.T. rate constants should be found, corresponding

146

to intra- and inter-stack energy transfer within each domain. Considering their excited state energies, also back transfer from H_2TOPP to ZnTOPP is expected to occur, and therefore has been incorporated in the model and the MC simulations.

Experimental

Materials

ZnTOPP and CuTOPP were prepared by metallization of H_2TOPP by refluxing in DMF with $ZnCl_2$ (Merck, p.a.) and $CuCl_2.2H_2O$ (Merck, p.a.), respectively [18]. H_2TOPP was synthesized by condensation of 4-(n-octyl)benzaldehyde (Kodak, 99%) with pyrrole (Janssen Chimica, 99%) in refluxing propionic acid (Merck, z.s.) [19]. The porphyrins were purified by chromatography on silica (Merck, silica gel 60) with toluene as eluent. For duplicate samples ZnTOPP purchased from Porphyrin Products was used. Results obtained with purchased or home-synthesized ZnTOPP were identical. All porphyrins are estimated to be >99% pure as shown by thin-layer chromatography and absorption- as well as fluorescence spectroscopy.

Thin films of ZnTOPP doped with various concentrations of CuTOPP and H_2TOPP as well as undoped films on quartz plates (suprasil, $\varnothing$ 15mm and 1 mm thickness) were prepared by spincoating from $5 \cdot 10^{-2}$ M toluene solutions. As the solutions already contained the appropriate amounts of ZnTOPP and CuTOPP, it may be assumed that in the films the CuTOPP molecules are distributed statistically among the ZnTOPP molecules. Before spincoating the quartz plates were subsequently rinsed with aqua regia, water, methanol and toluene and blown dry with nitrogen. All solvents were p.a. quality, if not stated otherwise.

For the time-resolved fluorescence measurements we used ZnTOPP films with the following composition: i)- iv): 0, 1, 2, 3 $\times 10^{-2}$ molar fraction of CuTOPP; v)- vii): 1, 2, 3 $\times 10^{-2}$ molar fraction of H_2TOPP.

Equipment

The instrumentation for time-resolved fluorescence measurement is time-correlated single photon counting equipment which has been described in detail elsewhere [1,20]. A mode-locked continuous wave Nd:YLF laser (Coherent model Antares 76-YLF, equipped with a LBO frequency doubler (Coherent model 7900 SHGTC) and BBO frequency tripler (Coherent model 7950 THG) was used to synchronously pump a continuous wave dye laser (Coherent radiation model CR 590). As a dye Coumarin 460 was used for excitation at 465 nm. A set-up with electro-optic modulators in a dual pass configuration was used to reduce the pulse rate to 594 kHz [21]. The final pulse duration of excitation pulses was ~ 4 ps FWHM and the maximum

pulse energy ~100 pJ. The spincoated samples were fixed on a thermostated, spring-loaded holder at an angle of 15° with respect to the direction of excitation. Data were collected using a multichannel analyzer (MCA board Nuclear Data model Accuspec B, in a PC) with a time window of 8192 channels at 3.125 ps/channel. To obtain a favorable dynamic instrumental response (~ 50 ps FWHM) for deconvolution purposes, the scatter of a rough-hewn, uncoated quartz substrate of 1 mm thickness was measured at the excitation wavelength.

The porphyrin films were measured at room temperature. Excitation was at 465 nm and detection was at 580 nm and 725 nm for the ZnTOPP and H_2TOPP fluorescence, respectively.

MC simulations

As previously found [1], ZnTOPP porphyrins on a quartz substrate are self-organizing in two-dimensional (2D) domains. Inside each domain the ZnTOPP monomers are presumably assembled in parallel stacks oriented along one of the domain axes (Fig. 2).
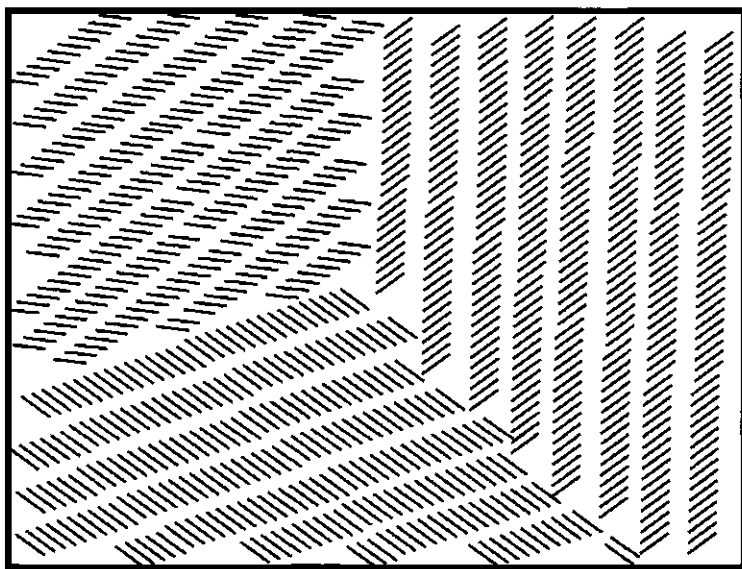
Figure 2. Schematic two-dimensional fragment of self-organized ZnTOPP film.

The center-to-center distances between the nearest neighbor ZnTOPPs in a stack and in nearby stacks are ~ 5 and ~ 10 – 50 Å, respectively, the latter distance depending on the particular domain structure. Three dominant E.T. pathways are expected for such a 2D domain: i) intra-stack E.T. along the porphyrin stack; ii) inter-stack E.T. between adjacent stacks; iii) inter-domain E.T. between adjacent stacks in two neighboring domains.

In ZnTOPP films doped with H_2TOPP or CuTOPP the latter are energy acceptors, acting as traps, in both film types. The long tail of the ZnTOPP fluorescence decay at 580 nm (see Fig. 6) indicates a relatively slow back transfer from H_2TOPP to ZnTOPP [1].

The presence of a non-intentional impurity, possibly H_2TOPP as a residue of the ZnTOPP preparation, results in non-exponential fluorescence decay of the undoped ZnTOPP films. This non-intentional impurity also acts as an energy acceptor and is assumed to have a constant concentration in all experiments. We also assume that singlet-singlet annihilation can be neglected at the low excitation rates which were used. Finally, we neglect E.T. between adjacent domains as compared to intra- and inter-stack E.T.

The MC model for E.T. processes in the ZnTOPP films is based on a single domain of 200 parallel porphyrin stacks, each containing 1000 molecules. Associating the x and y axes in the simulation model with the parallel and perpendicular directions to one of domain axes (Fig. 3), then the intra-stack E.T. rate constants in the x and in y directions are denoted as k^x_{ET} and k^y_{ET}, respectively.
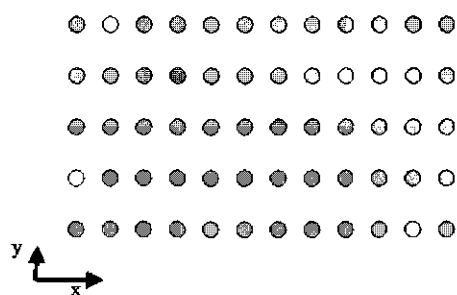
Figure 3. Schematic fragment of a single porphyrin domain used in the Monte Carlo simulations; ● ZnTOPP; ○ impurity trap.

Furthermore, N_{CuP}, N_{H_2P} and N_{imp} define the molar fractions of CuTOPP, H_2TOPP, and the non-intentional impurity molecules, respectively. The parameter k^{Back} is the E.T. rate constant for the back transfer from H_2TOPP to ZnTOPP and τ_{ZnP} and τ_{H_2P} indicate the ZnTOPP and H_2TOPP fluorescence lifetimes, respectively.

The parameters k^x_{ET}, k^y_{ET}, $(\tau_{ZnP})^{-1}$, k^{Back} and $(\tau_{H_2P})^{-1}$ are proportional to the probabilities P^x_{ET}, P^y_{ET}, and P^{ZnP}_τ, P^{Back} and $P^{H_2P}_\tau$, used in the simulation model related by

$$P^x_{ET} + P^y_{ET} + P^{ZnP}_\tau = 1$$

(1)

$$P^{Back} + P^{H_2P}_\tau = 1$$

(2)

The following assumptions have been made in the simulation model:

149

i)   rate constants for "left" and "right" E.T. in the x direction are equal as well as for "up" and "down" E.T. in the y direction (Fig. 3);

ii) the rate constant k^x_{ET}, corresponding to nearest neighbor transfer, is at least one order larger than to the next nearest neighbor or more distant molecules, i.e. E.T. beyond one or more neighboring molecules is neglected;

iii) the rate constant k^y_{ET} is a statistical mean value covering all E.T. pathways to the nearest nearby stack;

iv) the back transfer from CuTOPP to ZnTOPP is neglected.

Finally, the simulation model has the following set of the parameters:

a) k^x_{ET}, k^y_{ET}, and N_{imp}, and τ_{ZnP} for the undoped ZnTOPP film;

b) k^x_{ET}, k^y_{ET}, N_{CuP}, N_{imp}, and τ_{ZnP} for the CuTOPP doped ZnTOPP film;

c) k^x_{ET}, k^y_{ET}, N_{H_2P}, N_{imp}, τ_{ZnP}, k^{Back}, and τ_{H_2P} for the H$_2$TOPP doped ZnTOPP film.

A flow diagram for one run of the simulation model is shown in Fig. 4A. The molecular sites are numbered as $i = 1,...,1000$ in the x direction and $j = 1,...,200$ in the y direction, respectively. The position (i_0,j_0) of the first excited molecule, the positions (i^l,j^l), $l = 1,...,1000 \cdot N_{CuP}/N_{H_2P}$ of the N_{CuP}/N_{H_2P} impurity traps and the positions (i^k,j^k), $k = 1,..., 1000 \cdot N_{imp}$ of N_{imp} non-intentional impurity traps are randomly generated using a uniform standard number generator [24] at the start of every simulation run (**block 1**). After checking whether the first excited molecule is a trap (**block 2**), the events of the fluorescence emission or E.T. in the x or the y directions are simulated in **block 5** according to the discrete probability distribution, defined by P^x_{ET}, P^y_{ET}, and P^{ZnP}_τ, using a random number **R**, generated in **block 4**. The time of the excitation energy transfer is considered to be a continuous random variable, distributed exponentially. Thus, the time Δt for E.T. from one molecule to its next neighbor is given by [17]
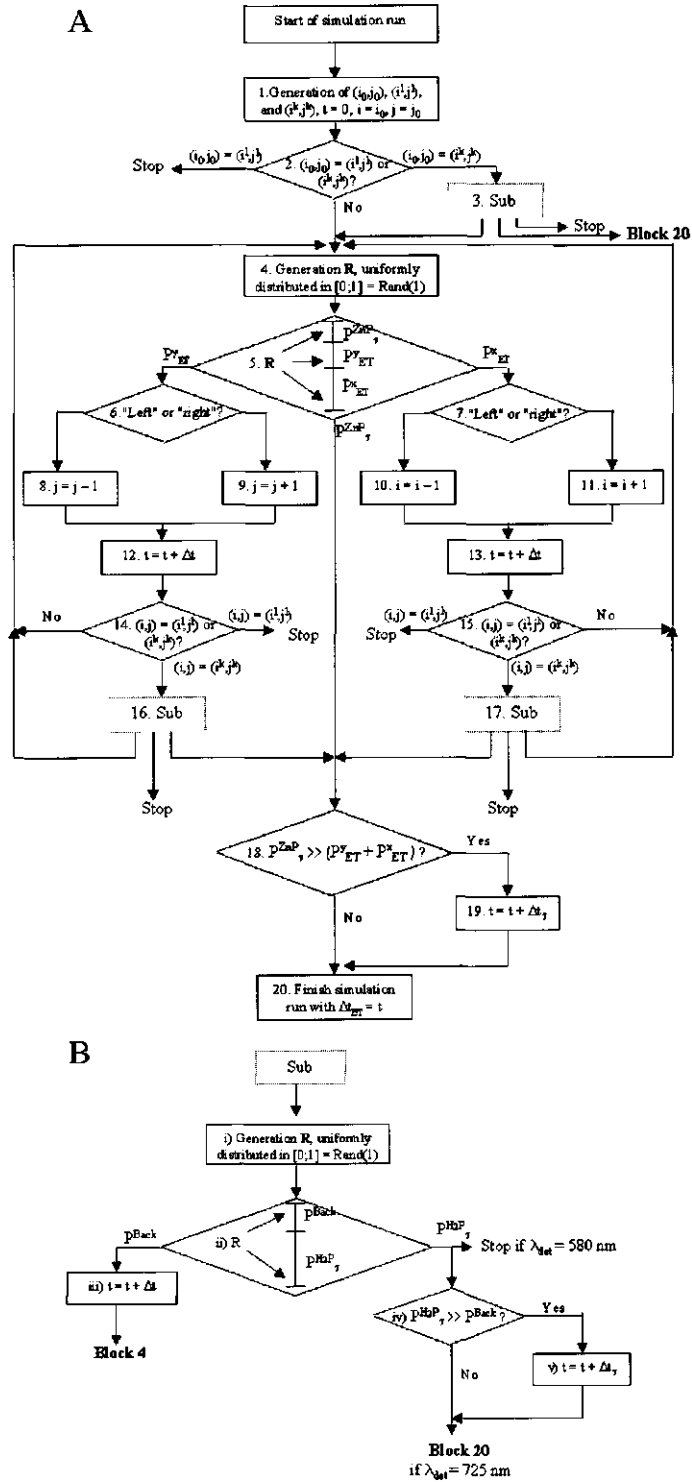
A

Start of simulation run

1. Generation of (i_0,j_0), (i^1,j^1), and (i^k,j^k), $t = 0$, $i = i_0$, $j = j_0$

Stop ← $(i_0,j_0) = (i^1,j^1)$ — 2. $(i_0,j_0) = (i^1,j^1)$ or (i^k,j^k)? — $(i_0,j_0) = (i^k,j^k)$

No

3. Sub → Stop → **Block 20**

4. Generation R, uniformly distributed in [0;1] = Rand(1)

p^y_{ET} — 5. R → p^{ZaP}_r, p^y_{ET}, p^x_{ET}, p^{ZaP}_r — p^x_{ET}

6. "Left" or "right"?   7. "Left" or "right"?

8. $j = j - 1$ 9. $j = j + 1$ 10. $i = i - 1$ 11. $i = i + 1$

12. $t = t + \Delta t$ 13. $t = t + \Delta t$

No ← 14. $(i,j) = (i^1,j^1)$ or (i^k,j^k)? → $(i,j) = (i^1,j^1)$ Stop ; $(i,j) = (i^k,j^k)$

Stop ← 15. $(i,j) = (i^1,j^1)$ or (i^k,j^k)? → No ; $(i,j) = (i^k,j^k)$

16. Sub   17. Sub

Stop   Stop

18. $p^{ZaP}_r \gg (p^y_{ET} + p^x_{ET})$? — Yes → 19. $t = t + \Delta t_r$

No

20. Finish simulation run with $\Delta t_{ET} = t$

B

Sub

i) Generation R, uniformly distributed in [0;1] = Rand(1)

p^{Back} — ii) R → p^{Back}, p^{HbP}_r — p^{HbP}_r → Stop if $\lambda_{det} = 580$ nm

iii) $t = t + \Delta t$

Block 4

iv) $p^{HbP}_r \gg p^{Back}$? — Yes → v) $t = t + \Delta t_r$

No

Block 20
if $\lambda_{det} = 725$ nm

Figure 4. (A) Flow diagram of one simulation run and (B) its subroutine.

151

$$\Delta t = - (k^q_{ET})^{-1} \ln(R)$$

(3)

where q is x or y, and R is a uniformly distributed random number in [0;1]. Random travel of excitation energy is simulated in **blocks 2 - 15** until the fluorescence event (**block 18,19**) or trapped by a CuTOPP or H$_2$TOPP site or non-intentional impurity in **blocks 3, 16,** and **17.** If a trap is CuTOPP or a non-intentional impurity molecule then the simulation run stops there without Δt having been determined, otherwise, Δt for the events of back ET or emission by a H$_2$TOPP trap is generated in **blocks 3, 16** and **17** using a discrete exponential probability distribution for P^{Back} and $P^{H_2P}_\tau$ (Fig. 4B). The finally simulated time Δt_{ET} is recorded in a histogram [17] representing the simulated decay. The simulation runs are repeated many times (typically more then 10^6 runs). The simulation program is stopped when the simulated decay has reached an acceptable signal to noise ratio.

The simulation-based parametric fitting [16,22] was applied to the fluorescence decay of ZnTOPP films. A time shift due to the convolution of the decay curve with the instrumental response function was simulated using a published algorithm [23]. Global analysis was then applied to analyze the fluorescence decay and its change with different molar fractions of the doped CuTOPP and H$_2$TOPP molecules. Since the fluorescence decays for different concentrations of impurity traps should result in the same values for the ZnTOPP- and H$_2$TOPP lifetimes and the corresponding E.T. rate constants, these parameters were globally linked and fitted.

The number of channels in the simulated histograms is 8096. The statistical χ^2 criterion as well as the plots of the weighted residuals and autocorrelation function were used to judge the quality of the fits. The 95% confidence intervals for the best fitted parameters were estimated using the method of asymptotic standard errors [24]. All computer simulations were performed on an IBM Pentium III 366 MHz PC.

To produce a simulated fluorescence decay with an acceptable signal to noise ratio typically 10^8 photon runs were needed to get stable χ^2 values, and, at the same time, a reasonably short simulation time.

Results and Discussion

The experimental fluorescence decay of all ZnTOPP films can be nicely fitted by the simulated decay curves. Fig. 5 shows the best fits of the ZnTOPP fluorescence with different molar fractions of CuTOPP traps and similarly Fig. 6 for H_2TOPP traps.
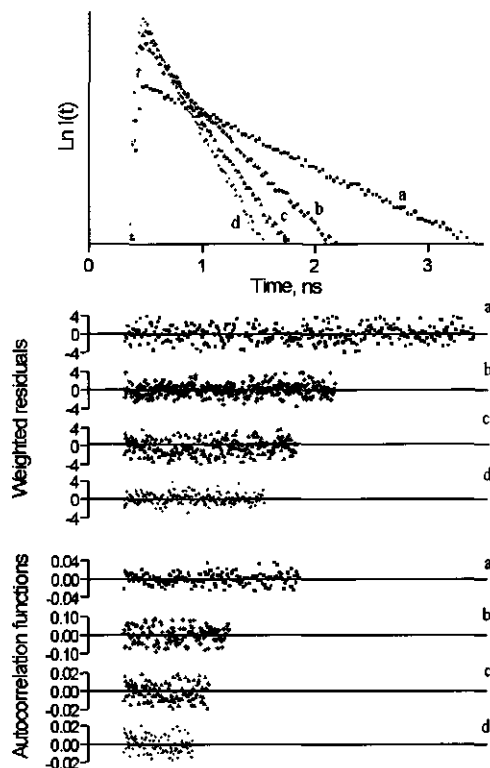
Figure 5. Parametric fit of the experimental ZnTOPP fluorescence decays (—) with 0 (a, ■), 1×10^{-2} (b, +), 2×10^{-2} (c, ▲), and 3×10^{-2} (d, ●) molar fractions of CuTOPP; $\lambda_{exc} = 465$ nm; $\lambda_{det} = 580$ nm.
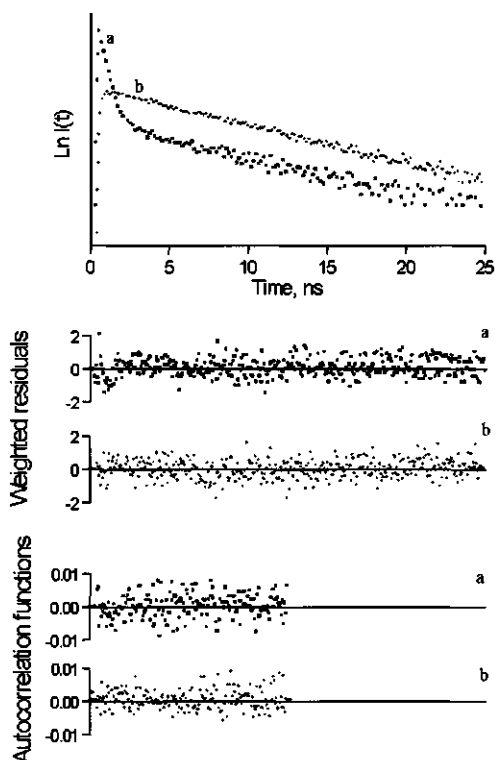
Figure 6. Parametric fit of the experimental ZnTOPP fluorescence decays (—) for a 1×10^{-2} molar fraction of H_2TOPP; $\lambda_{exc} = 465$ nm; (a, ■): $\lambda_{det} = 580$ nm; (b,●): $\lambda_{det} = 725$ nm.

The parameters corresponding to the best fits are collected in Table 1.

The ZnTOPP fluorescence lifetime found through MC simulations is in range of the $(1.80 - 1.88)$ $\times10^{-9}$ s for all ZnTOPP films, close to the experimental lifetime of $1.81\pm0.3 \times10^{-9}$ s in toluene, typical for a zinc porphyrin in organic solvents [25,26,27]. The intra-stack E.T. constant is in range of the $(0.8 - 1.1) \times10^{12}$ s^{-1} and almost one order higher than that of the $(71 - 91) \times10^{9}$ s^{-1} of inter stack. The calculated molar fractions of CuTOPP and H_2TOP were found to be in

accordance with those in the solution, used for spin coating. The simulated fluorescence lifetime of H$_2$TOPP is $(6.8 – 7.3) \times 10^9$ s, a little shorter than $9.2 \pm 0.5 \times 10^9$ s for H$_2$TPP in toluene.

Table 1. Fluorescence lifetimes, molar fraction, energy transfer parameters and corresponding 95% confidence intervals[a] determined by MC simulation of experimental fluorescence decay of undoped, CuTOPP- and H$_2$TOPP-doped ZnTOPP films.

System	λ_{det} (nm)	τ_{ZnP} ($\times 10^{-9}$ s)	N_{Imp} ($\times 10^{-2}$)	N_{CuP} ($\times 10^{-2}$)	N_{H_2P} ($\times 10^{-2}$)	k^{Back} ($\times 10^6$ s^{-1})	τ_{H_2P} ($\times 10^{-9}$ s)	k^x_{ET} ($\times 10^{12}$ s^{-1})	k^y_{ET} ($\times 10^9$ s^{-1})
Undoped ZnTOPP	580	1.80 [1.76;1.84]	0.6 [0.5;0.7]					1.1 [0.9;1.3]	71 [63;79]
ZnTOPP/ CuTOPP	580	1.81 [1.78;1.84]	0.5 [0.4;0.6]	1.0 [0.9;1.1]				0.9 [0.7;1.1]	81 [68;94]
				2.0 [1.9;2.1]					
				3.0 [2.9;3.1]					
ZnTOPP/ H$_2$TOPP	580	1.84 [1.82;1.86]	0.5 [0.4;0.6]		1.0 [0.9;1.1]	9.4 [6.0;12.8]	6.8 [6.5;7.1]	0.8 [0.6;1.0]	91 [71;111]
					2.0 [1.9;2.1]				
					3.0 [2.9;3.1]				
ZnTOPP/ H$_2$TOPP	725	1.88 [1.80;1.96]	0.4 [0.3;0.5]		1.0 [0.9;1.1]	8.8 [5.7;11.9]	7.3 [7.0;7.6]	1.0 [0.8;1.2]	71 [56;96]
					2.0 [1.9;2.1]				
					3.0 [2.9;3.1]				

[a] Between square brackets

The rate constant for back transfer from H$_2$TOPP to ZnTOPP comes out as $(8.8 – 9.4) \times 10^6$ s^{-1}. Although the back transfer is much slower than intra- or inter-stack E.T., this process obviously influences the ZnTOPP fluorescence, as revealed by the MC simulation. The simulated initial ingrowths of the H$_2$TOPP fluorescence at $\lambda_{det} = 725$ nm nicely fits the experiment (Fig. 6). Finally, the simulations reveal a $(0.4 – 0.6) \times 10^{-2}$ molar fraction of non-intentional impurity molecules, a more accurate number than could be determined by the analytical method [1].

Conclusions

- Monte Carlo simulation of the energy transfer processes in an undoped, self-organized ZnTOPP film, using a physical model of its structure and excited state kinetics, has been demonstrated to be a successful method to extract the relevant kinetic parameters from the experimental complex fluorescence decay of the film. The simulated fluorescence decay nicely fits the experimental three-exponential fluorescence decay, with fast intra- stack and much slower inter-stack energy transfer as the result.

  Generally, the method is not limited to the specific process or system as in this work. It is expected to be equally effective, when applied to other, more complex systems and/or different processes involving excited states, as long as a model can be constructed, which contains the essential parameters of the processes occurring in these systems.

- Notwithstanding the non-exponential experimental fluorescence decay fluorescence lifetimes of $(1.80 - 1.88) \times 10^{-9}$ s and $(6.8 - 7.3) \times 10^{-9}$ s for ZnTOPP and H$_2$TOPP films, respectively, have been determined in a 95% confidence interval with quite good accuracy.

- The different rate constants for intra-stack and inter-stack energy transfer in the ZnTOPP film of $(0.8 - 1.1) \times 10^{12}$ s^{-1} and $(71 - 91) \times 10^9$ s^{-1}, respectively, as well as the molar fractions of intentional and non-intentional traps, obtained from the Monte Carlo simulations, support the results and conclusions of previous work [1];

References

[1] H. Donker, R.B.M. Koehorst, A. van Hoek, W. van Schaik, M.M. Yatskou, T.J. Schaafsma, J. Phys. Chem. B submitted.

[2] B.A. Gregg, M.A. Fox, A.J. Bard, J. Phys. Chem. 93 (1989) 4227.

[3] T.J. Schaafsma, Sol. Energy Mat. Sol. Cells 38 (1995) 349.

[4] I. Leray, M.C. Verniéres, R. Pansu, C. Bied-Charreton, J. Faure, Thin Solid Films 303 (1997) 295.

[5] N. Kanayama, T.Kanbara, H. Kitano, J. Phys. Chem. B 104 (2000) 271.

[6] M. Quillec, Ed., Materials for Optoelectronics, Kluwer Academic Publishers, Boston, 1996.

[7] S. Donati, Photodetectors, Devices, Circuits and Applications, Plenum Press, New York, 2000.

[8] K.L. Chopra, S.R. Das, Thin Film Solar Cells, Plenum Press, New York, 1983.

[9] E.K.L. Yeow, K.P. Giggino, J.H.N. Reek, M.J. Crossley, A.W. Bosman, A.P.H.J. Schenning, E.W. Meijer, J. Phys. Chem. B 104 (2000) 2596.

[10] D. Markovitsi, A. Germain, P. Millié, P. Lécuyer, L. K. Gallos, P. Argyrakis, H. Bengs, H. Ringsdorf, J. Phys. Chem. 99 (1995) 1005.

[11] N. Kometani, H. Nakajima, K. Asami, Y. Yonezawa, O. Kajimoto, J. Phys. Chem. B 104 (2000) 9630.

[12] N. Kanayama, T. Kanbara, H. Kitano, J. Phys. Chem. B 104 (2000) 271.

[13] N. Sato, S. Ito, K. Sugiura, M. Yamamoto, J. Phys. Chem. A 103 (1999) 3402.

[14] L.M.S. Loura, M. Prieto, J. Chem. Phys. B 104 (2000) 6911.

[15] B. Kalman, L.B.-Å. Johansson, M. Lindberg, S. Engström, J. Phys. Chem. 93 (1989) 8371.

[16] M.M. Yatskou, H. Donker, E.G. Novikov, R.B.M. Koehorst, A. van Hoek, V.V. Apanasovich, T.J. Schaafsma, J. Phys. Chem. A submitted.

[17] L. Andrews, A. Demidov, Eds., Resonance Energy Transfer, Wiley, New York, 1999.

[18] A.D. Adler, F.R. Longo, F. Kampas, J. Kim, J. Inorg. Nucl. Chem. 32 (1970) 2443.

[19] A.D. Adler, F.R. Longo, W. J. Shergalis, Am. Chem. Soc. 86 (1964) 3145.

[20] A.J.W.G. Visser, P.A.W. van den Berg, N.V. Visser, A. van Hoek, H.A. van den Burg, D. Parsonage, A. Claiborne, J. Phys. Chem. B 102 (1998) 10431.

[21] A. van Hoek, A.J.W.G. Visser, Rev. Sci. Instrum. 52 (1981) 1199.

[22] V.V. Apanasovich, E.G. Novikov, N.N. Yatskov, Proc. SPIE 2980 (1997) 495.

[23] F.N. Chowdhury, Z.S. Kolber, M.D. Barkley, Rev. Sci. Instrum. 62 (1991) 47.

[24] P.R. Bevington, Data Reduction and Error Analysis for the Physical Sciences, McGraw-Hill, New York, 1969.

[25] N.C. Maiti, S. Mazumdar, N. Periasamy, J. Phys. Chem. 99 (1995) 10708.

[26] P. López-Cornejo, S.M.B. Costa, Langmuir 14 (1998) 2042.

[27] H.N. Fonda, J.V. Gilbert, R.A. Cormier, J.R. Sprague, K. Kamioka, J.S. Connoly, J. Phys. Chem. 97 (1993) 7024.

5.4. A fluorescence anisotropy decay study of energy transfer in spin coated porphyrin films

Zn(4-Py)TrPP films. To make films containing tetrameric structures on quartz substrate, the Zn(4-Py)TrPP/quartz films were spin coated from $(0.2 - 5.0) \cdot 10^{-5}$ M toluene and THF solutions. To investigate ET between close packed tetramers in the films, additional samples of the Zn(4-Py)TrOOPP/quartz films have been created by the same way as the Zn(4-Py)TrPP/quartz films. Since it is expected that the [Zn(4-Py)TrOOPP]$_4$ tetramers will be surrounded by long chains (tails) of OC$_8$, protecting the tetramers against close packing, ET between the tetramers should be reduced. ZnTPP/quartz films have been used as a reference the steady state spectra.

The steady state spectra of several porphyrin films are shown in Figs. 1 - 3.
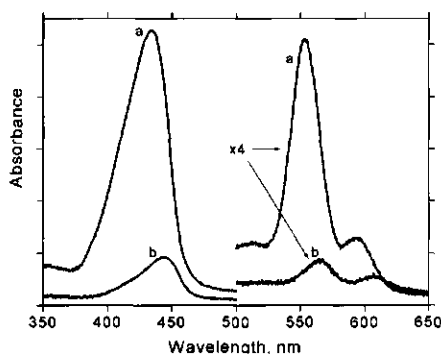
Fig. 1. Absorption spectra of (a) ZnTPP/quartz and (b) Zn(4-Py)TrPP/quartz films spin coated from 10^{-5} M toluene solutions.
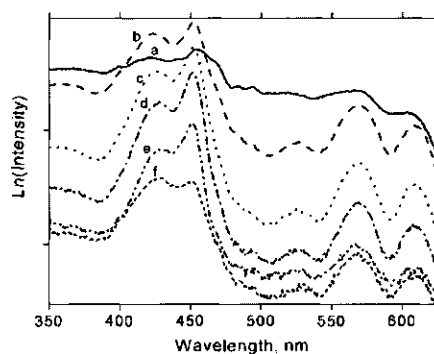
Fig. 2. Excitation spectra of Zn(4-Py)TrPP/quartz films spin coated from (a) $5.0 \cdot 10^{-5}$ M THF, and (b) $2.5 \cdot 10^{-5}$ M -, (c) $1.3 \cdot 10^{-5}$ M -, (d) $0.6 \cdot 10^{-5}$ M -, (e) $0.3 \cdot 10^{-5}$ M -, (f) $0.2 \cdot 10^{-5}$ M toluene solutions. λ_{em} = 675 nm.
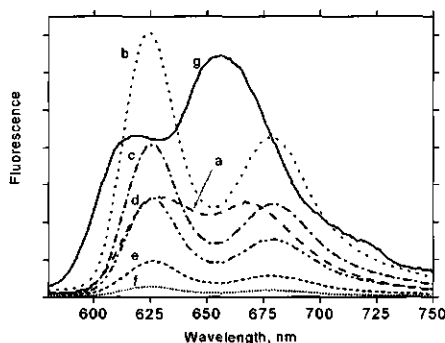
Fig. 3. Fluorescence spectra of Zn(4-Py)TrPP/quartz films spin coated from (a) $5.0 \cdot 10^{-5}$ M THF, and (b) $2.5 \cdot 10^{-5}$ M, (c) $1.3 \cdot 10^{-5}$ M, (d) $0.6 \cdot 10^{-5}$ M (e) $0.3 \cdot 10^{-5}$ M, (f) $0.5 \cdot 10^{-5}$ M, and ZnTPP/quartz film spin coated from (g) $1.0 \cdot 10^{-5}$ M toluene solutions. λ_{exc} = 450 nm.

With the exception of the Soret and Q maxima band shifts and a larger splitting in the Soret bands, the optical spectra of the porphyrin films are basically the same as those for solutions. The shifts and splitting in Soret and Q bands are most likely the result of the solid substrate environment.

Time-resolved fluorescence anisotropy has been measured for the Zn(4-Py)TrPP/quartz films, spin coated from $2.5 \cdot 10^{-5}$ M toluene and $5.0 \cdot 10^{-5}$ M THF solutions, and Zn(4-Py)TrOOPP/quartz films. Although the measurements were carried out almost at the detection limit at $\lambda_{det} = 665$ nm, where the fluorescence yield is very low, the results are most likely what we think that they indicate. The observed fluorescence decays of the porphyrin films were definitely multi-exponential, and typically contain two or three exponentials. There are a number of models explaining this multi-exponential decay:

- Tetramer-tetramer ET followed by trapping in non-intentional H_2(4-Py)TrPP impurity (see Section 5.3);

- Direct ET from the tetramer to a non-intentional H_2(4-Py)TrPP impurity. The energy transfer from the tetramer to the impurity trap is expected to be highly effective in view of the close packing and the relatively large spectral overlap for Zn(4-Py)TrPP and H_2(4-Py)TrPP. Therefore direct ET may well compete with intra-tetramer ET.

Some surprising and promising results have been obtained from the measurements of the fluorescence anisotropy decays of the porphyrin films. Setting the TCSPC spectrometer at high sensitive detection with ~50 ps FWHM as the instrumental response function, the short anisotropy components as low as 5 ps and the corresponding initial anisotropy values could be determined using single exponential fitting with parameters β_1, ϕ_1 (see eqn. (4) of Section 5.2.2).

Table 1. Fluorescence anisotropy decay parameters and corresponding 95% confidence intervals[a] determined by single exponential fitting for different porphyrin films.

Film/solvent/ Exponent 1	Zn(4-Py)TrPP /Toluene	Zn(4-Py)TrPP /THF	Zn(4-Py)TrOOPP /Toluene	Zn(4-Py)TrOOPP /THF
β_1	0.14 [0.11;0.18]	0.28 [0.16;0.42]	0.00 [-0.01;0.01]	0.06 [0.05;0.07]
$\phi_1, \times 10^{-12}$ s	25 [21;32]	10 [5;13]	∞	18 [14;26]

[a]Between brackets

The experimental and fitted fluorescence anisotropy decays for several spin coated porphyrin films and corresponding best-fitted parameters are shown in Fig. 4 and Table 1, respectively.
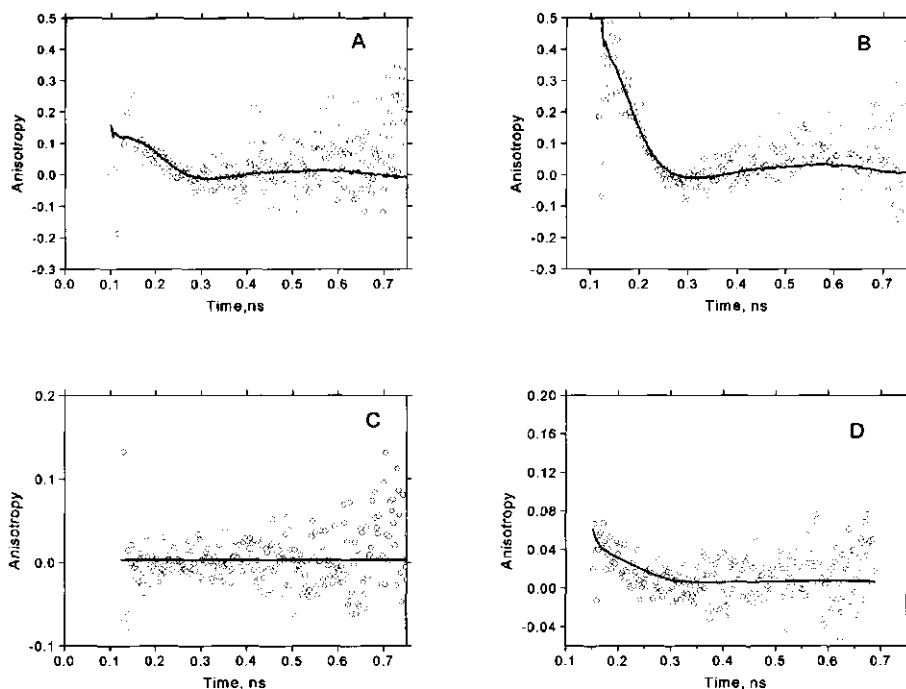

Fig. 4. Anisotropy decay of: (A) Zn(4-Py)TrPP/ quartz film spin coated from toluene; (B) Zn(4-Py)TrPP/quartz film spin coated from THF; (C) Zn(4-Py)TrOOPP/quartz film spin coated from toluene; (D) Zn(4-Py)TrOOPP/quartz film spin coated from THF; λ_{exc} = 440 nm; λ_{det} = 665 nm.

Granted that these results shown in Fig. 4 are preliminary and likely to contain experimental uncertainty, especially in the β_1 values, they obviously indicate that:

i) there is ET with an average rate constant of $(20 \times 10^{-12}$ s$)^{-1}$ present in the organized films;

ii) the anisotropy not affected by ET is expected to have the constant value of 0.1 as for the monomer in toluene solution at zero time. For Zn(4-Py)TrPP films the fluorescence anisotropy decays from above 0.1 down to 0 in $(10 - 25) \times 10^{-12}$ s (see Fig. 4A and Table 1). This time constant is close to that of $(20 - 30) \times 10^{-12}$ s obtained for the ET between nearest neighbor porphyrins within the tetramer in toluene. The constant component with 0.025 amplitude, as observed for the symmetrical tetramer in solution, has not been found in the films.

A possible reason for the absence of this long anisotropy component might be that the tetramers are deformed in such way that they are on the average not symmetrical as in solution. The excitation spectra of Zn(4-Py)TrPP films clearly show the splitting of Soret band, however, indicating ligation of each porphyrin unit as in toluene. A zero value for the anisotropy at long time in fact would be found for a linear polymer. The optical spectra of monomer, dimer, trimer, or higher linear polymer in ZnTPP and Zn(i-Py)TrPP films (i = 1,..,4), as previously reported [1,2], are quite different from those in Figs. 1 - 3. We therefore conclude that the absence of the long anisotropy component has a more trivial reason, i.e. very low emission intensity which cannot be distinguished from the noise;

iii) the fluorescence anisotropy for Zn(4-Py)TrOOPP films does not contain longer anisotropy components in addition to the one with the ~ 22×10^{-12} s time constant, as in Zn(4-Py)TrPP films, neither was a short anisotropy component resolved for this film. This finding is a strong argument against tetramer-tetramer ET in the films;

iv) considering the previous conclusion (ii) about intramolecular ligation between perpendicularly oriented porphyrins in the tetramer, the contribution of an exchange ET mechanism to the total ET within the tetramer is significantly small and for the films (just as in toluene solution) need not be considered.
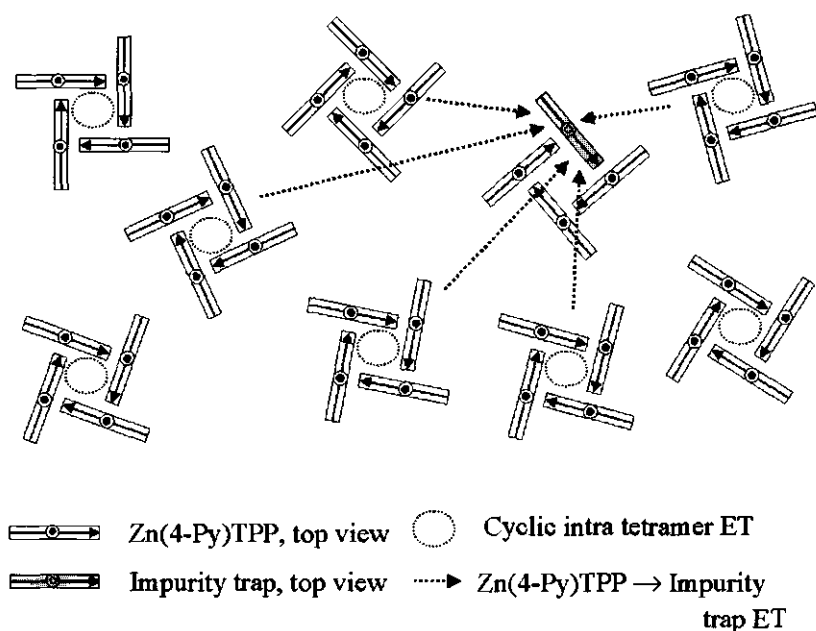
Fig. 5. ET processes in [Zn(4-Py)TrPP]₄ tetramers on a quartz substrate.

160

In view of this and previous arguments, we propose that the multi-exponential fluorescence intensity decay of Zn(4-Py)TrOOPP films is the result of tetramer-impurity trap ET with H_2(4-Py)TrPP as a likely non-intentional impurity. Fig. 5 shows a scheme of ET in [Zn(4-Py)TrPP]$_4$ films.

Summarizing the preliminary results on steady state and time-resolved anisotropy measurements, the tetramer structure of the porphyrin units forming the films is an *a priori* assumption, which agrees with the experimental data.

ZnTOPP films. In addition to the fluorescence decay measurements, the fluorescence anisotropy decay of undoped ZnTOPP films spin coated from toluene and CHCl$_3$ solutions was determined with the aim to extract the orientation of the porphyrin stacks on the quartz substrate and collecting complementary data on the ET processes in the film.

The fluorescence anisotropy decays of the undoped ZnTOPP films have satisfactorily been fitted with a sum of two exponentials with parameters: $\beta_1, \phi_1; \beta_2, \phi_2$. (see eqn. (4) of Section 5.2.2).
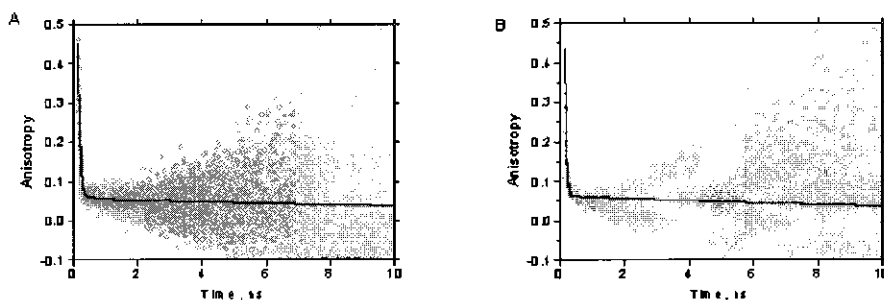
Fig. 6. Fluorescence anisotropy decay of ZnTOPP films spin coated from (A) toluene and (B) CHCl$_3$ solutions; λ_{exc} = 440 nm; λ_{det} = 650 nm.

Fig. 6 illustrates the experimental and fitted fluorescence anisotropy decays for different ZnTOPP films. The corresponding set of the best-fitted parameters is collected in Table 2.

Table 2. Fluorescence anisotropy decay parameters and corresponding 95% confidence intervals[a] determined by two exponential fitting for undoped ZnTOPP films spin coated from toluene and $CHCl_3$ solutions

Film/solvent	Exponent 1		Exponent 2	
	β_1	$\phi_1 \times 10^{-12}$ s	β_2	$\phi_2 \times 10^{-9}$ s
ZnTOPP/Toluene	0.24 [0.12;0.36]	14 [11;17]	0.053 [0.051; 0.056]	20 [18;~]
ZnTOPP/CHCl$_3$	0.25 [0.15;0.29]	12 [9;15]	0.059 [0.055;0.062]	16 [14;~]

[a] Between brackets

The initial anisotropy values of 0.29 – 0.31 are significantly higher than that of the porphyrin monomer (typically 0.1) and have broad 95% confidence intervals, i.e. [0.17;0.41] and [0.21;0.35] for ZnTOPP/toluene and ZnTOPP/CHCl$_3$ films, respectively, that are mainly due to an uncertainty in the β_1 values. The high initial anisotropy is the result of a special porphyrin ordering on the solid substrate, i.e. the porphyrin cores are randomly oriented in the planes perpendicular to the substrate. This conclusion is supported by Monte Carlo simulation of such a porphyrin assembling yielding the mean value 0.24 for the initial anisotropy with the film holder oriented at an angle of 25° with respect to the direction of the incident light (Fig. 7).
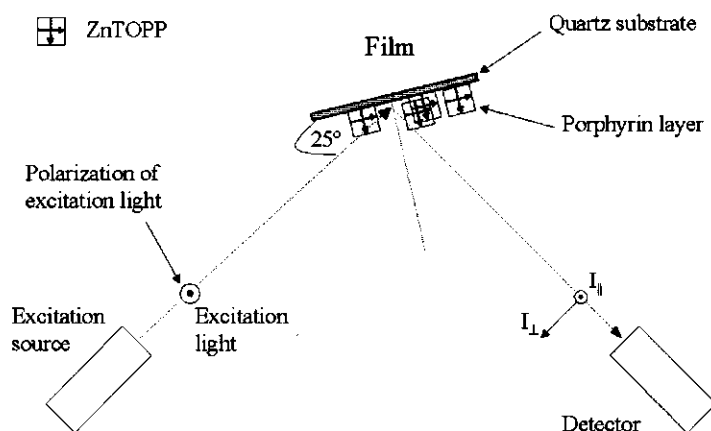
Fig. 7. Scheme for the fluorescence anisotropy decay measurement of the ZnTOPP film.

The other substantial conclusion from the initial anisotropy analysis is that the porphyrin planes are parallel within each stack, otherwise the initial anisotropy value should be much lower than observed.

The short anisotropy component with a correlation time of $\phi_1 = (12 - 14)\times10^{-12}$ s perfectly agrees with the ~ 80 $\times10^9$ s^{-1} rate constant for the inter-stack ET obtained through Monte Carlo simulations (see Section 5.2.3.). The long anisotropy component with $\phi_2 > 14\times10^{-9}$ s may correspond to inter-domain ET. The amplitude of the long component is 0.053 – 0.059 and should reflect the stack orientations. Again applying Monte Carlo simulation, the anisotropy amplitude of 0.053 – 0.059 has been found to be the result of a specific stack order on the substrate: the porphyrin planes of two neighboring stacks are mutually perpendicular and form an angle of 45˚ with the long stack axis as shown in Fig. 8.

ZnTOPP, top view
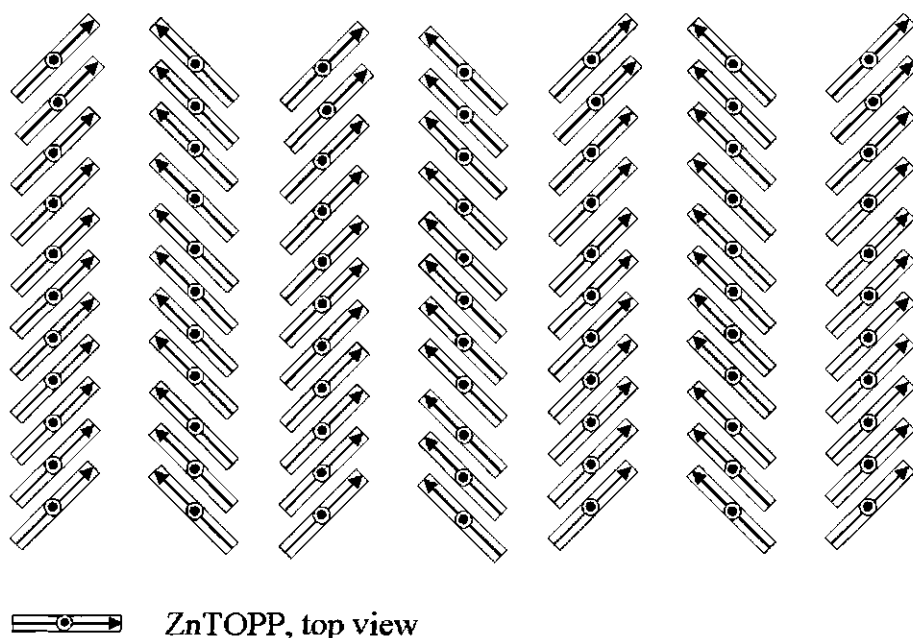
Fig. 8. Fragment of the stack arrangement in a domain.

The abovementioned results of the fluorescence anisotropy decay analysis for the ZnTOPP films strongly support the 2D multi-domain model of porphyrin stacks, yielding very fast intra-stack ET, $(70 – 80)\times10^9$ s^{-1} rate constant for inter-stack ET, and a slow < 70 $\times10^6$ s^{-1} rate constant for inter-domain ET. The porphyrins stacks have been found to be highly ordered as shown in Fig. 8.

5.5. Summary of the experimental results and computer simulation analysis

This Chapter reports the results of a study of self-organized [Zn(4-Py)TrPP]$_4$ tetramers in toluene and toluene/polystyrene solution and in ordered domains of solid films. A simple exciton model explains the optical spectra of porphyrin aggregates in the solutions as the result of internal porphyrin ligation in a symmetrical tetramer structure. The same cyclic tetramer structure is consistent with the enthalpy and entropy changes of the system calculated with a non-calorimetric thermodynamic method. These studies as well as the analysis of the optical spectra of [Zn(4-Py)TrPP]$_4$ tetramers in organic solution are presented in the Section 5.2.1. The results of the Sections 5.1. and 5.2.1. confirm that the symmetrical, cyclic tetramer is the only self-assembling structure in the solutions.

The tetramer excited state kinetic properties are presented in Section 5.2.2. The main conclusion from the fluorescence and anisotropy decay analysis, following from Monte Carlo simulations, is that singlet-singlet energy occurs within the tetramer with an average rate constant of $(23 \text{ ps})^{-1}$.

Applying the Monte Carlo simulations to ZnTOPP films (Section 5.2.3) results in a multi-domain model of parallel porphyrin stacks. In each stack the porphyrin planes are perpendicular to the substrate and make an angle of 45° with the long stack axis. MC simulation fitting yields rate constants for intra-stack and inter-stack ET as $\sim 1 \times 10^{12}$ s^{-1} and $\sim 80 \times 10^{9}$ s^{-1}; and a fluorescence lifetime of $\sim 1.8 \times 10^{-9}$ s.

Section 5.4. reports the preliminary results of fluorescence anisotropy decay measurements for ZnTOPP and Zn(4-Py)TrPP films, as well as a qualitatively analysis of these results. Optical spectra and fluorescence anisotropy decay of the Zn(4-Py)TrPP films are basically in agreement with a tetramer structure of the porphyrin assemblies in these films.

References

[1] Takahashi, K.; Komura, T.; Imanaga, H. *Bull. Chem. Soc. Jpn.* **1989**, *62*, 386.

[2] Leray, I.; Verniéres, M. C.; Pansu, R.; Bied-Charreton, C.; Faure, J. *Thin Solid Films* **1997**, *303*, 295.

Summary

The general goal of this Thesis was the development of an advanced computer simulation approach to improve the analysis of the complex fluorescence- and fluorescence anisotropy decay of porphyrin oligomers in solution as well as in thin solid films in the presence of energy transfer processes. With the application to light-harvesting antenna's in solar cells in mind, the energy transfer- and relaxation properties of several artificial antenna's, consisting of self-organized porphyrins in ultra-thin, spin coated films and as oligomers in different solutions, have been studied by the designed computer simulation approach.

Chapter 1 contains a general description of the photophysical processes in artificial photosynthesis, the steady state- and time-resolved fluorescence spectroscopy, the methods used to analyze the time correlated single photon counting data and the mathematical modeling methods. The theoretical framework presented in this Chapter forms the background for understanding the basics of the studied porphyrin systems and the experimental and calculational methods to investigate these systems.

Chapter 2 describes the analyzed porphyrin systems, the experimental steady state- and time-resolved absorption and fluorescence methods, technical details of the equipment, and typical results of the photophysics of some porphyrin systems.

Chapter 3 compares the various optimization methods for fitting the fluorescence decay with the aim to review their properties. These properties are important when applying Monte Carlo simulations to the investigated energy transfer processes. A number of methods have been found to be promising for practical application in data analysis using computer simulation approach: the Nealder and Mead method and its simulated annealing modification, the Marquardt method, the Powell, Box , and Levenberg-Marquardt methods and modified Gauss and Newton method. Also, the χ^2 criterion turned out to be one of the best criteria for judging the goodness of the simulation-based fits as well as for parameter fitting. By the method of asymptotic standard errors an optimal equilibrium could be achieved between CPU and the accuracy of the calculated parameters requiring a confidence interval evaluation procedure.

In **Chapter 4** a computer simulation approach, based on Monte Carlo and optimization methods, is described for the investigation of energy transport and -relaxation, as these processes affect the fluorescence- and fluorescence anisotropy decay. This novel type of analysis of time-resolved

fluorescence data is demonstrated for two differently organized porphyrin systems. Equations for the χ^2 criterion and its weighting factors, used in Monte Carlo simulation fitting procedure, are presented and modified for different types of time-resolved data analysis. This Chapter presents some illustrative examples demonstrating several fits of the fluorescence- and the fluorescence anisotropy decay using Monte Carlo simulation fitting. Also, the conceptual properties behind the fitting procedures are discussed.

Chapter 5 reports the results of a study of self-organized [Zn(4-Py)TrPP]$_4$ tetramers in toluene and polystyrene/toluene solutions and in solid films, as well as of ordered ZnTOPP domains in solid films. The effects of lowering the temperature or increasing the concentration of a ZnM(4-Py)TrPP/toluene solution on the absorption- and fluorescence spectra are the result of porphyrin aggregation. A simple exciton model can describe the optical spectra of porphyrin aggregates in solution as the result of porphyrin ligation within the symmetrical tetramer structure. The shifts, found in both the Q-band region of the absorption spectrum and in the fluorescence spectrum can be ascribed to coordination of the metal center of one ZnM(4-Py)TrPP molecule to the pyridyl substituent of a second, neighboring molecule. Excitonic interactions can be neglected for the S_1 state. The splitting of the Soret band in the absorption spectrum can be readily explained by an excitonic interaction in the S_2-state between the four mutually perpendicular ZnM(4-Py)TrPP monomers in the tetramer. This symmetrical tetramer is the smallest complex that can account for all of the observed shifts in the optical spectra. The experimental thermodynamic parameters are in good agreement with those expected for a tetramer. The global analysis of the time-resolved fluorescence decays of ZnM(4-Py)TrPP in toluene and PS/Tol at 10 ^{0}C yields two fluorescence components with 1.95 - 2.22 ns and 1.53 - 1.56 ns lifetime, where the shorter component is assigned to ligated monomers in the fraction of cyclic tetramers in the solution. The ~1.5 ns fluorescence component is associated with a rotational correlation time of ~ 1 ns, as compared to ~100 ps for the monomer at 10°C, in agreement the size of the tetramer.

The fluorescence- and anisotropy decay analysis by Monte Carlo simulations yields a singlet-singlet energy transfer rate constant of 40×10^9 s^{-1} for the average energy transfer within the tetramer.

Applying the Monte Carlo simulations to ZnTOPP films, the results of fluorescence- and anisotropy decay can be explained by assuming a multi-domain model of parallel porphyrin stacks. In each stack the porphyrin planes are perpendicular to the substrate and form an angle of 45° with the long stack axis. Monte Carlo simulation analysis yields the rate constants for intra-

stack and inter-stack energy transfer as $\sim 1 \times 10^{12}$ s^{-1} and $\sim 80 \times 10^{9}$ s^{-1}; whereas the fluorescence lifetime is $\sim 1.8 \times 10^{-9}$ s.

The results of fluorescence and fluorescence anisotropy decay measurements of Zn(4-Py)TrPP films are qualitatively described. A preliminary analysis of these results indicates that the optical spectra and the fluorescence anisotropy decay of the Zn(4-Py)TrPP films are basically in agreement with the tetramer porphyrin structure being the assembling unit in the solid film.

Samenvatting

Het hoofddoel van dit proefschrift was de ontwikkeling van een geavanceerde computersimulatiemethode om de analyse van het complexe fluorescentie- en fluorescentieanisotropieverval van porfyrine oligomeren, zowel in oplossing als in dunne vaste films, in de aanwezigheid van energieoverdrachtsprocessen, te verbeteren. Met de toepassing van lichtverzamelende antennes voor zonnecellen in gedachten, zijn de energieoverdrachts- en relaxatieprocessen van verschillende kunstmatige antennes bestudeerd met de ontworpen computersimulatiemethode. Deze antennes bestaan uit ultra dunne films van zelf-organiserende porfyrines en hun oligomeren. De films zijn gemaakt m.b.v. de spin-coating methode, gebruikmakend van verschillende oplosmiddelen.

Hoofdstuk 1 bevat een algemene beschrijving van de fotofysische processen in kunstmatige fotosynthetische systemen, de steady-state en tijdsopgeloste fluorescentiespectroscopie, de methoden die werden gebruikt om de tijdsgecorreleerde single photon counting gegevens te analyseren en de methoden, die zijn gebruikt voor de mathematische modellering. Het theoretische kader dat in dit hoofdstuk ontwikkeld wordt, vormt de achtergrond voor het begrijpen van niet alleen de basale eigenschappen van de bestudeerde porfyrine systemen, maar ook voor het inzicht in zowel de experimentele technieken als de rekenmethoden waarmee deze systemen zijn onderzocht.

Hoofdstuk 2 beschrijft de geanalyseerde porfyrine systemen, de experimentele steady-state en tijdsopgeloste absorptie- en fluorescentiemethoden, de technische details van de gebruikte apparatuur, en karakteristieke resultaten m.b.t. de fotofysica van enkele porfyrinesystemen.

In **Hoofdstuk 3** worden de verschillende optimalisatie methoden voor het fitten van de experimentele fluorescentie vervalcurves met elkaar vergeleken, om inzicht te geven in de eigenschappen van deze methoden. Deze eigenschappen zijn belangrijk bij toepassing van Monte Carlo simulaties op de onderzochte energieoverdrachtsprocessen. Een aantal methoden blijkt veelbelovend te zijn voor praktische toepassing in de data-analyse, die gebruik maakt van computersimulaties. Het gaat daarbij om de Nealder en Mead-methode en de simulated annealing modificatie daarvan, de Marquardt-methode, de Powell-, Box-, en Levenberg-Marquardt methoden, en de gemodificeerde Gauss- en Newton-methode. Ook bleek dat het χ^2-criterium een van de beste is om de kwaliteit van op simulatie gebaseerde fits, maar ook van parameterfitting te beoordelen. Met behulp van de methode van de asymptotische standaard

afwijkingen kon een optimaal evenwicht verkregen worden tussen de benodigde CPU tijd en de nauwkeurigheid van de berekende parameters. Voor de laatste is een evaluatieprocedure nodig voor de bepaling van het betrouwbaarheids-interval.

Hoofdstuk 4 beschrijft een computer simulatiemethode, die is gebaseerd op Monte Carlo- en optimalisatiemethoden. Deze methode kan worden gebruikt voor het bepalen van de energietransport- en -relaxatie eigenschappen, omdat deze processen het fluorescentie- en fluorescentieanisotropieverval beïnvloeden. Deze nieuwe manier van analyseren van tijdsopgeloste fluorescentiedata wordt gedemonstreerd aan de hand van twee verschillend georganiseerde porfyrine systemen. Vergelijkingen zijn ontwikkeld voor het χ^2-criterium en de daarbij behorende gewichtsfactoren, die in de Monte-Carlo-simulatiefittingprocedure worden gebruikt en zijn aangepastaan de verschillende soorten analyses van de tijdsopgeloste data. In dit hoofdstuk worden enkele illustraties gegeven van verschillende fits van fluorescentie- en fluorescentieanisotropieverval, gebruikmakend van de Monte Carlo simulatiefitting. Ook worden de achtergronden van de fitprocedures besproken.

Hoofdstuk 5 rapporteert de resultaten van een studie van enerzijds zelf-georganiseerde [Zn(4-Py)TrPP]$_4$ -tetrameren in tolueen en polystyreen/tolueen oplossingen en anderzijds van vaste films van geordende ZnTOPP-domeinen. De effecten van temperatuurverlaging en concentratieverhoging van een ZnM(4-Py)TrPP/tolueenoplossing op de absorptie- en fluorescentiespectra blijken het gevolg te zijn van porfyrineaggregatie. Met behulp van een eenvoudig excitonmodel kunnen de optische spectra van deze porfyrineaggregaten worden beschreven als het gevolg van ligandering van de porfyrine eenheden binnen een symmetrische tetrameer-structuur. De spectrale verschuivingen in het Q-band gebied van het absorptie- en het fluorescentie spectrum kunnen worden toegeschreven aan coördinatie van het centrale zink ion van een ZnM(4-Py)TrPP- molecuul met de pyridyl substituent van een tweede naburig porfyrine molecuul. Exciton interacties kunnen voor de S$_1$-toestand verwaarloosd worden. De opsplitsing van de Soret-band kan gemakkelijk verklaard worden door exciton interacties tussen de S$_2$-toestanden van de vier onderling loodrechte ZnM(4-Py)TrPP-monomeren in het tetrameer. Dit symmetrische tetrameer is het kleinste complex dat alle experimentele spectrale verschuivingen in de zichtbare spectra kan verklaren. De experimentele, thermodynamische parameters stemmen goed overeen met de verwachte waarden voor een tetrameer. Toepassing van de globale analyse methode op de tijdsopgeloste fluorescentievervalcurven van ZnM(4-Py)TrPP in tolueen en in PS/Tol bij 10 ^{0}C levert twee levensduurcomponenten op: 1.95 - 2.22 ns en 1.53 - 1.56 ns. De kortste daarvan kan worden toegeschreven aan de fractie geligandeerde monomeren in de

oplossing. De ~1.5 ns fluorescentie component is geassocieerd met een rotatiecorrelatietijd van ~ 1 ns, vergeleken met de ~100 ps voor het monomeer bij 10°C, in overeenstemming met wat men verwacht op grond van de grootte van het tetrameer.

De analyse van het fluorescentie- en anisotropie verval van het tetrameer met behulp van Monte Carlo simulaties levert een gemiddelde snelheidsconstante voor singlet-singlet energieoverdracht op van 40×10^9 s^{-1}.

Bij toepassing van Monte Carlo simulatie op ZnTOPP films kunnen de resultaten van het fluorescentie- en anisotropieverval verklaard worden door een multi-domein model van parallelle porfyrine kolommen aan te nemen. In elke kolom staan de porfyrinevlakken loodrecht op het substraat en maken een hoek van 45° met de kolom-as. Uit de Monte Carlo simulatie volgen snelheidsconstanten voor energie overdracht binnen en tussen de kolommen van ~ 1×10^{12} s^{-1} en ~ 80×10^9 s^{-1}, bij een fluorescentielevensduur ~ 1.8×10^{-9} s is.

De resultaten van de de metingen van het fluorescentie- en fluorescentie-anisotropie verval van Zn(4-Py)TrPP-films kunnen op dit moment alleen kwalitatief worden beschreven. Een voorlopige analyse van deze resultaten wijst erop dat de optische spectra en de fluorescentie-anisotropie van de Zn(4-Py)TrPP-films in principe overeenstemmen met een film die is opgebouwd uit afzonderlijke porfyrine tetrameren.

Резюме

Основная цель данной диссертационной работы состоит в разработке метода компьютерного моделирования, позволяющего значительно повысить эффективность анализа сложных кривых затухания флуоресценции и анизотропии флуоресценции порфириновых олигомеров в растворах и тонких твердотельных пленках с учетом процессов переноса энергии. Применение разработанного метода позволило исследовать свойства переноса и релаксации энергии в ряде искусственных светособирающих антенн, элементов солнечных батарей, сконструированных на основе тонких пленок самоорганизующихся порфириновых олигомеров.

Глава 1 содержит формальное описание фотофизических процессов искусственного фотосинтеза, методов стационарной и кинетической спектроскопии, методов анализа экспериментальных данных, регистрируемых по методу однофотонного счета, а так же методов математического моделирования. Данная глава формирует основу для понимания фотофизических процессов, вместе с тем рассмотрены экспериментальные и вычислительные методы исследования порфириновых систем.

В **Главе 2** дано описание исследуемых Zn- порфириновых систем, стационарных и кинетических методов регистрации поглощения и флуоресцентного испускания, технических деталей экспериментального оборудования. Рассмотрены типичные фотофизические результаты некоторых порфириновых систем.

В **Главе 3** приведены результаты сравнительного анализа различных методов оптимизации с целью исследования наиболее эффективных условий для аппроксимации кривых затухания флуоресценции и применения с использованием метода Монте Карло. Показано, что самыми перспективными методами при анализе данных являются: метод Нелдера-Мида и его "simulated annealing" модификация, метод Марквардта, метод Бокса, метод Поуэла, метод Левенберга-Марквардта, а также модифицированный метод Гауса-Ньютона. Критерий χ^2 обеспечивает достаточно точную оценку качества аппроксимаций с учетом моделирования, вместе с тем является наиболее удобным инструментом для оценки параметров. Метод асимптотических стандартных ошибок позволяет получить оптимальное соотношение между временем и точностью оценки доверительных интервалов для параметров.

Глава 4 посвящена разработке метода компьютерного моделирования на основе метода Монте Карло, который используется для исследования процессов переноса и релаксации энергии, обуславливающих затухание флуоресценции и анизотропию флуоресценции. Новый подход к анализу затухания флуоресценции представлен на примере двух порфириновых систем. Получены выражения для критерия χ^2 и весовых факторов, используемых в процедурах аппроксимации различных типов кинетических экспериментальных данных. В главе представлены примеры аппроксимации кривых затухания флуоресценции с использованием метода Монте Карло. Обсуждены концептуальные свойства имитационных процедур аппроксимации.

Результаты исследования самоорганизующихся [Zn(4-Py)TrPP]$_4$ тетрамеров в растворах и твердотельных пленках, а также упорядоченных ZnTOPP доменов в твердотельных пленках представлены в **Главе 5**. Результатом агрегации порфиринов объясняется эффект влияния изменения температуры или концентрации раствора образца ZnM(4-Py)TrPP на спектры поглощения и испускания. Доказано, что в соответствии с простейшей экситонной моделью, оптические спектры порфириновых агрегатов являются результатом лигандирования внутри симметричной тетрамерной структуры. Сдвиги Q- полос спектров поглощения и испускания соответствуют координации металлоцентра ZnM(4-Py)TrPP молекулы к пиридиловому заместителю второй, соседней молекулы. Экситонные взаимодействия пренебрежимо малы для возбужденных синглетных состояний S_1. Расщепление полосы Соре в спектре поглощения объясняется экситонным взаимодействием в возбужденном синглетном состоянии S_2 между четырьмя взаимно перпендикулярными ZnM(4-Py)TrPP мономерами в тетрамерной структуре. Такой симметричный тетрамер является наименьшей структурой удовлетворяющей наблюдаемым сдвигам в оптических спектрах. Термодинамические параметры, рассчитанные на основе оптических спектров, согласуются с теоретически параметрами вычисленными для структуры типа тетрамер. Глобальный анализ кинетических кривых затухания флуоресценции ZnM(4-Py)TrPP в растворах толуола и полистирена позволяет выделить две компоненты флуоресценции с временами жизни 1.95 - 2.22 нс и 1.53 - 1.56 нс, где короткая компонента соответствует лигандированным мономерам объединенным в циклические тетрамеры. Компонента флуоресценции ~1.5 нс ассоциирована с временем вращательной корреляции ~ 1 ns и соответствует геометрическому размеру тетрамерного комплекса, в то же время времени вращательной корреляции ~100 пс соответствует мономеру.

Анализ кривых затухания флуоресценции и анизотропии флуоресценции методом Монте Карло позволяет получить среднее значение константы скорости синглет-синглетного переноса энергии в тетрамере равное 40×10^9 с$^{-1}$.

Используя метод Монте Карло для анализа ZnTOPP пленок, кривые затухания флуоресценции и анизотропии флуоресценции объясняются мульти-доменной моделью параллельных порфириновых стеков. В каждом стеке молекулы ориентированны перпендикулярно к основанию подложки и формируют угол в 45° с продольной осью стека. Анализ, с использованием метода Монте Карло, позволяет получить константы скорости переноса энергии равные $\sim 1 \times 10^{12}$ с$^{-1}$ и $\sim 80 \times 10^9$ с$^{-1}$ для внутри стекового и меж стекового переноса соответственно. Оцененное время жизни флуоресценции $\sim 1.8 \times 10^{-9}$ с.

Качественно изучены результаты измерений кинетических кривых затухания флуоресценции и анизотропии флуоресценции Zn(4-Py)TrPP пленок. Предварительный анализ экспериментальных результатов показывает, что оптические спектры и затухание анизотропии флуоресценции Zn(4-Py)TrPP пленок соответствуют модели порфиринового тетрамера, который является образующим блоком в твердотельных пленках.

Acknowledgments

Curriculum vitae

Mikalai Yatskou was born on January 19th, 1974 in the city of Minsk, Belarus as son of Nikolai Yatskou and Galina Yatskova. His elementary studies were completed at the secondary school N 71 of Minsk (1991). After following undergraduate studies at the Belarusian State University, he obtained the degree of Master of Science in the field of Radio Physics and Electronics (1996). During that year he worked as an engineer at the Belarusian State University. At the end of 1996 he entered a Ph.D. position at the Department of Systems Analysis, Belarusian State University on a research project aimed at the development of computer simulation methods and optimization algorithms. At the end of 1998, he successfully applied for a Ph.D. position at the Laboratory of Molecular Physics, financially supported by a Wageningen University Sandwich Fellowship. The project was initiated in May 1999 and finished in December 2000.

Computer simulation of energy relaxation and -transport in organized porphyrin systems.
Yatskou, Mikalai.

Abstract

Yatskou, M., 2001. Computer simulation of energy relaxation and -transport in organized porphyrin systems.

This Thesis is devoted to the investigation of optical photophysical processes in organized porphyrin systems. These systems can serve as molecular antennas for organic solar cells, a field of research which recently has received increasing interest. Using a novel application of Monte Carlo computer simulation an improved analysis of the complex fluorescence and fluorescence anisotropy decay in the presence of energy transfer processes has been introduced.

Self-organized [Zn(4-Py)TrPP]$_4$ tetramers in solution and in solid films as well as ZnTOPP domains in spin coated films have been studied experimentally by steady state and time-resolved spectroscopy. The results have been analyzed using the abovementioned Monte Carlo simulation, yielding the characteristic rate constants for energy transfer- and relaxation processes.

The results of these Monte Carlo simulations are: for [Zn(4-Py)TrPP]$_4$ tetramers in solution the fluorescence lifetime is $\sim 1.5 \times 10^{-9}$ s and nearest neighbor energy transfer rate constant is $\sim 40 \times 10^9$ s^{-1}; ZnTOPP forms parallel porphyrin stacks within one domain in the films, whereas in each stack the porphyrin planes are perpendicularly oriented with respect to the substrate and make an angle of 45° with the long stack axis. As follows from the fit of simulated decay curves to the experimental fluorescence- and fluorescence anisotropy decay curves the rate constants for intra-stack and inter-stack energy transfer are $\sim 1 \times 10^{12}$ s^{-1} and $\sim 80 \times 10^9$ s^{-1}, respectively, whereas the fluorescence lifetime is $\sim 1.8 \times 10^{-9}$ s.